



UNIVERSIDAD  
DE BURGOS



UNIVERSITÀ  
DEGLI STUDI  
DI PALERMO

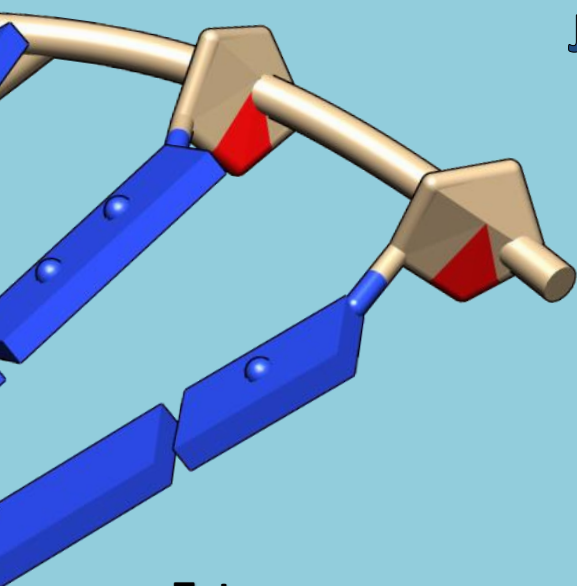
---

# THE INTERACTION OF NOVEL TRANSITION METAL COMPLEXES AND LIGANDS WITH BIOMOLECULAR TARGETS: KINETIC, THERMODYNAMIC AND COMPUTATIONAL INVESTIGATIONS

---

PhD Thesis

Javier Santolaya Rubio



27 February 2019

**Tutors:**

**Prof. Begoña García Ruiz (Universidad de Burgos)**

**Prof. Giampaolo Barone (Università degli studi di Palermo)**





<b>Index</b>	<b>3</b>
<b>Abstract</b>	<b>7</b>
<b>Acknowledgements</b>	<b>8</b>
<b>Prologue</b>	<b>10</b>
<b>Chapter I: Introduction</b>	<b>13</b>
<b>1.1 Cancer</b>	<b>14</b>
<b>1.1.1</b> Definition and main features	14
<b>1.1.2</b> Cancer throughout history	14
<b>1.1.3</b> Role of science in cancer treatment	15
<b>1.2 Nucleic acids</b>	<b>16</b>
<b>1.2.1</b> Definition and structure	16
<b>1.2.2</b> Double strand DNA	17
<b>1.2.3</b> G-quadruplex	18
<b>1.3 Mechanism of DNA/Drug binding</b>	<b>21</b>
<b>1.3.1</b> Interaction toward double strand DNA	21
<b>1.3.2</b> Interaction toward G-quadruplex	23
<b>Chapter II: Methods</b>	<b>25</b>
<b>2.1 Experimental section</b>	<b>26</b>
<b>2.1.1</b> Materials	26
<b>2.1.2</b> Experimental techniques	27
<b>2.1.2.1</b> pH measurements	27
<b>2.1.2.2</b> Absorption spectrophotometry	27
<b>2.1.2.3</b> Circular dichroism (CD)	28
<b>2.1.2.4</b> Viscosity	30
<b>2.1.2.5</b> Fluorescent resonance energy transfer (FRET) melting assays	30
<b>2.2 Computational methods</b>	<b>31</b>
<b>2.2.1</b> Quantum chemical calculations	32
<b>2.2.2</b> Molecular dynamics (MD) simulations	32
<b>2.2.3</b> Quantum mechanics/Molecular mechanics calculations	34



<b>Chapter III: DNA binding of half-sandwich Ru(II) and Ir(III) complexes: experimental and computational studies</b>	<b>35</b>
<b>3.1 Introduction</b>	<b>36</b>
<b>3.2 Materials and Methods</b>	<b>37</b>
<b>3.2.1</b> Materials	37
<b>3.2.2</b> Experimental techniques	37
<b>3.2.3</b> Computational details	39
<b>3.3 Results and discussion</b>	<b>40</b>
<b>3.3.1</b> Experimental results	40
<b>3.3.2</b> Computational results	48
<b>3.4 Conclusions</b>	<b>55</b>
<b>Chapter IV: Role of seroalbumin in the cytotoxicity of <i>cis</i>-dichloro Pt(II) complexes with (N<sup>^</sup>N)-donor ligands bearing functionalized tails</b>	<b>57</b>
<b>Summary</b>	<b>58</b>
<b>Article</b>	<b>62</b>
<b>Chapter V: <i>Cis</i>-dichlorodiamine complexes of Ni(II), Pd(II) and Pt(II): theoretical study of hydrolysis and DNA-binding</b>	<b>79</b>
<b>5.1 Introduction</b>	<b>80</b>
<b>5.2 Computational details</b>	<b>81</b>
<b>5.3 Results and discussion</b>	<b>81</b>
<b>5.4 Conclusion</b>	<b>87</b>
<b>Chapter VI: Kinetic evidence for interaction of TMPyP4 with two different G-quadruplex conformations of human telomeric DNA</b>	<b>89</b>
<b>Summary</b>	<b>90</b>
<b>Article</b>	<b>92</b>

<b>Chapter VII: Fishing for G-quadruplexes in solution with a perylene diimide derivative labeled with biotins</b>	<b>105</b>
<b>Summary</b>	<b>106</b>
<b>Article</b>	<b>108</b>
<b>Chapter VIII: Screening of Rh and Ir complexes interaction with different G-quadruplex conformations</b>	<b>141</b>
<b>8.1 Introduction</b>	<b>142</b>
<b>8.2 Materials and methods</b>	<b>142</b>
<b>8.2.1. Materials</b>	<b>142</b>
<b>8.2.2. Experimental techniques</b>	<b>144</b>
<b>8.3 Results and discussion</b>	<b>144</b>
<b>8.4 Conclusion</b>	<b>147</b>
<b>Chapter IX: General overview</b>	<b>149</b>
<b>Chapter X: Publications and conferences</b>	<b>151</b>
<b>Chapter XI: Abbreviations and bibliography</b>	<b>155</b>
<b>Annexed: Curriculum Vitae</b>	<b>169</b>



# Abstract

*“Doctor of Philosophy”*, Universidad de Burgos, Università degli studi di Palermo:

**“The interaction of novel transition metal complexes and ligands with biomolecular targets: kinetic, thermodynamic and computational investigations”** by Javier Santolaya Rubio.

## Spanish

A través de la combinación de métodos experimentales y computacionales se han estudiado diferentes tipos de interacciones de diversas moléculas con estructuras de ADN, en concreto ADN en conformación de doble hélice y la G-quadruplex. Las moléculas estudiadas se pueden dividir en 2 tipos: (I) compuestos formados por centros metálicos de transición y (II) compuestos orgánicos. La importancia biológica de este estudio es significativa, porque es bien sabido que la interacción con estructuras nucleicas (B-DNA o G-quadruplex) puede provocar la inhibición de sus funciones biológicas y con ello el fin de la replicación celular, pudiendo conducir por ejemplo al final de la replicación de células cancerosas y finalmente la muerte de estas. En la primera parte de la tesis se describen en profundidad los estudios de interacción con DNA en estructura de doble hélice (**Capítulos III-V**) mientras que la segunda parte se centra en los estudios sobre G-quadruplex (**Capítulos VI-VIII**).

## Italian

Attraverso la combinazione di metodi sperimentali e computazionali sono state studiate le interazioni di diverse molecole con DNA in conformazione a doppia elica e G-quadruplex. Le molecole considerate possono essere suddivise in due categorie: (I) composti formati da centri di metalli di transizione e (II) composti organici. L'importanza biologica di questi studi è significativa, perché è ben noto che l'interazione con le strutture di acidi nucleici può causare l'inibizione delle loro funzioni biologiche e con essa la fine della replicazione cellulare, essendo in grado di condurre, ad esempio, in casi di cancro a fine della replicazione di dette cellule cancerose e infine la morte di queste. La prima parte della tesi descrive gli studi di interazione con il DNA a doppia elica (**Capitoli III-V**) mentre la seconda parte si concentra sugli studi di interazione con DNA G-quadruplex (**Capitoli VI-VIII**).

# Acknowledgements

Después de redactar la tesis doctoral, es imposible no mirar atrás y pensar en todas aquellas personas que de una manera o de otra me han servido de apoyo durante este largo período.

Para comenzar agradezco a mi directora de tesis por parte de la Universidad de Burgos, Begoña García, por la confianza que ha depositado en mí durante todos estos años, no sólo durante el doctorado sino desde el Trabajo de Fin de Grado, permitiéndome formar parte de este grupo de investigación, y en particular por este proyecto en cotutela que me ha dado la oportunidad de obtener muchos conocimientos y experiencias muy útiles para el futuro.

A José María Leal por su atención, apoyo y disponibilidad durante todo el período que he estado en este laboratorio, y que junto a Begoña siempre ha favorecido tener un buen ambiente de trabajo.

Especialmente también agradezco a Natalia Busto, un pilar importante durante el trabajo experimental en el laboratorio, con explicaciones de cómo utilizar los equipos hasta consejos para trabajar un poquito más ha sido una de las personas fundamentales para que esta tesis esté completada. Por el laboratorio durante estos últimos 5 años han pasado muchas personas con las que compartes muchas horas diariamente, pero siempre se ha mantenido un ambiente óptimo donde uno se siente cómodo. Héctor y Matteo, me dieron un apoyo futbolístico importante para discutir los partidos del fin de semana y poder disfrutar del Comunio. Una vieja conocida desde el día que empezamos la carrera, Ana Rosa, buena trabajadora muy comprometida y que junto a un grupo de chicas (Quimi-uvis) consiguieron no sólo que acabara la carrera (que ya era un proyecto complicado), sino que gracias a sus mentiras los días de “exámenes falsos” seguramente este aquí hoy. También he tenido suerte de coincidir con Cristina, otra ya conocida, pero que después de compartir este tiempo uno se da cuenta de lo verdaderamente buena trabajadora que es y el alto grado de conocimientos que tiene, estando siempre a disponibilidad para lo que necesites. Posteriormente llegaron Nathalie y Carolina, dos chicas muy simpáticas y con muchas ganas de aprender que completan un grupo con un alto nivel de trabajo que estoy seguro ha tenido una fortísima influencia positiva en mí y en todo mi trabajo.

No se puede pasar por alto el agradecer la cofinanciación recibida por la Obra Social “La Caixa”, Project OSLC-2012-007, del que es I.P. la directora de la tesis, y por l’Università degli studi di Palermo, a través del MIUR, Ministero dell’istruzione, sin la cual la realización de este proyecto no hubiera sido posible.

D'altra parte, all'Università di Palermo voglio ringraziare il mio tutor Giampaolo Barone, che dallo stesso giorno in cui è iniziato il dottorato si è sempre preso cura di me. Quello che devo ringraziare di più è il trattamento ricevuto, che ha reso l'essere lontano da casa una cosa non molto difficile. Sono molto felice di aver condiviso queste dottorto con lui e ho anche conosciuto e condiviso molti momenti con la sua famiglia,

facendomi sentire bene e felice, che quando sei lontano dalle tuoi è qualcosa di più difficile. E d'altra parte apprezzo tutta la conoscenza che mi ha aiutato ad apprendere, soprattutto a livello di chimica computazionale, dove ho iniziato da zero e ho terminato il dottorato con un livello adeguato. A tutte le persone che ho incontrato lì, Riccardo B., Angelo, Elisa, Riccardo R., Lorenzo e Giuliana grazie per aver condiviso così tanti momenti con me e aiutami così tanto in tante cose.

Por último, uno de los apoyos más importantes de todos, a mi familia y mis amigos más cercanos, en especial a mis padres, hermana y mis abuelos, que son han los que me están soportando durante estos 3 años y que siempre me dado apoyo incondicional y muchas fuerzas para tirar para adelante cuando la cosa estaba negra. ¡Muchas gracias a todos!

# Prologue

For a long time and still nowadays, scientists have deepened the understanding and the treatment of cancer, one of the diseases that cause the highest mortality in the world. In fact, approximately about 8.2 million of persons die each year due to cancer and it is estimated that there are 32 million patients with this disease.<sup>[1]</sup>

Some of the main treatments for cancer are surgery, radiotherapy and chemotherapy, and specially the latter is where Chemistry plays an important role, because through over time it has been found that different drugs are effective for cancer treatment. However, despite the great effort, there are still many limitations. For example, drugs are not usually applicable to all range of tumors. Moreover, there are serious side effects in the treatments. Nucleic acids are essential in processes like replication or transcription, and it has been revealed that anti-cancer activity of many employed drugs is strongly related to their binding to DNA, which has become over these decades one of the most important biological target for cancer treatment. On the other hand, although this binding has been the object of several investigations over the last decades and many advances and discoveries have been achieved, there is still a long way to go.

This thesis is based on a set of studies, from both experimental and computational points of view, of the interaction between small molecules, organic ligands or transition metal complexes, with two different DNA conformations: (I) double-helical DNA (B-DNA) and (II) G-quadruplex DNA. The main aim is to show that complementing experimental results with computational approaches can easily allow to understand the binding mode and help to describe more accurately the binding mechanism. Several techniques have been used in both experimental and computational studies, such as UV-visible absorption spectroscopy, circular dichroism, viscosity and thermal denaturation, and molecular dynamics (MD) simulations and quantum mechanics/molecular mechanics (QM/MM) calculations. All employed methods are described in detail in **Chapter II: METHODS**.

The thesis can be divided in two main parts:

- **Part 1**, from **Chapter III to V**, based on experimental or/and computational studies of the interaction between small molecules and double helical DNA, includes the study and comparison of the binding of two half-sandwich transition metal complexes of Ru(II) and Ir(III) toward calf thymus DNA (ct-DNA), an examination of the biological properties of four Pt(II) complexes analogues to cisplatin and the role of serum albumin in their cytotoxicity as well as a computational study on the hydrolysis of cis-dichloro-diamino complexes of platinum(II), palladium(II) and nickel(II) and their binding to B-DNA.

- **Part 2, from Chapter VI to VIII**, both experimental and computational techniques were employed but, in this case, the biomolecular target were G-quadruplex structures. This part contains i) the binding study between G-quadruplex and a perylene diimide derivative labeled with biotins, ii) a kinetic and thermodynamic evaluation of TMPyP4 porphyrin toward the two hybrid structures of G-quadruplexes that are reported to be formed in  $K^+$  aqueous solution and iii) a screening of different transition metal complexes in presence of different G-quadruplex sequences, through FRET melting assays and competition assays, in order to evaluate the binding specificity of the complexes toward G-quadruplex in the presence of B-DNA.
- **Chapter IX** gives a short and general overview.





# **Chapter I**

---

## **Introduction**

## **1.1 Cancer**

### **1.1.1 Definition and main features**

As defined by *World Health Organization* (WHO, February 2018): “Cancer is the uncontrolled growth of cells, that can affect any part of the body. Cancer cells grow beyond their usual boundaries and can invade adjoining parts of the body and spread to other organs, the latter process is referred to as metastasizing. Metastases are the major cause of death from cancer”. Some features of this disease are described below based on *National Institutes of Health* (NIH, Bethesda, Maryland, U.S.A, February 2015) considerations: normally, human cells grow and divide as the body needs them and when cells grow old they die, however, when this disease develops these processes break down and old or damaged cells survive while they should die. These needless cells can divide without stopping and may form tissue growths called tumors. During their growth, cancer cells can break off and travel to distant places in the body (through blood or lymph system) and form tumors far from the original tumor, a phenomenon known as metastasis.

### **1.1.2 Cancer throughout history**

Historically the first references to cancer were found in Egypt, concretely in the “*Edwin Smith papyrus*”, which is dated 1600 years BC, and describes tumors or ulcers in the chest that were treated with cauterization. Later in the XVII century, significant cases of cancer treatment can be found, despite the rudimentary techniques of this period, among which Clara Jacobi’s case is mentioned. This Dutch woman had a huge tumor between her head and neck, and in 1689 the tumor was successfully removed surgically.

Subsequently, an important contribution was made by John Hunter, surgeon and anatomist that first used some words referred to this disease that still we hear nowadays: “No cure has yet been found”. Moreover, he suggested that since they had no such medicine techniques, they were often obliged to remove cancerous parts through surgery extirpation, and that in certain cancer types surgery could be effective.<sup>[2]</sup>

In the XX century, namely in 1953, J.D. Watson and F.H.C Crick, supported by Rosalind Franklin X-ray diffraction images, published the discovery of DNA double helix structure,<sup>[3]</sup> a work for which in 1962 they received the Nobel Prize in Medicine and which not only opened a door of new knowledge to science but also propelled it to where it has arrived nowadays. The understanding of the importance of DNA as the base of our genetic code as well as the research of different DNA structures and their biological role in living beings have helped to understand what we called “Central

dogma of molecular biology”, which is an explanation of the flow of genetic information within a biological system, **Figure 1**.

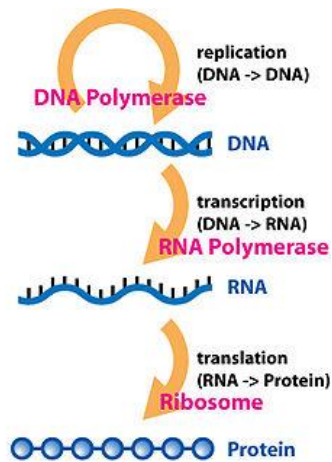


**Figure 1.** Central dogma of molecular biology as suggested by F. Crick in 1958.<sup>[4]</sup>

### 1.1.3 Role of Science in cancer treatment

Strong efforts and great advances achieved in Science has allowed to establish an appropriate definition and comprehension of cancer hallmarks as it is shown in **Figure 2**. The hallmarks comprise six biological capabilities acquired during multistep development of human tumors.<sup>[5]</sup>

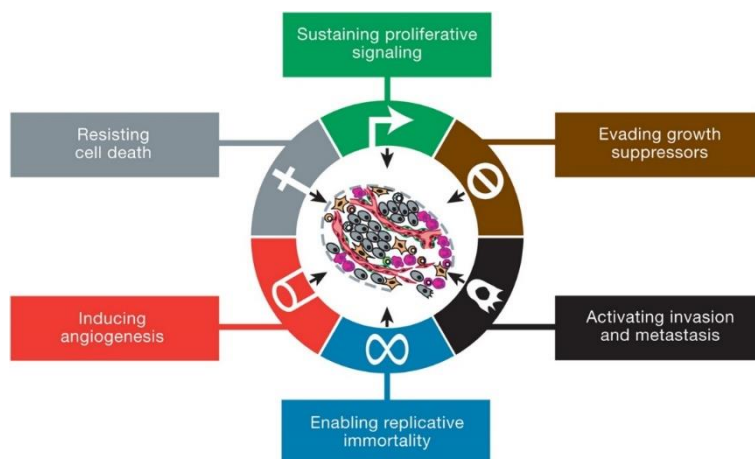


**Figure 2.** Cancer hallmarks.<sup>[5]</sup>

In consequence of the significant advances and discoveries during the last decades, it has been possible to considerably expand the types of cancer treatments,<sup>[6]</sup> some of which are briefly mentioned and described below.

- Surgery, the oldest known procedure, consist in the extirpation of the entire tumor, strongly limited if cancer is in metastasis phase.
- Chemotherapy, based on the use of drugs such as cisplatin<sup>[7]</sup> to decrease the growth of tumor cells has resulted in successful treatment of many types of cancer, but there is still a strong risk of serious side effects.
- Radiation therapy, used for cancer diagnosis and in treatment, usually cancer is removed by surgery and then the adjacent tissues are radiated. (In 20<sup>th</sup> century, it was found that radiation could cause cancer as well as cure it)
- Immunotherapy, is a biological treatment based on employing substances made by the body to improve or restore the immune system functions, boosting the natural defenses to fight cancer.

Interestingly, chemotherapy is often combined with surgery and/or radiation therapy, for a better outcome of the disease treatment. But although there are several methods to fight cancer and even some of them have evolved throughout history, there are still many limitations in all of them that Science keeps trying to minimize. Focusing on chemotherapy, side effects, low specificity of drugs towards cancer cells in presence of healthy cells and the narrow range of tumors in which drugs are effective, have generated a significant increase in the design and synthesis of new potential anticancer drugs. This PhD thesis represents a small contribution to the latter research approach.

## **1.2 Nucleic Acids**

### **1.2.1 Definition and structure**

Nucleic acids are linear polymers formed by the covalent binding of nucleotides and are characterized by the presence of three main structural components: (i) a phosphate group, (ii) a five-membered ring sugar (ribose or 2-deoxyribose for RNA and DNA, respectively) and (iii) a nitrogen base.<sup>[8-10]</sup>

Nitrogen bases, displayed in **Figure 3**, can be classified into two main groups: (i) purines, e.g. adenine and guanine and (ii) pyrimidines, e.g. cytosine, thymine and uracil. Thymine and uracil are only present in DNA and in RNA, respectively. RNA differs from DNA for the presence of a 2'-hydroxyl group in the sugar ring, as highlighted below.

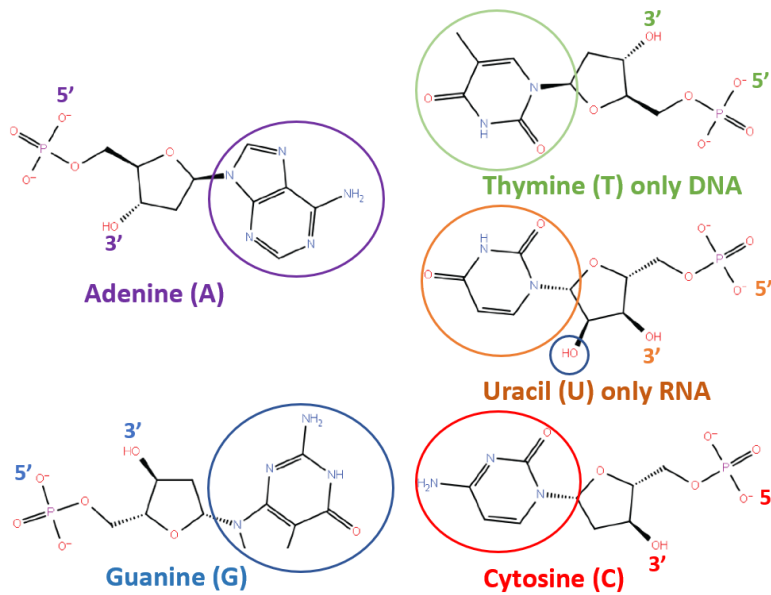


**Figure 3.** The structure of different nucleotides formed by the five different nitrogen bases.

The phosphate groups are the linking units between contiguous nucleotides, through a phosphodiester linkage between the 5' position of one nucleotide to the 3' position of the next. The deprotonation of the phosphate group at neutral pH creates a negatively charged backbone and the resulting strand is always described directionally from position 5' to 3', constituting the so-called primary structure of nucleic acids.<sup>[8]</sup>

### 1.2.2 Double strand DNA

DNA is preferably arranged in a double-stranded conformation, called secondary structure, which results from the combination of two complementary strands in an antiparallel sequence. Canonical Watson-Crick base pairs<sup>[3]</sup> establish that Guanine and Cytosine are bonded through 3 hydrogen bonds while Adenine and Thymine (of Uracil) through 2 hydrogen bonds, as shown in **Figure 4**. In addition to hydrogen bonds, another important contribution in the stabilization of double strand DNA is the  $\pi$ - $\pi$  interaction between stacked aromatic rings of neighboring base pairs. The Watson-Crick double helical structure is referred to as B-DNA, the most stable conformation for a random DNA sequence under physiological conditions, but also A and Z forms have been well characterized.<sup>[11]</sup> A-DNA<sup>[12]</sup> is favored in solutions that are relatively dry. As B-DNA is arranged in a right-handed double helix but in a wider and shorter conformation and the number of base pairs per helical turn is 11 rather than 10.5 as in B-DNA. On the other hand, Z-DNA<sup>[13]</sup> is arranged in a left-handed double helical conformation, with 12 base pairs per turn and showing a more slender and elongated

structure. Whether A-DNA presence in cells is uncertain, there are evidences for short stretches of Z-DNA in both prokaryotes and eukaryotes.

Due to the asymmetry of the two strands, each rotation around axis causes the formation of two grooves, as shown in **Figure 4**, major and minor,<sup>[14]</sup> having different sizes (about 15 Å and 6 Å wide, respectively). DNA in double helix conformation is a remarkably flexible molecule in solution, because of the possible rotations around the C-C, C-O and O-P bonds in the sugar-phosphate backbone.

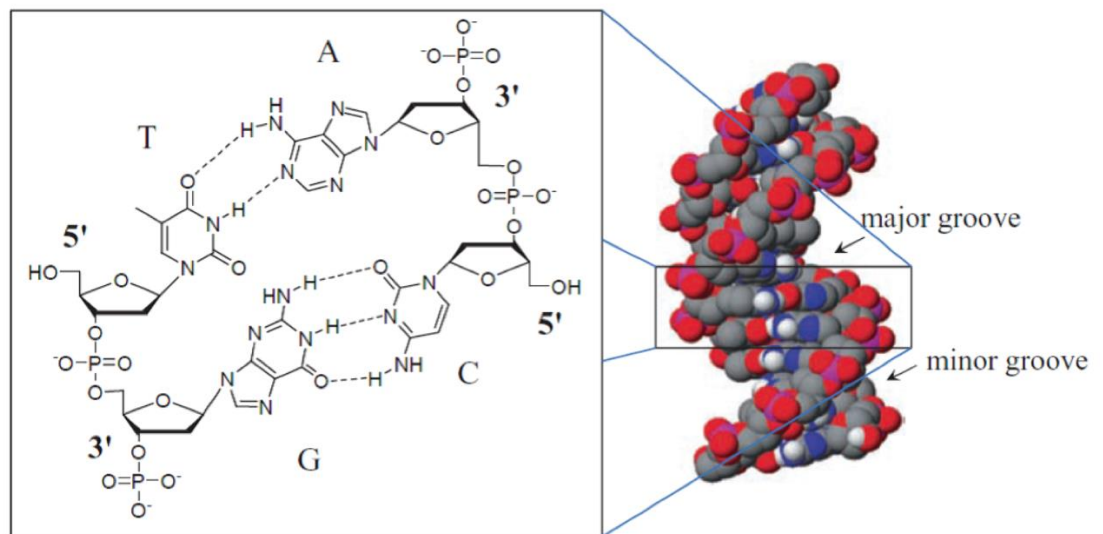


**Figure 4.** Representation of nucleotide base pairing in helical DNA proposed by Watson and Crick.

### 1.2.3 G-quadruplex

G-quadruplexes, are characteristic folded DNA or RNA structures appearing when guanine rich stretches of nucleic acids self-associate, forming guanine quartets.<sup>[15,16]</sup> These quartets are stabilized, by hydrogen bonds between the guanines based on Hoogsteen base-pairing, **Figure 5**, while Watson-Crick base pairing occurs in double stranded DNA. Moreover, a monovalent metal ion, usually sodium or potassium, is needed inside the central channel to compensate the negative charge of the quadruplex backbone.<sup>[17]</sup>

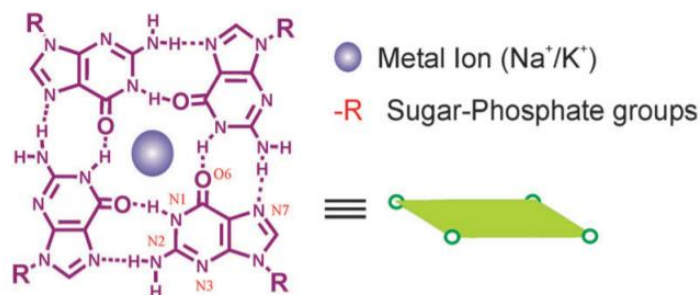


**Figure 5.** Schematic representation of the G-quartet/tetrad.<sup>[18]</sup>

It is possible to find different topologies in this type of structures, due to changes in the loops, positive ions and/or sequence.<sup>[19]</sup> The most common classifications for G-quadruplex depending on their folding are described below.<sup>[20]</sup> The most general classification considers the number of strands, **Figure 6**, forming the G-quadruplex, and it differs between: (i) intramolecular, folding of a single strand itself and (ii) intermolecular, involving two or more different DNA strands.

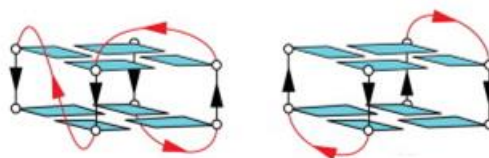


**Figure 6.** Examples of intramolecular (left) and intermolecular (right) G-quadruplex topologies.<sup>[21]</sup>

Based on the orientation of the strands, **Figure 7**, G-quadruplexes can be divided into (i) parallel, with all strands in the same direction, (ii) antiparallel, with two strands in one direction and the other two in the opposite, and (iii) hybrid, with three strands in the same direction.

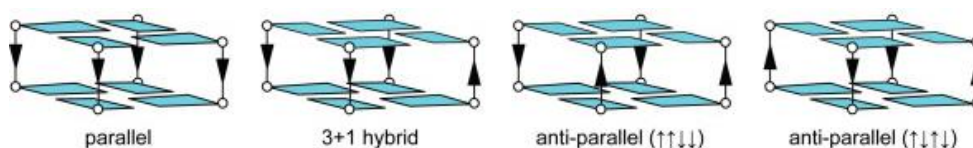


**Figure 7.** Classification of G-quadruplex topology as a function of the strand orientation.<sup>[21]</sup>

G-quadruplexes require a connecting loop, which can be propeller, diagonal or lateral (**Figure 8**), so the diversity of combinations of those leads to many more different G-quadruplex structures.



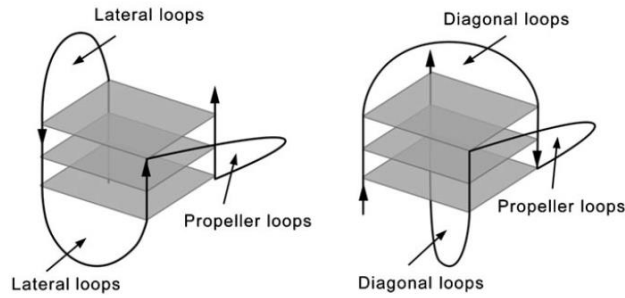


**Figure 8.** Loop regions in G-quadruplex structures.<sup>[16]</sup>

Human telomeres contain d(TTAGGG)<sub>n</sub> sequences which can form G-quadruplex structures. The stabilization of the latter block telomerase from binding to the terminal single-strands end of telomeres, driving to cell apoptosis (**Figure 9**) Interestingly, telomerase is a protein overexpressed in cancer cells. For this reason, the stabilization of G-quadruplex structures in the telomeres is considered successful for selectively targeting cancer cells.<sup>[16]</sup>

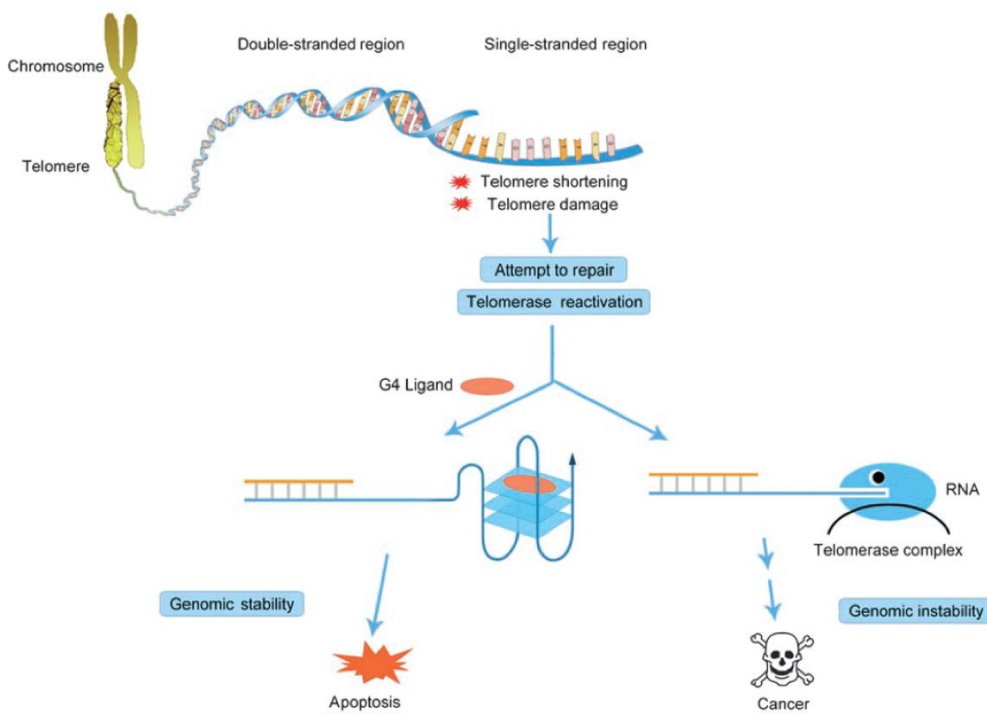


**Figure 9.** Structural and biological roles of telomeres and the effect of G-quadruplex formation.<sup>[16]</sup>

More recently several important regions in the human genome have been reported to adopt G-quadruplex structures, as immunoglobulin. Within these regions mutational hot spots and regulatory elements with oncogene promoters are found.<sup>[22]</sup> For instance, c-MYC, one of the most commonly deregulated genes in human cancers, has a DNA G-quadruplex motif in the promoter Nuclease Hypersensitive Element. The

highest abundance of G-quadruplex is found at telomeres and gene promoters, even though it also has been found in the region specifying the 5'-UTR (Untranslated Regions) of the encoded mRNA in cytoplasm and may repress translation. Some of these are recognized as targets for the design of antitumor drugs.

### 1.3 Mechanism of DNA/Drug binding

#### 1.3.1 Interaction toward double strand DNA

The interaction of small molecules toward the double stranded DNA can be classified in two main groups: (i) covalent binding and (ii) non-covalent binding, within non-covalent interactions different types of interaction can be found, and they are described below.

- Covalent binding, based on the formation of covalent bonds, usually toward guanine residues and more specifically guanine N7, **Figure 10**, as for example cisplatin,<sup>[23,24]</sup> one of the most employed anticancer drugs. Cisplatin-DNA binding mechanism is widely reported.<sup>[25]</sup> The anticancer activity is due to this interaction with DNA, since its structure is altered, and cellular proteins cannot process or correctly repairs the polynucleotide. Consequently, many important intracellular processes are interrupted, cells are not able to replicate and die.

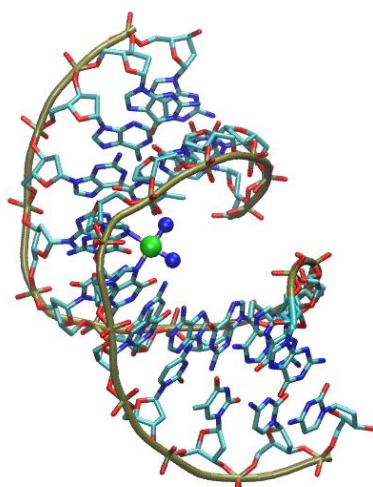


**Figure 10.** Cisplatin bound to guanine N7.

- Non-covalent interactions, which can be broadly divided into intercalation, groove binding and electrostatic interactions.

**Intercalation** is defined as the insertion of a planar and aromatic system between two consecutive base pairs of DNA bases, perpendicular to the axis of the double strand DNA.<sup>[26,27]</sup> This type of interaction is stabilized by  $\pi$ - $\pi$  stacking and hydrophobic interactions, **Figure 11**, and usually generate a decrease in the twist angle between

base pairs around the intercalation pocket with a consequent DNA elongation.<sup>[28]</sup> These structural modifications have important consequences on the functionality of the DNA molecule, since they can trigger the inhibition of DNA replication, transcription and repair processes leading to cell death.<sup>[29]</sup> Ethidium bromide, proflavine or acridine orange are examples of the most reported classical intercalators.<sup>[30]</sup>

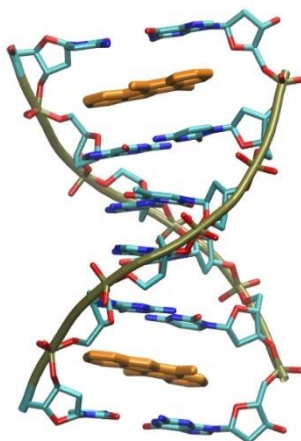


**Figure 11.** Ellipticine intercalative binding parallel to DNA base pairs, *PDB id: 1Z3F*.<sup>[31]</sup>

**Groove binding.** As mentioned above, double stranded DNA has two grooves, defined as major and minor. A groove binder refers to a molecule capable to bind DNA in the groove region through hydrogen bonds, Van der Waals forces and/or hydrophobic interactions, **Figure 12**. Grooves are binding sites for factors which regulate protein transcription or DNA replication, commonly linked through hydrogen bonds and hydrophobic interactions,<sup>[32]</sup> therefore, if a groove binder is occupying fundamental binding sites for the initiation of protein synthesis and genome replication, it inhibits those functions leading to cell death. Due to the different size of the furrows, oligonucleotides and proteins bind to the major groove<sup>[33,34]</sup> while small molecules prefer the minor groove,<sup>[35]</sup> where the quantity of bases and consequently the possibility of forming hydrogen bonds is lower. The natural molecule distamycin A, synthetic diarylamidines and bis-enzimidazoles are well-known groove binders. They are the most studied DNA-binding agents and they have shown several biological activities. Some have found clinical application in treating several diseases, like cancers, or as anti-viral and antibacterial agents.<sup>[36]</sup>

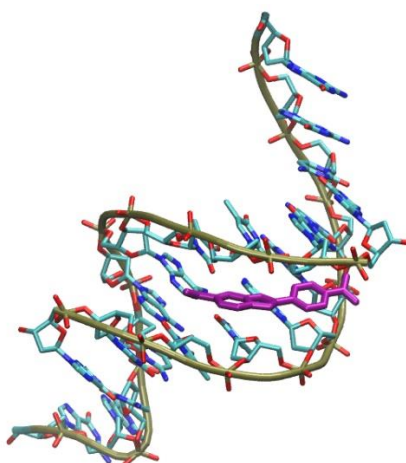


**Figure 12.** Schematic view of DAPI (purple) placed inside the minor groove of a double helical DNA, *PDB id: 432D*.<sup>[37]</sup>

**Electrostatic interactions**, an external bond which occurs between positively charged drugs and negatively charged phosphate groups of the DNA backbone. For this reason, it is a link mode that is very dependent on the ionic strength of the medium.<sup>[38]</sup>

### 1.3.2 Interaction with G-quadruplex

Due to the structural complexity of G-quadruplex the non-covalent interactions have been most often considered. High binding specificity toward G-quadruplex has been obtained through the design of specific drugs that do not interact with B-DNA, which is the physiologically most abundant conformation. The most common non-covalent interactions types for this biological target are classified as intercalation, groove binding and external stacking, as shown in **Figure 13**.

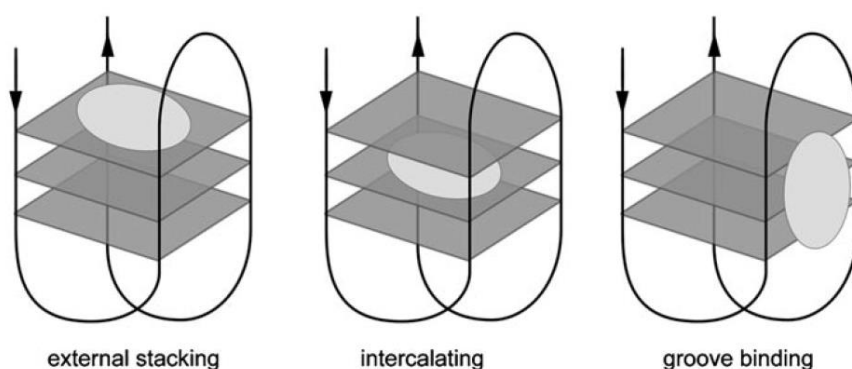


**Figure 13.** Schematic representation of the interaction types of a drug (gray sphere) toward G-quadruplex conformation.<sup>[16]</sup>

Several groups of compounds, such as cationic porphyrins (i.e. TMPyP4, see **Chapter VI**),<sup>[39]</sup> acridine (BSU6039),<sup>[40]</sup> polycyclic acridine (RHSP4),<sup>[41]</sup> salphen metal complexes<sup>[42,43]</sup> or N-N'-bis[2-(1-piperidino)ethyl]-3-4-9-10-perylenetetracarboxylic

diimide (PIPER)<sup>[44]</sup> have been widely reported during the last decades to interact specifically with G-quadruplex.

# **Chapter II**

---

## **Methods**

## 2.1 Experimental section

### 2.1.1 Materials

#### Solutions

Solutions were prepared with double deionized water from a Purity TU system (VWR). Sodium cacodylate,  $(\text{CH}_3)_2\text{AsO}_2\text{Na}$ , from now named as NaCaC, was used as buffer solution to adjust the ionic strength (I). In cases such as the G-quadruplex studies, the preparation of the solutions will be specified at each chapter in detail. Reagents for solution preparation were obtained from Sigma Aldrich (MERCK) with purity >99%.

#### Metal complexes

The employed metal complexes were synthesized and characterized together with the group of Dr. Espino, Inorganic Chemistry (University of Burgos, Spain).

#### Polynucleotides

The Calf Thymus DNA (ct-DNA) was purchased from Sigma Aldrich in the form of lyophilized sodium salt. This salt is dissolved in ultrapure water, aliquots of 10 mL are prepared and subjected to an ultrasonic homogenization process with UP400S equipment equipped with a 3 mm diameter titanium sonotrode (Hielscher, Germany), keeping the solutions on ice for avoid thermal effects during sonication. By means of agarose gel electrophoresis at 20 V/cm for 20 min, the average length of the DNA molecules after sonication is determined, being approximately 1000 base pairs (bp). To perform the assays, the concentration of DNA expressed in molarity in base pairs is always determined spectrophotometrically using the molar extinction coefficient  $\epsilon = 13200 \text{ M}^{-1} \text{ cm}^{-1}$  at  $\lambda = 260 \text{ nm}$ ,  $l = 0.1 \text{ M}$  and  $\text{pH} = 7.0$ .

#### G-quadruplex oligonucleotides

Different guanine-rich oligonucleotides, described in Table 1, labeled at 5' and 3' using FAM (6-carboxyfluorescein) and TAMRA (6-carboxytetramethylrhodamine) respectively have been employed,<sup>[45]</sup> mostly in FRET (Fluorescence Resonance Energy Transfer) melting assays. Oligonucleotide sequences have been supplied by Thermo Scientific™ (ThermoFisher Scientific), with HPLC purity degree.

**Table 1.** Sequences and topology of the employed oligonucleotides.

Name	Sequence (5'-3')	Topology
<b>21T</b>	GGGTTAGGGTTAGGGTTAGGG	3-tetrad Hybrid DNA G-quadruplex
<b>21RT</b>	GGGUUAGGGUUAGGGUUAGGG	3-tetrad Parallel RNA G-quadruplex
<b>25Ceb</b>	AGGGTGGGTGTAAGTGTGGGTGGGT	3-tetrad Parallel DNA G-quadruplex
<b>21CTA</b>	GGGCTAGGGCTAGGGCTAGGG	3-tetrad Antiparallel DNA G-quadruplex
<b>cmyc</b>	TGAGGGTGGGTAGGGTGGGTAA	3-tetrad Parallel DNA G-quadruplex
<b>Bom17</b>	GGTTAGGTTAGGTTAGG	2-tetrad Antiparallel DNA G-quadruplex
<b>TBA</b>	GGTTGGTGTGGTTGG	2-tetrad Antiparallel DNA G-quadruplex
<b>dx</b>	TATAGCTAT-hexaethylenglycol-TATAGCTATA	Intramolecular duplex
<b>ds26</b>	CAATCGGATCGAATTCGATCCGATTG	Double stranded DNA

Fluorescent labelled oligonucleotides were prepared in 90 mM LiCl, 10 mM lithium cacodylate, from now LiCaC, and 10mM KCl buffer at pH = 7.2 as a 0.25  $\mu$ M stock solutions and annealed by heating at 92°C for 5 minutes, and then fast cooled in ice. For F21RT the buffer employed was 99 LiCl mM, 10 mM LiCaC and 1mM KCl at pH = 7.2, decreasing the amount of K<sup>+</sup> due to the strong thermal stability of this G-quadruplex structure, and following the same procedure described above.

## 2.1.2 Experimental techniques

### 2.1.2.1 pH measurements

Metrohm pH-meter (Herisau, Suiza) equipped with a glass microelectrode, a reference electrode and a KCl salt bridge (3 M) has been used for pH measurements. The pH adjustment has been performed through sodium hydroxide, NaOH, (lithium hydroxide, LiOH, for G-quadruplex solutions) or hydrochloric acid, HCl.

### 2.1.2.2 Absorption spectrophotometry

Classically it can be defined as “the absorption of incident radiation, as a function of wavelength ( $\lambda$ ), upon passage through a given medium”- Tom D. Schlabech, Encyclopedia of Chemistry, 1966. In a chromophore solution through which passes a



beam of light with an initial intensity,  $I_0$ , and specific wavelength, a part of the radiation is absorbed by the chromophore and another unabsorbed part passes through the sample,  $I$ , and the rapport between the transmitted and the incident intensity is known as transmittance (T).

The absorbance of a given sample inside the cuvette is described as the logarithm of the inverse value of transmittance, and depends on the light path travel by light, related with cuvette width,  $l$ , the concentration of chromophore in solution,  $C$ , and the molar attenuation coefficient,  $\epsilon$ , leading to Lambert-Beer law (Eq.1).

$$\text{Abs} = \log \frac{1}{T} = -\log T = \log \frac{I_0}{I} = \epsilon \cdot C \cdot l \quad (1)$$

This technique is especially useful for the study of aggregation processes or perform spectrophotometric evaluations. Aggregation processes in solution are checked with compliance of Lambert-Beer law (Eq.1), recording the spectra of a buffer solution to which are added increasing amounts of our compound of interest solution with the same buffer, homogenizing the cuvette solution after each addition before recording each spectrum. If the plot of absorbance at a fixed wavelength in function of the increasing concentrations of compound is a line which passes through the origin (0,0) and the slope is the compound molar extinction coefficient Eq.1 is fulfilled. In case of a deviation from the linearity this could be related to aggregation processes in solution. Spectrophotometric evaluations provide information about whether there is interaction between the drug and a polynucleotide. Starting from a solution in cuvette of known volume and drug concentration, addition of a polynucleotide solution (known concentration) are made. Spectra are corrected by the dilution factor,  $\Delta F$ , which is expressed as  $\Delta F = C_D^0/C_D$ , the relationship between initial concentration of drug in cuvette,  $C_D^0$ , and the concentration after each addition,  $C_D$ .

The absorbance measurements have been carried out with an Agilent 8453 single beam spectrophotometer (Agilent Technologies, Palo Alto, California) with photodiode array detection in the range  $\lambda = 190 - 1100$  nm, equipped with Tungsten and Deuterium lamps for measurements in Visible and UV regions respectively, and a Peltier thermostatic system (HP-89090A) with an accuracy of  $\pm 0.1^\circ\text{C}$  for temperature control. The measurements were made in high precision quartz cuvettes with 1 cm light path (Hellma Analytics, Müllheim, Germany).

### **2.1.2.3 Circular dichroism (CD)**

Circular dichroism is a circularly polarized electromagnetic radiation absorption spectroscopy technique useful for molecules with chiral centers, where the incident radiation is divided in the two chiral polarized components, one on the left and one on the right, which are in phase and have the same amplitude. When the absorption of the light circularly polarized in one direction (e.g. right-handed) is different from the absorption of the light circularly polarized in the opposite direction (e.g. left handed),

the molecule is said to exhibit circular dichroism, **Figure 14**. As the DNA CD (Circular dichroism) spectra is well known and widely reported, this stand as a very useful technique for monitoring even just slight variations in its secondary structure due to the interaction with small molecules.<sup>[46–48]</sup>

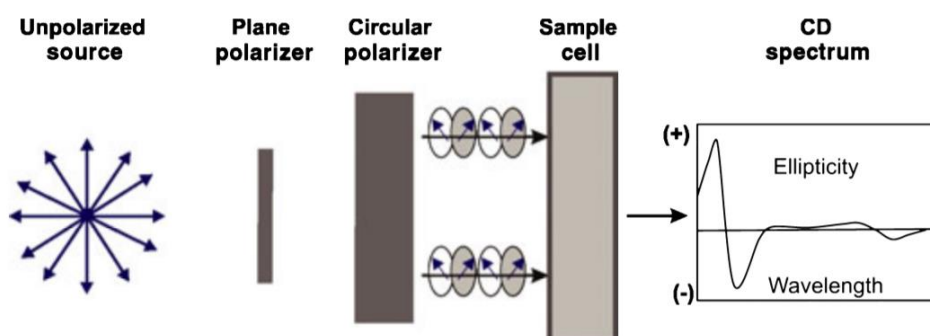


**Figure 14.** Circular dichroism instrument basics.<sup>[49]</sup>

Based on Bouguer-Lambert-Beer law<sup>[50]</sup> the absorbance of each chiral polarized components is defined as  $Abs_x = \log(I_0/I_x)$ , where X can be L (left) or R (right), therefore the difference in the absorption of both components when crossing the sample is defined as:

$$\Delta Abs = Abs_L - Abs_R = \log\left(\frac{I_0}{I_L}\right) - \log\left(\frac{I_0}{I_R}\right) = \log\left(\frac{I_R}{I_L}\right) \quad (2)$$

and circular dichroism:

$$\Delta \varepsilon = \frac{1}{c \cdot l} \Delta Abs \quad (3)$$

The physical parameter measured in the circular dichroism technique is the ellipticity,  $\theta$ , which is related to  $\Delta \varepsilon$  as is shown in **Eq.4**:

$$\tan \theta = \frac{E_R - E_L}{E_R + E_L} = \Delta \varepsilon \quad (4)$$

In the experimental measurements the software of the dichroism measuring instrument circular provides the value of  $\theta$  for each measured wavelength, and the results are presented as molar ellipticity,  $[\theta]$ :

$$[\theta] = \frac{100 \cdot \theta}{c \cdot l} \text{ (deg} \cdot \text{M}^{-1} \cdot \text{cm}^{-1}\text{)} \quad (5)$$

Modular instrument MOS-450 Biologic (Claix, France) equipped with a Xenon arc lamp and an electro-optic modulator to obtain the circularly polarized light on the left and the light alternately with a frequency of 50 kHz has been employed. Detection is done by means of a photomultiplier, and Biokine software 3.2 transform the received signal into ellipticity ( $\theta$ ). To perform the measurements high accuracy quartz cuvettes of 1cm

light path width were used, while temperature is controlled through an external Julabo bath.

#### 2.1.2.4 Viscosity

The viscosity of a double strand DNA solution represents a further important parameter useful in demonstrating if there is interaction whether between DNA and small molecules based on the chain length variations.<sup>[51]</sup> Small molecules able to intercalate generate an increase in axial separation between the contiguous base pairs present in the site of intercalation of the double helix and therefore an elongation of the polynucleotide which is reflected as an increase over viscosity values.<sup>[52]</sup> Otherwise, it has been reported that molecules capable to interact toward DNA through interstrand covalent bond, such as cis-diamminedichloroplatinum(II) (cisPt), cause a decrease in the values of DNA viscosity, while intrastrand covalent bond did not modify the DNA chain length.<sup>[53]</sup> An Ubbelodhe viscometer has been employed, with a volume capacity between 2 and 4 ml, immersed in a thermostated bath (T= 25°C). The procedure is based on collecting values (in triplicate) of the time it takes a 3 ml  $2 \cdot 10^{-4}$  M [DNA] sample to fall by gravity from one point to another of the viscometer to which are latter added increasing amounts of drug encompassing a range of different  $C_D/C_P$  ratios (where  $C_D$ = drug concentration and  $C_P$ = DNA concentration). The obtained results are expressed as relative viscosity, defined in Eq.6, where  $t_s$  is the solvent drop time,  $t_0$  is the nucleotide solution drop time and  $t$  the nucleotide solution drop time at a certain drug concentration:

$$\frac{\eta}{\eta_0} = \frac{t-t_s}{t_0-t_s} \quad (6)$$

Calculated relative viscosity is then related to the DNA relative elongation through Eq.7:

$$\frac{L}{L_0} = \sqrt[3]{\frac{\eta}{\eta_0}} \quad (7)$$

#### 2.1.2.5 Fluorescence resonance energy transfer (FRET) melting assays

Fluorescent resonance energy transfer<sup>[54]</sup> is a quantum phenomenon based in an energy transfer between two dye molecules, a donor fluorescent molecule and another acceptor molecule, so that this phenomenon can take place when the emission spectrum of the donor molecule overlaps with the absorption spectrum of the acceptor molecule. Excitation is transferred from the donor to acceptor fluorophore through dipole-dipole interaction without the emission of a photon. As a result, the donor molecule fluorescence is quenched, and the acceptor molecule becomes excited. It then loses energy via heat or fluorescent emission, called sensitized emission.<sup>[55]</sup> The spectrum overlapping is highly dependent on the distance between the two molecules, generally requiring a maximum distance between both

of 50-60 Å.<sup>[56]</sup> This is the key factor on which thermal denaturing FRET assay is based on, in which oligonucleotides of certain sequences capable of forming G-quadruplex are used, marked at their 5' and 3' ends, as is mentioned above in **Chapter 2.1.1**.

G-rich oligonucleotides labelled and folded in G-quadruplex conformation have FAM and TAMRA close together, so that when irradiating the sample at the FAM excitation wavelength an energy transfer occurs from FAM to TAMRA, thereby FAM does not present emission. While temperature increases, G-quadruplex denaturalization is favored, so that when it occurs that FAM and TAMRA move away to each other decreasing FRET process, **Figure 15**. Thus, a fluorescence signal for FAM can be recorded. The increase of FAM fluorescence as a function of the temperature allow to obtain the G-quadruplex thermal denaturing curves, through which melting temperature can be calculated ( $T_m$ ). FRET method has been used to measure the stabilization and selectivity of the drugs toward different G-quadruplex conformations by calculating the increase in G-quadruplex  $T_m$  values.<sup>[57]</sup>

Applied biosystem™ (Thermofisher Scientific) 7500 real time PCR has been used, with 96-well PCR plate in which MicroAmp® fast reactions tubes (Applied biosystem™) are placed with MicroAmp® optical 8 -cap strip (Applied biosystem™), so the fluorescence of 96 solutions can be followed simultaneously using small amounts of sample.

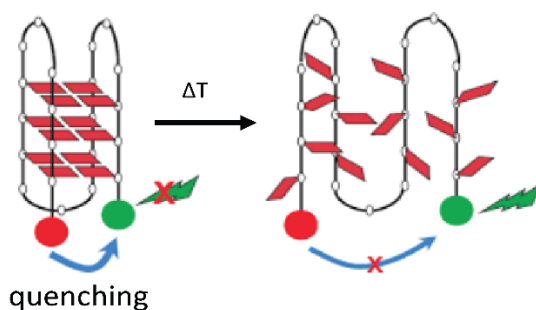


**Figure 15.** Schematic representation of G-quadruplex denaturalization marked with FAM (Green) and TAMRA (red) based on the FRET.<sup>[58]</sup>

## 2.2 Computational methods

To obtain atomic-level structural details of the binding site or the kind of interaction between the synthetic small molecules considered in this thesis work and their possible biomolecular targets, with the aim to support the interpretation of experimental data, complementary computational investigations have been carried out, in particular on model systems mimicking the binding between the small molecules and double stranded or G-quadruplex DNA.

### 2.2.1 Quantum chemistry calculations

The structure of the small molecules selected for the binding with DNA were all investigated by PM6 semi-empirical<sup>[59]</sup> and/or by DFT calculations, using the following functionals: M06-2X<sup>[60]</sup> (**Chapters III, IV, VI**), PBE1PBE (PBE0)<sup>[61]</sup> (**Chapters IV, V**), B3LYP<sup>[62,63]</sup> (**Chapters IV, V**), and basis sets: CEP-121G<sup>[64-66]</sup> (**Chapters III, VI**) and 6-31G\*\*<sup>[66,67]</sup> (**Chapters IV, V**).

Full geometry optimizations were performed for each considered structure. The contribution of the water solvent was considered by the “conductor-like polarized continuum model” implicit method.<sup>[68,69]</sup>

Where necessary, transition state structures were found through the synchronous transit-guided quasi-Newton (STQN) method.<sup>[70]</sup> Vibration frequency analysis, in the normal mode approximation, was performed to determine whether the optimized geometry corresponded to a local minimum or, in case of transition state structures, to a first order saddle point. The frequency analysis allowed also to obtain calculated values of thermodynamic data. All calculations have been performed with the Gaussian 09 package.<sup>[71]</sup>

### 2.2.2 Molecular dynamics (MD) simulations

The state of a classical system can be completely described by specifying the positions and momenta of all particles. Focusing on a three-dimensional space, all particles contained within a determined system are characterized by 6N coordinates, being N the number of particles. These coordinates define a 6N-dimensional space called phase space, in which at any instant in time the system occupies one point inside it. Hence, over time, a dynamical system maps out a trajectory in the phase space.<sup>[72]</sup> It is interesting to note that since a phase point is defined by the positions and momenta of all particles, it determines the location of the next phase point in absence of outside forces.

Therefore, MD simulations allow to measure the temporal evolution of the coordinates and momenta of a given macromolecule, the so called trajectory, by solving Newton’s equation of motion, defined as:

$$F_i = m_i \frac{d^2 r_i(t)}{dt^2} \quad (8)$$

Where  $r_i(t)$  is the position vector of a particle  $i$  with mass  $m_i$  and  $F_i$  the force acting upon the mentioned particle at a fixed time  $t$ .

The trajectory of a MD simulation of a system mimicking the interaction between small molecules and biomolecules can be displayed and analyzed with the aim of obtaining information about time-dependent properties,<sup>[73]</sup> such as important structural and molecular-recognition details. Force fields (FF) are mathematical expressions that describe the dependence of the total energy of a system on the coordinates of its particles. These are useful to calculate all terms related to short and long-range

interactions, including electrostatic and dispersion terms. Empirical force fields allow to reproduce structural and dynamic features of DNA models, and also their interaction with small molecules.<sup>[74]</sup> Periodic boundary conditions (PBC) are commonly employed to overcome the limits due to finite size of the considered system, **Figure 16**. The unit cell is initially built, and its conditions are defined, e.g. ionic strength and box size, related to the definition of the macroscopic solution concentration. PBC conditions generate an infinite system replicating the same unit cell, in a way that if any atom leaves the unit cell for example from the top face, it then enters the box by the bottom face leading to constant conditions inside the unit cell. Electrostatic interactions have been considered by the particle mesh Ewald (PME) method, which allows to commute the long-range interactions without cut-off approximations, i.e. without neglecting contributions from sites separated by distance larger than a certain cut-off.<sup>[75]</sup>

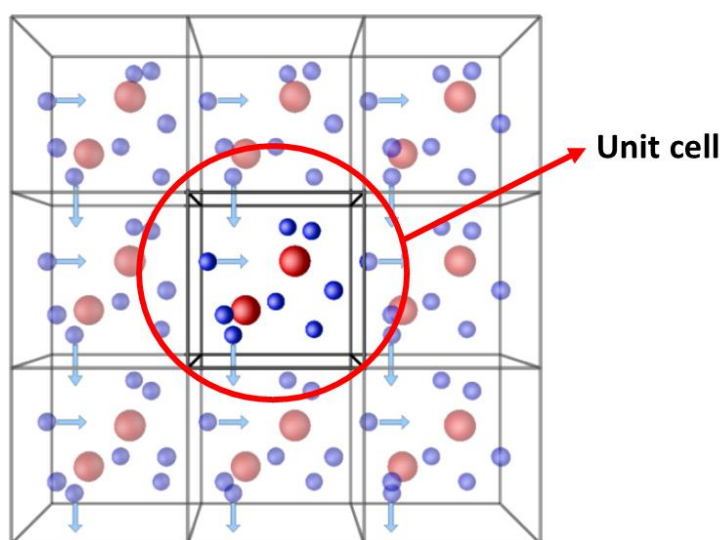


**Figure 16.** Scheme referred to periodic boundary conditions in which the built unit cell is shown in the center, while the other are infinite replicas in space.

In the present thesis, atomic partial charges of small molecules were obtained by DFT calculations, while other intra-molecular force field parameters were generated with the ACPYPE (Antechamber python parser interface) software.<sup>[76,77]</sup> MD simulations were performed by the Gromacs 5.0.4 software package,<sup>[78,79]</sup> using the Amber99SB force field with the ParmBSCO<sup>[80,81]</sup> treatment of nucleic acid torsion parameters for all DNA models.

### 2.2.3 Quantum mechanics/molecular mechanics (QM/MM) calculations

The application of quantum mechanics (QM) methods for the calculation of structure and properties of systems as large as those involving biomolecules are still nowadays extremely time-consuming. For this reason, during the last decades many efforts and research have been performed in order to develop methods to reduce the computational time without losing much accuracy. In this context, it is interestingly that Karplus, Levitt and Warshel were awarded the Nobel Prize in Chemistry in 2013 for the “Development of multiscale model for complex chemical systems”.

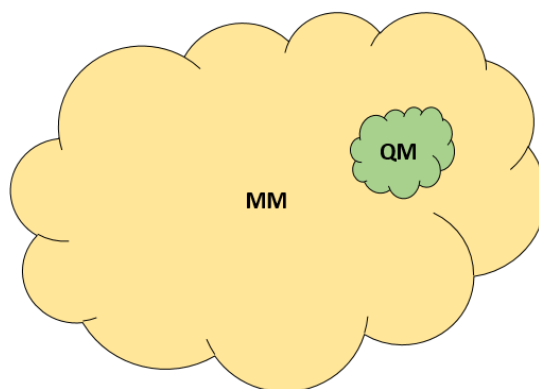


**Figure 17.** Schematic view of a certain system considered by QM/MM: in yellow the whole system treated at molecular mechanics level and in green a small portion of special interest, investigated by quantum mechanics methods.

The resulting hybrid method,<sup>[82–85]</sup> called QM/MM, is extremely useful for the theoretical investigation of large systems. The latter are divided into two (or more) parts, named layers, on which different methods are applied (**Figure 17**): accurate QM methods for a small portion of the full system, which represents the most interesting layer (high layer, hl) and a faster but less accurate molecular mechanics (MM) method of the whole macromolecular system (low layer, ll). The total energy of a two-layer system,  $E_{\text{QM/MM}}$ , is then defined as in **Eq.9**:

$$E_{\text{QM/MM}} = E_{\text{hl}}^{\text{QM}} + E_{\text{ll}}^{\text{MM}} - E_{\text{hl}}^{\text{MM}} \quad (9)$$

The low layer contains all atoms, and is calculated at the lower level, while the most interesting part, the high layer, is treated at the higher (QM) level,<sup>[86,87]</sup> along with the atoms that are used to cap dangling bonds resulting from the cut of covalent bonds between the high and low layer.

# **Chapter III**

---

**DNA binding of half-sandwich  
Ru(II) and Ir(III) complexes:  
experimental and computational  
studies**



### 3.1 Introduction

Cancer is part of the set of diseases characterized by the uncontrolled proliferation of cells and the destruction of tissues. The causes responsible for the initiation and promotion of this terrible disease may be both external (e.g., chemicals, radiation, viruses) and internal (e.g., hormones, immune conditions, inherited genes).<sup>[88]</sup> The treatment of cancer is accomplished by several optional therapies such as surgery, chemotherapy, radiation therapy, immunotherapy, and monoclonal antibody therapy. Since the discovered of the therapeutic activity of cisplatin and its derivatives there has been a great deal of interest in developing new metallodrugs, possibly targeting a higher number of cancer types, and with less toxic side effects.<sup>[89,90]</sup> In this context, heteroleptic compounds with general formula  $[(\eta^6\text{-arene})\text{M}(\text{X})(\text{N}^{\wedge}\text{N})]$  (M=transition metal cation), usually called “half-sandwich or piano stool complexes”, have displayed promising anticancer activity, as reported in the last decade.<sup>[91,92]</sup> Where the  $\eta^6\text{-arene}$  moiety which stabilizes the oxidation state of the metal cation and may facilitate transport through the cell membrane,  $\text{N}^{\wedge}\text{N}$  is a chelating diamine ligand, but it could also be  $\text{C}^{\wedge}\text{N}$ ,  $\text{O}^{\wedge}\text{N}$  or  $\text{O}^{\wedge}\text{C}$ ,<sup>[93]</sup> able to control the reactivity towards different biomolecules and even can play an important role in the interaction, and a leaving group (X), which undergoes easy dissociation to allow coordination of the metal ion to target biomolecules. The anticancer potential of these new metal-based compounds relies on three main conditions: i) they must be prone to functionalization, e.g. by hydrolysis of the M-X bond, so that they are able to selectively bind to specific significant biological targets; ii) they must easily cross human cell membranes to exert their cytotoxicity;<sup>[94]</sup> (iii) the overall charge and counterion identity must be the right ones because they are related to the solubility and permeability<sup>[95]</sup>. The binding to DNA is also considered responsible for the potential anticancer activity of these type of new compounds.<sup>[96,97]</sup> In recent years, ruthenium(II) and iridium(III) arene complexes have been found to exhibit varying degrees of *in vitro* selectivity activity against human cancer cells.<sup>[98,99]</sup> In the present work, the synthesis and characterization of a half-sandwich Ru<sup>II</sup> and Ir<sup>III</sup> complexes is reported, with thiabendazole as ancillary  $\text{N}^{\wedge}\text{N}$  ligand, and a  $\eta^6\text{-pentamethylcyclopentadienyl}$  and  $\eta^6\text{-p-cymene}$  for the Ir and Ru complexes, respectively. The thermodynamics and kinetics of the binding of the two metal complexes to ct-DNA, in water solution, was investigated by variable temperature absorption and circular dichroism spectroscopies and by viscosity measurements. Moreover, MD simulations followed by QM/MM calculations, were performed to provide atomistic models of the host/guest DNA-binding complexes, as recently reported,<sup>[100]</sup> (see **Chapter VI**). Interestingly, the computational investigations suggest that the stereoisomerism of the two metal complexes may affect their DNA-binding strength.

## 3.2 Materials and methods

### 3.2.1 Materials

Metal complexes have been synthesized and characterized by the group of Dr. Espino, Inorganic Chemistry (University of Burgos, Spain). Aqueous solutions were prepared with doubly deionized water from a Purity TU system (VWR). Stock solutions for Ru(II) and Ir(III) were prepared by dissolving weighed amounts in 2.5 mM sodium cacodylate (NaCaC) as buffer to maintain the pH constant at 7.4, where drug concentration is denoted as  $C_D$ .

### 3.2.2 Experimental techniques

#### Synthesis and characterization

Both syntheses were performed and reported by Dr. Martínez Alonso on her PhD thesis and are described based on it.<sup>[101]</sup>

- Synthesis of  $[(\eta^6\text{-p-cymene})\text{RuCl}(\kappa^2\text{-N,N-tbz})]\text{Cl}$ , **Figure 1**, from now called compound **1**.

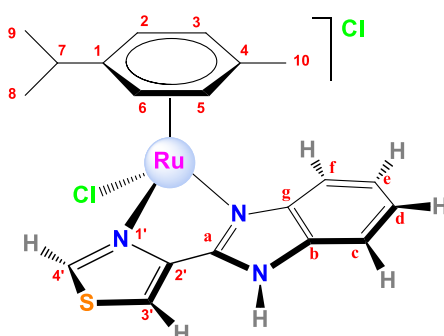


**Figure 1.** 2D schematic view for the Ru(II) complex, **1**.

In a 100 mL Schlenk flask, the commercial ligand thiabendazole, **tbz** (0.0664 g, 0.330 mmol) was added to a solution of  $[\text{RuCl}_2(\text{cym})]_2$  (0.1008 g, 0.165 mmol) in degassed methanol (18 mL), and the mixture was stirred at room temperature for 20 h and under a nitrogen atmosphere. The solution was filtered and concentrated. The product was precipitated with diethyl ether (15 mL) and isolated by filtration. The resulting yellow powder was dried under vacuum. Yield: 114.0 mg (0.225 mmol, 68%).  $M_r(\text{C}_{20}\text{H}_{21}\text{N}_3\text{SCl}_2\text{Ru}) = 507.4474 \text{ g/mol}$ . **Anal. Calcd for  $\text{C}_{20}\text{H}_{21}\text{N}_3\text{SCl}_2\text{Ru} (\text{H}_2\text{O})_2$ :** C 44.20; H 4.64; N 7.73; S 5.90; **Found:** C 44.11; H 4.10; N 7.30; S 5.94.  $^1\text{H NMR}$  (400 MHz,  $\text{CDCl}_3$ , 25 °C)  $\delta$  15.29 (s, 1H,  $\text{H}^{\text{N-H}}$ ), 10.34 (s, 1H,  $\text{H}^{\text{S}}$ ), 9.41 (s, 1H,  $\text{H}^{\text{3'}}$ ), 7.89 – 7.79 (m, 1H,  $\text{H}^{\text{c}}$ ), 7.77 – 7.65 (m, 1H,  $\text{H}^{\text{f}}$ ), 7.50 – 7.38 (m, 2H,  $\text{H}^{\text{d}}$ ,  $\text{H}^{\text{e}}$ ), 6.13 (d,  $J = 4.9 \text{ Hz}$ , 1H,  $\text{H}^{\text{2}}$  or  $\text{H}^{\text{6}}$ ), 6.03 (d,  $J = 5.4 \text{ Hz}$ , 1H,  $\text{H}^{\text{3}}$  or  $\text{H}^{\text{5}}$ ), 6.00 (d,  $J = 5.7 \text{ Hz}$ , 1H,  $\text{H}^{\text{6}}$  or  $\text{H}^{\text{2}}$ ), 5.84 (d,  $J = 5.9 \text{ Hz}$ , 1H,  $\text{H}^{\text{5}}$  or  $\text{H}^{\text{3}}$ ), 2.61 – 2.50 (sept,  $J = 7.0 \text{ Hz}$ , 1H,  $\text{H}^{\text{7}}$ ), 2.23 (s, 3H,  $\text{H}^{\text{10}}$ ), 1.00 (d,  $J = 6.8 \text{ Hz}$ , 3H,

H<sup>8</sup> or H<sup>9</sup>), 0.95 (d, J = 6.9 Hz, 3H, H<sup>9</sup> or H<sup>8</sup>) ppm. **<sup>13</sup>C{<sup>1</sup>H} NMR (101 MHz, CDCl<sub>3</sub>, 25 °C)** δ 160.9 (s, 1C, C<sup>a</sup>), 146.2 (s, 1C, C<sup>2'</sup>), 144.1 (s, 1C, C<sup>5'</sup>), 140.8 (s, 1C, C<sup>8</sup>), 135.0 (s, 1C, C<sup>b</sup>), 125.7 (s, 1C, C<sup>d</sup>), 124.8 (s, 1C, C<sup>e</sup>), 123.5 (s, 1C, C<sup>3'</sup>), 116.4 (s, 1C, C<sup>f</sup>), 115.0 (s, 1C, C<sup>c</sup>), 104.0 (s, 1C, C<sup>1</sup>), 103.0 (s, 1C, C<sup>4</sup>), 84.7 (s, 1C, C<sup>2</sup> or C<sup>6</sup>), 82.6 (s, 1C, C<sup>3</sup> or C<sup>5</sup>), 82.3 (s, 1C, C<sup>6</sup> or C<sup>2</sup>), 80.0 (s, 1C, C<sup>5</sup> or C<sup>3</sup>), 31.3 (s, 1C, C<sup>7</sup>), 22.4 (s, 1C, C<sup>8</sup> or C<sup>9</sup>), 22.3 (s, 1C, C<sup>9</sup> or C<sup>8</sup>), 19.3 (s, 1C, C<sup>10</sup>) ppm. **FT-IR (KBr, cm<sup>-1</sup>) selected bands:** 3387 (vs, ν<sub>N-H</sub>), 3049-3000-2969 (vs, ν<sub>CH</sub>, ν<sub>-CH</sub>), 2620 (s), 1624-1609 (m, ν<sub>C=N(imid)</sub>), 1515 (m, ν<sub>C=C</sub>), 1480 (s, ν<sub>C=N(thiaz)</sub>), 1431 (vs), 1329 (vs), 1227 (w, ν<sub>C-S</sub>), 1018 (s, ν<sub>C=S</sub>), 875-842 (s), 765 (vs, δ<sub>NHoop</sub>), 755 (vs, δ<sub>CHoop</sub>), 637 (w). **MS (FAB+):** m/z (%) = 472 (56) ([M-Cl]<sup>+</sup>), 436 (22) ([M-2Cl-H]<sup>+</sup>). **Molar Conductivity (H<sub>2</sub>O):** 164 S·cm<sup>2</sup>·mol<sup>-1</sup>. **Solubility:** soluble in water, methanol, ethanol, dichloromethane, chloroform and acetone.

- Synthesis of [(η<sup>5</sup>-Cp\*)IrCl(κ<sup>2</sup>-N,N-tbz)]Cl, **Figure 2**, from now called compound **2**.

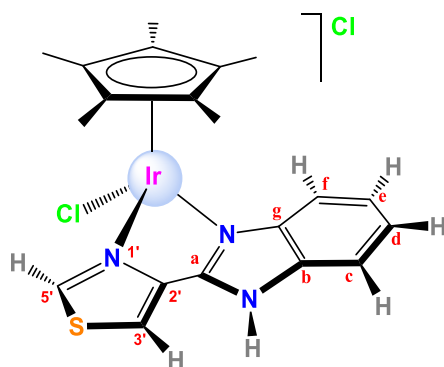


**Figure 2.** 2D schematic view for the Ir(III) complex, **2**.

In a 100 mL Schlenk flask, the commercial ligand thiabendazole, **tbz** (0.0521 g, 0.259 mmol) was added to a solution of [IrCl<sub>2</sub>(Cp\*)]<sub>2</sub> (0.1002 g, 0.129 mmol) in degassed dichloromethane (11 mL), and the mixture was stirred at room temperature for 20 h and under a nitrogen atmosphere. The solution was concentrated, and the product was precipitated with n-hexane (15 mL) and isolated by filtration. The resulting yellow powder was dried under vacuum. Yield: 145.2 mg (0.242 mmol, 94%). **M<sub>r</sub> (C<sub>20</sub>H<sub>22</sub>N<sub>3</sub>SCl<sub>2</sub>Ir) = 599.6053 g/mol. Anal. Calcd for C<sub>20</sub>H<sub>22</sub>N<sub>3</sub>SCl<sub>2</sub>Ir·(CH<sub>2</sub>Cl<sub>2</sub>)<sub>1.1</sub>:** C 36.57; H 3.52; N 6.06; S 4.63; **Found:** C 36.56; H 3.68; N 5.67; S 4.73. **<sup>1</sup>H NMR (400 MHz, CDCl<sub>3</sub>, 25 °C)** δ 15.91 (s, 1H, H<sup>N-H</sup>), 9.99 (s, J = 1.7 Hz, 1H, H<sup>3'</sup>), 9.14 (d, J = 2.1 Hz, 1H, H<sup>5'</sup>), 7.87 (d, J = 8.1 Hz, 1H, H<sup>c</sup>), 7.58 (d, J = 7.7 Hz, 1H, H<sup>f</sup>), 7.50 – 7.35 (m, 2H, H<sup>d</sup>, H<sup>e</sup>), 1.79 (s, 15H, H<sup>Cp(Me)</sup>) ppm. **<sup>13</sup>C{<sup>1</sup>H} NMR (101 MHz, CDCl<sub>3</sub>, 25 °C)** δ 154.1 (s, 1C, C<sup>5'</sup>), 147.5 (s, 1C, C<sup>a</sup>), 145.9 (s, 1C, C<sup>2'</sup>), 138.3 (s, 1C, C<sup>8</sup>), 135.4 (s, 1C, C<sup>b</sup>), 125.7 (s, 1C, C<sup>d</sup>), 124.7 (s, 1C, C<sup>e</sup>), 124.6 (s, 1C, C<sup>3'</sup>), 115.9 (s, 1C, C<sup>f</sup>), 115.6 (s, 1C, C<sup>c</sup>), 87.9 (s, 1C, C<sup>CpC</sup>), 9.9 (s, 1C, C<sup>Cp(Me)</sup>) ppm. **FT-IR (ATR, cm<sup>-1</sup>) selected bands:** 3466 (m, ν<sub>N-H</sub>), 3095-2910-2822-2739 (m, ν<sub>CH</sub>, ν<sub>-CH</sub>), 1614 (m, ν<sub>C=N(imid)</sub>), 1517 (m, ν<sub>C=C</sub>), 1481-1462-1428 (s, ν<sub>C=N(thiaz)</sub>), 1378 (m, δ<sub>CH<sub>3</sub></sub>), 1328 (m), 1226 (w, ν<sub>C-S</sub>), 1029-1015 (s, ν<sub>C=S</sub>), 879-846 (m), 763 (vs, δ<sub>NHoop</sub>), 747 (vs, δ<sub>CHoop</sub>), 638 (w). **MS (FAB+):** m/z (%) = 564 (15) ([M-Cl]<sup>+</sup>), 528 (4) ([M-2Cl-H]<sup>+</sup>),

363 (6) ([M-Cl-thbzol])<sup>+</sup>). **Molar Conductivity (CH<sub>3</sub>CN):** 35.4 S·cm<sup>2</sup>·mol<sup>-1</sup>. **Solubility:** soluble in water, dichloromethane, chloroform, acetonitrile and acetone. Partially soluble in methanol.

**UV-vis Spectroscopy.** Absorbance measurements were performed to prove the substitution of Cl for H<sub>2</sub>O. DNA melting assays were also accomplished by UV-vis measurements, spectra were recorded in a range T = 25 - 90 °C, at 0.3 °C min<sup>-1</sup> of scan rate with one-minute stabilization. All measures were performed by duplicate.

**Circular dichroism.** Circular dichroism Spectra were recorded for different DNA/Drug samples incubated for 24h, in NaCaC buffer (I= 2.5mM) at pH = 7.4 and T = 25 °C. All measures were performed by duplicate.

**Differential Scanning Calorimetry.** The study of the DNA thermal stabilization induced by the complexes was completed by DSC measurements, using a Nano DSC Instrument (TA, Waters LLC, New Castle, USA). Reference and sample were previously degassed in a degassed station (TA Instruments, Waters LLC, New Castle, USA) to minimize the formation of bubbles upon heating. The samples were scanned at 3 atm pressure from 20 to 110 °C at 1 °C min<sup>-1</sup> scan rate.

**Viscosity measurements.** Viscosity of stock solutions incubated overnight was measured in triplicate, the readings of the flow time was measured with a digital stopwatch. The viscosity readings were reported as  $L/L_0 = (\eta/\eta_0)^{1/3}$  versus  $C_D/C_P$ , where  $\eta$  and  $\eta_0$  stand for the polynucleotide viscosity in the presence and in the absence of drug respectively. All measures were performed by triplicate.

### 3.2.3 Computational details

**Molecular Dynamics.** The geometry of the two Ru(II) and Ir(III) complexes was fully optimized by PM6 calculations<sup>[59]</sup> and, subsequently, by DFT calculations, using the M06-2X<sup>[60]</sup> functional and the CEP-121G<sup>[61-64]</sup> basis set, as recently reported<sup>[102]</sup> (see **Chapter VII**). The double-helical B-DNA structure, with sequence d(AGCTAGCTCAGT)<sub>2</sub>, was designed by using the NUCLEIC routine of the TINKER software.<sup>[103]</sup> An intercalation pocket between DG6 and DC7 base pairs was created, to check if the intercalation of the ancillary ligand was possible. The starting structures for the computational studies of the complex/DNA systems were obtained using the Maestro software [Maestro, version 10.2, Schrödinger, LLC, New York, NY, 2015]. In such structures, the metal ion is covalently bonded to the N7 atom of a guanine base, with the metal complex approaching DNA from the major groove, and with the ancillary ligand intercalated between the sixth and seventh GC and CG base pairs. Force field parameters related to the metal cation were manually taken and included in Amber99sb force field from the literature.<sup>[104,105]</sup> Four MD simulations were conducted for 150 ns for each DNA/Drug system, considering both enantiomers.

**QM/MM calculations.** The relaxed geometries for both DNA/Drug systems, including the two enantiomers in each case, were optimized by two-layer QM/MM hybrid calculations, as implemented in the ONIOM method, with the aim to perform a high-level calculation for the drug and the bound guanine. The M06-2X<sup>[60]</sup> DFT functional and the lanl2dz<sup>[106]</sup> basis set were used for the higher DFT layer, to suitably model the bonding between the metal complex and guanine. The Amber99 force field was used in the lower MM layer of the QM/MM calculations. The highest layer of the model includes the drug and the guanine residue excluding the phosphate group, with charge set to +2 and multiplicity 1. Default atomic partial charges were used for the nucleic atoms, implicitly included in the force field parameters. Vibration frequency calculations, within the harmonic approximation, were performed on the optimized geometries by using the same QM/MM method, to confirm that their energies were true minima on the potential energy surface. All calculations were performed with Gaussian 09 software.<sup>[71]</sup>

### 3.3 Results and discussion

#### 3.3.1 Experimental Results

**Stability studies and formation of the aquo complexes.** As mentioned above, the two metal complexes are soluble in water, thus their stability in aqueous solution was studied through UV-vis techniques to check if the substitution of Cl by H<sub>2</sub>O was possible. These kinetic assays were performed by dissolving the ruthenium and the iridium complex in buffered aqueous solution and recording their UV-vis spectra every 20 s. Additionally, the initial absorbance spectra for **1** and **2** is reported in **Figure 3**. As it can be seen in **Figure 4**, a kinetic process has been found related to the formation of the aquo complex.

The absorbance time data were fitted using a monoexponential function, **Eq. 1**, being  $1/\tau$  the kinetic constant for the formation of the aquocomplex. The obtained values for **1** and **2** are shown in **Table 1**. Based on these results stock solutions were incubated overnight before using.

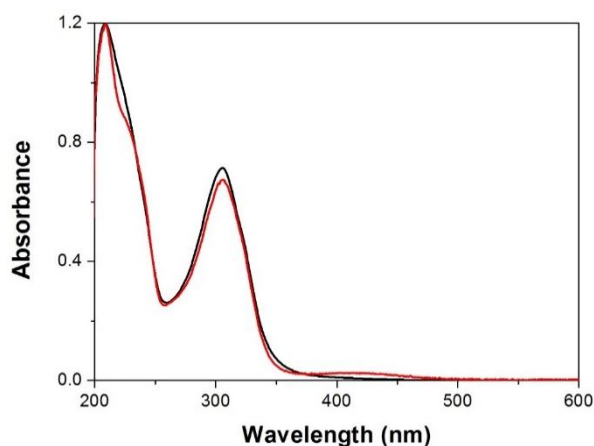


**Figure 3.** Absorbance spectra for compounds **1** (red) **2** (black) in aqueous solution.  $[C_D] = 6 \cdot 10^{-5} \text{ M}$

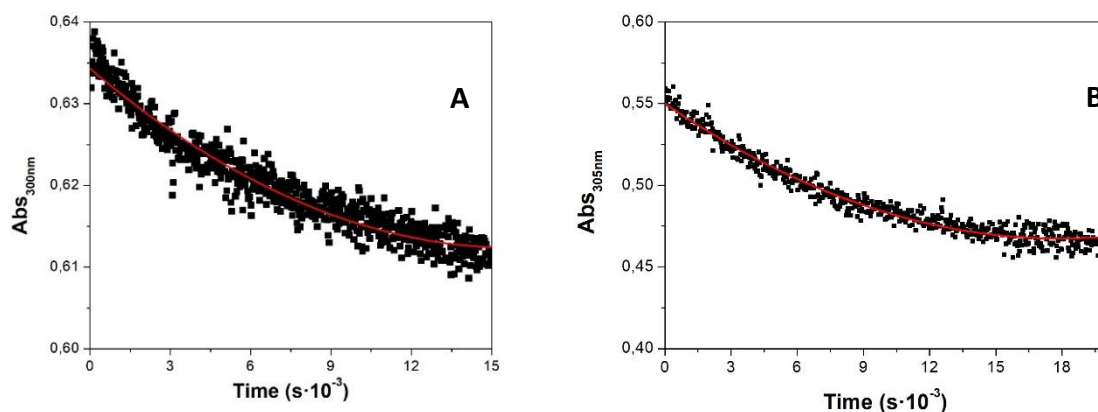


**Figure 4.** Absorbance at  $\lambda_{\text{max}}$  as function of time for **1** (A) and **2** (B).  $[C_D] = 4 \cdot 10^{-5} \text{ M}$ ,  $I = 2.5 \cdot 10^{-3} \text{ M NaCaC}$ . The red line represents the fitting of the absorbance-time data pairs to a monoexponential function, **Eq. 1**.

$$A = A_0 \cdot e^{-\frac{t}{\tau}} \quad (1)$$

**Table 1.** Kinetic constants,  $1/\tau$ , related to a quation process for **1** and **2**.

Compound	$1/\tau$
<b>1</b>	0.121
<b>2</b>	0.130

**Determination of the  $pK_a$  values of compounds **1** and **2**.** The acid dissociation constants ( $pK_a$ ) were determined by measuring the evolution of the absorbance spectra, as a function of pH for both metal complexes. The UV-vis absorbance

spectrum for Ru(II) and Ir(III) complexes at different acidity levels are shown in **Figure 5**.

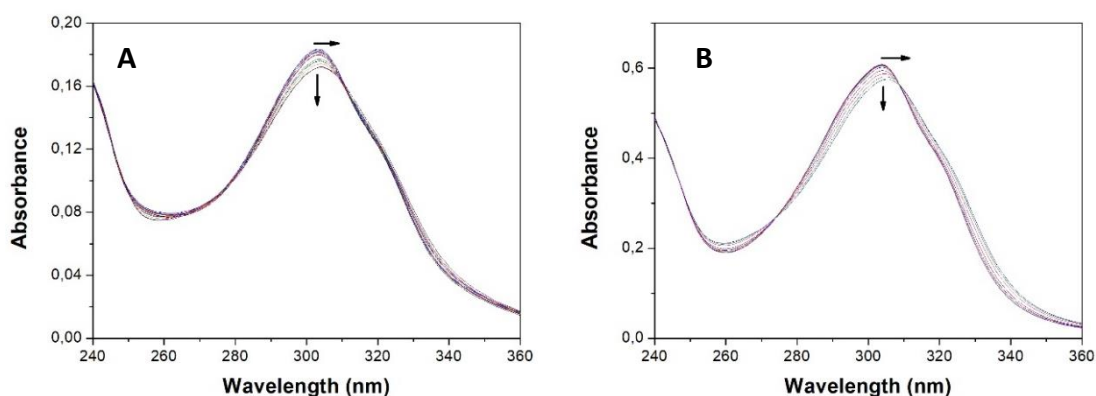


**Figure 5.** Evolution of the absorbance spectra of compounds **1** (A), **2** (B) with increasing pH (from 3 to 12, arrow sense),  $[1]= 9 \cdot 10^{-6}$  M,  $[2]= 4 \cdot 10^{-5}$  M.

$pK_a$  values were obtained plotting absorbance, at a fixed wavelength ( $\lambda$ ), in function of pH variation as shown in **Figure 6**, data were analyzed according to the Henderson-Hasselbach equation, **Eq. 2**.

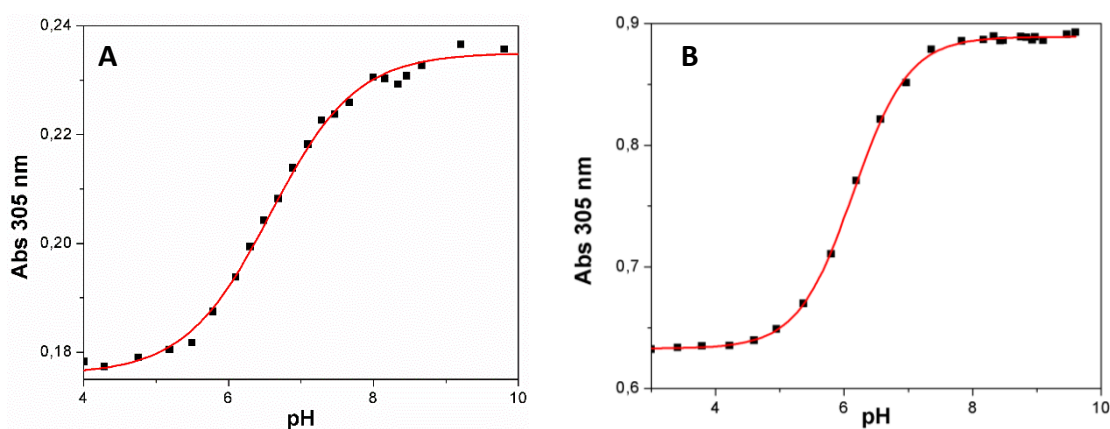


**Figure 6.** Absorbance at  $\lambda_{max}$  as function of pH fitted according to **Eq. 2** for compounds **1** (A) and **2** (B).

$$A = \frac{(A_{HB} - A_{B^-})}{(1 + 10^{m(pKa - pH)})} \quad (2)$$

Where  $A_{HB}$  and  $A_{B^-}$  stand for the absorbance of the acid and basic forms respectively, HB and  $B^-$  refer to the species involved in the deprotonation of the N-H group of the thiabendazole coordinated to the metal center, see **Fig. 7**,  $A$  is the total absorbance at each point and the  $m$  parameter is interpreted in terms of activity coefficient of the species involved in the equilibrium. The obtained  $pK_a$  values are shown in **Table 2**.

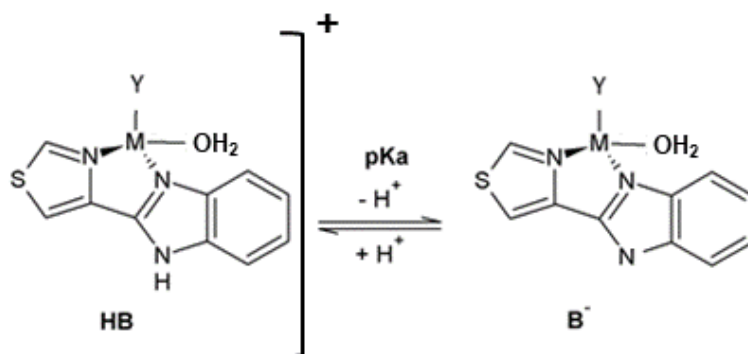


**Figure 7.** Acid-base equilibria of thiabendazole, relating to HB and B<sup>-</sup>, where M is the metal center (Ru or Ir), Y is the stabilizing arene ligand.

**Table 2.** Obtained pK<sub>a</sub> values using Eq.2.

Compounds	pK <sub>a</sub>
<b>1</b>	6.6
<b>2</b>	6.1

The existence of isosbestic points at  $\lambda = 310$  nm and  $\lambda = 308$  nm for **1** and **2** respectively evidence the presence of different species in equilibrium, also it can be seen a small maximum hypsochromic shift ( $\approx 3$ nm) for both. One ionization equilibrium was found for both metal complexes, in which the pK<sub>a</sub> 6.6 and 6.1 for Ru(II) and Ir(III) complexes respectively is referred to the deprotonation of N-H group present in the ancillary ligand. The effect of coordination in the pK<sub>a</sub> value for thiabendazole deprotonation has been reported previously,<sup>[107]</sup> in which the pK<sub>a</sub> is 12.50 for thiabendazole but drop to 5.75 when it is coordinated to ruthenium, in good agreement to what is reported herein. Therefore, at pH 7.4 in which DNA binding has been studied prevails the monocationic species for the metal aquo complexes, conversely the initial chloro complexes would be neutral under these conditions.

**Interaction with ct-DNA.** Different instrumental techniques and methods were utilised to study the interaction between ct-DNA and the synthesized **1** and **2** metal complexes. As the procedure is the same for both complexes, this allows to compare and analyse the effect and importance of the metal center. The techniques that were used to study the interaction included absorbance spectroscopy (UV-vis), circular dichroism (CD), thermal denaturation assays and viscosity measurements.

Covalent binding. The reactions were run at room temperature (25°C). Metal complex solution incubated overnight was added to an aqueous solution  $I = 2.5 \cdot 10^{-3}$  M, pH = 7.4



and varying concentration of ct-DNA. Different  $C_P/C_D$  ratios were proven, from 10 to 40, being  $C_P$  and  $C_D$  the concentrations of ct-DNA (**P**) and metal complex (**D**).

As it shows **Figure 8**, the isotherm obtained as a consequence of plotting absorbance at  $\lambda_{320\text{nm}}$  as function of time indicate product formation according to the global reaction  $\text{P} + \text{D} \rightarrow \text{PD}$ , being **PD** the ct-DNA/metal product. In order to clarify if the reaction can be affected by the high level of radiation during the assay, another kinetic assay was performed in which absorbance is measured each hour (**Figure 8B**), instead of each 20 s (**Figure 7A**). The trend is the same, so it has been concluded that the isotherm is associated to the binding of metal complex to ct-DNA.

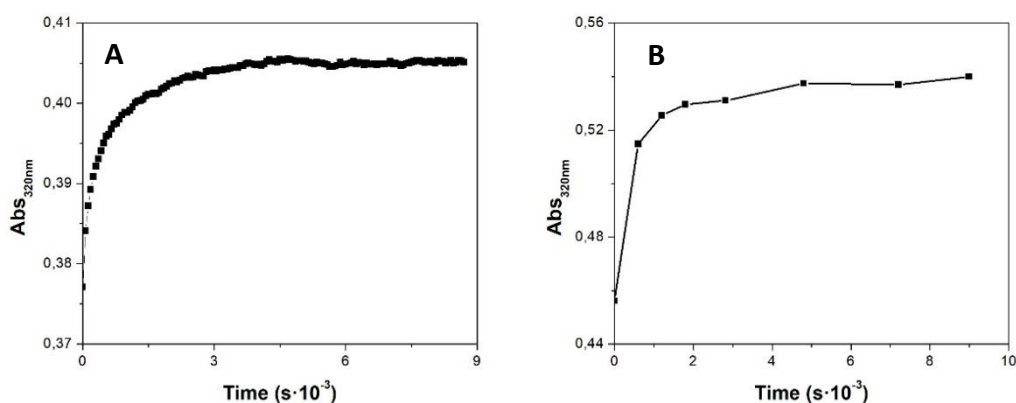


**Figure 8.** (A) Absorbance at  $\lambda_{320\text{nm}}$  in function of time for **2**/ct-DNA,  $\Delta t= 20$  s; (B) Absorbance at  $\lambda_{320\text{nm}}$  in function of time for **2**/ct-DNA,  $\Delta t= 1$  h.  $[\mathbf{2}] = 3 \cdot 10^{-5}$  M,  $C_P/C_D = 10$ ,  $\text{pH} = 7.4$ ,  $T = 25^\circ\text{C}$ .

The absorbance time data were fitted using **Eq. 1**, and the values of the calculated constants at different  $C_P/C_D$  ratios are shown in **Table 3**. Subsequently, for both the obtained kinetic constants were plotted in function of  $C_P$ , **Figure 9**.

**Table 3.**  $1/\tau$  values at different  $C_P/C_D$  for **1** and **2**.  $[C_D] = 3 \cdot 10^{-5}$  M,  $I = 2.5 \cdot 10^{-3}$  M,  $\text{pH} = 7.4$ ,  $T = 25^\circ\text{C}$ .

$C_P/C_D$	$1/\tau \cdot 10^3$	
	<b>1</b>	<b>2</b>
10	$1.33 \pm 0.33$	$7.64 \pm 0.37$
20	$2.15 \pm 0.37$	$8.10 \pm 0.44$
30	$2.90 \pm 0.41$	$7.56 \pm 0.33$
40	$2.77 \pm 0.29$	$7.68 \pm 0.37$

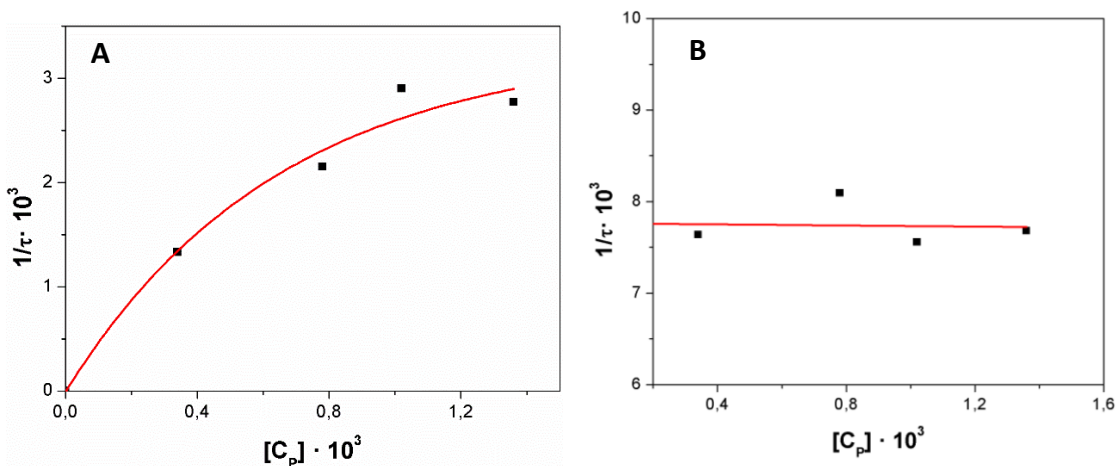


**Figure 9.** Kinetic constants in function of  $[C_p]$  for (A) 1/ct-DNA and (B) 2/ct-DNA systems.  $[C_D] = 3 \cdot 10^{-5} \text{ M}$ ,  $I = 2.5 \cdot 10^{-3} \text{ M}$ ,  $\text{pH} = 7.4$ ,  $T = 25^\circ \text{C}$ .

The curvature observed in **Figure 8A** suggests a two steps mechanism as defined in **Eq. 3**.



The first step is referred to the formation of  $PD_1$  in equilibrium with P and D, whose constant is  $K_1$ . Once the equilibrium is reached  $PD_1$  evolves toward PD through a slow process where  $k_2$  is the kinetic constant corresponding to the formation of a covalent bond<sup>[108]</sup>. The proposed mechanism entails that the formation of  $PD_1$  is faster than PD, otherwise the equilibria will not be reached. Consequently,  $PD_1$  can be identified as a non-covalent complex (intercalation or groove binding), while PD can be monofunctional covalent or bifunctional (non-covalent-covalent) complex. The parameters  $K_1$  and  $k_2$  can be calculated fitting the data pairs  $(1/\tau, C_p)$  to **Eq.4**.

$$\frac{1}{\tau} = K_1 \cdot \frac{k_2 \cdot C_p}{(1 + K_1 \cdot C_p)} \quad (4)$$

For the ruthenium complex, **Figure 8A** shows that initially the values of kinetic constant increase when increasing the  $C_p/C_D$  ratio until plateau.

So, if **Eq. 4** is fitted to the experimental data (red line in **Figure 9A**) the values for  $K_1$ , referred to the thermodynamic constant for the first equilibrium shown in **Eq. 3**, and  $k_2$ , referred to the kinetic constant concerning the formation of the covalent bond can be calculated, leading to  $K_1 = 1.2 \cdot 10^3 \text{ M}^{-1}$  and  $k_2 = 4.7 \cdot 10^{-3} \text{ s}^{-1}$  respectively. The value of  $K_1$  at  $I = 2.5 \text{ mM}$  is relatively low and supports the reaction path proposed above in **Eq. 4**, where  $PD_1$  is the intermediate for the formation PD.

Otherwise in the representation of **Eq. 4** for the iridium complex, as no curvature is appreciated in **Figure 9B**, it is assumed that in the proposed two steps mechanism  $K_1 C_p \ll 1$  and  $1/\tau = k_2$ , being  $k_2 = 7.8 \cdot 10^{-3} \text{ s}^{-1}$ , the double compared to  $k_2$  for ruthenium complex, **1**.

**Melting temperature experiments.**  $T_m$  has been calculated for different  $C_D/C_P$  ratios, all samples were incubated overnight before being measured. For **1**, an initial increase in melting temperature is observed, reaching a maximum at  $C_D/C_P = 0.2$ , **Figure 10A**. This behaviour is compatible with intercalation since this type of interaction increases the  $T_m$ . Then when  $C_D/C_P > 0.2$  descends noticeably to lower values than the initial  $T_m$  of ct-DNA alone, reaching constant  $T_m$  values at  $C_D/C_P \approx 0.7$ . It is possible that at  $C_D/C_P \leq 0.2$  the effect of the intercalation on the  $T_m$  is higher than the covalent binding, but as  $C_D/C_P$  increases DNA partial denaturalization is induced by the covalent bond easing the H-bonds breakdown of the base pairs, reaching the saturation at  $C_D/C_P \approx 0.7$ . Similar explanation is adequate for the iridium complex, **2**, but in this case the effect of the intercalation is not appreciated, nevertheless at  $C_D/C_P < 0.2$   $T_m$  remains constant, **Figure 10B**. The interpretation of the results reported herein is supported by viscosity results shown below.

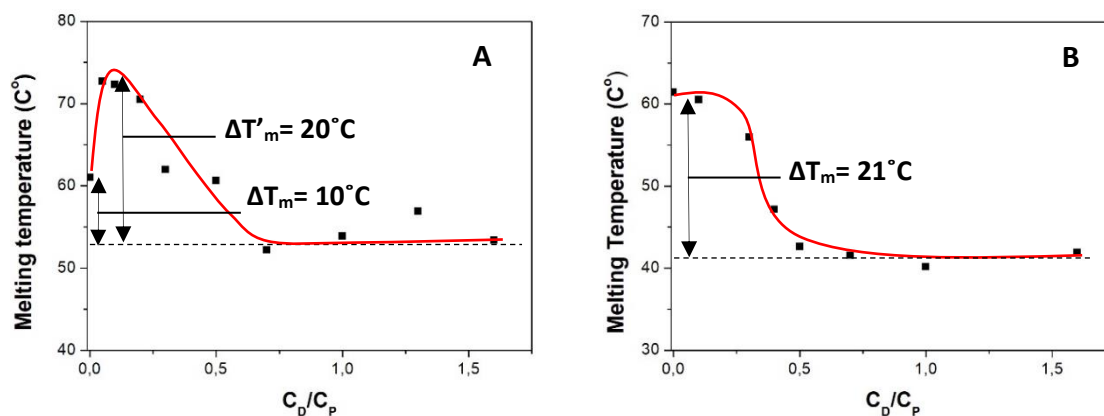
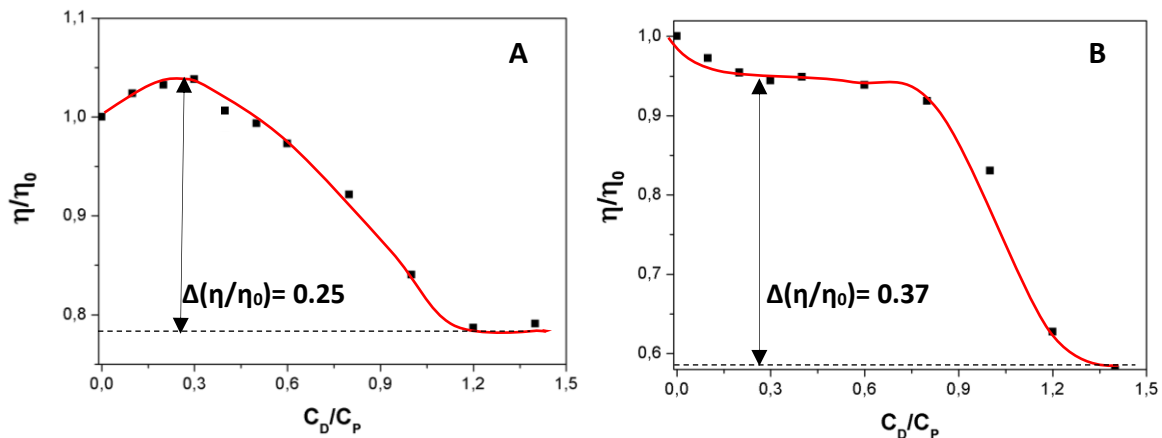


**Figure 10.** Melting temperature,  $T_m$ , for the **1**/ct-DNA (left) and **2**/ct-DNA (right) systems.  $C_D/C_P = 0 - 1.6$ ,  $I = 2.5 \cdot 10^{-3}$  M NaCaC and pH = 7.4.

**Viscosity measurements.** Samples were prepared analogously as mentioned above for melting temperature experiments. In both cases two stretches with different trends are observed. For the ruthenium complex when  $C_D/C_P < 0.2$ ,  $\eta/\eta_0$  increases, and then decreases noticeably, **Figure 11 A**. It is well known that intercalation increase the length of DNA, therefore viscosity increase; while the intrastrand covalent binding decrease viscosity., so analogous to melting temperature experiments at  $C_D/C_P < 0.2$  the effect of intercalation is stronger than that of the covalent binding. When increasing  $C_D$  there is a drastic decrease of  $\eta/\eta_0$ , reaching the saturation at  $C_D/C_P \approx 1.2$ . In the case of **2** the initial decrease of  $\eta/\eta_0$  makes intercalation not so perceptible as for **1**, or the increase of the viscosity induced by intercalation does not compensate the decrease of this by the covalent binding, **Figure 11 B**. Although, similar dramatic decrease of viscosity values was found when  $C_D/C_P > 0.9$ , until plateau at  $C_D/C_P \approx 1.3$ .

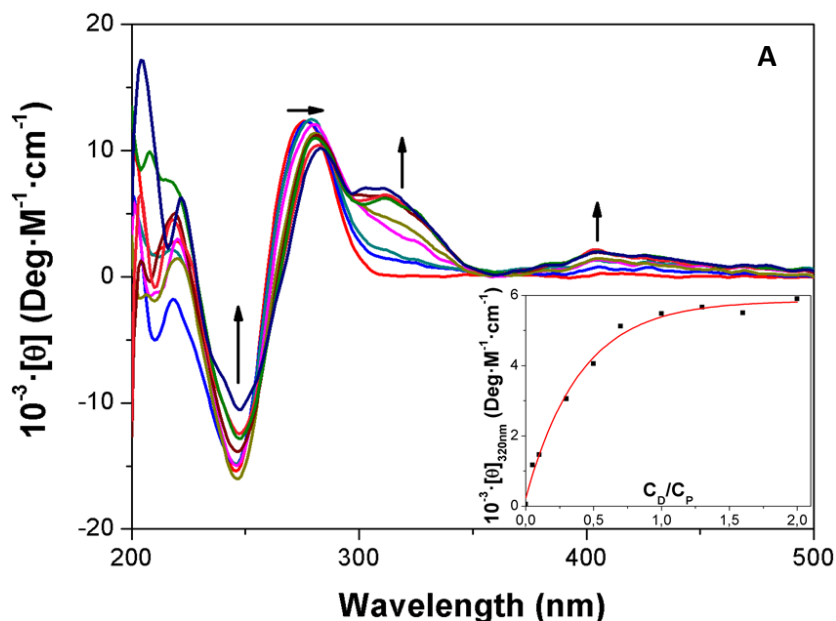
With the differences inherent in each procedure, this behaviour is similar to that observed for the melting temperature experiments. The partial denaturalization of ct-DNA induced by the complexes, consistent with the high values of  $\Delta T_m$  (see **Figure 10**),

favours ct-DNA compactation and the formation of aggregates,  $PD_{III}$ , that strongly decrease  $\eta/\eta_0$  values.



**Figure 11.** Relative viscosity of the (A) **1**/ct-DNA and (B) **2**/ct-DNA systems.  $C_P = 2 \cdot 10^{-4}$  M,  $I = 2.5$  mM NaCaC and  $T = 25^\circ\text{C}$ .

Circular Dichroism (CD). The interaction of **1** and **2** with ct-DNA has been confirmed by CD, melting temperature and viscosity measurements. CD spectra recorded at different  $C_D/C_P$  ratios are shown in **Figure 12**, the samples were incubated overnight before the measurements. In addition, measurements of CD were recorded for both complexes in buffer solution certifying that they did not show any dichroic signal.



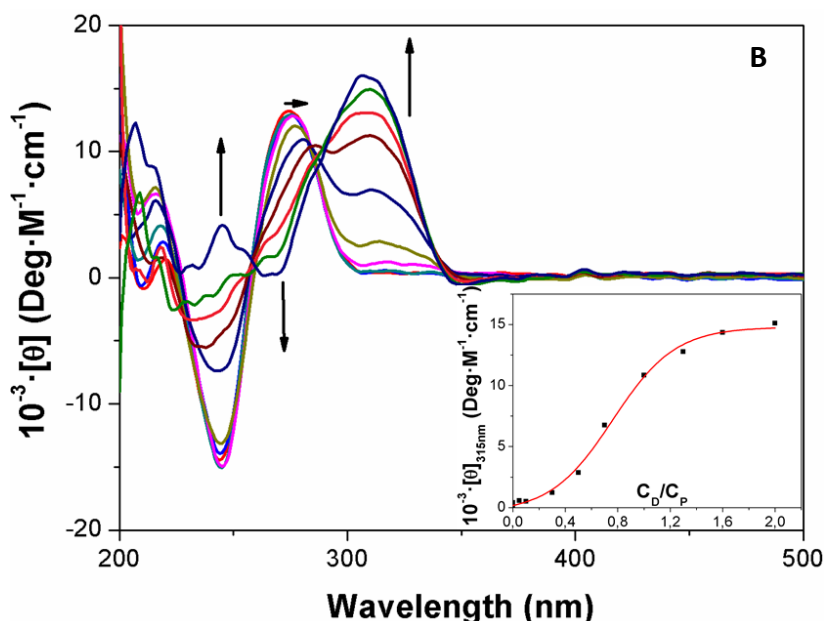


**Figure 12.** CD spectra for (A) **1**/ct-DNA and (B) **2**/ct-DNA systems. Inserted: binding isotherm at  $\lambda = 320$  nm and  $315$  nm, for **1** and **2** respectively.  $C_P = 5 \cdot 10^{-5}$  M,  $I = 2.5 \cdot 10^{-3}$  M NaCaC, pH= 7.4 and  $T = 25^\circ\text{C}$ .

The evidence of isodichroic points at  $\lambda = 259$  nm and at  $\lambda = 259$  nm and  $285$  nm, for ruthenium and iridium complexes respectively, indicates the presence of species in equilibrium. Strong changes induced in the ct-DNA CD spectra were observed in both positive ( $\lambda = 245$  nm) and negative bands ( $\lambda = 275$  nm). These changes are not usual when a covalent bond is formed by binding to a single DNA strand, as it is necessarily in this case, so we considered that another type of interaction is occurring while the complex is covalently bonded to DNA, so that both generate remarkable modifications in the helicity of the structure and therefore in the secondary conformation of ct-DNA.

Presumably there is a partial denaturalization of ct-DNA; this effect is more evident in the case of the iridium complex (**Figure 12B**), where the positive and negative characteristic bands of ct-DNA ( $245$  and  $275$  nm respectively) diminish until disappearing, at the same time that the induced CD signal of the complex covalently bound to one of the ct-DNA strands increase ( $315$  nm). This effect is less pronounced in the case of the ruthenium complex (**Figure 12A**)

Considering the UV-vis spectra for these metal complexes in aqueous solution, **Figure 3**, the induced dichroism bands agree with the absorbance peaks for each complex. Plotting molar ellipticity at a fixed wavelength,  $\lambda = 320$  nm and  $315$  nm for **1** and **2** respectively, as a function of  $C_P/C_D$  (**Figure 12** inserted graphs), isotherms related to the binding between the metal complex and ct-DNA were obtained for both metal complexes.

As both, **1** and **2**, are positively charged, the influence of the metal does not seem significant. In order to ease the interpretation of the experimental results, computational studies have been carried out.

### 3.3.2 Computational results.

Molecular dynamics (MD) simulations and quantum mechanics/molecular mechanics (QM/MM) calculations have been performed, with the aim to interpret the experimental results and in particular, to understand the role of the metal center in the binding mode of the metal complex with DNA. In fact, the experimental results suggest, as mentioned in **Eq. 3**, that both **1** and **2** are covalently bonded to ct-DNA (**PD<sub>II</sub>**) preceded by an intermediate in which the ancillary ligand is intercalated (**PD<sub>I</sub>**) as it has been recently reported.<sup>[110]</sup> QM/MM calculations were performed to calculate the energy of the metal complex/DNA and metal complex/guanine system, with the aim to comparing the stability of the two enantiomers of compounds **1** and **2** when bonded to DNA, to assess stereoisomer specificity toward DNA binding.

MD simulations. The effect of the metal ion-N7 covalent bond on the double-helical structure was evaluated analysing the changes induced in the B-DNA conformation. Moreover, the MD simulations allowed to monitor: (i) the effect of the substituents, (ii) the metal complex orientation and position on the DNA structure. The possible intercalation of the ancillary ligand while the complex is covalently bonded has been also tested. The binding of both the Ru(II) and Ir(III) complexes with the B-DNA sequence d(AGCTAGCTCAGT)<sub>2</sub> was investigated, in which the metal ion is covalently bonded to the N7 atom of the central guanine base. **Figure 13** shows the optimized structures of the enantiomers corresponding to the “S” configuration for **1** and **2**, in which the chloride ligand can be substituted by water in aqueous solution, presumably giving rise to a racemic mixture of the two “S” or “R” enantiomers.

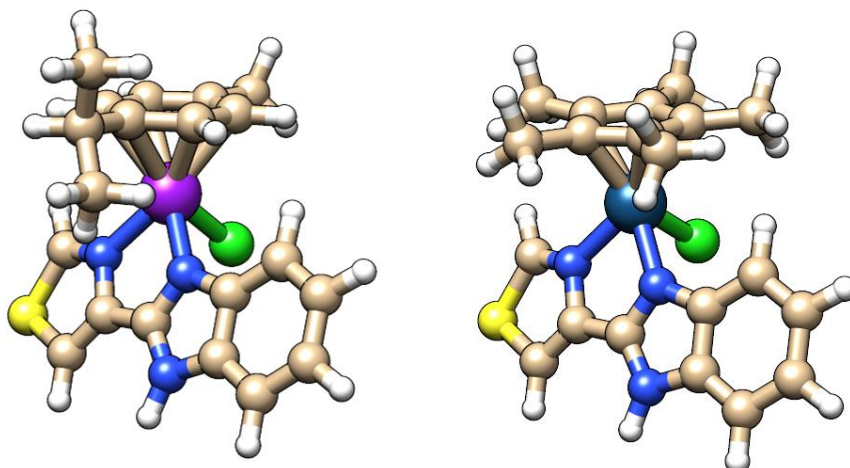


**Figure 13.** Optimized structures obtained by DFT calculations for the ruthenium(II) complex **1** (left) and the iridium(III) complex **2** (right) corresponding to the “S” configuration.

The Root Mean Square Deviation (RMSD) plots, **Figures 14-15** enable to follow the structural changes occurring along the MD trajectory, where important conformational changes, for both the B-DNA and the metal complex, occur before and at the equilibrium phase. Some snapshots of **1/B-DNA** and **2/B-DNA**, occurring along the MD simulation are shown in **Figures 13-14**, which allow to describe and compare the dynamics of the two systems. The corresponding video files are available as supplementary files, through the QR codes shown in **Figures 13** and **14**.

In addition, the variations of a dihedral angle formed by the atoms: C8, N7, M and CA, see **Figure 16**, has been monitored. C8 and N7 form part of the guanine nitrogen base, M can be Ru or Ir and CA is one of the six carbon atoms of the aromatic ligand, p-cymene or pentamethylcyclopentadiene respectively. This angle allows to monitor the rotation around the N7-M covalent bond during the MD simulation.



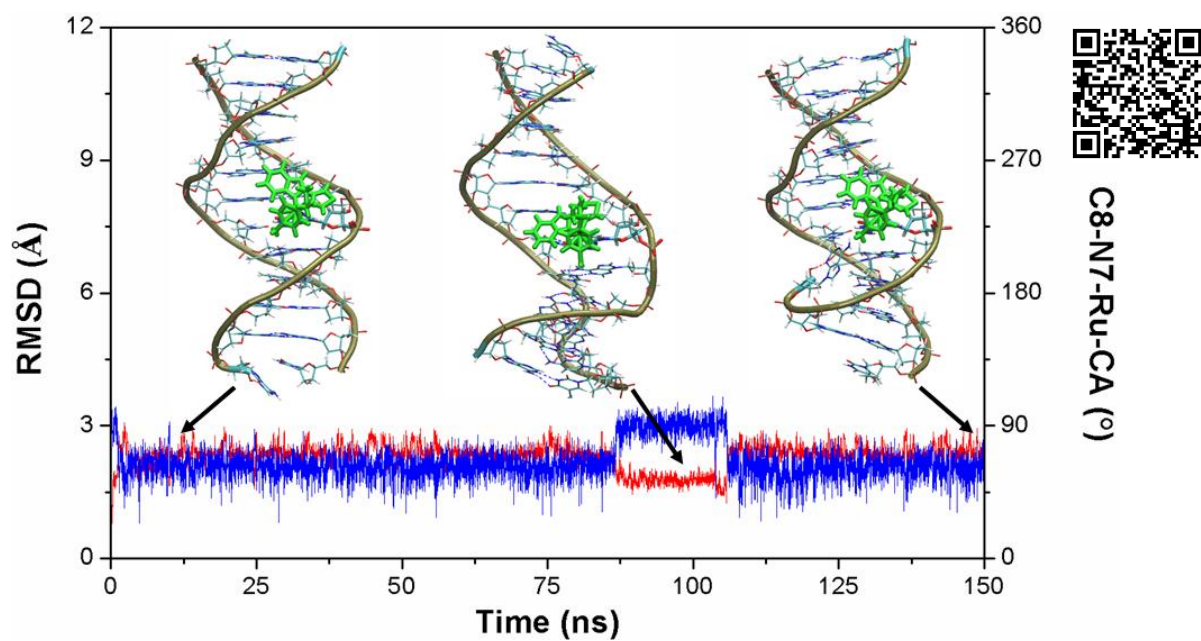
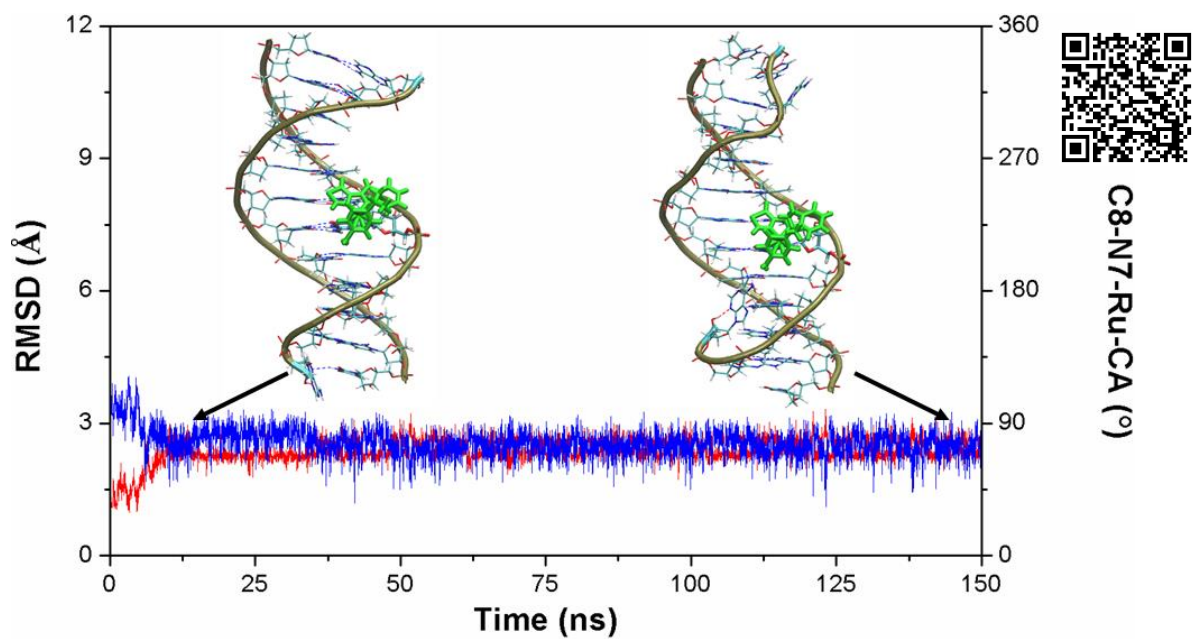


**Figure 14.** RMSD plot of the fragment **1** coordinated to the guanine base (red line) and variation of the dihedral plane C8-N7-M-CA (blue line). R diastereomer above and S diastereomer below.



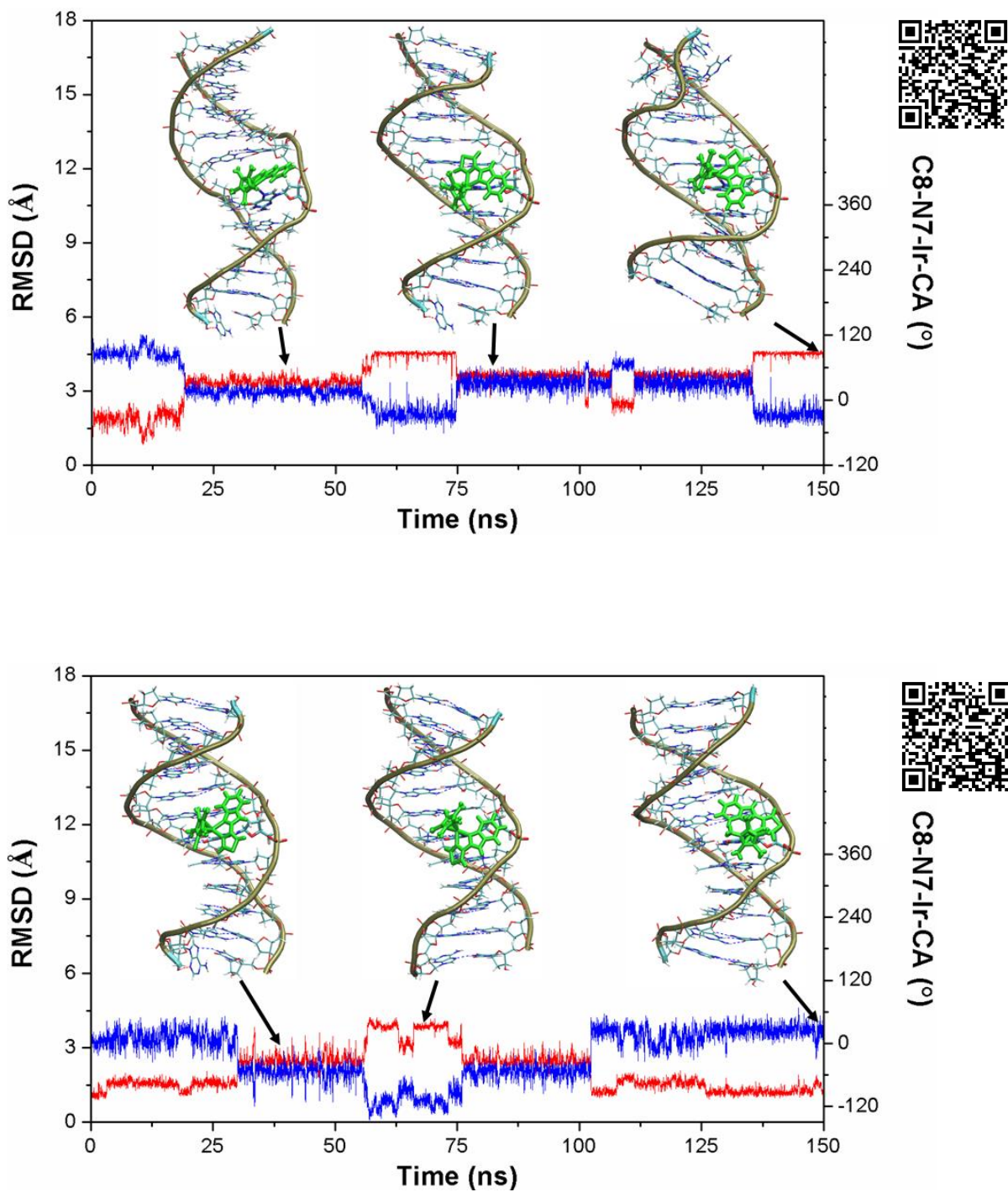


**Figure 15.** RMSD plot of the fragment **2** coordinated to the guanine base (red line) and variation of the dihedral plane C8-N7-M-CA (blue line). R diastereomer above and S diastereomer below.

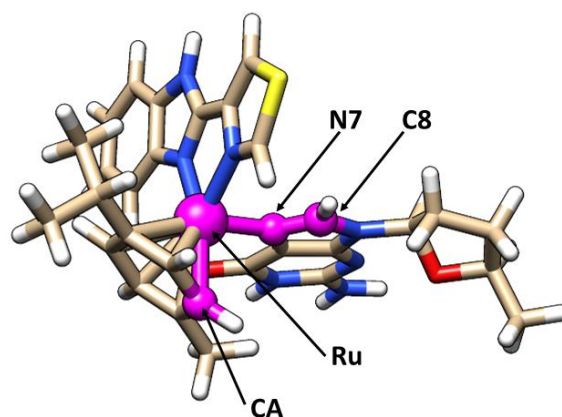


**Figure 16.** Definition of the dihedral plane monitored in the MD simulations, in magenta.

The results of the MD simulations show that there are some differences between the behaviour of the Ru(II) and Ir(III) complexes, and in particular also between the two diastereomers of each metal complex. Although the kinetics investigations confirm the occurrence of a fast intercalation, before the formation of the covalent bonding, the results of the MD simulations allow to exclude the concomitant intercalation of the ancillary ligand while the metal complex is covalently bonded. In fact, the thiabenzazole always exits from the intercalation pocket after few ns. Remarkably the obtained results have proven that the ancillary ligand plays an important role in the overall stability and structure of the metal complex-DNA system. Indeed, while the complex is covalently bonded to the N7 atom, the ancillary ligand is placed in the major groove and each rotation around the N7-M covalent bond is always followed by a large conformational change in the DNA structure. Interestingly, the ancillary ligand of the Ru(II) compound **1**, **Figure 14**, leaves the intercalation pocket and remains oriented along the DNA major groove till the end of the simulation. On the other hand, more simulation time is necessary to the ancillary ligand of the Ir(III) compound **2**, **Figure 15**, to leave the intercalation pocket. Larger conformational changes in the DNA double-helix occur mainly for the “R” diastereomer. Such DNA conformational changes are in good agreement with the spectral changes observed in the CD at increasing values of the metal complex concentration. In conclusion, the interaction of the metal complex bonded to guanine while the ancillary ligand performs a groove binding type interaction toward the major groove induces important B-DNA conformational changes, such as: (i) backbone deformation and (ii) decrease and distortion of helicity.

QM/MM calculations. Significant structural details can be obtained by the analysis of the optimized structures reported in, **Figures 17-20**, obtained identifying and sampling the structures more often occurring during the MD simulations of both **1**/B-DNA and **2**/B-DNA systems through geometry clustering, assumed as equilibrium structures.

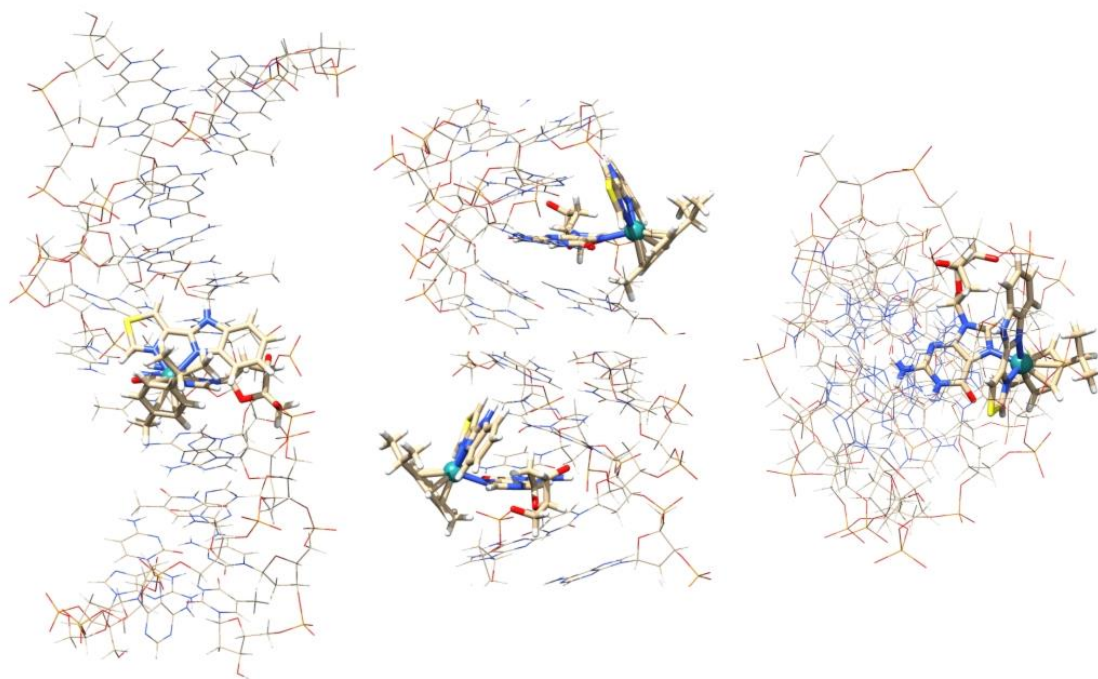


**Figure 17.** Different views of the optimized structures of the Ru(II) compound **1**, R diastereomer, binding to B-DNA, obtained by QM/MM calculations. The high layer is shown in bold sticks while the lower layer in wires.

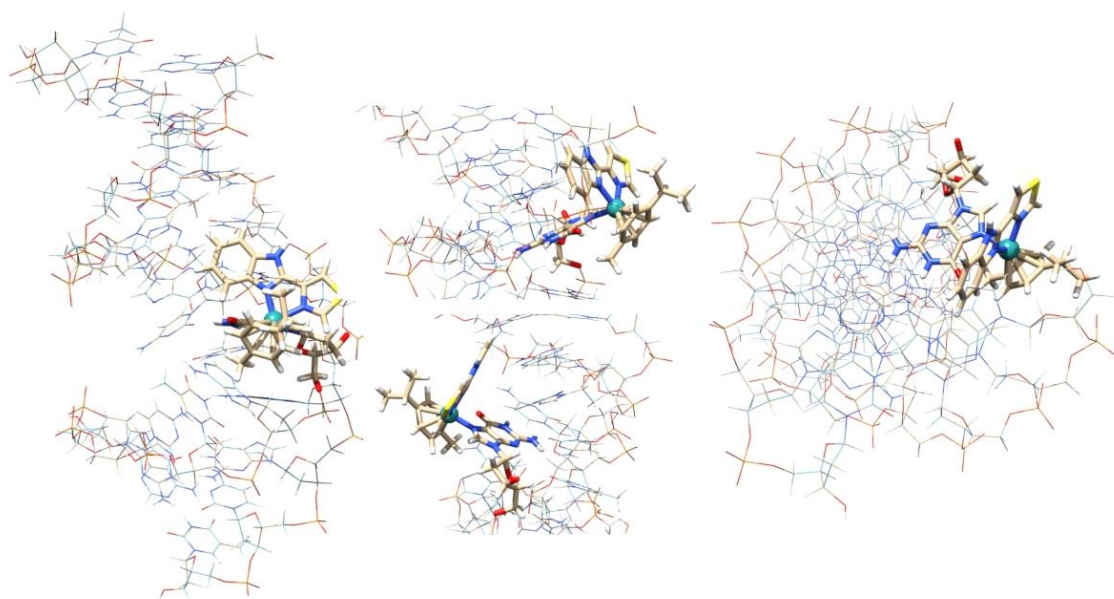


**Figure 18.** Different views of the optimized structures of the Ru(II) compound **1**, S diastereomer, binding to B-DNA, obtained by QM/MM calculations. The high layer is shown in bold sticks while the lower layer in wires.



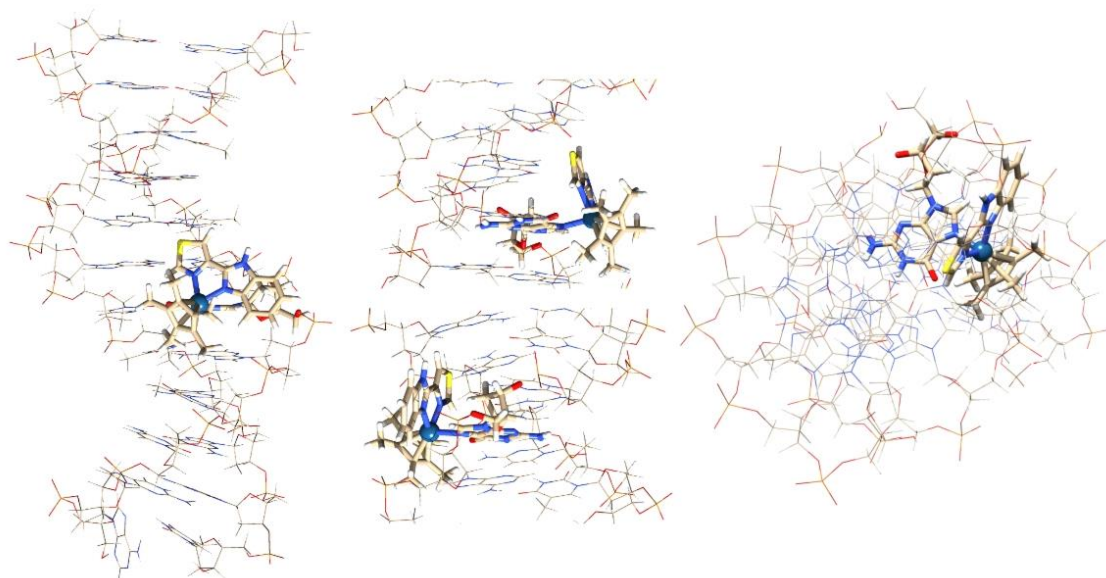


**Figure 19.** Different views of the optimized structures of the Ru(II) compound **2**, R diastereomer, binding to B-DNA, obtained by QM/MM calculations. The high layer is shown in bold sticks while the lower layer in wires.

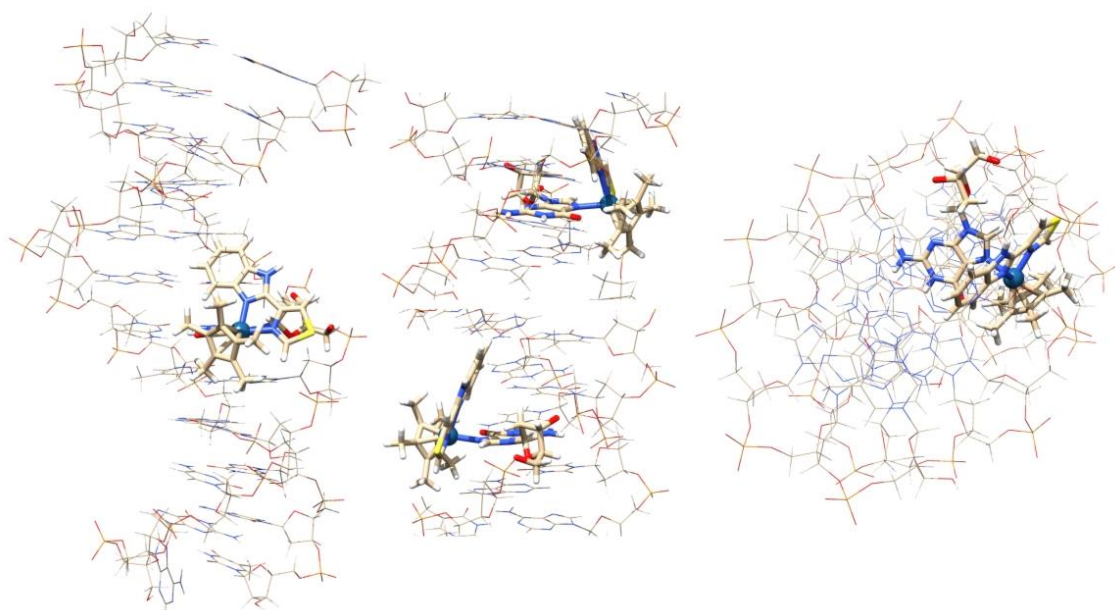


**Figure 20.** Different views of the optimized structures of the Ru(II) compound **2**, S diastereomer, binding to B-DNA, obtained by QM/MM calculations. The high layer is shown in bold sticks while the lower layer in wires.

Through the two-layer QM/MM hybrid calculations, the energy of each metal complex/B-DNA system can be obtained and, in particular, the effect of the two diastereomers of each metal complex can be evaluated. **Table 4** shows the calculated energy differences for both enantiomers, R show less energy than S.

**Table 4.** Diastereomer SCF energy comparison for compounds **1** and **2**.

Energy <sub>Drug/BNDA</sub> (kJ/mol)	
E <sub>1-S</sub> - E <sub>1-R</sub>	6,39
E <sub>2-S</sub> - E <sub>2-R</sub>	30,69

*Calculated force constants.* From the resulting QM/MM structures the force constants,  $k$ , of the metal-N7 bond for each diastereomer of the two metal complexes was calculated through the Compliance 3.0.2 program.<sup>[111,112]</sup> The obtained values are shown in **Table 5**. Interestingly, such force constants for the two diastereomers of compound **1** are similar while for the two diastereomers of compound **2** they are different. Such result agrees with the energy data reported in **Table 2**. In fact, the DNA binding of the two diastereomers of compound **1**, does not cause a large difference in energy, whereas the DNA binding of the R diastereomer of **2** is more stable of about 30 kJ/mol than that of the S diastereomer. It is also interesting that in the case of compound **1** the obtained binding constant is slightly higher than that of compound **2**, indicating that the Ru(II) compound binds more tightly DNA than the Ir(III) compound.

**Table 5.** Calculated force constants for the M-N7 bond (M= Ru or Ir) for the R and S diastereomers of compounds **1** and **2**.

Compounds	k (mdyn/ang)
1-R	1,63
1-S	1,63
2-R	1,21
2-S	1,46

### 3.4 Conclusions

The interaction of the Ru(II) and Ir(III) compounds **1** and **2**, with double helical DNA occurs through a two-step mechanism, where first the thiabendazole ligand is intercalated, forming the labile **PD<sub>i</sub>** complex, and then a covalent bond is formed, presumably with the N7 atom of a guanine base, forming a stabile **PD** complex, where the auxiliary thiabendazole ligand interacts with DNA through major groove binding. These conclusions have been experimentally proven through UV-vis absorption, CD, viscosity and melting temperature assays. Moreover, MD simulations have shown that the DNA-binding of both **1** and **2** complexes generates a remarkable distortion of the DNA backbone, in good agreement with the results from CD spectroscopy. Altogether the results obtained highlight the importance of the role played by the ancillary ligand in the interaction of these half-sandwich complexes with DNA, as well as the importance of the metal center in determining the DNA binding strength. In fact, although the DNA binding of both diastereomers of the two metal compounds follows

a qualitatively similar recognition mechanism, the results of QM/MM and, in particular, the evaluation of the Metal-N7 force constants, indicate that the ruthenium complex, **1**, binds DNA more strongly than the analogous iridium complex, **2**. Interestingly, the energy differences obtained by QM/MM calculations show that both S diastereomers of **1** and **2** bind DNA more strongly than the R diastereomers.

# Chapter IV

---

**Role of seroalbumin in the cytotoxicity of *cis*-dichloro Pt(II) complexes with (N<sup>^</sup>N)-donor ligands bearing functionalized tails**

## Summary

In this chapter the synthesis of four new cis-[PtCl<sub>2</sub>(N^N)] organoplatinum complexes is reported as well as the study of their cytotoxicity and binding ability toward dGMP (deoxyguanine monophosphate), ct-DNA and albumin models.

Due to its analogy with cisplatin, [PtCl<sub>2</sub>(bpyst)] (bpyst = 4,4'-bis( $\alpha$ -styrene)-2,2'-bipyridine), **Figure 1**, has been considered as an interesting potential DNA targeting drug, but surprisingly it does not covalently bind DNA.

My main contribution to the work was to compare, by DFT calculations, the solution behavior of the two molecules, cisplatin and [PtCl<sub>2</sub>(bpyst)], providing support to the interpretation of the experimental results. DFT calculations were carried out, using three different functionals: B3LYP,<sup>[62,63]</sup> PBE0<sup>[61]</sup> and M06-2X,<sup>[60]</sup> the CEP-121G effective potential basis set<sup>[64-66]</sup> for the Pt atom and the 6-31G(d,p) basis set for the other atoms.<sup>[66,67]</sup> It is well known that the hydrolysis of platinum(II) complexes is the key step before DNA binding. As described below, we have theoretically investigated the structures and the relative stability of the species involved in the commonly accepted reaction pathway for hydrolysis, leading the dichloro reactant to the diaquo product.

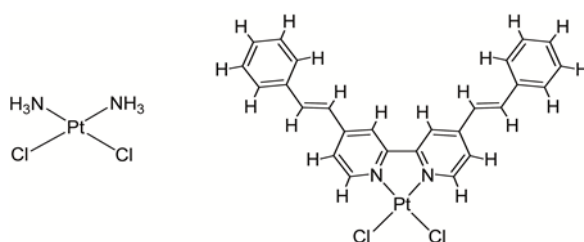


**Figure 1.** Structure of cisplatin (left) and [PtCl<sub>2</sub>(bpyst)] (right).

Experimentally, due to the low solubility of the complex in water, the solutions were initially prepared in DMSO. The calculations showed that DMSO can easily substitute [PtCl<sub>2</sub>(bpyst)] chlorides through a S<sub>N</sub>2 mechanism, see **Figure 2**. This substitution is in fact thermodynamically favoured. The published article is attached below.



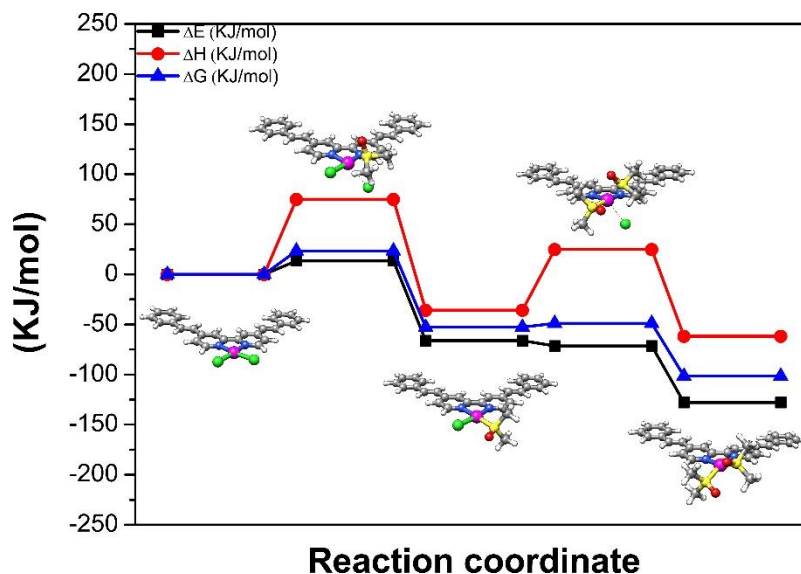


**Figure 2.** Pt coordination geometry, relative energy, enthalpy and Gibbs free energy of the species involved in the reaction pathway for the Cl-DMSO substitution of  $[\text{PtCl}_2(\text{bpyst})]$ , obtained by DFT calculations in the implicit DMSO solvent.

The aqueous buffer solutions, used in the experimental section, were prepared from the stock solution in 100% DMSO. The DNA binding mechanism for cisplatin and its derivatives occurs through an initial hydrolysis, after which the Pt complex is able to covalently bind the nucleic acid, through the N7 nitrogen atom of guanine. As a consequence, we expect that the  $[\text{Pt}(\text{DMSO})_2(\text{bpyst})]$  complex undergoes a similar hydrolysis process. This second process was computationally studied in two different solvents: 1) DMSO and 2) water, see **Figures 3** and **4**. In the mentioned figures, in either case the hydrolysis of the DMSO complex is thermodynamically disfavoured, so that the hydrolysis product, in the two cases, has higher energy than the reactants. These result support the hypothesis that the hydrolysis reaction does not occur.

In conclusion, the key step for the binding of cisplatin and its derivative complexes is the initial hydrolysis process. However, in DMSO, due to the chloro-DMSO substitution, the DMSO-water substitution does not occur. This result can be directly related to the absence of cytotoxicity experimentally detected: the molecule cannot interact with DNA because the Pt ion remains coordinated by two DMSO molecules. Previous calculations showed that the chloro-complex can be hydrolysed, in water solution, by a similar mechanism of cisplatin, see **Figure 5** and **6**. So that, a possible solution could be the use of a different solvent, not DMSO, before dissolving it in water solution, to investigate its biological properties and its interaction with DNA. This theoretical study of cisplatin hydrolysis is the starting point of the study that gives rise to **Chapter V**, where it is evaluated in greater depth.

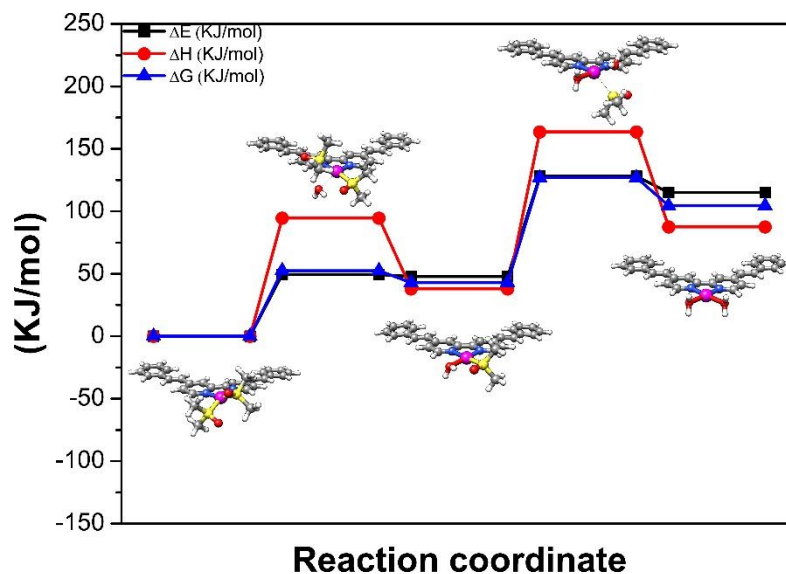


**Figure 3.** Pt coordination geometry, relative energy, enthalpy and Gibbs free energy of the species involved in the reaction pathway for the hydrolysis of [Pt(DMSO)<sub>2</sub>(bpyst)], obtained by DFT calculations in the implicit DMSO solvent.

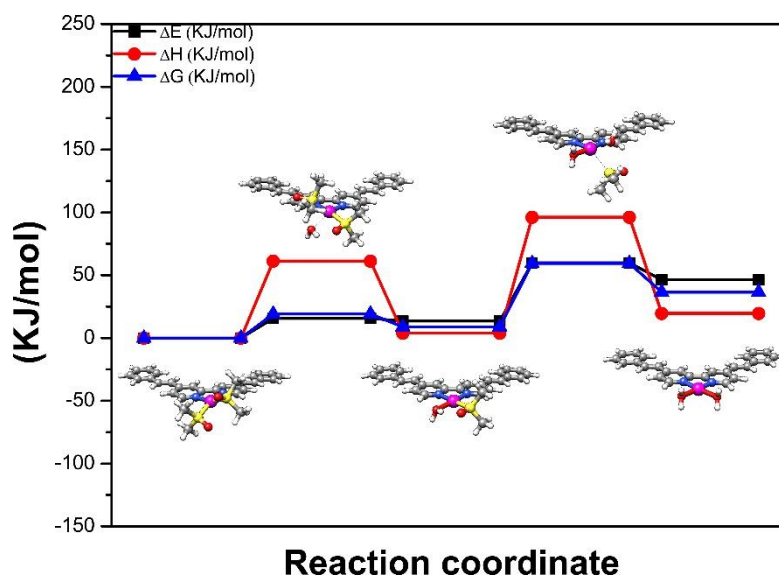


**Figure 4.** Pt coordination geometry, relative energy, enthalpy and Gibbs free energy of the species involved in the reaction pathway for the hydrolysis of [Pt(DMSO)<sub>2</sub>(bpyst)], obtained by DFT calculations in the implicit water solvent.

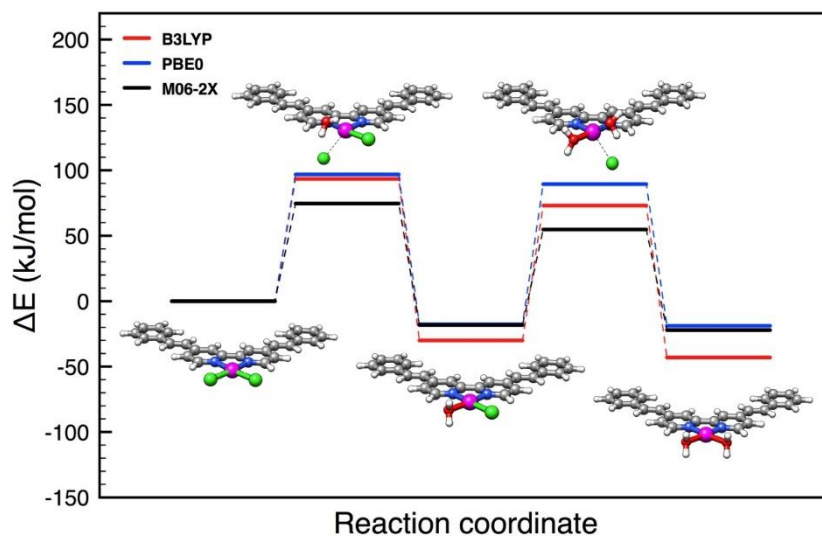


**Figure 5.** Pt coordination geometry and relative energy of the species involved in the reaction pathway for the hydrolysis of  $[\text{PtCl}_2(\text{bpyst})]$ , obtained by DFT calculations in the implicit water solvent.

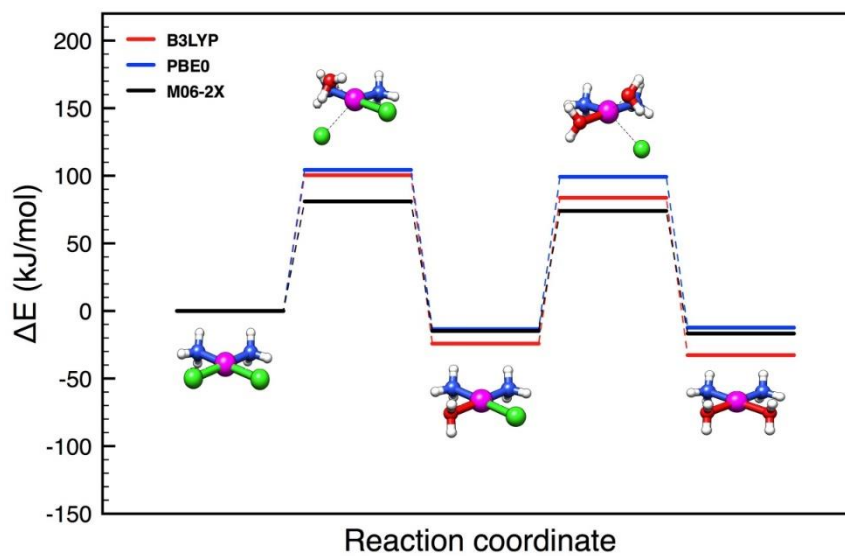


**Figure 6.** Pt coordination geometry and relative energy of the species involved in the reaction pathway for the hydrolysis of cisplatin, obtained by DFT calculations in the implicit water solvent.

## Role of Seroalbumin in the Cytotoxicity of *cis*-Dichloro Pt(II) Complexes with (N<sup>^</sup>N)-Donor Ligands Bearing Functionalized Tails

Cristina Pérez-Arnaiz,<sup>‡</sup> Jorge Leal,<sup>†</sup> Natalia Busto,<sup>‡</sup> María C. Carrión,<sup>†</sup> Ana R. Rubio,<sup>‡</sup> Imanol Ortiz,<sup>†</sup> Giampaolo Barone,<sup>§</sup> Borja Díaz de Greñu,<sup>†</sup> Javier Santolaya,<sup>‡</sup> José M. Leal,<sup>‡</sup> Mónica Vaquero,<sup>‡</sup> Félix A. Jalón,<sup>‡</sup> Blanca R. Manzano,<sup>†</sup> and Begoña García<sup>\*,†</sup>

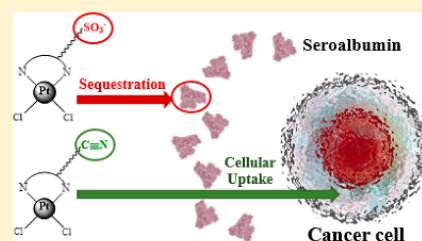
<sup>‡</sup>Departamento de Química, Universidad de Burgos, Plaza Misael Bañuelos s/n, 09001 Burgos, Spain

<sup>†</sup>Facultad de Ciencias y Tecnologías Químicas-IRICA, Universidad de Castilla-La Mancha, Avda. Camilo J. Cela 10, 13071 Ciudad Real, Spain

<sup>§</sup>Dipartimento di Scienze e Tecnologie Biologiche, Chimiche e Farmaceutiche, Università degli Studi di Palermo, Viale delle Scienze Ed. 17, 90128 Palermo, Italy

### Supporting Information

**ABSTRACT:** Given the potent anticancer properties of *cis*-diamminedichloroplatinum(II) and knowing its mode of action, we synthesized four new *cis*-[PtCl<sub>2</sub>(N<sup>^</sup>N)] organoplatinum complexes, two with N-substituted pbi ligands (pbiR = 1-R-2-(2-pyridyl)benzimidazole) (namely, 1 and 2) and two more with 4,4'-disubstituted bpy ligands (bpy = 2,2'-bipyridine) (namely, 3 and 4). We explored their cytotoxicity and ability to bind to deoxyguanosine monophosphate (dGMP), DNA, and albumin models. By <sup>1</sup>H NMR and UV-vis spectroscopies, circular dichroism, agarose gel electrophoresis, differential scanning calorimetry measurements, and density functional theory calculations, we verified that only 3 can form aquacomplex species after dimethyl sulfoxide solvation; surprisingly, 1, 2, and 3 can bind covalently to DNA, whereas 4 can form a noncovalent complex. Interestingly, only complexes 1 and 4 exhibit good cytotoxicity against human ovarian carcinoma (HeLa) cell line, whereas 2 and 3 are inactive. Although lung carcinoma (A549) cells are more resistant to the four platinum complexes than HeLa cells, when the protein concentration in the extracellular media is lower, the cytotoxicity becomes substantially enhanced. By native electrophoresis of bovine seroalbumin (BSA) and inductively coupled plasma mass spectrometry uptake studies we bear out, on one hand, that 2 and 3 can interact strongly with BSA and its cellular uptake is negligible and, on the other hand, that 1 and 4 can interact with BSA only weakly, its cellular uptake being higher by several orders. These results point up the important role of the protein binding features on their biological activity and cellular uptake of *cis*-"PtCl<sub>2</sub>" derivatives. Our results are valuable in the future rational design of new platinum complexes with improved biological properties, as they expose the importance not only of their DNA binding abilities but also of additional factors such as protein binding.



## INTRODUCTION

Despite the notable advances in the discovery of new anticancer drugs that could become alternative to cisplatin, some of the disadvantages of this compound still remain satisfactorily unsolved so far.<sup>1,2</sup> It is therefore necessary to continue designing new active structural fragments and modify those that have proved to be ineffective, probably because they present limitations to reach their target. For example, factors such as protein binding and lipophilicity have a determinant impact on the absorption, distribution, metabolism, and excretion processes of the organic anticancer drugs.<sup>3</sup>

Thus, the favorable chemical formulation, size and shape, and the judicious inclusion of functional groups to achieve a favorable balance between lipophilicity and hydrophilicity are essential for the correct formulation of drugs. The presence of both lipophilic and hydrophilic groups in a drug can facilitate its administration and cell uptake. In the design of anticancer

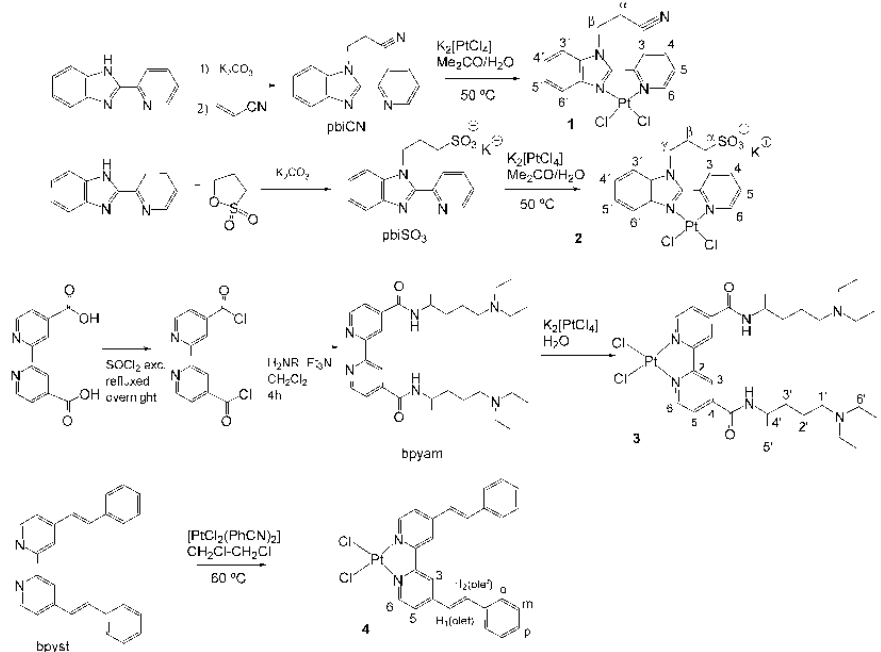
drugs, cellular uptake, lipophilicity, and cytotoxicity correlate in some instances.<sup>4</sup>

[PtCl<sub>2</sub>(bpy)] (bpy = 2,2'-bipyridine) and other complexes with bpy bisubstituted in the 4,4' positions and rollover cyclometalated Pt compounds based in the same backbone exhibit lower cytotoxic activity than cisplatin.<sup>5,6</sup> Comparable lack of marked activity has been found for the [PtCl<sub>2</sub>(Hpb)] (Hpb = 2-(2'-pyridyl)benzimidazole) counterparts.<sup>7,8</sup> These results are surprising if one takes into account the notable cytotoxicity of many compounds with the *cis*-"PtCl<sub>2</sub>" unit, and it might indicate the existence of limitations for these molecules to achieve their targets. By contrast, the organometallic derivate [PtMe(DMSO)(pbi)] (pbi = deprotonated form of Hpb; DMSO = dimethyl sulfoxide), also neutral, shows a notable

Received: March 16, 2018

Published: May 3, 2018

Chart 1. Synthesis of Ligands and Complexes 1–4 and Atom Numbering Scheme



activity against A2780 and A2780R cancer lines,<sup>9</sup> indicating that minor changes can induce pronounced differences in the biological activity.

In this work, we propose introducing side lateral functionalized chains in both pbi and bpy ligands, synthesizing their *cis*-PtCl<sub>2</sub> derivatives and exploring their effect on the cytotoxicity and their ability to bind to DNA and protein models. With this in mind, the ligands and *cis*-PtCl<sub>2</sub> complexes included in Chart 1 were prepared. The side chains and functional groups were chosen considering bibliographic background in which these substituents exert a favorable action on the effect of different drugs. Thus, the cyano-ethyl fragment, present in complex 1, had improved the cell permeability of drugs such as various Janus protein tyrosine kinases (JAK) inhibitors.<sup>10</sup> Alkyl-sulfonate groups, like that included in complex 2, should become deprotonated in biological media if the low pK<sub>a</sub> values for this functional group were considered, which could favor the solubility under physiological conditions. The biological activity of gold and silver N-heterocyclic carbenes bearing this group has been demonstrated both in bacteria<sup>11</sup> and in cancer cells.<sup>12</sup> The propylsulfonate chain forms part of merocyanine 540. This popular probe has been used as a model to study the permeation of cell membranes<sup>13</sup> and is an important active molecule, able to differentiate between the subtle differences in the plasma membranes of very similar cells such as leukemic and nonleukemic lymphocytes, depending on the composition of the culture medium.<sup>14</sup> The 5-diethylamino-2-pentylamino group, present in 4,4'-bis(*N*-(4-pentyl-diethylamine)-carbamoyl)-2,2'-bipyridine (bpyam) ligand (see Chart 1) and in complex 3, is a fragment widely used in drugs. Particularly relevant is its role in the formulation of the antimalarial drugs, chloroquine (CQ) and quinacrine (QC), where the stated aminated tail is responsible for the accumulation of the drug in

the digestive vacuole of the pathogen, the site of the drug action.<sup>15</sup> Both of them are strong DNA intercalating agents with cytotoxic activity<sup>16,17</sup> that displays a synergistic effect in tumor cells treated with cisplatin.<sup>18,19</sup> In the case of the 4,4'-bis( $\alpha$ -styrene)-2,2'-bipyridine (bpyst)<sup>20,21</sup> ligand (Chart 1) the conjugation of the phenyl (Ph) ring and the ethylene fragment with the bpy unit renders this ligand very attractive due to its rigidity that enforces a plane structure.<sup>22–24</sup> Concerning our aims, the plane architecture makes [PtCl<sub>2</sub>(bpyst)] (complex 4) an interesting compound to be analyzed as a potential drug targeting DNA.

In this work, the synthesis, characterization and biological properties of these four new organocisplatin analogues are reported. Their binding properties to relevant biomolecules such as DNA and serum proteins and their cellular uptake are explored to establish which factors are determinant to their cytotoxicity, which could, in turn, lead to future rational structural modifications with improved biological activity.

## RESULTS AND DISCUSSION

**Synthesis and Structural Characterization.** The complexes prepared in this work and their respective ligands are listed in Chart 1 along with their preparation methods. Even though the 1-(cyanoethyl)-2-(2-pyridyl)benzimidazole (pbiCN) ligand has been prepared previously,<sup>25</sup> the method described here is easier and provides a higher yield. This method consists of the deprotonation of the NH group of the commercially available 2-(2-pyridyl)benzimidazole and subsequent addition of acrylonitrile. The 1-(3-*n*-propylsulfonate)-2-(2-pyridyl)benzimidazole (pbiSO<sub>3</sub>) and bpyam ligands are reported in this work for the first time. The pbiSO<sub>3</sub> ligand was prepared according to the procedure described for other *n*-propylsulfonate compounds,<sup>26</sup> by the reaction of 2-(2-pyridyl)-



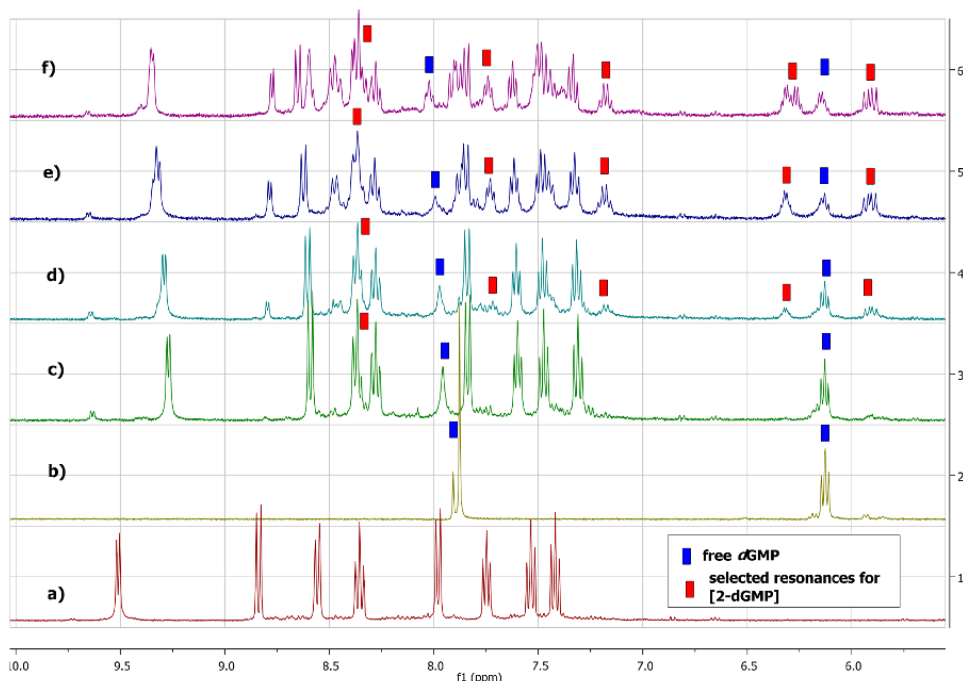


**Figure 1.** Aromatic area of  $^1\text{H}$  NMR spectra in  $\text{DMSO}-d_6$  of **2** + dGMP. (a) Complex **2** after 14 d in  $\text{DMSO}-d_6$  +  $\text{D}_2\text{O}$  before addition of dGMP, (b) free dGMP, (c)  $t = 0$ , (d)  $t = 30$  min, (e),  $t = 2$  h, (f)  $t = 3$  d.

benzimidazole in dimethylformamide (DMF) with 1,3-propane sultone in the presence of  $\text{K}_2\text{CO}_3$  as deprotonating salt. The synthesis of the ligand bpyam was achieved by a classical amide formation procedure,<sup>27</sup> starting by the formation of the acid chloride of the 4,4'-dicarboxy-2,2'-bipyridine and ulterior reaction with the commercially available 5-diethylamino-2-pentylamine. Ligand 4,4'-bis( $\alpha$ -styrene)-2,2'-bipyridine (bpyst) was prepared as previously reported.<sup>28</sup>

Complexes **1–3** were prepared by the reaction of the  $\text{K}_2[\text{PtCl}_4]$  salt with the respective ligands in water (**3**) or acetone/water (70:30 for **1** and 50:50 for **2**). While complex **3** was obtained at room temperature, the reaction to obtain **1** and **2** was performed at  $50^\circ\text{C}$ . Complex **4** was obtained from the platinum precursor  $[\text{PtCl}_2(\text{PhCN})_2]$  from a 1,2-dichloroethane solution heated at  $60^\circ\text{C}$ .

All the complexes were isolated in moderate-to-good yields (ranging from 54 to 74%) as yellow or orange-brown solids that were air and moisture stable. All of them are soluble in DMSO and relatively soluble in  $\text{DMSO}/\text{H}_2\text{O}$  mixtures, which facilitate the biological studies. The ligands and the complexes were characterized by  $^1\text{H}$ ,  $^{13}\text{C}\{^1\text{H}\}$  NMR, and IR spectroscopies. Fast atom bombardment (FAB) mass spectra for the complexes were also recorded. The peaks observed are in accordance with the proposed formulations (see [Experimental Section](#)). The anionic complex **2** was characterized by  $\text{FAB}^-$  spectrometry, showing the corresponding peak of the anion salt. In the IR spectra, the absorptions corresponding to the stretching vibrations of the  $\text{C}\equiv\text{N}$ ,<sup>29</sup>  $\text{SO}_3^-$ ,<sup>30</sup>  $(\text{CO})\text{NH}$ , and  $\text{C}=\text{C}$ <sup>31</sup> functional groups were observed. The assignment of the NMR resonances was facilitated in some cases by two-dimensional experiments such as gCOSY, NOESY, gHSQC, and gHMBC.

The NMR data with the corresponding assignments for the new ligands and for complexes **1–4** are shown in the [Experimental Section](#). As expected, the coordination of the ligands causes deshielding in the  $^1\text{H}$  NMR resonances of the protons of the coordinated rings. The effect is more marked ( $\sim 1$  ppm) in the protons adjacent to the N-donor atoms and in  $\text{H}^{6'}$  of **1** and **2** and  $\text{H}^3$  of **3**. It is interesting to note the splitting of some proton ( $-\text{C}(\text{O})\text{NH}$ ,  $\text{H}^3$ ) or carbon ( $\text{CO}$ ,  $\text{C}^2$ ,  $\text{C}^4$ ,  $\text{C}^3$ , and  $\text{C}^{4'}$ ) resonances of **3** as a consequence of the existence of two diastereomers, due to the presence of two chiral centers in the molecule. The weak base nature of the terminal  $-\text{NEt}_2$  groups in **3** ( $\text{p}K_a = 12.8$  in chloroquine) was evidenced in  $^1\text{H}$  NMR spectrum in deuterated dimethyl sulfoxide ( $\text{DMSO}-d_6$ ), since a very broad resonance around 9.5 ppm was present that disappeared as  $\text{D}_2\text{O}$  was added, as a consequence of deuterium exchange ([Figure S3](#)). The presence of this resonance was interpreted as evidence for protonation of this group by the residual water in the  $\text{DMSO}-d_6$ . As expected, the resonance assigned to the  $-\text{C}(\text{O})\text{NH}$  group also exchanged with  $\text{D}_2\text{O}$ , and the corresponding signal was not observed in the spectrum.

**Stability in DMSO and Aqueous Solution.** The biological activity of cisplatin and its derivatives is known to be related to substitution of the chloride ligands by other solvent molecules such as  $\text{H}_2\text{O}$ , which then leads to covalent binding with DNA.<sup>32</sup> As the **1–4** complexes are very soluble in DMSO, the concentrated stock solutions (20 mM) were prepared in this solvent, and diluted solutions in aqueous buffer were then prepared prior to performing the biological experiments. Because of this, the stability of the complexes both in DMSO and in aqueous buffered solution was studied by

means of NMR, spectrophotometric measurements, and/or theoretical calculations.

Complex **1** is not soluble in DMSO/D<sub>2</sub>O mixtures at the concentration required for the NMR experiments. Thus, the study of the substitution of the chloride ligand by DMSO and H<sub>2</sub>O was studied by means of UV–vis spectroscopy, which allows working at much lower concentrations. As shown in Figure S1, after complex **1** dissolved in DMSO (10 μM) a two-exponential process takes place, pointing up the substitution of the two chloride ligands by DMSO molecules with rate constants of  $k_1 = 0.0017 \text{ s}^{-1}$  (corresponding to formation of [PtCl(DMSO)(pbiCN)]Cl) starting from **1** and  $k_2 = 0.0002 \text{ s}^{-1}$  (corresponding to formation of [Pt(DMSO)<sub>2</sub>(pbiCN)]Cl<sub>2</sub>). When water is added, the [Pt(DMSO)<sub>2</sub>(pbiCN)]Cl<sub>2</sub> complex remains stable in solution, and no spectral changes with time are observed. Interestingly, <sup>1</sup>H NMR measurements show that, despite the similar structure of complexes **1** and **2**, the second is stable in solution and undergoes no substitution of the chloride ligands by DMSO-*d*<sub>6</sub> molecules in DMSO-*d*<sub>6</sub> solvent, neither by D<sub>2</sub>O (see Figure S2). The <sup>1</sup>H NMR spectrum of the complex **3** in DMSO-*d*<sub>6</sub> shows a displacement with time of several resonances in the aromatic region of the spectrum, which indicates exchange of chloride ligands by one or two solvent molecules (see Figure S3.A). When deuterated water is added, aquation takes place, since a new complex appeared in solution after 10 h (Figure S3.B). The signals of complex **4** with time become broad both in DMSO-*d*<sub>6</sub> (Figure S4.A) and when deuterated water is added (Figure S4.B), making it difficult to obtain a reliable conclusion. To clarify this issue, UV–vis spectroscopy and density functional theory (DFT) calculations were also performed. The absorption spectra of **4** were recorded at different times after dissolution of the complex in DMSO (Figure S5.A). A monoexponential equation was fitted to the absorbance–time data pairs (Figure S5.B), indicating that the substitution occurs at least by one chloride ligand, the rate constant being  $k = 0.0005 \text{ s}^{-1}$ . On the contrary, no kinetic effects are observed in solution when H<sub>2</sub>O is added, indicating that aquation is absent. Indeed, DFT calculations reveal that the substitution of not only one but also two chloride units by DMSO molecules in **4** is thermodynamically favored through SN<sub>2</sub> substitution (Figure S6.A), whereas the following substitution of DMSO by H<sub>2</sub>O is not favored, as the hydrolysis product presents higher energy than the reactants (Figure S6.B). In details, both show higher values of the enthalpy versus the Gibbs free energy values for the transition states involved. The three self-consistent field (SCF) energy, enthalpy, and Gibbs free energy values point to same thermodynamic trend of the reaction pathway. In conclusion, from both the UV–vis experiments and DFT calculations, aquation for compound **4** can be discarded.

**DNA Binding.** As mentioned above, the biological activity of cisplatin analogues is usually related to formulation of covalent bonds with DNA. In particular, cisplatin is an inert compound that is activated by a series of aquation reactions in which one or both chloride ligands are substituted by H<sub>2</sub>O molecules.<sup>32</sup> These mono- and biquated cisplatin forms are highly reactive and prone to interact with different substrates, including DNA.<sup>33</sup> Because of this, the ability of **1–4** to bind to dGMP was first tested by means of <sup>1</sup>H NMR and <sup>31</sup>P{<sup>1</sup>H} NMR studies. After addition of dGMP to a solution of complex **2**, <sup>1</sup>H NMR spectra showed the decrease of the intensity of the signals corresponding to free dGMP (see signal at 6.12 ppm) in the mixture, and new signals of the complex bound to the

dGMP molecule were observed (see Figure 1). An incipient singlet at 8.35 ppm could be assigned to H8 of dGMP due to the binding of the platinum center to the N7 of the dGMP. The <sup>31</sup>P{<sup>1</sup>H} spectra present a broad singlet centered at –1.5 ppm, and no more signals were observed in the spectra after time (see Figure S7). The nonobservation of resonances for lower fields conveys that O-coordination of dGMP is absent or is not significant. In the case of complex **3**, broadening of the <sup>1</sup>H NMR signals occurs after addition of dGMP, and an incipient singlet can be observed at 8.16 ppm after 2 d in solution, probably due to binding of the platinum center to N7 of dGMP (see Figure S8). This feature reveals that the covalent binding on **3** is rather slow compared to that of **2**.

Again, **1** could not be included in the NMR studies due to its insolubility in DMSO/D<sub>2</sub>O mixtures at the required concentrations. Complex **4** also precipitated after addition of dGMP due to the relatively high concentrations needed.

To overcome this problem, circular dichroism (CD) experiments were performed in the presence of calf-thymus DNA (ctDNA). When complexes **1–4** were added to a ctDNA solution, **1–3** induced slow changes with time in the CD spectra, which stopped after 72 h, whereas the changes brought about by complex **4** were immediate. This observation excludes fast modes of binding like intercalation, which causes remarkable changes in the DNA structure in the microsecond time scale,<sup>34</sup> for complexes **1–3**. On the contrary, covalent binding to DNA is usually slower. Actually, the first signals related to formation of a covalent bond between **3** and dGMP appeared after 2 d of incubation. Thus, ctDNA was incubated with complexes **1–4** for 72 h to properly compare their ability to bind to DNA, thus distorting its structure in a longer time scale under the same experimental conditions. The CD spectra shown in Figure 2.A reveal pronounced structural changes in the DNA molecule upon binding of complexes **1–3**. As to complex **4**, as stated before, the NMR experiments with dGMP could not be performed, and the absence of changes in the CD spectra with time does not suffice to rule out covalent binding with DNA, as platinum complexes that can form monodentate covalent bonds do not significantly affect the CD spectra of DNA.<sup>35</sup> For that reason, agarose gel electrophoresis with pUC18 plasmid incubated with different contents of complex **4** (and also with cisplatin as a positive control for covalent binding) was performed. As shown in Figure S9, complex **4** does not induce changes in the migration of the characteristic plasmid DNA bands, whereas cisplatin provokes remarkable differences. This outcome allows one to exclude the presence of covalent binding between **4** and DNA. However, other modes of noncovalent interaction should not be ruled out. To assess such hypothesis, additional CD experiments were performed, and the relative elongation ( $L/L_0$ ) was evaluated for different [complex]/[DNA] concentration ( $C_D/C_P$ ) ratios. The CD spectra display an isoelliptic point at 250 nm, a slight lateral shift of the band centered at 275 nm, and a new induced CD band at 310 nm (Figure S10.A). This behavior, along with the changes in relative viscosity (Figure S10.B), is consistent with formation of a noncovalent complex between **4** and DNA.

Differential scanning calorimetry (DSC) experiments were performed to provide additional information about the binding features of complexes **1–4** to ctDNA. Figure 2.B shows the thermograms obtained at 25 °C for ctDNA incubated alone or in the presence of **1–4** at 0.5  $C_D/C_P$  ratio for 72 h (higher concentration ratios could not be studied due to precipitation phenomena). In the case of complexes **1**, **2**, and **3**, for which

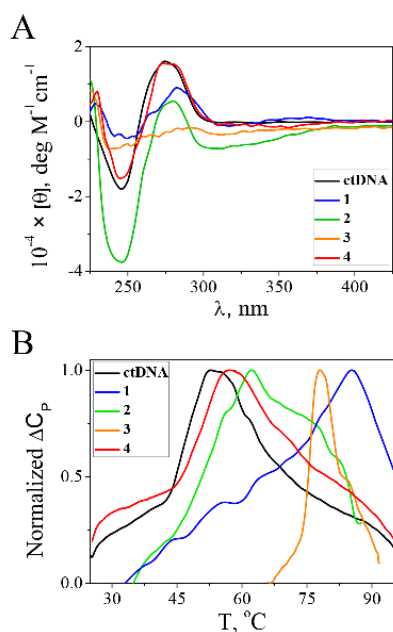


**Figure 2.** (A) CD spectra of ctDNA (P) incubated for 72 h with complexes 1–4 (D) at a concentration ratio  $C_D/C_P = 1$  ( $C_P = 8 \times 10^{-5}$  M) at  $T = 25$  °C,  $C_{DMSO} = 0.4\%$ . (B) DSC thermograms of ctDNA incubated for 72 h with complexes 1–4 at a concentration ratio  $C_D/C_P = 0.5$  ( $C_P = 4 \times 10^{-4}$  M) at a scan rate = 1 °C/min,  $C_{DMSO} = 1\%$ .  $I = 2.5$  mM sodium cacodylate (NaCac), pH = 7.4.

the covalent binding to dGMP has been confirmed previously by NMR experiments, the increases in  $T_m$  were 32.5, 9.7, and 25.3 °C, respectively. On the one hand, the largest  $\Delta T_m$  values are induced by 1 and 3 and could be related to formation of interstrand cross-linking, which stabilizes the double-stranded DNA structure.<sup>36</sup> On the other hand, complex 4 induces a slight increase in  $T_m$  of 4.7 °C, which could be due to the presence of a noncovalent interaction between complex 4 and DNA, concurrent with the CD and viscosity observations.

The results obtained for the substitution of the chloride groups and for the covalent binding to dGMP and DNA for the four platinum complexes as well are summarized in Table 1. Interestingly, unlike cisplatin, clear correlation between the chloro substitution by DMSO and H<sub>2</sub>O and the covalent binding with DNA for complexes 1–3 seems to be absent.

**Table 1. Summary of the Results of the Substitution of the Chloride Ligands by DMSO and H<sub>2</sub>O. Covalent Binding with DNA and Binding to BSA for the Complexes 1–4**

complex	DMSO substitution	H <sub>2</sub> O substitution	covalent binding to dGMP <sup>a</sup>	covalent binding to DNA	BSA binding <sup>b</sup>
1	✓	×	n.o.	✓	×
2	×	×	✓	✓	✓
3	✓	✓	✓	✓	✓
4	✓	×	n.o.	×	×

<sup>a</sup>1 and 4 could not be studied due to precipitation under the <sup>1</sup>H NMR experimental conditions. n.o., not observed. <sup>b</sup>For complex 4, the interaction is only observed at high concentrations.

Only complex 3 can form the aqua complex, and, hence, it can bind to DNA by a similar mechanism as to cisplatin.

**Cytotoxicity Studies.** Once the binding ability of the four platinum complexes with DNA was assessed, their cytotoxic activity against human cervical carcinoma (HeLa) and human lung carcinoma (A549) cell lines was also evaluated by the 3-(4,5-dimethylthiazol-2-yl)-2,5-diphenyltetrazolium bromide (MTT) assay after 72 h of incubation time. For comparison purposes, the cytotoxicity of cisplatin was also tested. The half-maximal inhibitory concentration (IC<sub>50</sub>) values are summarized in Table 2. Complexes 2 and 3 are essentially nontoxic, whereas

**Table 2. Cytotoxic Activity of Complexes 1–4 and Cisplatin Expressed as IC<sub>50</sub> Values (μM)**

	IC <sub>50</sub> μM		
	HeLa <sup>a</sup>	A549 <sup>a</sup>	A549 <sup>b</sup>
1	15.4 ± 0.9	>100	39.7 ± 0.7
2	>100	>100	65 ± 3
3	>100	>100	>100
4	33 ± 2	>100	41.9 ± 0.9
cisplatin	14.0 ± 0.9 <sup>c</sup>	17 ± 1	14 ± 1

<sup>a</sup>Serum-supplemented media (10% FBS). <sup>b</sup>Serum-deprived media (1% FBS). <sup>c</sup>Taken from ref 40.

1 is cytotoxic only toward HeLa cells. This is noteworthy, because all three complexes have been shown to bind covalently to DNA. As to complex 4, it can interact noncovalently with DNA and presents intermediate cytotoxicity toward HeLa cells. Note that 3 displays no cytotoxicity, even though it can form the aquacomplex and interact by covalent binding with DNA, a behavior similar to that of cisplatin; that is, the type of the DNA interaction is not the determining factor in the cytotoxicity of these *cis*-PtCl<sub>2</sub> derivatives. This set of results raises the question of which factors, such as cellular uptake or protein binding, could play a key role in their cytotoxicity.<sup>4</sup>

Many new metal complexes with novel modes of action have been reported, and their anticancer activity was linked to selective protein interaction that may lead to improved accumulation in the tumor, higher selectivity, and/or enhanced antiproliferative efficacy.<sup>37</sup> However, it was reported previously that the binding of metal complexes to certain proteins present in the cell culture media can affect negatively their uptake due to protein sequestration of the drug, thus affecting their biological activity.<sup>3,38</sup> To shed some light into this issue, the cytotoxic activity of the complexes was tested against A549 cells in a comparative manner, using not only standard serum supplemented (10% fetal bovine serum (FBS)) but also a serum-deprived (1% FBS) cell culture media. FBS contains a large amount of proteins that can interact strongly with certain drugs, which can in turn decrease drastically their bioavailability. Indeed, the cytotoxicity of complexes 1, 2, and 4 increased notably in serum-deprived media (see Table 2), in which the protein concentration is much lower. Cisplatin is known to interact very weakly with human serum albumin (HSA;  $K = 8.52 \times 10^2$  M<sup>-1</sup>),<sup>39</sup> which explains why its cytotoxicity is nearly the same in the presence of 10% or 1% FBS. Taking into account this set of results, it seems clear that the interaction with serum albumin present in the culture medium plays a critical role in the antiproliferative activity of cisplatin derivatives. This behavior has been observed recently in organic complexes<sup>3</sup> and gold derivatives.<sup>33</sup>



**Protein Binding.** Serum albumin plays a key role in drug delivery due to its binding properties and abundance in blood plasma. Bovine serum albumin (BSA) is a suitable model for protein binding because of its resemblance to HSA.<sup>41</sup> Therefore, in view of the effect of the FBS concentration in the cytotoxicity of platinum complexes, native acrylamide electrophoresis experiments of BSA were performed to further examine whether the protein binding could be determinant as to their cytotoxic activity. BSA was incubated for 72 h with complexes 1–4 in the dark at 25 °C for  $C_D/C_P$  concentration ratios of 10 and 20, and then native acrylamide electrophoresis was performed (Figure 3). Lanes 1 and 2 correspond to BSA

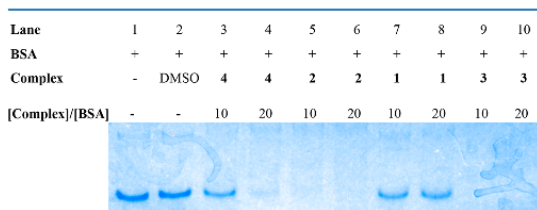


**Figure 3.** Native acrylamide electrophoresis of BSA incubated with complexes 1–4 for 72 h for [complex]/[BSA] concentrations ratios of 10 and 20.  $C_{BSA} = 1.5 \mu\text{M}$ ,  $C_{DMSO} = 0.3\%$ .

alone and in the presence of the maximum DMSO concentration used in the experiment (0.3%). Noteworthy, complexes 2 and 3, which can interact with DNA through covalent bonding but display poor cytotoxicity, affect in a deep manner the protein conformation (lanes 5–6 and 9–10). Complex 4 also interacts with BSA, but higher concentrations are needed to affect the BSA conformation, as there is still no noticeable effect on the protein conformation at  $C_D/C_P = 10$  (lane 3). On the contrary, complex 1, the most cytotoxic, does not affect the BSA conformation even at high  $C_D/C_P$  ratios (lanes 7–8).

As shown in Figure 4, circular dichroism experiments confirmed the native electrophoresis results. The incubation

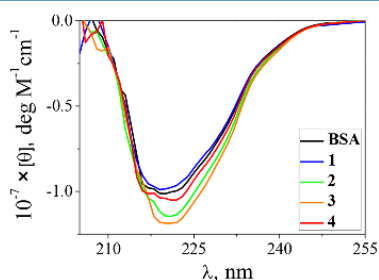


**Figure 4.** CD spectra of BSA in the absence and in the presence of the four platinum complexes 1–4 at a [complex]/[BSA] concentration ratio of 5.  $C_{BSA} = 0.5 \mu\text{M}$ ,  $C_{DMSO} = 0.002\%$ ,  $I = 2.5 \text{ mM}$  sodium cacodylate (NaCac),  $\text{pH} = 7.4$ , and  $T = 25 \text{ }^\circ\text{C}$ .

of BSA with complexes 2 and 3 induced a marked change in its characteristic  $\lambda = 220 \text{ nm}$  negative band. Complex 4 also modified slightly this band, whereas complex 1 had almost no effect on the shape and intensity of the protein band.

As, on one hand 1 and 2 and on the other hand 3 and 4 differ only in their tails, we can conclude that the tail plays a determining role in their interaction with the protein. Very

recently it has been reported that chloroquine (the lateral chain located on the backbone of complex 3) can bind to HSA.<sup>42</sup> At  $\text{pH} = 7$ , chloroquine (CQ) is doubly protonated in both the N pyridine and ethylamine sites, as the resulting  $\text{p}K_a$  values are 8.4 and 10.8, respectively.<sup>43</sup> From comparison of CQ with complex 3, we can state that in aqueous solution at  $\text{pH} = 7$  the two ethylenamine groups are protonated (see  $^1\text{H NMR}$  in Figure S3A). In this sense, MS-FABS<sup>+</sup> shows that, in 15% DMSO, complex 3 is in the  $[\text{M}^+2\text{H}]^+$  form; therefore, in 0.3% DMSO (the solvent utilized to study the interaction with BSA) the two amines of the lateral chains will be fully protonated. Thus, the positive charge favors the electrostatic interaction with the negative net charge of the protein. Likewise, it was found that negatively charged compounds bind to HSA more strongly than expected from the lipophilicity of the ionized species at  $\text{pH} 7.4$ ,<sup>44</sup> which is the case of complex 2. Moreover, it has been observed that the binding of Merocyanine 540 to erythroid cells is hindered by the presence of serum proteins in the media,<sup>14</sup> probably due to the presence of a propylsulfonate chain in its structure. Thus, this moiety is determining for the interaction of complex 2 with BSA. In summary, the sets of observations point to a key role of protein binding in the cytotoxic properties of the platinum complexes, insofar as it could prevent the complexes from entering the cell. The binding to BSA clearly depends on the structure and charge of side lateral functionalized chains, the neutral chain remaining essentially non-interacting. For this reason, the cellular uptake of each complex was studied by inductively coupled plasma mass spectrometry (ICP-MS).

**Cellular Uptake.** The ability of the platinum complexes 1–4 to enter the cell was also studied to compare their uptake rates with their protein binding properties. Cells were incubated for 24 h with  $10 \mu\text{M}$  of each complex, and then the amount of Pt in one million cells was measured by ICP-MS. In excellent agreement with the native protein electrophoresis and CD results, complexes 1 and 4, which display weak affinity to BSA, are capable of entering the cell, showing high accumulation rates (Figure 5). On the contrary, complexes 2

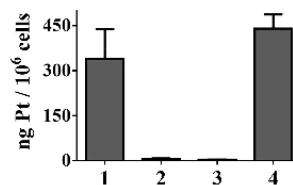


**Figure 5.** Metal accumulation in A549 cells after 24 h of exposure to  $10 \mu\text{M}$  of complexes 1–4 expressed as microgram of Pt in one million cells.

and 3 were unable to enter the cell, probably due to protein sequestration in the media, which also explains their poor cytotoxicity in all cell lines.

## CONCLUSIONS

Four new platinum(II) analogue complexes (1–4) to cisplatin have been synthesized and characterized, and their biological properties have been studied. Investigations on new antitumor Pt complexes have been focused since several decades ago on finding similar behaviors to that of cisplatin. Interestingly, we have verified that aquation is not a necessary step to bind covalently to DNA. Moreover, although albumin proteins have

been largely regarded as potential anticancer targets, we have shown that the interaction with BSA correlates with poor cell uptake of the platinum complexes, as occurs with complexes 2 and 3, which can interact covalently with DNA but are prevented from reaching their target because of this strong interaction. By contrast, complexes 1 and 4, which interact with DNA by covalent and noncovalent binding, respectively, are more cytotoxic, because they display weak effect on BSA, and, consequently, accumulation of the metal complex in tumor cells increases, improving their antiproliferative efficacy. In view that 1 and 2, on one hand, and 3 and 4, on the other hand, differ only by the lateral chain located on the same structural backbone, we can conclude that the nature of these chains is key to their remarkably different behavior. In conclusion, although the anticancer activity of *cis*-PtCl<sub>2</sub> derivatives has been linked to DNA interaction through covalent binding, we have demonstrated that their antiproliferative capacity can be diminished due to sequestration of the complexes by serum albumin, which could be useful in the future design of more potent platinum derivatives.

## EXPERIMENTAL SECTION

**Physical Methods.** All synthetic manipulations were performed under an inert, oxygen-free, dry nitrogen atmosphere using standard Schlenk techniques. Solvents were distilled from the appropriate drying agents and degassed before use. Elemental analyses were performed with a Thermo Quest FlashEA 1112 microanalyser. The analytical data for the new complexes were obtained from crystalline samples where possible. IR spectra were recorded on a Shimadzu IR Prestige-21 IR spectrophotometer equipped with a Pike Technologies ATR. Only relevant bands are collected. FAB MS (position of the peaks in Da) were recorded with an Autospec spectrometer or a Thermo MAT95XP mass spectrometer with a magnetic sector. NMR spectra were recorded at 298 K on a Varian Unity Inova 400 or on a Varian Inova 500 spectrometer. <sup>1</sup>H and <sup>13</sup>C{<sup>1</sup>H} NMR chemical shifts were internally referenced to tetramethylsilane (TMS) via the residual <sup>1</sup>H and <sup>13</sup>C signals of CDCl<sub>3</sub> ( $\delta = 7.26$  ppm and  $\delta = 77.16$  ppm), DMSO-*d*<sub>6</sub> ( $\delta = 2.50$  ppm and  $\delta = 39.52$  ppm), and D<sub>2</sub>O ( $\delta = 4.79$  ppm) according to the values reported by Fulmer et al.<sup>45</sup> Chemical shift values are reported in parts per million, and coupling constants (*J*) are in hertz. The splitting of proton resonances is defined as *s* = singlet, *d* = doublet, *t* = triplet, *q* = quadruplet, *m* = multiplet, *bs* = broad singlet. 2D NMR spectra were recorded using standard pulse–pulse sequences: COReLation SpectroscopY (COSY), Nuclear Overhauser Enhancement SpectroscopY (NOESY), Heteronuclear Multiple Quantum Coherence (HMQC), Heteronuclear Multiple Bond Correlation (HMBC). The probe temperature ( $\pm 1$  K) was controlled by a standard unit calibrated with a methanol reference. All NMR data processing was performed using MestReNova version 6.1.1.

**Materials.** Unless otherwise stated, reagents and solvents used were commercially available reagent quality. Conventional solvents and K<sub>2</sub>CO<sub>3</sub> were purchased from Scharlab. Deuterated solvents were purchased from Eurisotop. K<sub>2</sub>[PtCl<sub>4</sub>] was purchased from Johnson Matthey PLC. [PtCl<sub>2</sub>(PhCN)<sub>2</sub>]<sup>16</sup> and the ligands pbiCN<sup>25</sup> and bpyst<sup>28</sup> were prepared according to the literature. 4,4'-dicarboxy-2,2'-bipyridine, 4,4'-dimethyl-2,2'-bipyridine, 2-(2-pyridyl)benzimidazole, acrylonitrile, 1,3-propanesultone, SOCl<sub>2</sub>, 2-amine-5-diethylaminopentane, and trimethylamine were purchased from Across Organics.

The synthesized Pt(II) complexes can be referred to as dyes/drugs, and their molar concentration is expressed as C<sub>D</sub>. Calf thymus DNA (lyophilized sodium salt, highly polymerized) from Sigma-Aldrich was dissolved in water and sonicated, producing short polynucleotide fragments (ca. 1000 base pairs). The molar DNA concentration is expressed in base pairs,  $\epsilon$  (260 nm) = 13 200 M<sup>-1</sup> cm<sup>-1</sup>.<sup>47</sup> BSA was supplied by Sigma-Aldrich as crystallized and lyophilized powder ( $\geq 98\%$ , agarose gel electrophoresis and  $\leq 0.005\%$  fatty acids); its concentration was spectrophotometrically determined at 278 nm using

absorptivity ( $\epsilon$ ) of 45 000 M<sup>-1</sup> cm<sup>-1</sup>.<sup>48</sup> Plasmid pUC18 (2686 bp) was extracted from *Escherichia coli* DH5 $\alpha$  and purified by a HP Plasmid Midi kit (Omega Biotek, VWR). The concentrations of the polymers (ctDNA, BSA, and pUC18) are denoted as C<sub>p</sub>.

**Synthesis of Ligands and Complexes.** 1-(Cyanoeethyl)-2-(2-pyridyl)benzimidazole (pbiCN). K<sub>2</sub>CO<sub>3</sub> (318.6 mg, 2.3 mmol) was added to a solution of 2-(2-pyridyl)benzimidazole (300 mg, 1.5 mmol) in DMF (3 mL). The mixture was stirred at room temperature for 30 min. Then, 101  $\mu$ L of acrylonitrile (1.5 mmol) was added, and the reaction was stirred for 4 h. The solvent was removed by vacuum evaporation resulting in a beige solid that was extracted with 10  $\times$  3 mL of CHCl<sub>3</sub>. The organic extracts were combined, obtaining 289.2 mg of the pure product, beige colored, after drying under vacuum. Yield, 76%.

3-(2-(2-pyridyl)-benzimidazol-1-yl)propane-1-sulfonate (pbiSO<sub>3</sub>). A solution containing 318.6 mg of K<sub>2</sub>CO<sub>3</sub> (2.3 mmol) was added over another with 2-(2-pyridyl)benzimidazole (300 mg, 1.5 mmol) in DMF (3 mL). The mixture was stirred at room temperature for 30 min. Then, 135  $\mu$ L of 1,3-propanesultone (1.5 mmol) was added, and the mixture was stirred for 24 h. The mixture was filtered, and the solvent was removed by evaporation under vacuum. A yellow solid was obtained. 265.3 mg, yield: 55%. <sup>1</sup>H NMR (DMSO-*d*<sub>6</sub>, 298 K): 8.79 (d, *J*<sub>HH</sub> = 4.7 Hz, 1H, H<sup>a</sup>); 8.34 (d, *J*<sub>HH</sub> = 8 Hz, 1H, H<sup>b</sup>); 8.05 (t, *J*<sub>HH</sub> = 8 Hz, 1H, H<sup>c</sup>); 7.82 (d, *J*<sub>HH</sub> = 7.2 Hz, 1H, H<sup>d</sup>); 7.76 (d, *J*<sub>HH</sub> = 7.7 Hz, 1H, H<sup>e</sup>); 7.57 (m, 1H, H<sup>f</sup>); 7.40 (t, *J*<sub>HH</sub> = 7.7 Hz, 1H, H<sup>g</sup>); 7.35 (t, *J*<sub>HH</sub> = 7.7 Hz, 1H, H<sup>h</sup>); 4.97 (t, *J*<sub>HH</sub> = 7.2 Hz, 2H, H<sup>i</sup>); 2.43 (t, *J*<sub>HH</sub> = 7.8 Hz, 2H, H<sup>j</sup>); 2.13 (m, 2H, H<sup>k</sup>) ppm. <sup>1</sup>H NMR (D<sub>2</sub>O, 298 K): 8.61 (bs, 1H); 7.95 (t, *J*<sub>HH</sub> = 7.8 Hz, 1H); 7.84 (d, *J*<sub>HH</sub> = 7.4 Hz, 1H); 7.66 (d, *J*<sub>HH</sub> = 7.8 Hz, 1H); 7.60 (d, *J*<sub>HH</sub> = 7.8 Hz, 1H); 7.49 (t, *J*<sub>HH</sub> = 6 Hz, 1H); 7.35 (t, *J*<sub>HH</sub> = 7.4 Hz, 1H); 7.29 (t, *J*<sub>HH</sub> = 7.8 Hz, 1H); 4.57 (t, *J*<sub>HH</sub> = 7.2 Hz, 2H); 2.58 (m, *J*<sub>HH</sub> = 7.2 Hz, 2H); 2.02 (q, *J*<sub>HH</sub> = 7.2 Hz, 2H) ppm. <sup>13</sup>C{<sup>1</sup>H} NMR (DMSO-*d*<sub>6</sub>, 298 K): 149.2(C<sup>6</sup>); 137.6(C<sup>4</sup>); 124.8(C<sup>5</sup>); 125.7(C<sup>3</sup>); 123.8(C<sup>5'</sup>); 123.2(C<sup>4'</sup>); 118.5(C<sup>6'</sup>); 111.7(C<sup>3'</sup>); 48.4(C<sup>a</sup>); 44.4(C<sup>b</sup>); 26.3(C<sup>b</sup>) ppm. Elemental analysis (%): Calculated (C<sub>15</sub>H<sub>14</sub>Cl<sub>2</sub>KN<sub>3</sub>O<sub>3</sub>S·H<sub>2</sub>O): C, 48.32; H, 4.32; N, 11.25; S, 8.59. Found: C, 48.43; H, 4.38; N, 10.86; S, 8.69%. IR (ATR):  $\nu$ (=O) 1184, 1041 cm<sup>-1</sup>.

4,4'-bis(N-(4-pentyl)diethylamine)carbamoyl)-2,2'-bipyridine (bpyam). Ligand bpyam was synthesized in several steps in nitrogen atmosphere. SOCl<sub>2</sub> (3 mL) was added to 200.0 mg (0.8 mmol) of the starting dicarboxylic bipyridine under inert atmosphere, and the mixture was refluxed overnight. The initial white suspension changed to bright yellow solution during the reaction. Solvent was removed under vacuum, and the resulting solid was used without further purification for the following step. 2-Amine-5-diethylaminopentane (320.0  $\mu$ L, 1.6 mmol) and 230.0  $\mu$ L (1.6 mmol) of trimethylamine were dissolved in 10 mL of dry dichloromethane, and on this solution another of the acylchloride derivative in 10 mL of dry CH<sub>2</sub>Cl<sub>2</sub> was added drop by drop from a pressure equalizing dropping funnel. After it was stirred overnight at room temperature, the solvent was evaporated, obtaining a pink solid, which was washed with diethyl ether four times (4  $\times$  10 mL). In this operation, the remaining chloride acid is removed from the solid mixture. This mixture contains a big amount of NHEt<sub>3</sub>Cl, which can be removed using an aluminum column of 10 cm long and 1 cm<sup>2</sup> section. The mixture was eluted in 2 mL of MeOH and transferred to the column that was previously wetted with CH<sub>2</sub>Cl<sub>2</sub>. The reaction product elutes with MeOH/CH<sub>2</sub>Cl<sub>2</sub> (4/30 mL). The NHEt<sub>3</sub>Cl salt is retained in the column. A pinky-white colored solid was obtained after complete evaporation of the solvents. Yield: 93% (401.5 mg). Elemental analysis (%): Calculated (C<sub>30</sub>H<sub>48</sub>N<sub>6</sub>O<sub>2</sub>): C, 68.67; H, 9.22; N, 16.02. Found: C, 68.36; H, 9.82; N, 15.76. <sup>1</sup>H NMR (DMSO-*d*<sub>6</sub>, 298 K),  $\delta$ : 8.87 (d, 2H, *J* = 5.4 Hz, H<sup>a</sup>), 8.80 (bd, 2H, *J* = 7.3 Hz, NH), 8.79 (s, 2H, H<sup>b</sup>), 7.89 (dd, 2H, *J* = 5.2, *J* = 1.7 Hz, H<sup>c</sup>), 4.10 (m, 2H, H<sup>d</sup>), 2.42 (q, 8H, *J* = 7.4 Hz, H<sup>e</sup>), 2.35 (t, 4H, *J* = 7.3 Hz, H<sup>f</sup>), 1.50–1.56 (m, 4H, H<sup>g</sup>), 1.40–1.44 (m, 4H, H<sup>h</sup>), 1.21 (d, 6H, *J* = 6.9 Hz, H<sup>i</sup>), 1.18 (t, 12H, *J* = 8.8 Hz, H<sup>j</sup>) ppm. <sup>13</sup>C{<sup>1</sup>H} NMR (DMSO-*d*<sub>6</sub>, 298 K): 164.21 (CO), 155.49 (C<sup>2</sup>), 149.97 (C<sup>6</sup>), 143.14 (C<sup>3</sup>), 122.11 (C<sup>5</sup>), 118.31 (C<sup>3'</sup>), 50.46 (C<sup>1'</sup>), 46.64 (C<sup>6'</sup>), 44.70 (C<sup>4'</sup>), 32.83 (C<sup>3'</sup>), 20.62 (C<sup>2'</sup>), 20.25 (C<sup>5'</sup>), 8.53



(C<sup>7</sup>) ppm. FTIR (ATR): 3429  $\nu$ (NH), 1635  $\nu$ (C=O)  $\text{cm}^{-1}$ . MS-FAB<sup>+</sup>: 526 (100%, [M+2H]<sup>+</sup>)  $m/z$ .

[PtCl<sub>2</sub>(pbiCN)], **1**. A solution containing 50 mg of pbiCN (0.2 mmol) in 9 mL of acetone was added to another with 83.6 mg of K<sub>2</sub>[PtCl<sub>4</sub>] (0.2 mmol) in 4 mL of water. The mixture was stirred at 50 °C for 4 d. The yellow precipitate was filtered and washed with water, ethanol, and diethyl ether (3 mL each one). A yellow solid was obtained. 55.9 mg, yield: 54%. Elemental analysis (%): Calculated (C<sub>15</sub>H<sub>12</sub>Cl<sub>2</sub>N<sub>4</sub>Pt): C, 35.03; H, 2.35; N, 10.89. Found: C, 35.51; H, 1.91; N, 10.11. <sup>1</sup>H NMR (DMSO-*d*<sub>6</sub>, 298 K): 9.66 (d, *J*<sub>HH</sub> = 6.5 Hz, 1H, H<sup>6</sup>); 9.01 (d, *J*<sub>HH</sub> = 8.3 Hz, 1H, H<sup>6'</sup>); 8.42 (m, 2H, H<sup>3</sup> and H<sup>4</sup>); 8.09 (d, *J*<sub>HH</sub> = 8.3 Hz, 1H, H<sup>3'</sup>); 7.84 (t, *J*<sub>HH</sub> = 6.5 Hz, 1H, H<sup>5</sup>); 7.60 (t, *J*<sub>HH</sub> = 7.8 Hz, 1H, H<sup>4'</sup>); 7.50 (t, *J*<sub>HH</sub> = 7.8 Hz, 1H, H<sup>5'</sup>); 5.20 (t, *J*<sub>HH</sub> = 6.4 Hz, 2H, H<sup>2</sup>, H<sup>2'</sup>); 3.24 (t, *J*<sub>HH</sub> = 6.4 Hz, 2H, H<sup>2</sup>, H<sup>2'</sup>) ppm. The corresponding <sup>13</sup>C{<sup>1</sup>H} NMR was not registered, because the complex evolves in DMSO solution. MS-FAB<sup>+</sup>: 557 (M-Cl+DMSO)  $m/z$ . IR (ATR):  $\nu$ (CN) 2249  $\text{cm}^{-1}$ .

[PtCl<sub>2</sub>(pbiSO<sub>3</sub>)], **2**. Over a solution containing 76.21 mg of pbiSO<sub>3</sub> (0.24 mmol) in 5 mL of acetone, another of K<sub>2</sub>[PtCl<sub>4</sub>] (100 mg, 0.24 mmol) in 5 mL of water was added. The mixture was stirred at 50 °C for 24 h. The solvent was removed by vacuum evaporation, leaving a brown solid. 111 mg, yield: 74%. Elemental analysis (%): Calculated (C<sub>15</sub>H<sub>14</sub>Cl<sub>2</sub>KN<sub>3</sub>O<sub>3</sub>PtS): C, 28.29; H, 2.27; N, 6.76; S, 5.26. Found: C, 28.21; H, 2.16; N, 6.82; S, 5.23. <sup>1</sup>H NMR (DMSO-*d*<sub>6</sub>, 298 K): 9.63 (d, *J* = 6.1 Hz, 1H, H<sup>6</sup>); 8.95 (d, *J* = 8.2 Hz, 1H, H<sup>6'</sup>); 8.70 (d, *J* = 7.9 Hz, 1H, H<sup>3</sup>); 8.32 (t, *J* = 7.9 Hz, 1H, H<sup>4</sup>); 8.03 (d, *J* = 8.2 Hz, 1H, H<sup>3'</sup>); 7.79 (t, *J* = 6.1 Hz, 1H, H<sup>5</sup>); 7.53 (t, *J* = 7.6 Hz, 1H, H<sup>4'</sup>); 7.43 (t, *J* = 7.6 Hz, 1H, H<sup>5'</sup>); 4.97 (t, *J* = 7.9 Hz, 2H, H<sup>2</sup>, H<sup>2'</sup>); 2.67 (t, *J* = 6.2 Hz, 2H, H<sup>2</sup>, H<sup>2'</sup>); 2.13 (m, 2H, H<sup>2</sup>, H<sup>2'</sup>) ppm. <sup>13</sup>C{<sup>1</sup>H} NMR (DMSO-*d*<sub>6</sub>, 298 K): 150.54 (C<sup>6</sup>); 141.18 (C<sup>3</sup>); 128.07 (C<sup>5</sup>); 126.16 (C<sup>4'</sup>); 125.98 (C<sup>3'</sup>); 125.74 (C<sup>5'</sup>); 119.07 (C<sup>6'</sup>); 112.81 (C<sup>3'</sup>); 47.99 (C<sup>2'</sup>); 44.80 (C<sup>2</sup>); 25.87 (C<sup>6</sup>) ppm. MS-FAB<sup>-</sup>: 582 [M-K]<sup>-</sup>  $m/z$ . IR (ATR):  $\nu$ (S=O) 1184, 1043  $\text{cm}^{-1}$ .

[PtCl<sub>2</sub>(bpyam)], **3**. The product was obtained by diffusion of the reactants in phases. In a crystallization tube under inert atmosphere, three phases were added: the lower phase consisted of a K<sub>2</sub>[PtCl<sub>4</sub>] solution (15.8 mg, 0.04 mmol) in 2 mL of water; middle phase of 1 mL of water; the upper phase consisted of the ligand solution of (20.0 mg, 0.04 mmol) in 1 mL of water. Phases were allowed to fully diffuse. The precipitate was filtered and washed with water, affording the product as a yellow solid. Yield: 56% (17.7 mg). The product can be obtained in a bigger amount by direct reaction in Schlenk, by stirring overnight. Elemental analysis (%): Calculated (C<sub>30</sub>H<sub>48</sub>Cl<sub>2</sub>N<sub>6</sub>O<sub>2</sub>Pt): C: 45.57, H: 6.12, N: 10.63. Found: C: 45.31, H: 6.25, N: 10.42. <sup>1</sup>H NMR (DMSO-*d*<sub>6</sub>, 298 K),  $\delta$ : 9.63 (d, 2H, *J* = 5.4, H<sup>6</sup>), 9.60 (bs, 2H, H<sup>3</sup><sub>A or B</sub>), 9.46 (bs, 2H, H<sup>3</sup><sub>A or B</sub>), 9.45 (bs, 2H, -NHEt<sub>2</sub>), 9.16 (d, 2H, *J* = 5.3, NH<sub>A or B</sub>), 9.13 (d, 2H, *J* = 5.3, NH<sub>A or B</sub>), 8.23 (m, 2H, H<sup>2</sup>), 4.14 (m, 2H, H<sup>4'</sup>), 2.92 (m, 12H, H<sup>1'</sup> + H<sup>6'</sup>), 1.55–1.80 (m, 8H, H<sup>2'</sup> + H<sup>3'</sup>), 1.27 (d, 6H, *J* = 6.3 Hz, H<sup>5'</sup>), 1.13 (bs, 12H, H<sup>7'</sup>) ppm. <sup>13</sup>C{<sup>1</sup>H} NMR (DMSO-*d*<sub>6</sub>, 298 K): 161.60 (CO<sub>A or B</sub>), 161.52 (CO<sub>A or B</sub>), 157.27 (C<sup>2</sup><sub>A or B</sub>), 157.23 (C<sup>2</sup><sub>A or B</sub>), 148.96 (C<sup>6</sup>), 143.77 (C<sup>4</sup><sub>A or B</sub>), 143.65 (C<sup>4</sup><sub>A or B</sub>), 126.12 (C<sup>5</sup>), 121.74 (C<sup>3</sup><sub>A or B</sub>), 121.68 (C<sup>3</sup><sub>A or B</sub>), 50.71 (C<sup>1'</sup>), 46.10 (C<sup>6'</sup>), 45.48 (C<sup>4'</sup><sub>A or B</sub>), 45.42 (C<sup>4'</sup><sub>A or B</sub>), 32.73 (C<sup>3'</sup>), 20.59 (C<sup>5'</sup>), 20.56 (C<sup>2'</sup>), 9.14 (C<sup>7'</sup>) ppm. A and B stands for the two diastereomers (if not indicated, the resonance signal for both diastereomers is the same). Fourier transform infrared attenuated total reflectance (FTIR ATR): 3432  $\nu$ (NH), 1637  $\nu$ (C=O)  $\text{cm}^{-1}$ . MS-FAB<sup>+</sup>: 792 (15%, [M+2H]<sup>+</sup>); 756 (7%, [M-Cl + H]<sup>+</sup>); 526 (100%, [L+2H]<sup>+</sup>)  $m/z$ .

[PtCl<sub>2</sub>(bpyst)], **4**. Ligand of this complex ((4,4'-bis( $\alpha$ -styrene)-2,2'-bipyridine (bpyst)) was prepared as previously reported.<sup>25</sup> A yellow colored solution of [PtCl<sub>2</sub>(NCPH)<sub>2</sub>] was prepared in 40 mL of dichloroethane (106.7 mg, 0.226 mmol). Over this solution another solution of the ligand bpyst was added (82 mg, 0.226 mmol). The suspension was maintained for 2 d at 60 °C. The formation of a yellow precipitate was observed, and the solution turned to yellow-brown. The precipitate was filtered, and the solution was evaporated to 3 mL. Diethyl ether was added to complete precipitation of a solid. The solution was sonicated for 5 min and filtered out in a porous glass filter. The obtained brown solid was washed with diethyl ether (3  $\times$  3

mL) and dried under vacuum. Yield: 65% (92.3 mg). Elemental analysis (%): Calculated (C<sub>26</sub>H<sub>22</sub>Cl<sub>2</sub>N<sub>2</sub>Pt): C: 49.69, H: 3.53, N: 4.46. Found: C: 49.51, H: 3.64, N: 4.37. <sup>1</sup>H NMR (DMSO-*d*<sub>6</sub>, 298 K),  $\delta$ : 9.40 (d, 2H, *J*<sub>HH</sub> = 6.2 Hz, H<sup>6</sup>); 8.85 (s, 2H, H<sup>3</sup>); 7.99 (d, 2H, *J*<sub>HH</sub> = 16.5 Hz, H<sup>olef</sup>), 7.94 (d, 2H, *J*<sub>HH</sub> = 6.2 Hz, H<sup>5</sup>); 7.77 (d, 4H, *J*<sub>HH</sub> = 7.8 Hz, H<sup>2</sup>); 7.53–7.45 (m, 8H, H<sup>m</sup>, H<sup>p</sup>, and H<sup>olef</sup>) ppm. The corresponding <sup>13</sup>C{<sup>1</sup>H} NMR resonances are not indicated, because the signals are too broad for a proper assignment. FTIR (ATR): 1612 ( $\nu$ (C=C))  $\text{cm}^{-1}$ . MS-FAB<sup>+</sup>: 591 (4%, M-Cl-2H)  $m/z$ .

**General Procedure of Stability and Binding to dGMP by NMR Studies.** Stability in DMSO-*d*<sub>6</sub>. Complexes 1–4 (5–8 mg) were dissolved in 0.5 mL of DMSO-*d*<sub>6</sub>, and <sup>1</sup>H NMR spectra were recorded during 7 d in a 400 MHz spectrometer.

**Aquation Studies.** Over the previous solution, 50  $\mu$ L of D<sub>2</sub>O was added, and <sup>1</sup>H NMR spectra were recorded during 7 d in a 400 MHz spectrometer.

**Binding Studies to dGMP.** Over the solution coming from the aquation studies, 5 mg of dGMP dissolved in 20  $\mu$ L of D<sub>2</sub>O was added, and <sup>1</sup>H NMR and <sup>31</sup>P{<sup>1</sup>H} spectra were recorded during 5 d in a 400 MHz spectrometer.

**UV-Vis Spectroscopy.** Absorbance measurements were performed to study the substitution of the chloro ligands of the metal complexes for DMSO and H<sub>2</sub>O molecules when NMR experiments were not suitable because of precipitation phenomena. Measurements were performed on a Hewlett-Packard 8453A (Agilent Technologies) photodiode array spectrophotometer fitted out with a Peltier temperature control system at *T* = 25 °C in 1.0 cm path-length cells.

**Circular Dichroism.** CD studies were performed by incubating ctDNA or BSA with the metal complexes for 72 h, in sodium cacodylate (NaCac) buffer (*I* = 2.5 mM) at pH = 7.4 and *T* = 25 °C and recording the CD spectra with a MOS-450 biological spectrophotometer (Bio-Logic SAS) in 1.0 cm path-length cells. As DMSO can affect the CD spectra of the biomolecules, the control measurements (ctDNA or BSA in the absence of metal complex) were incubated with the same DMSO percentage as the samples under the same experimental condition.

**Differential Scanning Calorimetry.** To prepare the DSC samples, ctDNA (4  $\times$  10<sup>-4</sup> M) was incubated with the metal complexes for 72 h, in NaCac buffer (*I* = 2.5 mM) at pH = 7.4 and *T* = 25 °C. For the control measurement, ctDNA in the absence of metal complex was incubated with the same DMSO content as the other samples under the same experimental conditions. Before recording the DSC measurements, the samples were degassed for 30 min in a degassing station (TA Instruments). DSC thermal denaturation studies were performed with a nano DSC (TA Instruments) by scanning at 3 atm pressure from 25 to 95 °C at 1 °C·min<sup>-1</sup> scan rate. The DCS curves were analyzed using the NanoAnalyze (TA Instruments) software.

**Viscosity Measurements.** Viscosity measurements were performed with an Ubbelohde viscometer (Schott) immersed in a water bath at *T* = 25 °C. The flow time was measured with a digital stopwatch. The sample viscosity was evaluated as the mean value of at least four replicated measurements. The viscosity readings were reported as  $L/L_0 = (\eta/\eta_0)^{1/3}$  versus C<sub>D</sub>/C<sub>T</sub> ratio, where  $\eta$  and  $\eta_0$  stand for the polynucleotide viscosity in the presence and in the absence of the metal complex, respectively.

**Cytotoxic Activity.** 2.5  $\times$  10<sup>3</sup> HeLa (human cervical carcinoma) or A549 (human lung carcinoma) cells were seeded in 200  $\mu$ L culture medium per well (DMEM medium), supplemented with 10% FBS and 1% amphotericin-penicillin-streptomycin solution in 96-well plates and incubated in a humid atmosphere at 37 °C under 5% CO<sub>2</sub> atmosphere for 24 h. Cells were then incubated for 72 h with 100  $\mu$ L of culture medium (supplemented either with 10% or 1% of FBS) with different concentrations of the metal complexes in culture medium. Cisplatin was also included as a positive control. Then, 100  $\mu$ L of 500  $\mu$ g/mL of MTT (thiazolyl blue tetrazolium bromide) was added to each well and incubated for 4 h. Lastly, the formazan product was dissolved by adding 100  $\mu$ L of solubilizing solution (10% sodium dodecyl sulfate (SDS) in 0.01 M HCl) and allowing the solution to solubilize overnight. Absorbance was read at 590 nm in a microplate reader

(Biotek Instruments). Four replicates per dose were included in each experiment, and half-maximal inhibitory concentration ( $IC_{50}$ ) values were calculated using the GraphPad Prism 6.01 analysis software (GraphPad Software Inc.) from three independent experiments.

**Native Protein Electrophoresis.** Native polyacrylamide gel electrophoresis (PAGE) was performed by incubating BSA overnight with different concentrations of the platinum complexes for  $[complex]/[protein]$  concentration ratios of 10 and 20 in Tris HCl buffer (0.5 M, pH = 6.8) and  $T = 25$  °C. After that, 5  $\mu$ L of sample buffer 2X (0.01% bromophenol blue and 20% glycerol in Tris HCl buffer (0.5 M, pH 6.8) were added to 5  $\mu$ L of the sample solutions and loaded onto 10% polyacrylamide gels. Gels were run in tris borate and EDTA (TBE)  $\times 1$  buffer at 80 V for 4 h at 4 °C to avoid denaturation of the protein. Finally, gels were stained with Coomassie Brilliant Blue R-250 and visualized with a Gel Doc XR+ Imaging System (Bio-Rad).

**Agarose Gel Electrophoresis.** Agarose gel electrophoresis of plasmid DNA (pUC18) was performed after incubation of the plasmid (15  $\mu$ M, base pairs) in the presence of different concentrations of complex 4 (1.5–750  $\mu$ M) or cisplatin (15 and 150  $\mu$ M) for 72 h. A vehicle-treated pUC18 sample was included with the maximum DMSO concentration used in the electrophoresis experiment. Loading buffer (2  $\mu$ L) was added to each sample (10  $\mu$ L) prior to being loaded onto a 1% agarose gel containing 0.05  $\mu$ g mL<sup>-1</sup> ethidium bromide. Electrophoresis was run at 5 V/cm for 2 h in TBE  $\times 1$  buffer, and the gel was visualized with a Gel Doc XR+ Imaging System (Bio-Rad).

**Cellular Uptake Studies.** A549 cells were seeded in culture flasks ( $2.5 \times 10^6$  cells in 6 mL DMEM culture medium and incubated for 24 h at 37 °C and 5% CO<sub>2</sub>). After that, cells were treated with the indicated concentrations of the Pt complexes for 24 h and harvested in phosphate buffered saline. The samples were digested with 65% HNO<sub>3</sub> at room temperature for 24 h and then diluted with Milli-Q water to obtain 2% HNO<sub>3</sub> solutions to be analyzed by inductively coupled plasma-mass spectrometry (ICP-MS).

**Computational Details.** The geometries of reactants, intermediates, products, and transition states were fully optimized by DFT calculations, using the B3LYP,<sup>49</sup> PBE0,<sup>50</sup> and M06-2X<sup>51</sup> functionals, the CEP-121G<sup>52</sup> effective potential basis set for the Pt atom, and the 6-31G(d,p)<sup>53</sup> basis set for the other atoms, as recently reported.<sup>54,55</sup> Water solvent effects were mimicked by the “conductor-like polarized continuum model” implicit method.<sup>56</sup> The reaction pathway leading to hydrolysis of 4 was followed by a two-step nucleophilic substitution mechanism, widely accepted and reported in the literature.<sup>57</sup> The geometry of the transition states was optimized by the synchronous transit quasi-Newton method.<sup>58</sup> Vibrational analysis, in the harmonic approximation, was performed. This allowed us to evaluate also the enthalpy and the Gibbs free energy differences along the reaction pathways. Energy minimum structures presented no imaginary frequencies, while all transition states were first-order saddle points in the potential energy surface. All calculations were performed with the Gaussian09 package.<sup>59</sup>

## ■ ASSOCIATED CONTENT

### ● Supporting Information

The Supporting Information is available free of charge on the ACS Publications website at DOI: 10.1021/acs.inorgchem.8b00713.

Experimental details including the stability in DMSO and aqueous buffer of compound 1, NMR spectra for compounds 2 and 3 in the presence of dGMP and for compound 4: relative energy obtained by DFT calculations, agarose gel electrophoresis of plasmid pUC18, CD spectra, and relative elongation of ctDNA in the presence of different concentrations of complex (PDF)

## ■ AUTHOR INFORMATION

### Corresponding Author

\*E-mail: begar@ubu.es.

### ORCID

Natalia Busto: 0000-0001-9637-1209

Giampaolo Barone: 0000-0001-8773-2359

Mónica Vaquero: 0000-0002-4550-4072

Félix A. Jalón: 0000-0002-6622-044X

Blanca R. Manzano: 0000-0002-4908-4503

Begoña García: 0000-0002-0817-1651

### Notes

The authors declare no competing financial interest.

## ■ ACKNOWLEDGMENTS

The authors gratefully acknowledge the financial support by La Caixa Foundation (LCF/PR/PR12/11070003), Ministerio de Economía y Competitividad-FEDER (CTQ2014-58812-C2-2-R, CTQ2014-58812-C2-1-R, and CTQ2015-70371-REDT), Consejería de Educación–Junta de Castilla y León-FEDER (BU042U16), Spain. C.P.-A. is grateful for the FPU grant from Ministry of Education, Culture and Sports, Madrid, Spain (FPU13/00180).

## ■ REFERENCES

- Galluzzi, L.; Senovilla, L.; Vitale, I.; Michels, J.; Martins, I.; Kepp, O.; Castedo, M.; Kroemer, G. Molecular Mechanisms of Cisplatin Resistance. *Oncogene* **2012**, *31*, 1869–1883.
- Florea, A.-M.; Buesselberg, D. Cisplatin as an Anti-Tumor Drug: Cellular Mechanisms of Activity, Drug Resistance and Induced Side Effects. *Cancers* **2011**, *3*, 1351–1371.
- Shekar, K.; McDonald, C. I.; Mullany, D. V.; Fraser, J. F.; Roberts, J. A.; Wallis, S. C.; Ghassabian, S.; Anstey, C.; Fung, Y. L. Protein-Bound Drugs Are Prone to Sequestration in the Extracellular Membrane Oxygenation Circuit: Results from an Ex Vivo Study. *Crit. Care* **2015**, *19*, 164.
- Haghdoust, M. M.; Golbaghi, G.; Létourneau, M.; Patten, S. A.; Castonguay, A. Lipophilicity-Antiproliferative Activity Relationship Study Leads to the Preparation of a ruthenium(II) Arene Complex with Considerable in Vitro Cytotoxicity against Cancer Cells and a Lower in Vivo Toxicity in Zebrafish Embryos than Clinically Approved c. *Eur. J. Med. Chem.* **2017**, *132*, 282–293.
- Babak, M. V.; Pfaffeneder-Kmen, M.; Meier-Menches, S. M.; Legina, M. S.; Theiner, S.; Licon, C.; Orvain, C.; Hejl, M.; Hanif, M.; Jakupec, M. A.; Keppler, B. K.; Gaiddon, C.; Hartinger, C. G. Rollover Cyclometalated Bipyridine Platinum Complexes as Potent Anticancer Agents: Impact of the Ancillary Ligands on the Mode of Action. *Inorg. Chem.* **2018**, *57*, 2851–2864.
- Gabano, E.; Gama, S.; Mendes, F.; Fregonese, F.; Paulo, A.; Ravera, M. Application of Microwave-Assisted Heating to the Synthesis of Pt(II) Complexes. *Inorg. Chim. Acta* **2015**, *437*, 16–19.
- Mock, C.; Puscasu, I.; Rauterkus, M. J.; Tallen, G.; Wolff, J. E. A.; Krebs, B. Novel Pt(II) Anticancer Agents and Their Pd(II) Analogues: Syntheses, Crystal Structures, Reactions with Nucleobases and Cytotoxicities. *Inorg. Chim. Acta* **2001**, *319*, 109–116.
- Casas, J. S.; Castiñeiras, A.; García-Martínez, E.; Parajó, Y.; Pérez-Parallé, M. L.; Sánchez-González, A.; Sordo, J. Synthesis and Cytotoxicity of 2-(2'-Pyridyl)benzimidazole Complexes of palladium(II) and platinum(II). *Z. Anorg. Allg. Chem.* **2005**, *631*, 2258–2264.
- Serratrice, M.; Maiore, L.; Zucca, A.; Stoccoro, S.; Landini, I.; Mini, E.; Massai, L.; Ferraro, G.; Merlino, A.; Messori, L.; Cinelli, M. A. Cytotoxic Properties of a New Organometallic platinum(II) Complex and Its gold(I) Heterobimetallic Derivatives. *Dalton Trans.* **2016**, *45*, 579–590.
- Labadie, S.; Dragovich, P. S.; Barrett, K.; Blair, W. S.; Bergeron, P.; Chang, C.; Deshmukh, G.; Eigenbrot, C.; Ghilardi, N.; Gibbons, P.;



- Hurley, C. A.; Johnson, A.; Kenny, J. R.; Kohli, P. B.; Kulagowski, J. J.; Liimatta, M.; Lupardus, P. J.; Mendonca, R.; Murray, J. M.; Pulk, R.; Shia, S.; Steffek, M.; Ubhayakar, S.; Ultsch, M.; van Abbema, A.; Ward, S.; Zak, M. Structure-Based Discovery of C-2 Substituted Imidazo-Pyrrolopyridine JAK1 Inhibitors with Improved Selectivity over JAK2. *Bioorg. Med. Chem. Lett.* **2012**, *22*, 7627–7633.
- (11) Fernandez, G. A.; Vela Gurovic, M. S.; Olivera, N. L.; Chopra, A. B.; Silbestri, G. F. Antibacterial Properties of Water-Soluble gold(I) N-Heterocyclic Carbene Complexes. *J. Inorg. Biochem.* **2014**, *135*, 54–57.
- (12) Marinelli, M.; Pellei, M.; Cimarelli, C.; Dias, H. V. R.; Marzano, C.; Tisato, F.; Porchia, M.; Gandin, V.; Santini, C. Novel Multicharged silver(I)-NHC Complexes Derived from Zwitterionic 1,3-Symmetrically and 1,3-Unsymmetrically Substituted Imidazoles and Benzimidazoles: Synthesis and Cytotoxic Properties. *J. Organomet. Chem.* **2016**, *806*, 45–53.
- (13) Smith, K. A.; Conboy, J. C. Using Micropatterned Lipid Bilayer Arrays to Measure the Effect of Membrane Composition on Merocyanine 540 Binding. *Biochim. Biophys. Acta, Biomembr.* **2011**, *1808*, 1611–1617.
- (14) Schlegel, R. A.; Phelps, B. M.; Waggoner, A.; Terada, L.; Williamson, P. Binding of Merocyanine 540 to Normal and Leukemic Erythroid Cells. *Cell* **1980**, *20*, 321–328.
- (15) Ecker, A.; Lehane, A. M.; Clain, J.; Fidock, D. A. PfCRT and Its Role in Antimalarial Drug Resistance. *Trends Parasitol.* **2012**, *28*, 504–514.
- (16) Rahim, R.; Strobl, J. S. Hydroxychloroquine, Chloroquine, and All-Trans Retinoic Acid Regulate Growth, Survival, and Histone Acetylation in Breast Cancer Cells. *Anti-Cancer Drugs* **2009**, *20*, 736–745.
- (17) Das, S.; Preet, R.; Siddharth, S.; Nayak, A.; Kundu, C. N.; Tripathi, N.; Bharatam, P. V. Quinacrine Induces Apoptosis in Cancer Cells by Forming a Functional Bridge between TRAIL-DRS Complex and Modulating the Mitochondrial Intrinsic Cascade. *Oncotarget* **2017**, *8*, 248–267.
- (18) Zhu, J.; Zheng, Y.; Zhang, H.; Zhu, J.; Sun, H.; Zhu, J.; Zheng, Y.; Zhang, H.; Zhu, J. Low Concentration of Chloroquine Enhanced Efficacy of Cisplatin in the Treatment of Human Ovarian Cancer Dependent on Autophagy. *Am. J. Transl. Res.* **2017**, *9*, 4046–4058.
- (19) Wang, Y.; Bi, Q.; Dong, L.; Li, X.; Ge, X.; Zhang, X.; Fu, J.; Wu, D.; Li, S. Quinacrine Enhances Cisplatin-Induced Cytotoxicity in Four Cancer Cell Lines. *Chemotherapy* **2010**, *56*, 127–134.
- (20) Dreyse, P.; Gonzalez, I.; Cortes-Arriagada, D.; Ramirez, O.; Salas, I.; Gonzalez, A.; Toro-Labbe, A.; Loeb, B. New Cyclometalated Ir(III) Complexes with Bulky Ligands with Potential Applications in LEC Devices: Experimental and Theoretical Studies of Their Photophysical Properties. *New J. Chem.* **2016**, *40*, 6253–6263.
- (21) Gajardo, F.; Barrera, M.; Vargas, R.; Crivelli, I.; Loeb, B. Influence of the Nature of the Absorption Band on the Potential Performance of High Molar Extinction Coefficient Ruthenium(II) Polypyridinic Complexes As Dyes for Sensitized Solar Cells. *Inorg. Chem.* **2011**, *50*, 5910–5924.
- (22) Dreyse, P.; Loeb, B.; Soto-Arriaza, M.; Tordera, D.; Orti, E.; Serrano-Perez, J. J.; Bolink, H. J. Effect of Free Rotation in Polypyridinic Ligands of Ru(II) Complexes Applied in Light-Emitting Electrochemical Cells. *Dalton Trans.* **2013**, *42*, 15502–15513.
- (23) Maury, O.; Guegan, J.-P.; Renouard, T.; Hilton, A.; Dupau, P.; Sandon, N.; Toupet, L.; Le Bozec, H. Design and Synthesis of 4,4'- $\pi$ -conjugated[2,2']-Bipyridines: A Versatile Class of Tunable Chromophores and Fluorophores. *New J. Chem.* **2001**, *25*, 1553–1566.
- (24) Baccouche, A.; Peigne, B.; Ibersiene, F.; Hammoutene, D.; Boutarfaia, A.; Boucekkine, A.; Feuvrie, C.; Maury, O.; Ledoux, I.; Le Bozec, H. Effects of the Metal Center and Substituting Groups on the Linear and Nonlinear Optical Properties of Substituted Styryl-Bipyridine Metal(II) Dichloride Complexes: DFT and TDDFT Computational Investigations and Harmonic Light Scattering Measurements. *J. Phys. Chem. A* **2010**, *114*, 5429–5438.
- (25) Hossain, M. D.; Haga, M.-A.; Gholamkhash, B.; Nozaki, K.; Tsushima, M.; Ikeda, N.; Ohno, T. Syntheses, Spectroelectrochemistry and Photoinduced Electron-Transfer Processes of Novel Ru and Os Dyad and Triad Complexes with Functionalized Diimide Ligands. *Collect. Czech. Chem. Commun.* **2001**, *66*, 307–337.
- (26) Po, C.; Tam, A. Y.-Y.; Wong, K. M.-C.; Yam, V. W.-W. Supramolecular Self-Assembly of Amphiphilic Anionic Platinum(II) Complexes: A Correlation between Spectroscopic and Morphological Properties. *J. Am. Chem. Soc.* **2011**, *133*, 12136–12143.
- (27) N'Dongo, H. W. P.; Neundorff, I.; Merz, K.; Schatzschneider, U. Synthesis, Characterization, X-Ray Crystallography, and Cytotoxicity of a Cymantrene Keto Carboxylic Acid for IR Labelling of Bioactive Peptides on a Solid Support. *J. Inorg. Biochem.* **2008**, *102*, 2114–2119.
- (28) Kuang, D.; Klein, C.; Ito, S.; Moser, J.-E.; Humphry-Baker, R.; Evans, N.; Duriaux, F.; Gratzel, C.; Zakeeruddin, S. M.; Gratzel, M. High-Efficiency and Stable Mesoscopic Dye-Sensitized Solar Cells Based on a High Molar Extinction Coefficient Ruthenium Sensitizer and Nonvolatile Electrolyte. *Adv. Mater.* **2007**, *19*, 1133–1137.
- (29) Andrews, S. S.; Boxer, S. G. Vibrational Stark Effects of Nitriles I. Methods and Experimental Results. *J. Phys. Chem. A* **2000**, *104*, 11853–11863.
- (30) Czegegi, C. E.; Papp, G.; Katho, A.; Joo, F. Water-Soluble gold(I)-NHC Complexes of Sulfonated IMES and SIMES and Their Catalytic Activity in Hydration of Alkynes. *J. Mol. Catal. A: Chem.* **2011**, *340*, 1–8.
- (31) Condirston, D. A.; Laposa, J. D. Vibrational Spectra of Styrene-H<sub>8</sub>, -D<sub>3</sub>, -D<sub>5</sub>, and -D<sub>8</sub>. *J. Mol. Spectrosc.* **1976**, *63*, 466–477.
- (32) Kelland, L. R. Preclinical Perspectives on Platinum Resistance. *Drugs* **2000**, *59*, 1–8.
- (33) Michalke, B. Platinum Speciation Used for Elucidating Activation or Inhibition of Pt-Containing Anti-Cancer Drugs. *J. Trace Elem. Med. Biol.* **2010**, *24*, 69–77.
- (34) Busto, N.; Valladolid, J.; Martinez-Alonso, M.; Lozano, H. J.; Jalon, F. A.; Manzano, B. R.; Rodriguez, A. M.; Carrion, M. C.; Biver, T.; Leal, J. M.; Espino, G.; Garcia, B. Anticancer Activity and DNA Binding of a Bifunctional Ru(II) Arene Aqua-Complex with the 2,4-Diamino-6-(2-Pyridyl)-1,3,5-Triazine Ligand. *Inorg. Chem.* **2013**, *52*, 9962–9974.
- (35) Macquet, J. P.; Butour, J. L. A Circular Dichroism Study of DNA-platinum Complexes. Differentiation between Monofunctional, Cis-Bidentate and Trans-Bidentate Platinum Fixation on a Series of DNAs. *Eur. J. Biochem.* **1978**, *83*, 375–387.
- (36) Fridman, A. S.; Galyuk, E. N.; Vorob'ev, V. I.; Skvortsov, A. N.; Lando, D. Y. Melting of Crosslinked DNA: VI. Comparison of Influence of Interstrand Crosslinks and Other Chemical Modifications Formed by Antitumor Compounds on DNA Stability. *J. Biomol. Struct. Dyn.* **2008**, *26*, 175–185.
- (37) Sullivan, M. P.; Holtkamp, H. U.; Hartinger, C. G. Antitumor Metallo-drugs That Target Proteins. *Met. Ions Life Sci.* **2018**, *18*, 351–386.
- (38) Rubbiani, R.; Can, S.; Kitanovic, I.; Alborzina, H.; Stefanopoulou, M.; Kokoschka, M.; Mönchgesang, S.; Sheldrick, W. S.; Wölfl, S.; Ott, I. Comparative In Vitro Evaluation of N-Heterocyclic Carbene gold(I) Complexes of the Benzimidazolylidene Type. *J. Med. Chem.* **2011**, *54*, 8646–8657.
- (39) Neault, J. F.; Tajmir-Riahi, H. A. Interaction of Cisplatin with Human Serum Albumin. Drug Binding Mode and Protein Secondary Structure. *Biochim. Biophys. Acta, Protein Struct. Mol. Enzymol.* **1998**, *1384*, 153–159.
- (40) Pracharova, J.; Viguera, G.; Novohradsky, V.; Cutillas, N.; Janiak, C.; Kostrhunova, H.; Kasparkova, J.; Ruiz, J.; Brabec, V. Exploring the Effect of Polypyridyl Ligands on the Anticancer Activity of Phosphorescent Iridium(III) Complexes: From Proteosynthesis Inhibitors to Photodynamic Therapy Agents. *Chem. - Eur. J.* **2018**, *24*, 1–14.
- (41) Kragh-Hansen, U. Molecular Aspects of Ligand Binding to Serum Albumin. *Pharmacol. Rev.* **1981**, *33* (1), 17–53.
- (42) Markovic, O. S.; Cvijetic, I. N.; Zlatovic, M. V.; Opsenica, I. M.; Konstantinovic, J. M.; Terzic Jovanovic, N. V.; Solaja, B. A.; Verbic, T. Z. Human Serum Albumin Binding of Certain Antimalarials. *Spectrochim. Acta, Part A* **2018**, *192*, 128–139.

- (43) Schroeder, R. L.; Pendleton, P.; Gerber, J. P. Physical Factors Affecting Chloroquine Binding to Melanin. *Colloids Surf, B* **2015**, *134*, 8–16.
- (44) Valko, K.; Nunhuck, S.; Bevan, C.; Abraham, M. H.; Reynolds, D. P. Fast Gradient HPLC Method to Determine Compounds Binding to Human Serum Albumin. Relationships with Octanol/water and Immobilized Artificial Membrane Lipophilicity. *J. Pharm. Sci.* **2003**, *92*, 2236–2248.
- (45) Fulmer, G. R.; Miller, A. J. M.; Sherden, N. H.; Gottlieb, H. E.; Nudelman, A.; Stoltz, B. M.; Bercaw, J. E.; Goldberg, K. I. NMR Chemical Shifts of Trace Impurities: Common Laboratory Solvents, Organics, and Gases in Deuterated Solvents Relevant to the Organometallic Chemist. *Organometallics* **2010**, *29*, 2176–2179.
- (46) Boutain, M.; Duckett, S. B.; Dunne, J. P.; Godard, C.; Hernandez, J. M.; Holmes, A. J.; Khazal, I. G.; Lopez-Serrano, J. A Parahydrogen Based NMR Study of Pt Catalysed Alkyne Hydrogenation. *Dalton Trans.* **2010**, *39*, 3495–3500.
- (47) Felsenfeld, G.; Hirschman, S. Z. A Neighbor-Interaction Analysis of the Hypochromism and Spectra of DNA. *J. Mol. Biol.* **1965**, *13*, 407–427.
- (48) Azzazy, H. M. E.; Christenson, R. H. *All about Albumin: Biochemistry, Genetics, and Medical Applications*; Academic Press, 1996.
- (49) Devlin, F. J.; Finley, J. W.; Stephens, P. J.; Frisch, M. J. Ab Initio Calculation of Vibrational Absorption and Circular Dichroism Spectra Using Density Functional Force Fields: A Comparison of Local, Nonlocal, and Hybrid Density Functionals. *J. Phys. Chem.* **1995**, *99*, 16883–16902.
- (50) Adamo, C.; Barone, V. Toward Reliable Density Functional Methods without Adjustable Parameters: The PBE0Model. *J. Chem. Phys.* **1999**, *110*, 6158–6170.
- (51) Zhao, Y.; Truhlar, D. G. The M06 Suite of Density Functionals for Main Group Thermochemistry, Thermochemical Kinetics, Non-covalent Interactions, Excited States, and Transition Elements: Two New Functionals and Systematic Testing of Four M06-Class Functionals and 12 Other Function. *Theor. Chem. Acc.* **2008**, *120*, 215–241.
- (52) Stevens, W. J.; Krauss, M.; Basch, H.; Jasien, P. G. Relativistic Compact Effective Potentials and Efficient, Shared-Exponent Basis Sets for the Third-, Fourth-, and Fifth-Row Atoms. *Can. J. Chem.* **1992**, *70*, 612–630.
- (53) Petersson, G. A.; Bennett, A.; Tensfeldt, T. G.; Al-Laham, M. A.; Shirley, W. A.; Mantzaris, J. A Complete Basis Set Model Chemistry. I. The Total Energies of Closed-Shell Atoms and Hydrides of the First-Row Elements. *J. Chem. Phys.* **1988**, *89*, 2193–2218.
- (54) Lauria, A.; Almerico, A. M.; Barone, G. The Influence of Substitution in the Quinoxaline Nucleus on 1,3-Dipolar Cycloaddition Reactions: A DFT Study. *Comput. Theor. Chem.* **2013**, *1013*, 116–122.
- (55) Bonsignore, R.; Russo, F.; Terenzi, A.; Spinello, A.; Lauria, A.; Gennaro, G.; Almerico, A. M.; Keppler, B. K.; Barone, G. The Interaction of Schiff Base Complexes of nickel(II) and zinc(II) with Duplex and G-Quadruplex DNA. *J. Inorg. Biochem.* **2018**, *178*, 106–114.
- (56) Cossi, M.; Rega, N.; Scalmani, G.; Barone, V. Energies, Structures, and Electronic Properties of Molecules in Solution with the C-PCM Solvation Model. *J. Comput. Chem.* **2003**, *24*, 669–681.
- (57) Lau, J. K.-C.; Ensing, B. Hydrolysis of Cisplatin—a First-Principles Metadynamics Study. *Phys. Chem. Chem. Phys.* **2010**, *12* (35), 10348–10355.
- (58) Peng, C.; Ayala, P.; Schlegel, H. B.; Frisch, M. J. Using Redundant Internal Coordinates to Optimize Equilibrium Geometries and Transition States. *J. Comput. Chem.* **1996**, *17*, 49–56.
- (59) Frisch, M. J.; Trucks, G. W.; Schlegel, H. B.; Scuseria, G. E.; Robb, M. A.; Cheeseman, J. R.; Scalmani, G.; Barone, V.; Petersson, G. A.; Nakatsuji, H.; Li, X.; Caricato, M.; Marenich, A.; Bloino, J.; Janesko, B. G.; Gomperts, R.; Menucci, B.; Hratchian, H. P.; Ortiz, J. V.; Izmaylov, A. F.; Sonnenberg, J. L.; Williams-Young, D.; Ding, F.; Lipparini, F.; Egidi, F.; Goings, J.; Peng, B.; Petrone, A.; Henderson, T.; Ranasinghe, D.; Zakrzewski, V. G.; Gao, J.; Rega, N.; Zheng, G.; Liang, W.; Hada, M.; Ehara, M.; Toyota, K.; Fukuda, R.; Hasegawa, J.;

## SUPPORTING INFORMATION

### Role of Seroalbumin in the Cytotoxicity of *cis*-Dichloro Pt(II) Complexes with (N<sup>^</sup>N)-Donor Ligands Bearing Functionalized Tails

Cristina Pérez-Arnaiz,<sup>‡</sup> Jorge Leal,<sup>†</sup> Natalia Busto,<sup>‡\*</sup> María C. Carrión,<sup>†</sup> Ana R. Rubio,<sup>‡</sup> Imanol Ortiz,<sup>†</sup> Giampaolo Barone<sup>§</sup>, Borja Díaz de Greñu,<sup>†</sup> Javier Santolaya,<sup>‡</sup> Jose M. Leal,<sup>‡</sup> Mónica Vaquero,<sup>‡</sup> Félix A. Jalón,<sup>†\*</sup> Blanca R. Manzano,<sup>†\*</sup> Begoña García<sup>‡\*</sup>

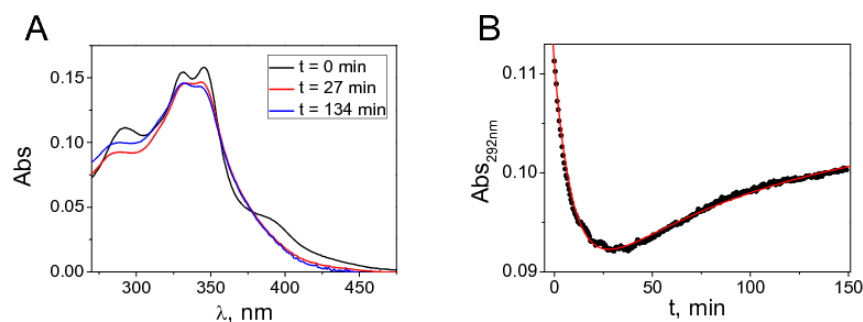
<sup>‡</sup>Universidad de Burgos, Departamento de Química, Plaza Misael Bañuelos s/n, 09001, Burgos, Spain.

<sup>†</sup>Universidad de Castilla-La Mancha, Facultad de Ciencias y Tecnologías Químicas-IRICA, Avda. Camilo J. Cela 10, 13071 Ciudad Real, Spain.

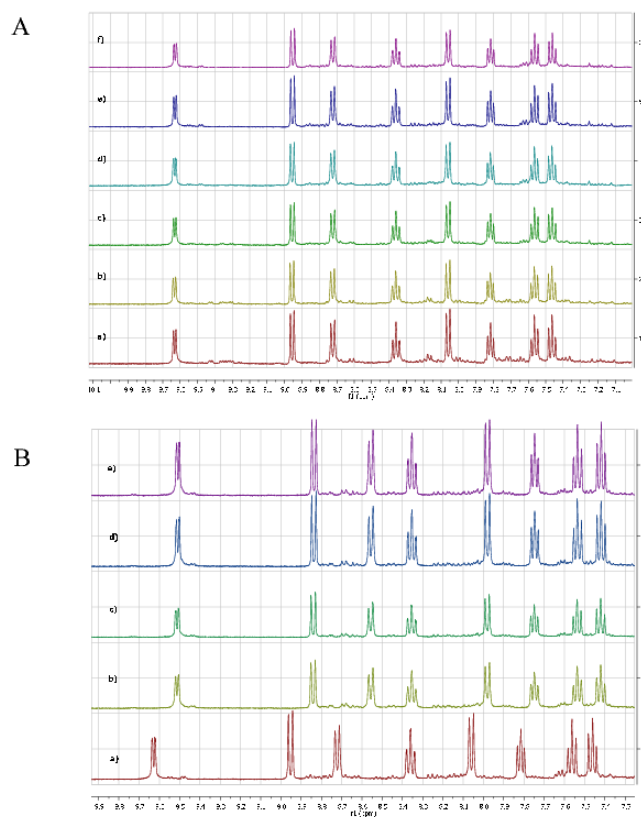
<sup>§</sup>Dipartimento di Scienze e Tecnologie Biologiche, Chimiche e Farmaceutiche (STEBICEF), Università degli Studi di Palermo, Viale delle Scienze Ed. 17, 90128, Palermo, Italy

\*E-mail: begar@ubu.es

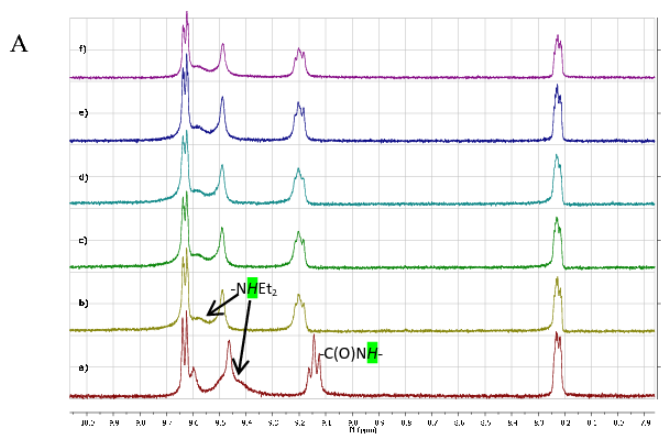
#### Stability in DMSO and aqueous buffer



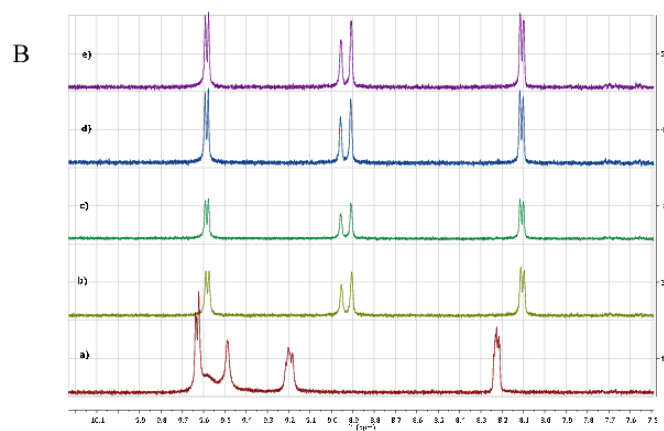
**Figure S1.** A) Representative absorbance spectra of complex **1** dissolved in DMSO at t = 0 min, 27 min and 134 min. B) Absorbance of complex **1** at  $\lambda = 292$  nm vs time after being dissolved in DMSO and fitting of a biexponential equation to the experimental data (red line).  $C_D = 10 \mu\text{M}$ ,  $T = 25 \text{ }^\circ\text{C}$ , DMSO.



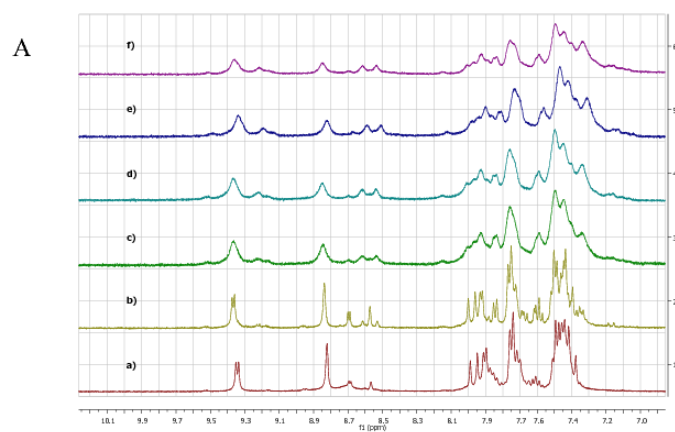
**Figure S2.** **A)** Aromatic area of  $^1\text{H}$  NMR spectra (400 MHz) in (0.5 mL)  $\text{DMSO-d}_6$  of **2**. From bottom, up: a)  $t=0$ , b)  $t= 3\text{h}$ , c)  $t= 1\text{ day}$ , d)  $t=2\text{ days}$ , e)  $t=6\text{ days}$ , f)  $t=7\text{ days}$ . **B)** Aromatic area of  $^1\text{H}$  NMR spectra (400 MHz) (0.5 ml  $\text{DMSO-d}_6+50\ \mu\text{L D}_2\text{O}$ ) of **2**. From bottom, u: a) complex **2** after 7 days in  $\text{DMSO-d}_6$  before the addition of  $\text{D}_2\text{O}$ , b)  $t=10\text{ h}$ , c)  $t= 2\text{ days}$ , d)  $t= 4\text{ days}$ , e)  $t= 5\text{ days}$ .







**Figure S3.** **A)** Aromatic area of  $^1\text{H}$  NMR spectra (400 MHz) in 0.5 mL of  $\text{DMSO-d}_6$  of **3**. From bottom, up: a)  $t=0$ , b)  $t= 3$  h, c)  $t= 1$  day, d)  $t= 2$  days, e)  $t= 6$  days, f)  $t= 7$  days. **B)** Aromatic area of  $^1\text{H}$  NMR spectra (400 MHz) (0.5 ml of  $\text{DMSO-d}_6 + 50 \mu\text{l}$  of  $\text{D}_2\text{O}$ ) of **3**. From bottom, up: a) complex **3** after 7 days in  $\text{DMSO-d}_6$  before the addition of  $\text{D}_2\text{O}$ , b)  $t= 10$  h, c)  $t= 34$  h, d)  $t= 106$  h, e)  $t= 7$  days.



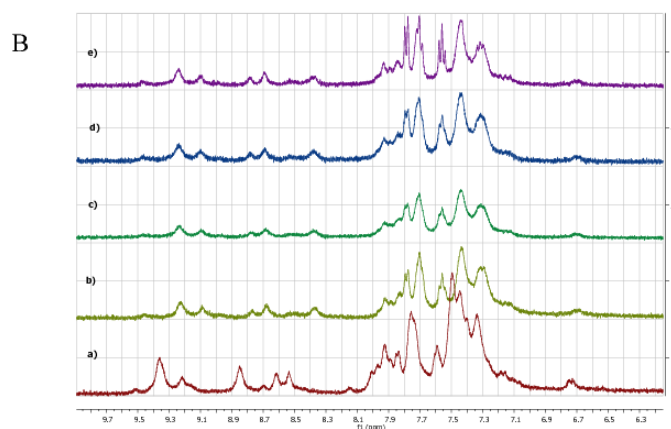


**Figure S4.** A) Aromatic area of  $^1\text{H}$  NMR spectra (400 MHz) in 0.5 mL of  $\text{DMSO-d}_6$  of **4**. From bottom, up: a)  $t = 0$ , b)  $t = 3\text{h}$ , c)  $t = 1\text{ day}$ , d)  $t = 2\text{ days}$ , e)  $t = 6\text{ days}$ , f)  $t = 7\text{ days}$ . B) Aromatic area of  $^1\text{H}$  NMR spectra (400 MHz) 0.5 mL of  $\text{DMSO-d}_6 + 50\ \mu\text{L D}_2\text{O}$  of **4**. a) complex **4** after 7 days in  $\text{DMSO-d}_6$  before the addition of  $\text{D}_2\text{O}$ , b)  $t = 10\text{h}$ , c)  $t = 34\text{ h}$ , d)  $t = 106\text{ h}$ , e)  $t = 7\text{ days}$ .

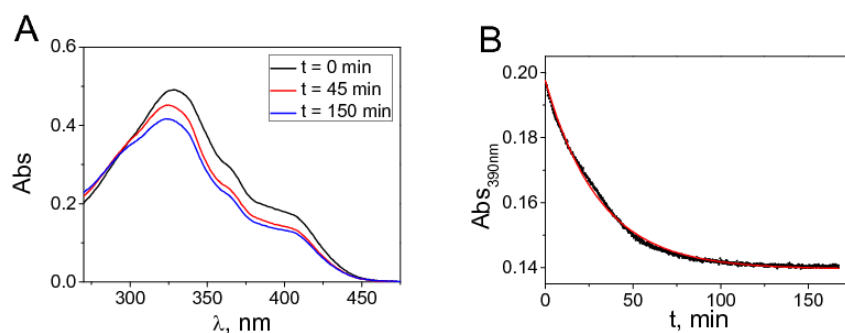


**Figure S5.** A) Representative absorbance spectra of complex **4** dissolved in  $\text{DMSO}$  at  $t = 0\text{ min}$ , 45 min and 150 min. B) Absorbance of complex **1** at  $\lambda = 390\text{ nm}$  Vs time after being dissolved in  $\text{DMSO}$  and fitting of a monoexponential equation to the experimental data (red line).  $\tau = 30.9\text{ min}$ ,  $C_D = 10\ \mu\text{M}$ ,  $T = 25\ ^\circ\text{C}$ ,  $\text{DMSO}$ .

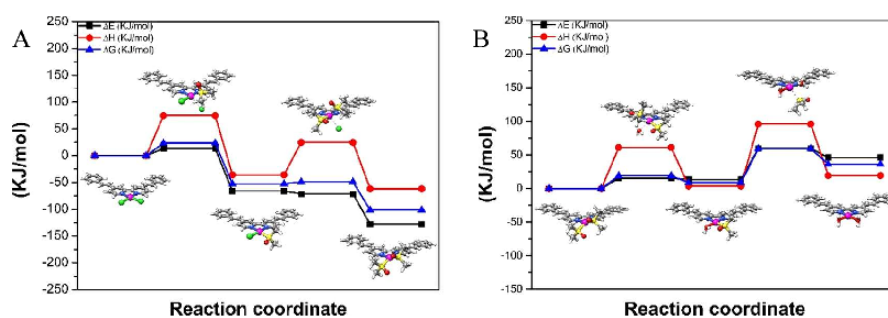


**Figure S6.** A) Pt coordination geometry, relative energy, enthalpy and Gibbs free energy of the species involved in the reaction pathway for the  $\text{Cl-DMSO}$   $\text{S}_{\text{N}}2$  substitution in **4**, obtained by DFT calculations in the implicit  $\text{DMSO}$  solvent. B) Pt coordination geometry, relative energy, enthalpy and Gibbs free energy of the species involved in the reaction pathway for the hydrolysis of **4**, obtained by DFT calculations in water solvent.

### Interaction with *d*GMP

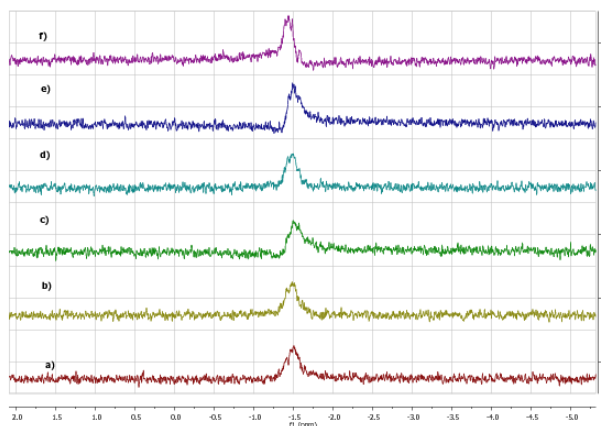


**Figure S7.**  $^{31}\text{P}$  NMR (162 MHz) spectra in (0.5 ml)  $\text{DMSO-d}_6$  + (50  $\mu\text{L}$ )  $\text{D}_2\text{O}$  of **2** + *d*GMP (5 mg in 20  $\mu\text{L}$  of  $\text{D}_2\text{O}$ ). From bottom, up: a) complex **2** after 14 days in  $\text{DMSO-d}_6$  +  $\text{D}_2\text{O}$  before the addition of *d*GMP, b)  $t=5$  min, c)  $t=15$  min, d)  $t=30$  min, e)  $t=2$  h, f)  $t=3$  days.

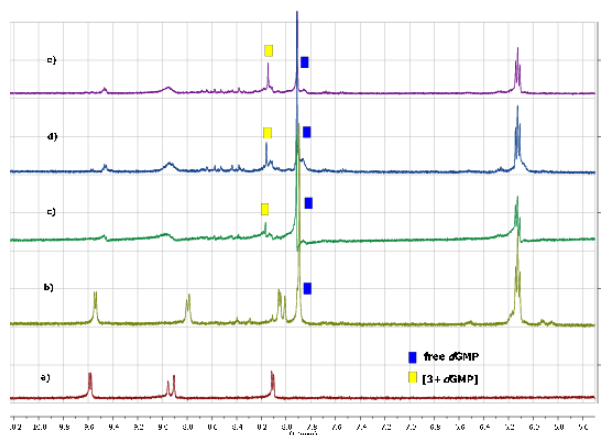


**Figure S8.** Aromatic area of  $^1\text{H}$  NMR spectra (400 MHz) (0.5 ml)  $\text{DMSO-d}_6$  + (50  $\mu\text{L}$ )  $\text{D}_2\text{O}$  of **3** + *d*GMP (5 mg in 20  $\mu\text{L}$  of  $\text{D}_2\text{O}$ ). From bottom, up: a) complex **3** after 14 days in  $\text{DMSO-d}_6$  +  $\text{D}_2\text{O}$  before the addition of *d*GMP, b)  $t=0$ , c)  $t=2$  days, d)  $t=6$  days, e)  $t=2$  weeks.

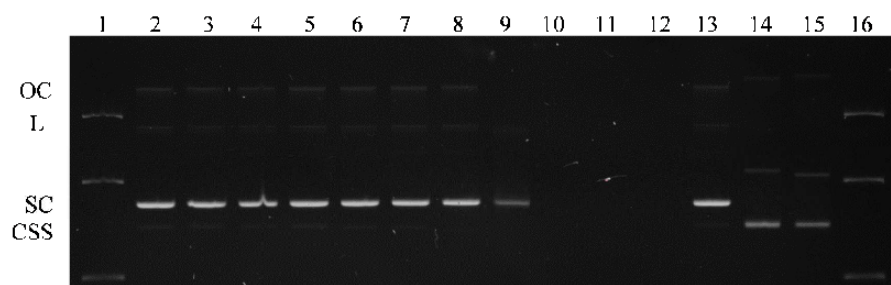


**Figure S9.** Agarose gel electrophoresis of plasmid pUC18 incubated overnight with different concentrations of complex **4** and with cisplatin as a positive control for covalent binding. Lanes 1 and 16: DNA ladder, lane 2 and 13: pUC18 alone; lane 3: pUC18 + DMSO; lanes 4-12: pUC18 + complex **4** at  $C_D/C_P$  concentration ratios = 0.1, 0.2, 0.5, 1, 2, 5, 10, 20 and 50; lanes 14 and 15: pUC18 + cisplatin at  $C_D/C_P$  concentration ratios = 1 and 10, respectively. Labelling: OC (nicked, open circular), L (linear), SC (supercoiled) and C, SS (circular, single-stranded).

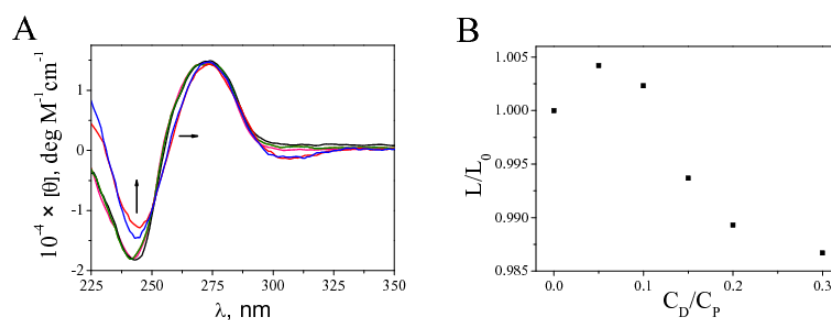


**Figure S10.** **A)** CD spectra of ctDNA in the presence of different concentrations of complex **4** ( $C_D/C_P = 0 - 1.2$ ),  $C_P = 8 \times 10^{-5}$  M. **B)** Relative elongation ( $L/L_0$ ) of ctDNA in the presence of different concentrations of complex **4** ( $C_D/C_P = 0 - 0.3$ ),  $C_P = 2 \times 10^{-4}$  M.  $I = 2.5$  mM sodium cacodylate (NaCac), pH = 7.4, T = 25°C.

# Chapter V

---

***Cis*-dichlorodiamine complexes of Ni(II), Pd(II) and Pt(II): theoretical study of hydrolysis and DNA-binding**

## 5.1 Introduction

Platinum(II,IV) complexes have been studied in different fields, because of their performance in catalysis,<sup>[113]</sup> or as anticancer drugs, in particular the already mentioned cisplatin and its derivatives.<sup>[114,115]</sup> In anticancer therapies, Pt(II) complexes are usually administrated as cis-dichloro complexes. However, inside the cells the chloride concentration is lower than that present in the extracellular fluids.<sup>[116]</sup> This condition usually induces the hydrolysis of the dichloro complexes  $[RR'-Pt-Cl_2]$ ,<sup>[117]</sup> leading to the analogous cis-diaquo complexes. In this context, it has been proved that Pt(II) can covalently bind B-DNA, through coordination bonds between the Pt atom and the N7 atom of one or two axially neighboring guanine bases.<sup>[118]</sup> It has been also reported that the two guanine bases binding to cisplatin could belong to the same or to different DNA molecules, leading to intra- or inter-molecular binding, respectively.<sup>[119,120]</sup> As a consequence of this DNA-binding, many important intracellular processes are interrupted, and this mechanism has been associated with the anticancer activity of cisplatin and its derivatives. Moreover, due to both the success and the limitations of such Pt compounds, for example their high toxicity or their success only with certain types of tumors,<sup>[121,122]</sup> many other analogous metal derivatives, including nickel(II) and palladium(II) complexes, have been considered as alternative potential antitumor agents.

Pd(II) complexes show a notable analogy with the coordination chemistry of Pt(II) complexes. One noteworthy difference is the kinetics of ligand exchange which seems to be the main reason why Pd(II) compounds do not show anticancer properties compared to the analogous Pt(II) derivatives. For example, hydrolysis of Pd(II) compounds is about  $10^5$  times faster than that of their Pt(II) analogues.<sup>[123]</sup> Probably, such reactions is so fast and, as a consequence, the resulting aquo complexes are so stable that such Pd(II) complexes are unable to bind to their biological targets. Interestingly, also Ni(II) complexes have been reported showing also potential in antitumor activities<sup>[114]</sup>, although with much less attention than the other two elements of the same group 10 of the periodic table. In particular, to the best of our knowledge, no experimental studies are reported in the literature concerning the synthesis and properties of Ni(II) analogue of cisplatin (called cisnickel), nor investigations on its hydrolysis pathway. We have only found a reference concerning a DFT study of the binding of cisnickel and with the N7 and O4 atoms of a guanine DNA base.<sup>[124]</sup>

In the present chapter, DFT calculations have been carried out to compare the structure and stability of the species involved along the commonly accepted reaction pathway for hydrolysis of the cis-dichloro-diamino complexes of Ni(II), Pd(II) (called cisplatinum) and Pt(II). Moreover, MD simulations have been performed for the two intrastrand DNA-binding complexes of cisplatin and cisnickel, in order to obtain insights of their N7 coordination on the DNA secondary structure.

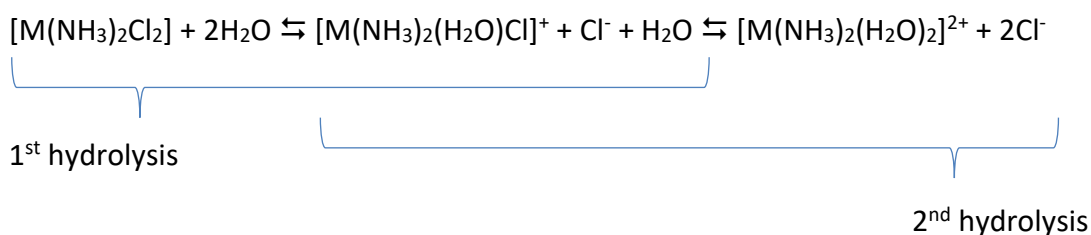
## 5.2 Computational details

**DFT calculations.** The geometries of reactants, intermediates, products and transition states have been fully optimized by DFT calculations, using the B3YLP,<sup>[62,63]</sup> PBE0<sup>[61]</sup> and M06-2X<sup>[60]</sup> functionals and CEP-121G effective potential basis set for the metal center<sup>[64-66]</sup> and 6-31G(d,p) basis set for the other atoms.<sup>[66,67]</sup> Water solvent effects are mimicked by the conductor-like polarized continuum model<sup>''</sup> implicit method (CPCM). Hydrolysis reaction pathway was followed by a two-step nucleophilic substitution mechanism, widely accepted and reported.<sup>[125-128]</sup> Transition states were optimized by the transit quasi-Newton method. Vibrational analysis, in harmonic approximation was performed. This allowed to evaluate enthalpy and Gibbs free energy differences along the reaction pathway. Basis set superposition errors were neglected. Energy minimum structures presented no imaginary frequencies, while all transition states were first order saddle points in the potential energy surface. All calculations were performed with Gaussian 09 software package.<sup>[71]</sup>

**MD simulations.** A random B-DNA dodecamer, with sequence 5'-AGCTAGGTCAGT-3' has been design by the Tinker software<sup>[100]</sup> to which cisplatin and cisnickel have been covalently bound to both central GG bases (residue 6 and 7), using the Molden software for the modelling.<sup>[129,130]</sup> The force field parameters involving the metal center (bonds, angle, dihedrals) were taken from the literature<sup>[105,131]</sup> and added to the Amber99sb force field with parmbsc0 nucleic acid torsion parameters. A triclinic box of TIP3P water was generated around the drug/B-DNA system, to a 1 nm depth on each side of the solutes, for a total of about 7800 solvent molecules; 43 K<sup>+</sup> ions and 23 Cl<sup>-</sup> ions were added to neutralize the DNA negative charge of the sugar- phosphate backbone and to set the solution ionic strength to about 0.15 M. MD simulations were conducted for 100 ns for both cisplatin/B-DNA and cisnickel/B-DNA model systems by using the Gromacs 5.0.4. software.<sup>[78,79]</sup>

## 5.3 Results and discussion

**DFT calculations.** The standard Gibbs free energy ( $\Delta G^\circ$ ) of the species, compared to reactants, were calculated by the following reaction scheme (M = Pt, Ni or Pd):



The results obtained for cisplatin are summarized in **Figure 1**. Calculated free energy variations along the hydrolysis pathway for each step (**r1** and **r2**, respectively) and the corresponding experimental values from the literature, are shown in **Table 1**.

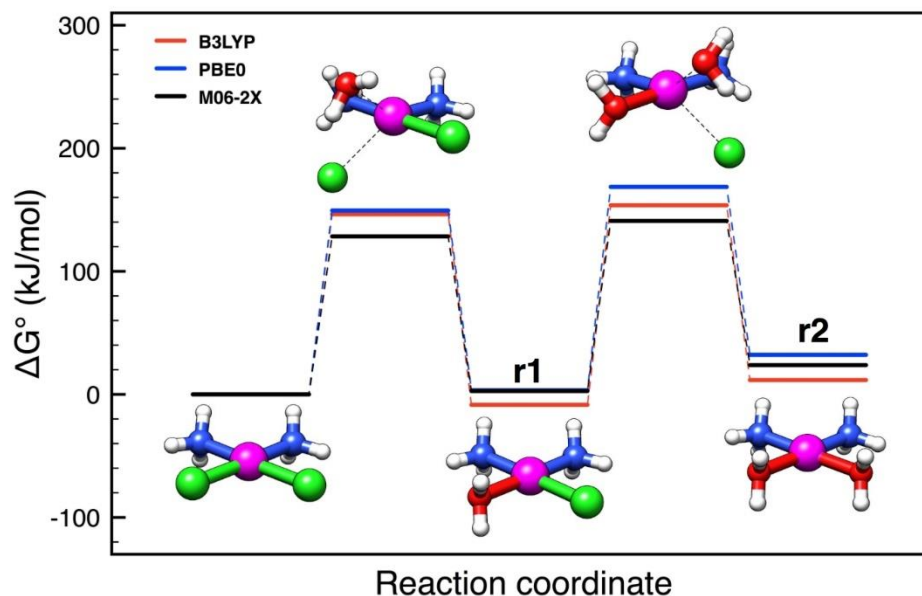


**Figure 1.** Pt coordination geometry and calculated standard Gibbs free energy values, relative to the reactant, of the species involved in the hydrolysis reaction pathway for cisplatin, obtained by DFT calculations.

**Table 1.** Calculated Gibbs free energy ( $\Delta G^\circ$ , kJ/mol) and literature theoretical/experimental data (kJ/mol) for the hydrolysis of the cisplatin.  $\Delta G_a$  refers to the activation energy and  $\Delta G_r$  to the energy difference between reactant and product of each hydrolysis step.

	Theoretical				Experimental	
	<b>M06-2X</b>	<b>B3LYP</b>	<b>PBE0</b>	<b>Ref. (a)</b>	<b>Ref. (b)</b>	<b>Ref. (c)</b>
$\Delta G_{a1}$	128.34	146.39	149.37	104.18	99.24	98.95
$\Delta G_{a2}$	104.95	153.67	168.61	105.85	98.55	99.23
$\Delta G_{r1}$	2.71	-8.54	3.28	-	4.2	3.6
$\Delta G_{r2}$	23.76	11.62	32.10	-	-	-

(a) J. K. Lau and D. V. Deubel. *J. Chem. Theory Comput.* (2006), 2, 103-106. (b) J. W. Reishus, D.S. Martin Jr. *J. Am. Chem. Soc.* (1961), 83 (11), 2457-1462. (c) J. R. Perumareddi, A. W. Adamson. *J. Phys. Chem.* (1967), 72, 414-420.

Based on the results obtained for cisplatin, the M06-2X functional was chosen for the study of the analogous reactions of cisnickel and cispalladium. The results obtained, compared with cisplatin, are summarized in **Figure 2**.



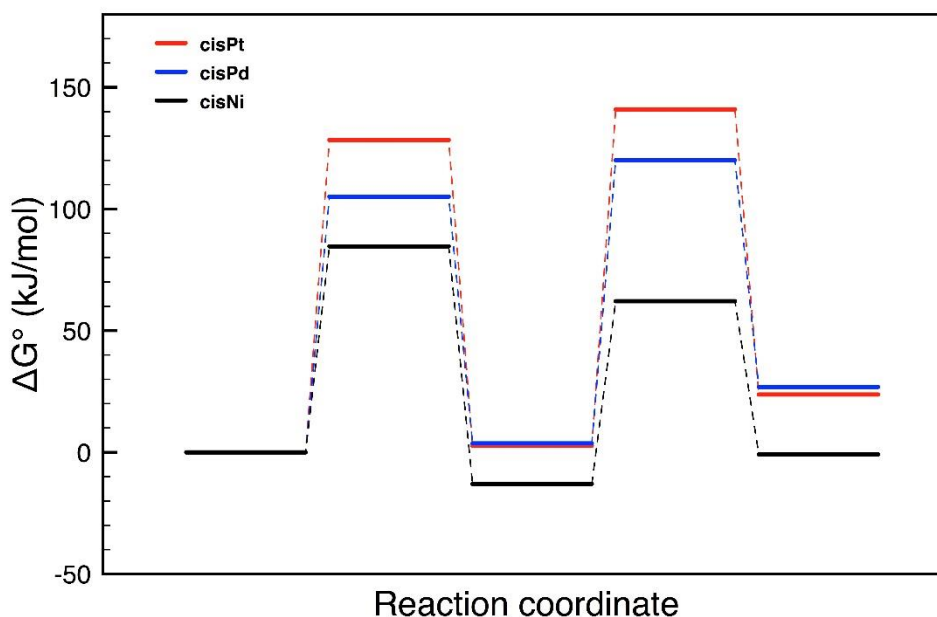


**Figure 2.** Calculated standard Gibbs free energy values, relative to the reactants, for cisplatin (red) cisnickel (black) and cispalladium (blue), obtained by DFT calculations.

These results show that, indeed, the activation barriers are higher for cisplatin and decrease in the order cisplatin > cispalladium > cisnickel. Moreover, the stability of the hydrolysis products is much higher for cisnickel than for both cispalladium and cisplatin. Such results well explain the known higher hydrolysis reactivity of Pd(II) compared to Pt(II) compounds and show also that cisnickel is the most reactive of the three considered compounds.

The relative kinetic constants have been calculated from the computational results for each hydrolysis step for the Pd(II), Ni(II) and Pt(II) complexes, using the following equations:

Method 1

$$E_a = \Delta H_{\#}^0 + RT; \quad \Delta H_{\#}^0 = E_a - RT \quad (1)$$

$$\Delta S_{\#}^0 = (\Delta G_{\#}^0 - \Delta H_{\#}^0) / T \quad (2)$$

$$k_v = k_B T / h \cdot \exp(\Delta S_{\#}^0 / R) \cdot \exp(-\Delta H_{\#}^0 / RT) \quad (3)$$

Where  $E_a$  is the activation energy for each hydrolysis step,  $\Delta H_{\#}^0$ ,  $\Delta S_{\#}^0$  and  $\Delta G_{\#}^0$  are enthalpy, entropy and free energy differences between reactant and transition state,  $R$  is the gas constant and  $k_b$  and  $h$  are the Boltzman and Planck constants respectively.

Method 2

$$k_v = (k_B T / h) \cdot \exp(\Delta G_{\#}^0 / RT) \quad (4)$$

**Eq. 4** corresponds to Eyring's equation, with the same parameters described above.

Using **Eq 3.** and **Eq. 4** the calculated kinetic constants (**Table 2**) of each hydrolysis step are equal.

**Table 2.** Calculated kinetic constants for the first and second hydrolysis steps.

	$k_1$ (s <sup>-1</sup> )	$k_2$ (s <sup>-1</sup> )
<b>Pt</b>	$1,98 \cdot 10^{-10}$	$3,64 \cdot 10^{-12}$
<b>Pd</b>	$2,41 \cdot 10^{-06}$	$2,48 \cdot 10^{-08}$
<b>Ni</b>	$8,99 \cdot 10^{-03}$	$4,27 \cdot 10^{-01}$

A comparison between the calculated kinetic constants of cispalladium and cisnickel, with those of cisplatin, is reported in **Table 3**. It can be noticed that  $k_1$  and  $k_2$  are  $10^4$  and  $10^3$  times bigger for cispalladium, of the same order of magnitude with literature values, reporting that the hydrolysis of palladium complexes is  $10^5$  times faster than that of the corresponding platinum analogues.<sup>[123]</sup> Remarkably, the values of  $k_1$  and  $k_2$  for nickel are  $10^7$  and  $10^{11}$  times bigger than those of cisplatin. The latter result is also in agreement with reported literature data,<sup>[123]</sup> claiming that nickel(II) complexes are always much more labile and reactive. In fact, ligand exchange processes in Ni(II) complexes tend to be associative, because Ni(II) forms a large number of complexes with a coordination number between three and six. On the other hand ligand exchange processes are predominantly dissociative for both Pd(II) and Pt(II) complexes, because they preferentially assume coordination number four in square planar geometry.<sup>[123]</sup>

**Table 3.** Comparison between the first and second hydrolysis kinetic constants of cispalladium and cisnickel, relative to cisplatin.

<b>M</b>	$k_{1(M)}/k_{1(Pt)}$	$k_{2(M)}/k_{2(Pt)}$
<b>Pd</b>	$1,21 \cdot 10^4$	$6,81 \cdot 10^3$
<b>Ni</b>	$4,54 \cdot 10^7$	$1,17 \cdot 10^{11}$

**MD simulations.** The effect of the DNA binding of cisplatin and cisnickel on the double helical structure has been investigated through MD simulations. The DNA binding of cisnickel has been considered in the hypothesis that it would remain stable and in square planar geometry in solution, despite literature data and the results of previous section evidence their high reactivity and ligand lability. This part still needs to be deepened through further investigations. The results of the MD simulations allow to visualize the effects caused by the crosslinking of cisplatin and cisnickel on the same B-DNA sequence and with the same binding mode, see **Figures 3** and **4**. The different structural changes induced on the DNA secondary structure can be then associated to the effect of the metal center. In both systems, due to the square planar coordination geometry of the two metal complexes, the value of the N7-M-N7' angle (where N7 and N7' are the nitrogen atoms from the two guanine ligands coordinated to the M

metal center) rapidly assume the approximate value of 90°, as expected, and remaining constant till the end of the MD simulation. At the same time, and as a consequence, the DNA structure is strongly bended, and a loss of helicity is also observed, without breaking of the Watson-Crick hydrogen bonds between complementary DNA bases. The corresponding video files are available as supplementary files, through the QR codes shown in of **Figures 3** and **4**.

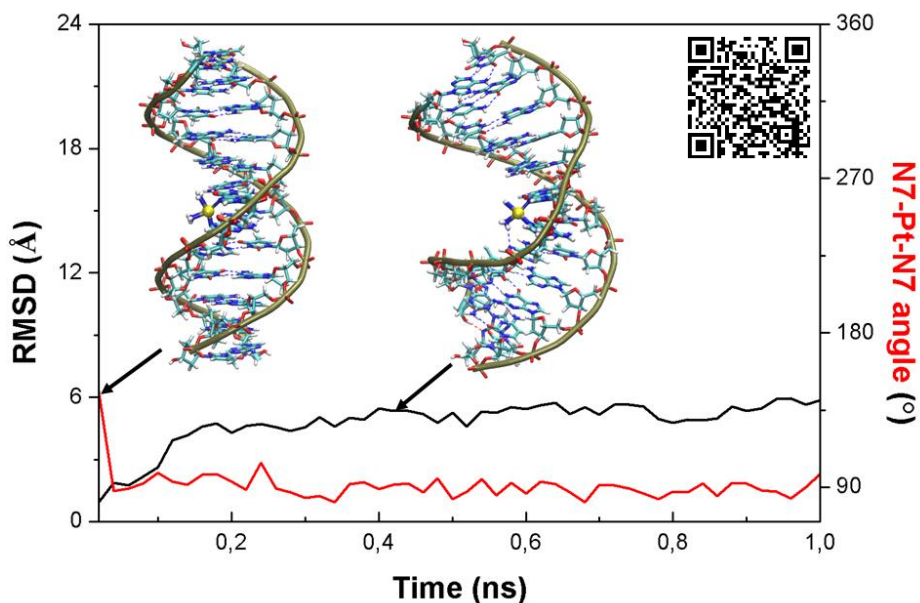


**Figure 3.** RMSD plot for cisplatin/B-DNA system, black line nucleic plot, red line variation of the defined angle value during the first ns of MD simulation.

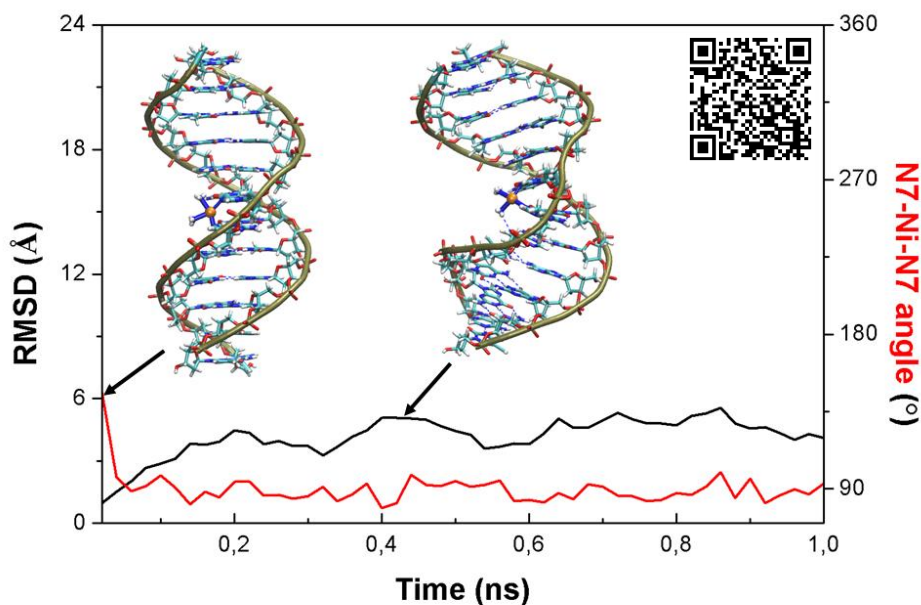


**Figure 4.** RMSD plot for cisnickel/B-DNA system, black line nucleic plot, red line variation of the defined angle values during the first ns of MD simulation.

The effect of crosslinking is so fast that no significant changes can be identified between the structures at 0,4 ns of MD simulation and at 100 ns, as it can be seen in **Figure 5** and **6**. Analogously, if we look at the complete RMSD, both for the nucleic structure and for the variation in the described angle, no significant variations are seen after 0,4 ns of MD simulation, see **Figure 7**.

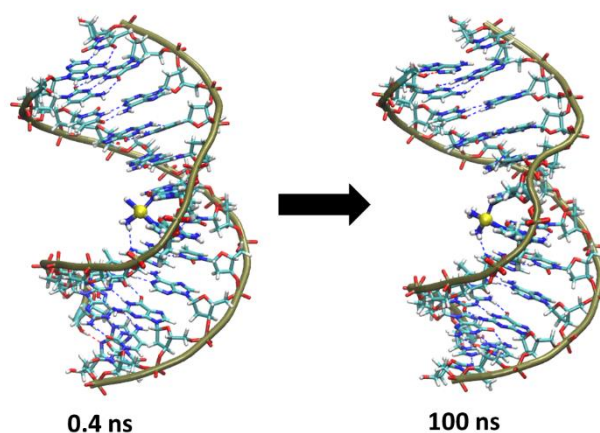


**Figure 5.** Structures for cisplatin/B-DNA system at 0.4 ns and 100 ns.

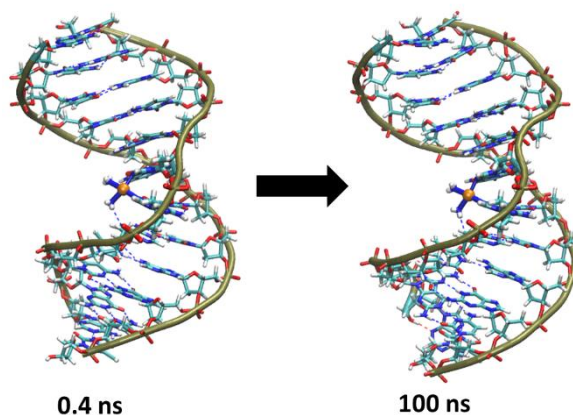


**Figure 6.** Structures for cisnickel/B-DNA system at 0.4 ns and 100 ns.

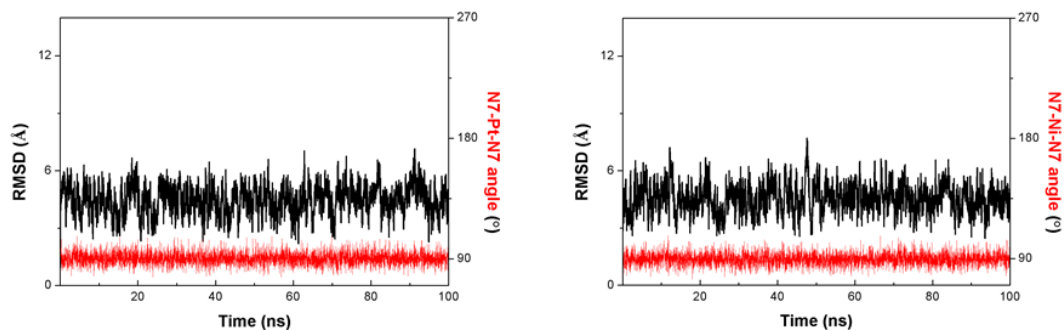


**Figure 7.** Complete RMSD analysis for cisplatin/B-DNA (left) and cisnickel/B-DNA (right) systems over the 100 ns of MD simulation.

Remarkably, the equilibrium structure of the complex between cisplatin and DNA, obtained by the MD simulations, is in excellent agreement with the corresponding experimental structure obtained by x-ray diffraction, *PDB id: 1AIO*,<sup>[132]</sup> and despite the different sequences of the two systems, as shown by the superimposed structures in **Figure 8**. Remarkably, cisplatin binding induces the same modifications leading to the same DNA bending. Such results confirm that our MD simulations properly reproduce the experimentally observed effects of cisplatin coordination on the conformation of double helical DNA.

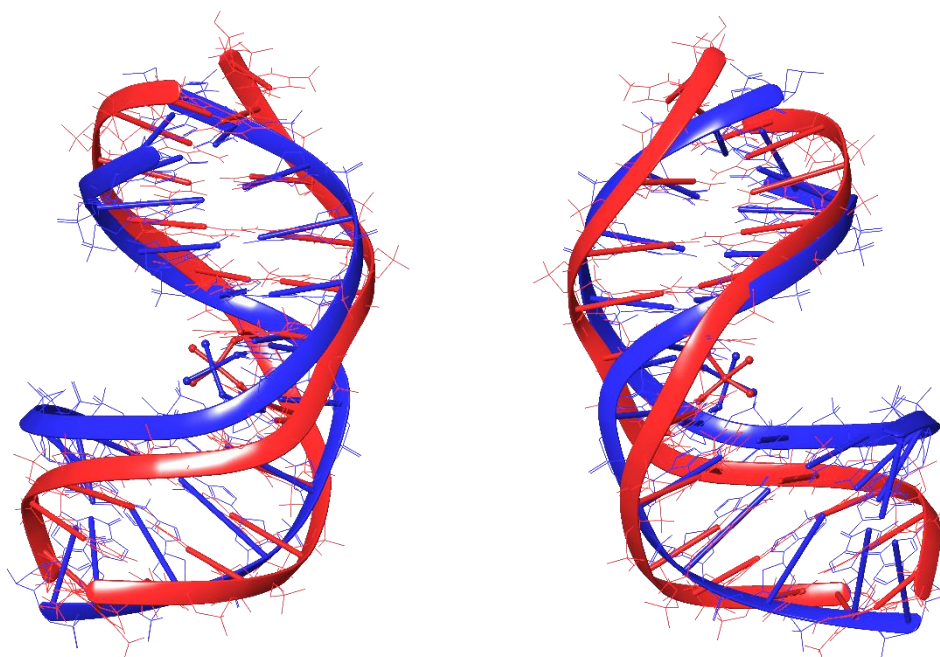


**Figure 8.** Different views of the superimposed cisplatin/DNA structures obtained from MD simulations (**red**) and from X-ray crystallography, *PDB id: 1AIO* <sup>[132]</sup> (**blue**).

#### 5.4 Conclusions

Through DFT calculations it has been possible to obtain the relative energies for the species involved in cisplatin hydrolysis and to compare them with those of the nickel and palladium analogues. It can be concluded that both cisnickel and cispalladium are more susceptible to hydrolysis than cisplatin. In particular, the reaction speed decreases in the order cisnickel > cispalladium > cisplatin. Since cisplatin hydrolysis is considered the key-step before DNA binding, both cispalladium and cisnickel, and eventually their derivatives, should be also able to bind DNA. However, it must be considered that the rapid formation of the aquo complex sets the charge of the three complexes to +2, reducing their ability to cross the cell membrane. The results obtained have proven that the effect of cisplatin binding on double stranded DNA is correctly replicated by MD simulations. Moreover, in the hypothesis that the nickel

complex could be stable in solution, its binding to DNA would produce similar distortions on the double helical conformation.

# **Chapter VI**

---

**Kinetic evidence for interaction of TMPyP4 with two different G-quadruplex conformations of human telomeric DNA**

## Summary

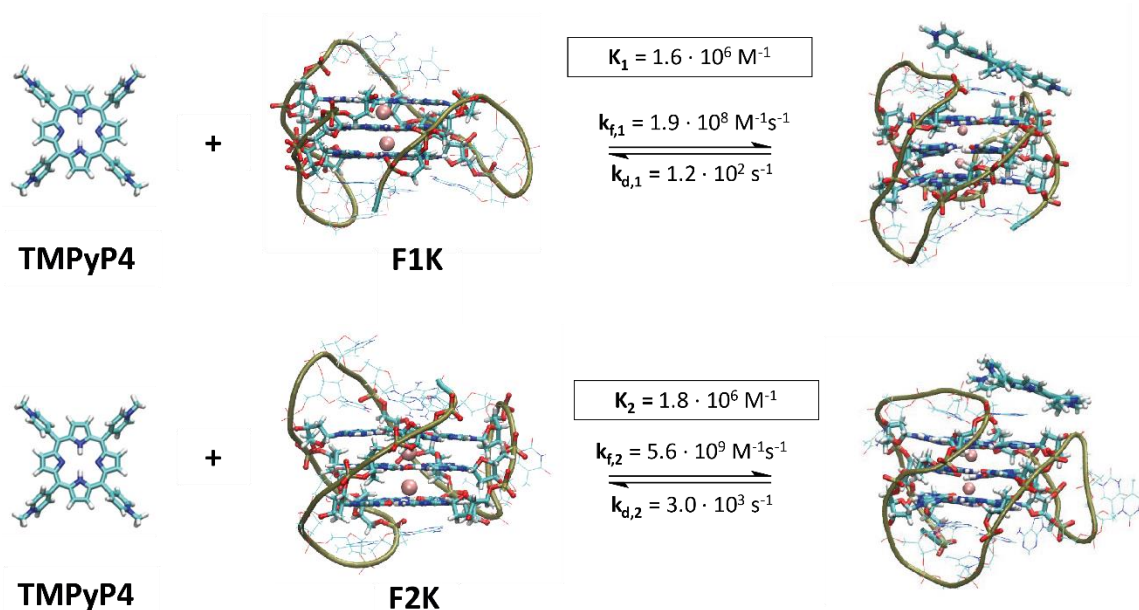


**Figure 1.** Kinetic behavior of TMPyP4 binding to G-quadruplex hybrid structures: hybrid-1 named F1K, *PDB id: 2HY9*<sup>[133]</sup> and hybrid-2 named F2K, *PDB id: 2JPZ*,<sup>[134]</sup> based on kinetic experimental results.

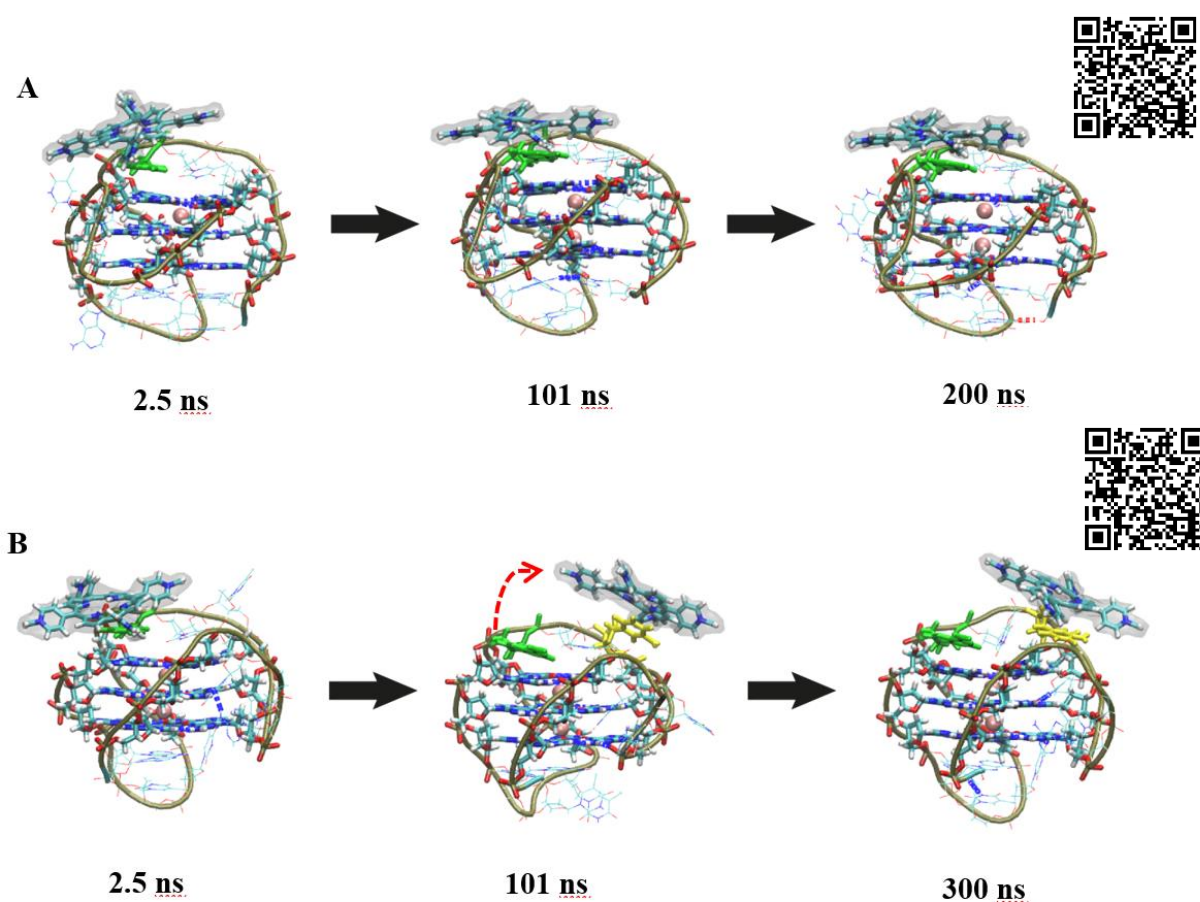
It is well known that TMPyP4 is a G-quadruplex binder with a very high affinity. However, kinetic investigations, through T-Jump measurements, as reported in the present chapter, suggest that TMPyP4 shows a different binding kinetics toward the two different hybrid G-quadruplex conformations formed in  $\text{K}^+$  solution: **F1K** and **F2K** (**Figure 1**), although the values of the thermodynamic constants for the equilibrium represented in **Figure 1**, calculated as  $K = k_d/k_f$ , are very similar. Usually only the thermodynamic constants have been reported in the literature concerning the binding of TMPyP4 to G-quadruplex structures. To the best of our knowledge the binding kinetics has not been considered before.

To support the interpretation of the experimental studies, my main contribution to the study was to carry out MD simulations for the TMPyP4/**F1K** and TMPyP4/**F2K** systems, to obtain a molecular recognition process, a possible binding mode and to evaluate if there were indications related to the different binding kinetics of TMPyP4 to the two G-quadruplex isomers **F1K** and **F2K**. Moreover, experimentally it was not been possible to demonstrate which calculated kinetics constants corresponded to each of the G-quadruplex hybrid structure in solution, but the computational results allowed to suggest which of the two kinetics corresponded to the binding to **F1K** or to **F2K**.

Surprisingly, the results of MD simulations showed that TMPyP4 binds rapidly to an adenine residue of both G-quadruplex systems. For the TMPyP4/**F2K** system (showing



the higher  $k_f$  value) it persists leading to a fast equilibrium structure, while for the TMPyP4/**F1K** system (showing the lower  $k_f$  value), during the MD simulation, a second binding occurs with a thymine residue in the loop, where it finally reaches an equilibrium state, **Figure 2**. In the study, it has been assumed that such binding variation was related to the kinetic difference during the molecular recognition process. The corresponding video files are available as supplementary files, through the QR codes shown in **Figure 2**. Also, it must be mentioned that as TMPyP4 shows the same binding mode for the two structures, i.e. external stacking with a dangling adenine base in the loop, and that the final structures are very similar. These results are also in agreement with the similar values of the experimentally determined thermodynamic DNA-binding constants. The published article is attached below.

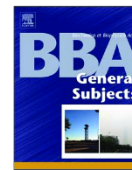


**Figure 2.** Molecular recognition scheme during the MD simulation: (A) TMPyP4/**F2K** (B) TMPyP4/**F1K**.



Contents lists available at ScienceDirect

BBA - General Subjects

journal homepage: [www.elsevier.com/locate/bbagen](http://www.elsevier.com/locate/bbagen)

## Kinetic evidence for interaction of TMPyP4 with two different G-quadruplex conformations of human telomeric DNA



Cristina Pérez-Arnaiz<sup>a</sup>, Natalia Busto<sup>a</sup>, Javier Santolaya<sup>a,b</sup>, José M. Leal<sup>a</sup>, Giampaolo Barone<sup>b,\*</sup>, Begoña García<sup>a,\*</sup>

<sup>a</sup> Department of Chemistry, University of Burgos, 09001 Burgos, Spain

<sup>b</sup> Dipartimento di Scienze e Tecnologie Biologiche, Chimiche e Farmaceutiche (STEBICEF), Università degli Studi di Palermo, Viale delle Scienze Ed. 17, 90128 Palermo, Italy

### ARTICLE INFO

#### Keywords:

Tel22 conformations  
TMPyP4  
Fast reactions  
Molecular dynamics

### ABSTRACT

**Background:** Stabilization of G-quadruplex helices by small ligands has attracted growing attention because they inhibit the activity of the enzyme telomerase, which is overexpressed in > 80% cancer cells. TMPyP4, one of the most studied G-quadruplex ligands, is used as a model to show that the ligands can exhibit different binding features with different conformations of a human telomeric specific sequence.

**Methods:** UV-Vis, FRET melting Assay, Isothermal Titration Calorimetry, Time-resolved Fluorescence lifetime, T-Jump and Molecular Dynamics.

**Results:** TMPyP4 yields two different complexes with two Tel22 telomeric conformations in the presence of Na<sup>+</sup> or K<sup>+</sup>. T-Jump kinetic experiments show that the rates of formation and dissociation of these complexes in the ms time scale differ by one order of magnitude. MD simulations reveal that, in K<sup>+</sup> buffer, “hybrid 1” conformation yields kinetic constants on interaction with TMPyP4 one order lower than “hybrid 2”. The binding involves  $\pi$ - $\pi$  stacking with external loop bases.

**Conclusions:** For the first time we show that for a particular buffer TMPyP4 interacts in a kinetically different way with the two Tel22 conformations even if the complexes formed are thermodynamically indistinguishable.

**General significance:** G-quadruplexes, endowed with technological applications and potential impact on regulation mechanisms, define a new research field. The possibility of building different conformations from same sequence is a complex issue that confers G-quadruplexes very interesting features. The obtaining of reliable kinetic data constitutes an efficient tool to determine reaction mechanisms between conformations and small molecules.

### 1. Introduction

The study and advancement of small molecules capable of binding and stabilizing higher-order DNA structures, such as G-quadruplexes, has attracted growing interest [1]. G-quadruplexes can be formed in guanine-rich DNA stretches in the presence of stabilizing ions such as Na<sup>+</sup> or K<sup>+</sup>. Although the *in vivo* existence of such structures is still a matter of debate [2], under physiological conditions the human genome contains a large number of potential quadruplex-forming sequences [3,4]. Human telomeric DNA consisting of TTAGGG repeats is an interesting instance of such sequences. Stabilization of telomeric G-quadruplex helices by small ligands is known to inhibit the activity of the enzyme telomerase, which is overexpressed in > 80% of cancer cells and acts as tumour promoter [5].

In intracellular media, potassium ions abound more than sodium

ions, giving way to extensive research of G-quadruplex conformations stabilized by K<sup>+</sup> [6]. The main conformation reported for the human telomeric sequence in K<sup>+</sup> solutions “Tel22” (d[AGGG(TTAGGG)<sub>3</sub>]) consists of a G-quadruplex fold with (3 + 1) G-tetrad core containing three tetrads, one side-chain reversal loop and two lateral loops [7]. Two distinguishable conformations (known as hybrid-1 and hybrid-2) have been identified containing this core with the same number and type of loops but different loop arrangement [8]. On the other hand, in Na<sup>+</sup> solutions the antiparallel basket-type structure was found for human telomeric DNA. Although this basket form is the only folded conformation fully characterized under these conditions [9], subsequent studies provide evidence for the polymorphism of telomeric sequences in Na<sup>+</sup> solutions, with possible interconversion between various structural forms [10].

In line with these observations, we have reported recently the fast

\* Corresponding authors.

E-mail addresses: [giampaolo.barone@unipa.it](mailto:giampaolo.barone@unipa.it) (G. Barone), [begar@ubu.es](mailto:begar@ubu.es) (B. García).

<https://doi.org/10.1016/j.bbagen.2017.10.020>

Received 16 May 2017; Received in revised form 13 October 2017; Accepted 27 October 2017  
Available online 31 October 2017

0304-4165/© 2017 Elsevier B.V. All rights reserved.

processes that govern different Tel22 structures in equilibrium at 25 °C. Kinetic T-jump measurements provide evidence for the presence of two G-quadruplex conformations, F1M and F2M, in equilibrium with G-triplex structures, F1'M and F2'M, with  $M = \text{Na}^+$  or  $\text{K}^+$  [11]. These results, along with other studies, evince the complexity of this system [12–15], thus posing the question of whether small molecules can differentiate between different specific sequence conformations coexisting in solution, a striking feature not reported hitherto. To this aim, we have studied the interaction of Tel22 with the cationic *meso*-tetrakis(*N*-methyl-4-pyridyl)porphyrin (TMPyP4), capable of stabilizing quadruplex structures and inhibiting the telomerase activity [16]. In spite of being nonselective for quadruplex helices over duplex DNA [17], TMPyP4 is one of the most studied G-quadruplex ligands ever and its structure has inspired the development of other porphyrin derivatives [18,19]. Nevertheless, certain controversy over the nature of the G-quadruplex/TMPyP4 interactions still remains, and intercalation between adjacent G-tetrads or end-stacking onto the external faces of the G-quadruplex have been proposed [20–22].

Due to its demonstrated affinity with G-quadruplex structures, TMPyP4 has been used in this work as a model molecule to show that certain ligands can exhibit different binding features towards different conformations of a specific sequence. Even though these features can be thermodynamically indistinguishable, they take place at different rates, as suggested recently by J. Lah et al. [23] and shown here by T-jump measurements and MD calculations. The F1M/TMPyP4 and F2M/TMPyP4 complexes get formed at low TMPyP4/Tel22 concentration ratio and have very close binding constants ( $K_1 = k_f/k_d$ ), whereas the formation,  $k_f$ , and dissociation,  $k_d$ , kinetic constants differ considerably. At higher TMPyP4/Tel22 concentration ratio, another type of complex with binding constant  $K_2$  gets formed. This complex has been reported before and is assumed to involve an external mode of binding [24]. This work is a starting point; actually, the interactions of other types of ligands biologically more relevant than TMPyP4 with different oligonucleotides are to be explored in future studies.

## 2. Materials and methods

### 2.1. Sample preparation

The DNA oligonucleotide d[AGGG(TTAGGG)<sub>3</sub>], known as “Tel22”, was purchased from Thermo Fisher Scientific Inc. as dried samples. Stock solutions were prepared with nuclease free water in buffers containing 10 mM Tris-HCl, 1 mM EDTA and 0.15 M of either NaCl or KCl at pH = 7.5 unless otherwise specified. The formation of the G-quadruplex was carried out by incubating for 6 min the oligonucleotide solution at 90 °C and slowly cooling down (~5 h) to room temperature in order to obtain the thermodynamically equilibrated G-quadruplex structures [13]. Solutions were then stored at 4 °C overnight to avoid degradation processes and afterwards allow reaching room temperature prior to carry out the measurements. The concentration of the single stranded oligonucleotide was determined by measuring at 90 °C the absorbance at 260 nm using the absorptivity value of  $228,500 \text{ M}^{-1} \text{ cm}^{-1}$  provided by the supplier. The double-labeled oligonucleotide FAM-Tel22-TAMRA (F-Tel22-T) was purchased from Thermo Fisher Scientific Inc. TMPyP4 was supplied by Sigma Aldrich. Stock aliquots of TMPyP4 were prepared in water and stored in the dark at –20 °C.

### 2.2. UV spectroscopy

Spectrophotometric measurements were performed with a HP 8453A photodiode array spectrophotometer (Agilent Technologies, Palo Alto, CA) endowed with a temperature control Peltier system. Titrations were carried out by adding increasing amounts of Tel22 solutions to the TMPyP4 solution in 1 cm path-length cells with black quartz sides at 25 °C. The data were corrected by the dilution factor  $C_D/C_P$

$C_D$ .

### 2.3. ITC titrations

Isothermal titration calorimetry (ITC) experiments were performed at 25 °C using a Nano ITC (TA Instruments, Newcastle, USA). The stirring speed was maintained constant at 250 rpm. The TMPyP4 solution was injected into the calorimetric cell containing the Tel22 solution. Prior to use, all solutions were degassed to reduce to a minimum the formation of bubbles during the experiments. Control experiments were carried out to determine the contribution of the heat of dilution of TMPyP4 and rule out the presence of aggregation processes of the drug that would interfere with the analysis of the ITC data to obtain the TMPyP4/Tel22 thermodynamic parameters. The thermograms (integrated area of the peak/mole of injectant versus  $C_D/C_P$  ratio) obtained in the titrations were fitted by a “two-site model”, as simpler models including the “one-site model” were insufficient to fit the data suitably.

### 2.4. FRET melting assay

F-Tel22-T was dissolved in water as 100 μM stock solutions and then annealed for 5 min at 0.4 μM concentration at  $T = 90$  °C in a buffer containing 0.15 M KCl or NaCl, 10 mM Tris-HCl and 1 mM EDTA at pH = 7.5. Each well of a 96-well plate contained 0.2 μM of F-Tel22-T and different concentrations of TMPyP4. Measurements were performed in a 7500 Real-Time PCR (Applied Biosystems). Readings were performed with excitation at 450–495 nm and detection at 515–545 nm from 25 to 95 °C at a scan rate of 0.5 °C/min.

### 2.5. Time-resolved fluorescence lifetime

Fluorescence lifetime measurements of TMPyP4 were performed both in the absence and in the presence of different amounts of Tel22 in  $\text{Na}^+$  or  $\text{K}^+$  buffer using FLS980 equipment (Edinburg Instruments). The excitation was accomplished at 405 nm using an EPL 405 pulsed diode laser and the emission was collected at 705 nm. Data were analyzed by FAST 3.4.0 software.

### 2.6. T-Jump measurements

The fast kinetic measurements were performed with a Dialog T-jump instrument built up according to the Riegler et al. prototype [25] in 1.0 cm path-length cells, working in the absorbance mode. The kinetic curves, collected with an Agilent 54622A oscilloscope (Santa Clara, CA, USA), were transferred to a PC and evaluated with the Table Curve program of the Jandel Scientific package (AISN software, Richmond, CA, USA). The time constants were averaged out from 6-fold repeated kinetic experiments.

### 2.7. Molecular dynamics

The structures of the Tel22 G-quadruplex in  $\text{K}^+$  solution were taken from the *Protein Data Bank*, with PDB id “2HY9” for hybrid-1, F1K, and PDB id “2JPZ” for hybrid-2, F2K [26]. In detail, the first and last two nucleotides of the G-quadruplex chain of the two PDB id files, both 26-mer hybrids, have been removed to generate the same Tel22 sequence of the experimental studies. The starting molecular structure of TMPyP4 was obtained by full geometry optimization, firstly through semiempirical PM6 calculations [27] and, subsequently, through DFT calculations, using the M06-2X functional [28] in the presence of water as implicit solvent, mimicked by the “conductor-like polarized continuum model” implicit method [29,30]. Atomic partial charges of TMPyP4 were obtained by DFT calculations and force field parameters of TMPyP4 and DNA models were generated with the ACPYPE software (AnteChamber Python Parser interface) [31,32]. The Amber99SB force field ParmBSC0 nucleic acid torsion parameters were used for the DNA



models [33]. A triclinic box of TIP3P water was generated around the G-quadruplex/TMPyP4 system, to a 0.8 nm depth on each side of the solutes, for a total of about 5500 solvent molecules; 39 K<sup>+</sup> ions and 17 Cl<sup>-</sup> ions were added to neutralize the DNA negative charge of the sugar-phosphate backbone and to set the solution ionic strength to about 0.15 M.

Explicit solvent molecular dynamics (MD) simulations for F1K/TMPyP4 and F2K/TMPyP4 systems were performed using the Gromacs 5.0.4 software package, [34,35] in the canonical NPT ensemble (for which number of particles, N, pressure, P, and temperature, T, are constant), at 300 K, under control of a velocity-rescaling thermostat [36]. The mesh particle Ewald method was used to describe long-range interactions [37]. Preliminary energy minimizations were run for 5000 steps with the steepest descent algorithm, during which the equilibration of the G-quadruplex/TMPyP4 systems were harmonically restrained with a force constant of 1000 kJ mol<sup>-1</sup> nm<sup>-2</sup>, gradually relaxed in five consecutive steps of 100 ps each, to 500, 200, 100 and 50 kJ mol<sup>-1</sup> nm<sup>-2</sup>. Four MD simulations with different initial poses of TMPyP4 (see Figure 4S) were initially conducted for 100 ns for the binding of TMPyP4 with each DNA hybrid. The starting structures were obtained by the Maestro software [Maestro, version 10.2, Schrödinger, LLC, New York, NY, 2015]. Two final MD simulations were conducted for 300 ns and 200 ns, for the TMPyP4/F1K and TMPyP4/F2K systems, respectively.

### 3. Results and discussion

UV-vis and ITC measurements were carried out to set the most adequate concentration range to conduct the kinetic study. Same experiments were performed in Na<sup>+</sup> and K<sup>+</sup> media to gather information about the similarities and differences of the studied system in the presence of these representative ions.

#### 3.1. Isothermal titration calorimetry

ITC titrations of Tel22 (P) with increasing amounts of TMPyP4 (D) in 0.15 M NaCl and 0.15 M KCl were carried out. The profile of the titration isotherms (Fig. 1) shows two well differentiated steps. A general mechanism for this behaviour is represented in Eqs. (1) and (2). For low C<sub>D</sub>/C<sub>P</sub> concentration ratios, the complex PD<sub>1</sub> gets formed (Eq. (1)). As to the second process, PD<sub>2</sub> gets formed from PD<sub>1</sub> when the C<sub>D</sub>/C<sub>P</sub>

ratio increases (Eq. (2)), and is probably related to formation of external aggregates when the TMPyP4 concentration is raised.



The “two-site model” best fitted the experimental data, and the thermodynamic parameters obtained are listed in Table 1. The thermodynamic constant, K<sub>1</sub>, for formation of PD<sub>1</sub> in the presence of K<sup>+</sup> was one order higher compared to Na<sup>+</sup>, whereas with K<sub>2</sub> the opposite effect occurs. The reaction enthalpies were always negative. ΔH<sub>1</sub> varied with the type of buffer used, ΔH<sub>1</sub> (Na<sup>+</sup>) < ΔH<sub>1</sub> (K<sup>+</sup>), whereas ΔS<sub>1</sub> (Na<sup>+</sup>) < 0 and ΔS<sub>1</sub> (K<sup>+</sup>) > 0, indicating different hydration extent of the Tel22 conformations in Na<sup>+</sup> and K<sup>+</sup> buffers [38]. The ΔH<sub>2</sub> values remained nearly constant, whereas for the reaction entropy ΔS<sub>2</sub> (Na<sup>+</sup>) > ΔS<sub>2</sub> (K<sup>+</sup>) > 0, an effect attributed to dehydration of PD<sub>1</sub> to yield PD<sub>2</sub>, in good agreement with formation of an external complex. The K<sub>1</sub> and K<sub>2</sub> values concur with those reported before in KCl buffer for the interaction of TMPyP4 and different types of human telomeric G-quadruplexes [24,39].

#### 3.2. Spectrophotometric titration

The two differentiated processes observed with ITC measurements were also observed by spectrophotometric titrations of the Tel22/TMPyP4 system in 0.15 M NaCl (Fig. 2A) and 0.15 M KCl (Fig. 1SIA). The spectral curves recorded upon addition of increasing amounts of Tel22 to a TMPyP4 solution displayed a biphasic isotherm at λ = 433 nm with minimum at C<sub>D</sub>/C<sub>P</sub> = 0.5 (Fig. 2A, inset). An isosbestic point at λ = 429 nm with pronounced bathochromic shift of the maximum is observed for low TMPyP4 concentration (C<sub>D</sub>/C<sub>P</sub> < 2) (Fig. 2B), whereas for C<sub>D</sub>/C<sub>P</sub> > 2 a new isosbestic point at λ = 437 nm appears and the location of the maximum remains unaltered (Fig. 2C). This behaviour points to the existence of different types of Tel22/TMPyP4 complexes depending on the C<sub>D</sub>/C<sub>P</sub> concentration ratio, concurrent with the ITC results and with the scheme shown in Eqs. (1) and (2).

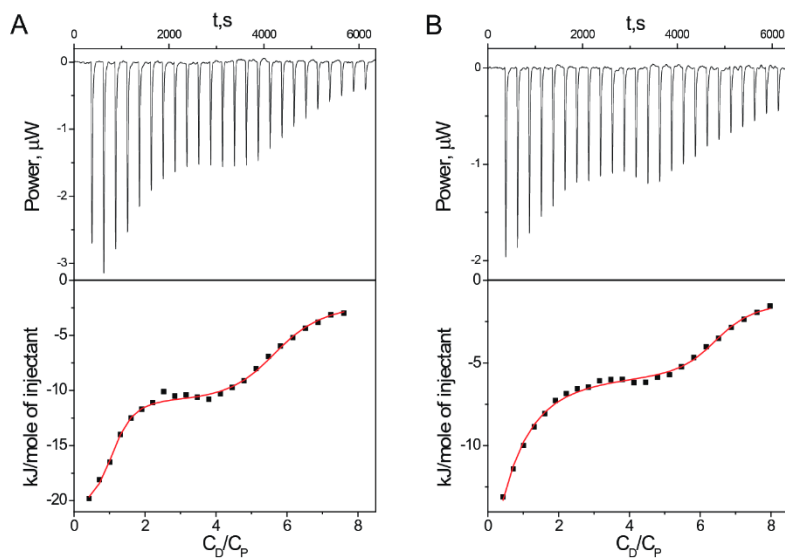


Fig. 1. ITC titrations of Tel22 with TMPyP4 in 0.15 M NaCl (A) and 0.15 M KCl (B). C<sub>P</sub><sup>0</sup> = 0.065 mM, C<sub>D</sub><sup>0</sup> = 1.7 mM, pH = 7.5 (10 mM Tris-HCl, 1 mM EDTA), T = 25 °C.

**Table 1**

Thermodynamic parameters determined for the binding of TMPyP4 to Tel22 using a “two-site model”.  $K_1$  and  $K_2$  are the thermodynamic constants and  $\Delta H_1$  and  $\Delta H_2$  the enthalpy change for the processes in Eqs. (1) and (2).

	$10^{-5} K_1, M^{-1}$	$\Delta H_1, kJ mol^{-1}$	$10^{-5} K_2, M^{-1}$	$\Delta H_2, kJ mol^{-1}$
Tel22/TMPyP4 <sup>a</sup>	$1.6 \pm 0.6$	$-45 \pm 2$	$70 \pm 30$	$-21 \pm 2$
Tel22/TMPyP4 <sup>b</sup>	$25 \pm 7$	$-15 \pm 1$	$3.5 \pm 0.9$	$-27 \pm 1$

<sup>a</sup> 0.15 M NaCl.

<sup>b</sup> 0.15 M KCl.

### 3.3. FRET melting measurements

A number of secondary structures, such as different G-quadruplex conformations, i-motifs and triplexes, can be present in solution for Tel22 and other important G-quadruplex sequences [11,40]. TMPyP4 promotes a notable increase in the melting temperature of G-quadruplex DNA structures [41]. Förster resonance energy transfer (FRET) melting experiments were carried out to obtain information about the main features of the Tel22/TMPyP4 interaction. Tel22 become stabilized upon binding with TMPyP4 both in  $Na^+$  and  $K^+$  buffers. Fig. 3A and B show the normalized FRET melting curves, whereas Fig. 3C and D show the  $T_m$  values determined in the mid-transition ( $T_{1/2}$ ) for each  $C_D/C_P$  ratio. In the presence of TMPyP4, the  $\Delta T_m$  value obtained for the dual fluorescently labeled (FAM and TAMRA) Tel22 oligonucleotide in the presence of  $Na^+$  is equal to or greater than in the presence of  $K^+$  for the same  $\Delta(C_D/C_P)$ , which reveals the influence of the ligand on the stabilization of different G-quadruplex Tel22 structures.

### 3.4. Time-resolved fluorescence lifetime measurements

Fluorescence lifetime measurements have been widely used to study the existence and main features of ligand/G-quadruplex complexes

[42]. The emission properties of the Tel22/TMPyP4 system were determined at different  $C_D/C_P$  ratios (Fig. 2SI). A monoexponential decay fitting was applied for free TMPyP4, whereas a biexponential fitting was needed to obtain acceptable  $\chi^2$  values when Tel22 is present. The  $\tau_1$  values were quite close to those of TMPyP4 alone, whereas the  $\tau_2$  values correspond to PD<sub>1</sub> (Table S11). By means of this technique it was unfeasible to differentiate between different hybrid/TMPyP4 complexes, probably due to the close fluorescence lifetime values ascribable to their similar structure.

### 3.5. Kinetic T-Jump measurements

Thermodynamic data is valuable material to assess the final state of interacting systems, even though they cannot provide detailed mechanistic information. We studied the kinetic features of the Tel22/TMPyP4 interaction with the T-Jump technique in the microsecond time scale to verify if the presence of the two different G-quadruplex conformations, F1M and F2M, entail any significance on the way the ligands do interact with Tel22 in the presence of  $Na^+$  and  $K^+$ . To this aim, T-Jump measurements were performed for  $C_D/C_P$  ratio  $< 2$ , where PD<sub>1</sub> (Eq. (1)) prevails. Kinetic measurements monitoring the absorbance were carried out at two different wavelengths, one at each

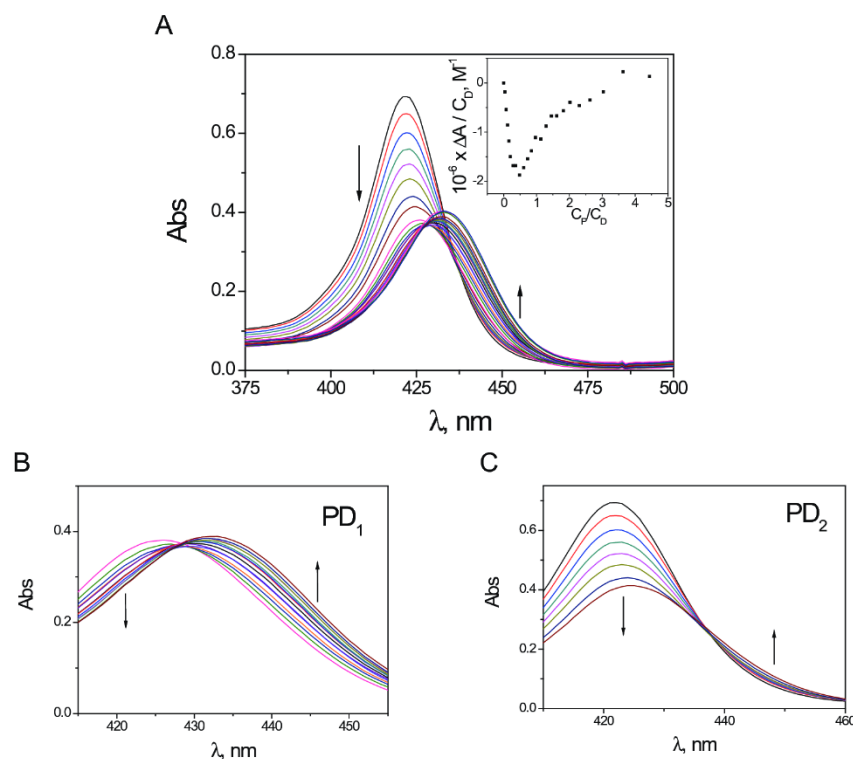


**Fig. 2.** Absorption spectra obtained from the titration of the TMPyP4/Tel22 system in 0.15 M NaCl. Inset: Binding isotherm at 433 nm (A). The spectral curves of Fig. 2A show two differentiated behaviours with two different isosbestic points at  $C_D/C_P < 2$  (B) and at  $C_D/C_P > 2$  (C).  $C_D^0 = 3.5 \mu M$ , pH = 7.5 (10 mM Tris-HCl, 1 mM EDTA),  $T = 25^\circ C$ .

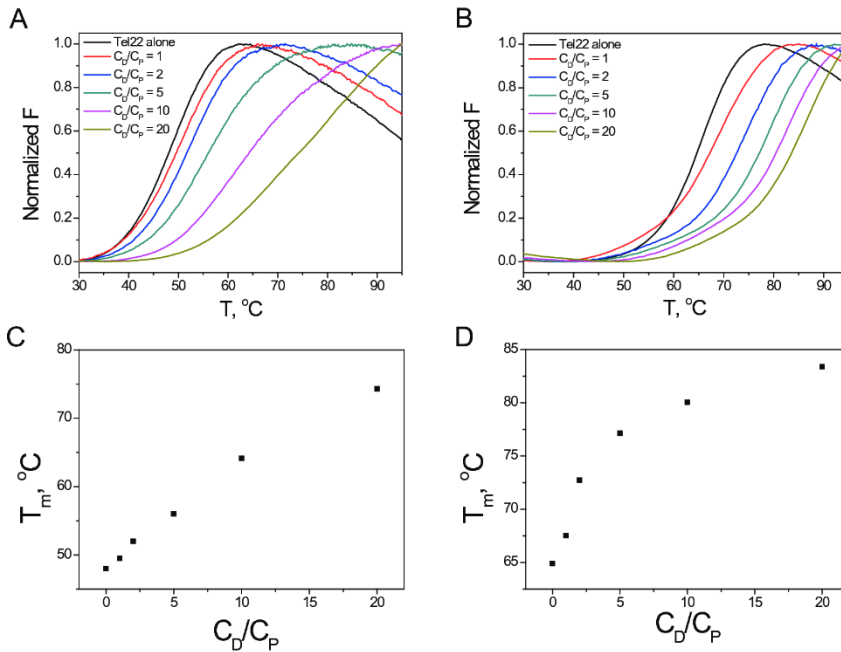


**Fig. 3.** FRET melting curves obtained for the TMPyP4/Tel22 system in 0.15 M NaCl (A) and in 0.15 M KCl (B) at different  $C_D/C_P$  ratios. Representation of the melting temperature ( $T_m$ ) versus the  $C_D/C_P$  ratio in NaCl (C) and in KCl (D).  $C_P = 0.2 \mu\text{M}$ , pH = 7.5 (10 mM Tris-HCl, 1 mM EDTA).

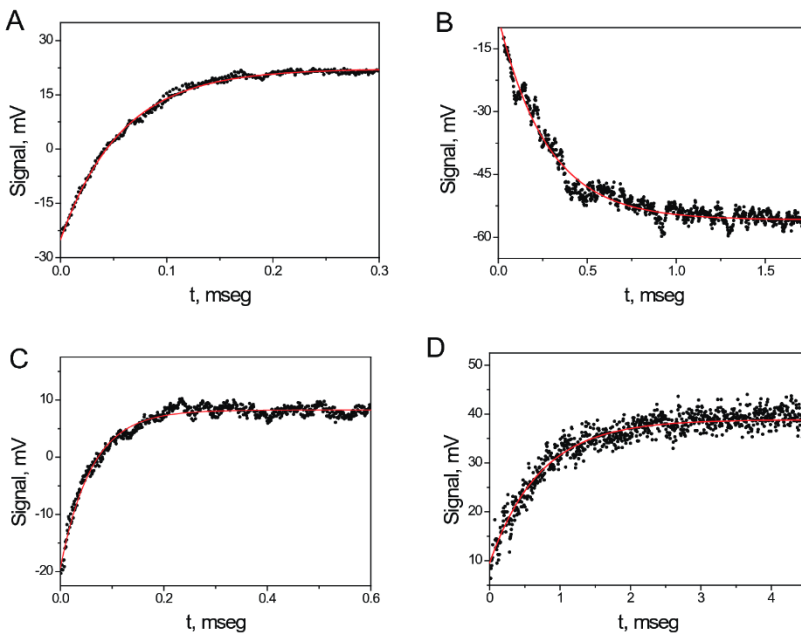


**Fig. 4.** Examples of kinetic curves obtained for the Tel22/TMPyP4 system in 0.15 M NaCl at  $\lambda = 437 \text{ nm}$  (A) and  $\lambda = 422 \text{ nm}$  (B) and in 0.15 M KCl at  $\lambda = 437 \text{ nm}$  (C) and  $\lambda = 422 \text{ nm}$  (D).  $C_D = 3.5\text{--}15 \mu\text{M}$ ,  $C_P = 6\text{--}20 \mu\text{M}$ . pH = 7.5 (10 mM Tris-HCl, 1 mM EDTA),  $T = 25^\circ\text{C}$ .

side of the 429 nm isosbestic point. Fig. 4 collects examples of kinetic curves for the Tel22/TMPyP4 system in  $\text{Na}^+$  and in  $\text{K}^+$ , recorded at 422 nm and 437 nm (see Figs. 2B and 1SIB). Single exponential functions were fitted to the experimental data (red line), from which the reciprocal relaxation time  $1/\tau$  was obtained. Interestingly, the kinetics observed with equal concentration of Tel22 and TMPyP4 and same type of ion, showed that two reactions with quite different kinetic behaviour are at work. The faster reaction, which lasts  $< 1 \text{ ms}$ , could be observed

at  $\lambda = 437 \text{ nm}$  for both  $\text{Na}^+$  and  $\text{K}^+$  buffers (Fig. 4A and C, respectively), whereas the slower reaction can be followed at  $\lambda = 422 \text{ nm}$  (Fig. 4B and D).

To obtain the forward and reverse kinetic constants of the four processes, plots of the reciprocal relaxation time ( $1/\tau$ ) versus the equilibrium concentration function ( $[P] + [D]$ ) (Fig. 5) were fitted according to Eq. (3):

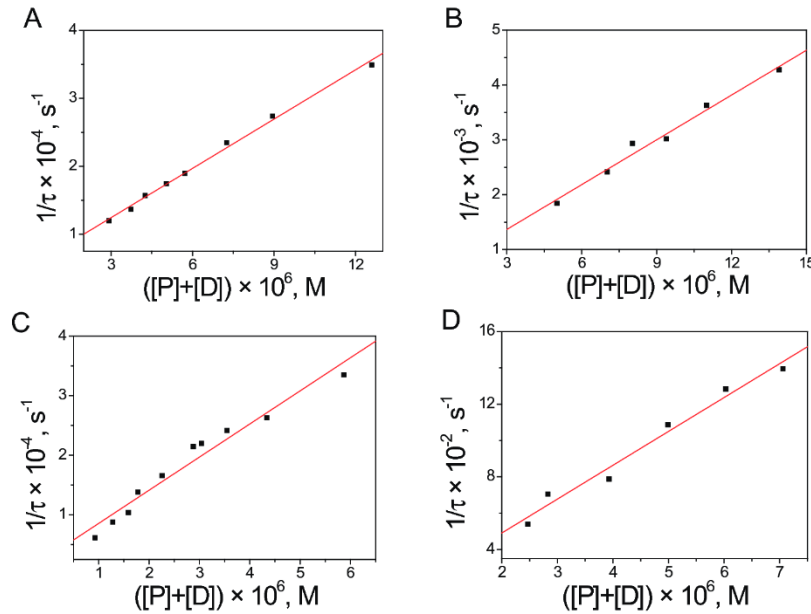


**Fig. 5.**  $(1/\tau)$  versus  $([P] + [D])$  plot and fitting of Eq. (3) to the data obtained for the Tel22/TMPyP4 system in 0.15 M NaCl at (A)  $\lambda = 437$  nm, and (B)  $\lambda = 422$  nm and in 0.15 M KCl at (C)  $\lambda = 437$  nm and (D)  $\lambda = 422$  nm.

$$\frac{1}{\tau} = k_f \cdot ([P] + [D]) + k_d \quad (3)$$

where  $k_f$  and  $k_d$  represent the formation and dissociation rate constants between Tel22 and TMPyP4 obtained at a specific wavelength.

Table 2 lists the rate constants together with the kinetic equilibrium constant,  $K_1$ , obtained from the ratio of the forward over the reverse kinetic constant ( $k_{f,i}/k_{d,i}$ ). The kinetic constants  $k_{f,2}$  and  $k_{d,2}$  obtained at 437 nm were one order higher than  $k_{f,1}$  and  $k_{d,1}$  obtained at 422 nm both in NaCl and KCl, whereas the thermodynamic value  $K_1$  obtained at the two wavelengths are quite close for a particular buffer, being  $K_1 \sim 4 \times 10^5 \text{ M}^{-1}$  and  $2 \times 10^6 \text{ M}^{-1}$  in the presence of  $\text{Na}^+$  and  $\text{K}^+$  ions, respectively. This means that, although the two processes observed in the presence of each of the ions display well-differentiated kinetic behaviour, the overall thermodynamic equilibrium constant remains virtually unaffected. The binding constants concur fairly well with the  $K_1$  value obtained from the ITC measurements in Table 1 for formation of PD<sub>1</sub> (Eq. (1)).

In conclusion, P in Eq. (1) is the sum (F1M + F2M) and PD<sub>1</sub> is the sum (F1M/TMPyP4 + F2M/TMPyP4) in the presence of each M =  $\text{Na}^+$  or  $\text{K}^+$  ions. Therefore, the equilibrium in Eq. (1) can be split into Eq. (4) and Eq. (5),  $k_{f,i}$  and  $k_{d,i}$  being the kinetic constants (Table 1)

corresponding to two different conformations. However, so far the experimental results are insufficient to unambiguously assign the Tel22 conformation and the kinetic constants. This difficulty will be overcome below by means of the MD simulations.



Several other possible mechanisms could describe the kinetic data in terms of induced-fit and/or conformational selection pathways. However, on one side the existence of two hybrid forms in  $\text{K}^+$  buffer (F1K and F2K) has been described amply (See, for instance, refs [10] and [11] and references therein), providing useful hints about the types of processes observed. On the other hand, if, together with the formation of the TMPyP4/Tel22 complexes, there would exist other T-jump processes, then some other complex reactions should be observed, prone to fitting with multiexponential functions. However, as a matter of fact single exponential functions sufficed to fit absolutely all the T-jump kinetic curves, which indicate that, under the different conditions studied, only a single kinetic process in the T-Jump time scale is at work. Likewise, the good linearity fulfilled by the different instances shown in Fig. 5 reveals independent reactions from one another in every case.

To analyze the formation of PD<sub>2</sub> (Eq. (2)), a number of T-Jump experiments were conducted in the concentrated region,  $C_D/C_P \geq 2$ , at different wavelengths around 422 nm, but no signals could be recorded, probably because the reaction is too fast to be observed by T-jump, which is compatible with the binding of additional TMPyP4 molecules to PD<sub>1</sub> to build the external complex PD<sub>2</sub>.

As to the type of interaction of TMPyP4 with G quadruplex, different modes of binding have been proposed, including intercalation of the ligand between adjacent G-quartets, end-stacking on the external G-tetrads and groove-binding with external loops [20,22,43]. On one hand, the rather high  $k_d$  values obtained by T-jump measurements (Table 2) appear to be incompatible with intercalation of TMPyP4 into the G-tetrads, as the residence time is too short compared to other processes involving this mode of binding [44]. On the other hand, the

**Table 2**  
Kinetic ( $k_{f,i}$  and  $k_{d,i}$ ) and thermodynamic ( $K_1 = k_{f,i}/k_{d,i}$ ) constants of the equilibrium represented in Eqs. (4) and (5) for the Tel22/TMPyP4 system at low TMPyP4 concentration ( $C_D/C_P < 2$ ).

	$10^{-8} k_{f,i}$ , $\text{M}^{-1} \text{s}^{-1}$	$10^{-2} k_{d,i}$ , $\text{s}^{-1}$	$10^{-5} K_1$ , $\text{M}^{-1}$
F1Na/TMPyP4 (0.15 M NaCl) <sup>a</sup>	$2.5 \pm 0.2$	$5.5 \pm 0.2$	$4.5 \pm 0.2$
F2Na/TMPyP4 (0.15 M NaCl) <sup>b</sup>	$24.2 \pm 0.6$	$52 \pm 4$	$4.7 \pm 2$
F1K/TMPyP4 (0.15 M KCl) <sup>a</sup>	$1.9 \pm 0.1$	$1.2 \pm 0.7$	$16 \pm 1$
F2K/TMPyP4 (0.15 M KCl) <sup>b</sup>	$56 \pm 4$	$30 \pm 10$	$19 \pm 7$

<sup>a</sup>  $\lambda = 422$  nm.

<sup>b</sup>  $\lambda = 437$  nm.



pronounced red shift observed (Figs. 2B and 1S1B) indicates that PD<sub>1</sub> involves stacking between TMPyP4 and Tel22. This shift has been attributed to end-stacking of TMPyP4 on the external G-tetrads of the G-quadruplex [22,39]. However, the X-ray structure reported by Neidle et al. for human telomeric G-quadruplex/TMPyP4 complex has shown that TMPyP4 failed to directly interact with the external G-tetrad due to steric clashes between the G-tetrad edges and the *N*-methylpyridyl groups of TMPyP4 [21]. Instead, TMPyP4 established  $\pi$ - $\pi$  interactions with external bases and electrostatic interactions between the cationic *N*-methylpyridyl groups and the phosphate ions of the telomeric DNA. Hence, MD simulations were carried out to shed light both on i) the distinct experimental kinetic behaviour observed as a consequence of the interaction of TMPyP4 with the two G-quadruplex conformations of Tel22, and ii) on the nature of its mode of binding.

### 3.6. MD simulations

The T-jump technique demonstrated quantitatively that the rates of formation of F1M/TMPyP4 and F2M/TMPyP4 were different, but it is unable to differentiate which of the two complexes gets formed faster. Moreover, the structural difference between F1M and F2M provides a convincing explanation for the different reaction rates which, notwithstanding, does not alter the affinity for TMPyP4, thus presenting very similar values of the affinity constants  $K_1$ . To discern this issue, explain the reasons for such a difference and shed some light into the binding features of the Tel22/TMPyP4 system, MD simulations were carried out using the well-characterized hybrid Tel22 conformations in  $K^+$ . These two conformations display quite similar structure containing the same type and number of loops (one reversal and two lateral loops), but their arrangement is actually different. In the hybrid-1 (F1K), the 5' loop is in the reversed configuration, whereas in the hybrid-2 (F2K) the 3' loop is the one in the reversed configuration, as represented in Scheme 1 [40]. Fig. 3S1 shows the optimized structure of TMPyP4, where the central aromatic moiety remains planar, while the methylpyridine groups can rotate nearly perpendicular to the molecular plane. The Root-Mean-Square Deviation (RMSD) plot, red line in Fig. 6, and the atom-atom distance between TMPyP4 and a selected nucleotide, blue line in Fig. 6, both enable one to follow the host-guest binding process occurring along the MD trajectory, where important conformational changes occur before and at the equilibrium phase. Different intermediate structures of the F1K/TMPyP4 and F2K/TMPyP4 complexes, occurring along the MD simulation are also shown (Fig. 6A and B), and describe the molecular recognition process until the

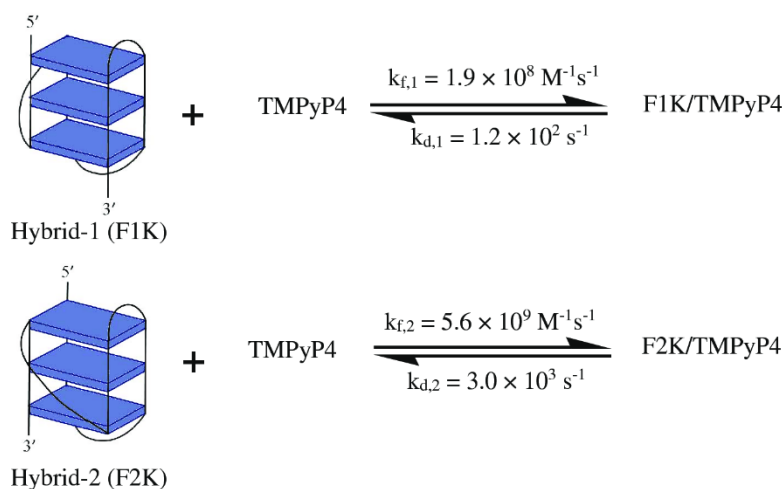
equilibrium (plateau) is reached. In particular, the distance between one of the four pyrrole nitrogen atoms of TMPyP4 and one atom of the external bases, thymine O1 for F1K and adenine N1 for F2K, reveals that the final stacking distance between TMPyP4 and both DNA hybrids oscillates around 4 Å when the equilibrium phase has been reached. The initial and final position of TMPyP4 (gray) is shown in Fig. 7 (see also Fig. 4S1 for all considered starting positions). It can be observed that TMPyP4 binds to the nucleic acid through  $\pi$ - $\pi$  stacking interactions with a nitrogen base in the groove (thymine in F1K and adenine in F2K). In addition, the methylpyridyl groups, positively charged, remain oriented towards the negatively charged phosphate groups of the G-quadruplex chain.

The analysis of the experimental data demonstrates that the thermodynamics of the binding of TMPyP4 to F1K and F2K are similar, as indicated by the very close values of the thermodynamic constant,  $K_1 = k_f/k_d$ , of the equilibria represented in Eqs. (4) and (5). The results of the MD simulations provide a plausible explanation for such phenomena, as the binding mode and the final structure of the F1K/TMPyP4 complex and those of the F2K/TMPyP4 complex are closely akin (Fig. 7), which render them thermodynamically indistinguishable.

On the other hand, the values of the kinetic constants  $k_f$  and  $k_d$  indicate that one of the two binding processes is faster by one order of magnitude than the other (Table 2). Interestingly, remarkable differences were found in the molecular recognition process along the MD trajectory. In fact, Fig. 8 reveals that TMPyP4 binds rapidly to an adenine residue (highlighted green) in both hybrids, F1K and F2K, at roughly 2.5 ns. However, in the F2K/TMPyP4 system the binding to the adenine base persists up to the end of the simulation (Fig. 8A), so the equilibrium is attained faster. By contrast, an important change in the position of the ligand is observed at 101 ns for the F1K/TMPyP4 system (Fig. 8B). In particular, it is released from the binding site at the adenine base and binds to a thymine residue (highlighted yellow), finally reaching an equilibrium state. In our opinion, this difference can be related to the slower kinetics of binding experimentally observed by T-jump for one of the two hybrids.

In summary, the pathway observed during the molecular recognition process points to a difference in the time needed to reach the equilibrium structure for the F1K/TMPyP4 and F2K/TMPyP4 complexes. As  $k_f$  and  $k_d$  are directly related to the reciprocal time of formation and dissociation of the F1K/TMPyP4 and F2K/TMPyP4 complexes, the MD simulation results are in fairly good agreement with the two different experimental values observed for  $k_{f,i}$  and  $k_{d,i}$ .

It also allows one to assess that, in the case of Tel22 in  $K^+$ , the faster



**Scheme 1.** Schematic representation of the kinetic behaviour of the Tel22/TMPyP4 system in  $K^+$ .



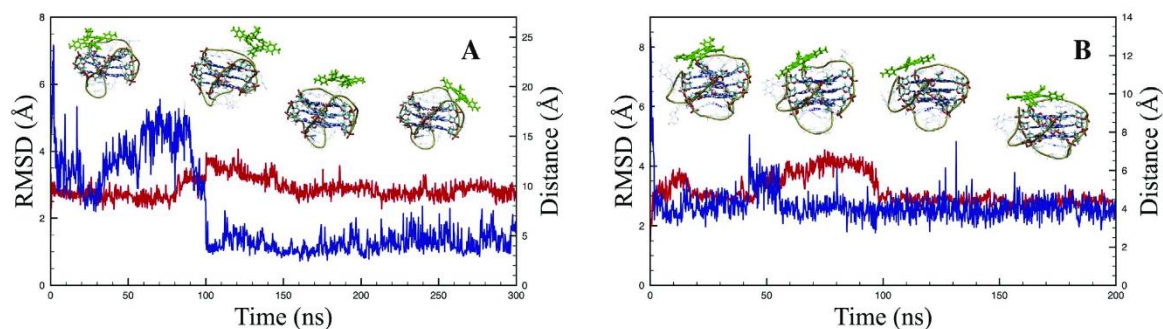


Fig. 6. RMSD plot (red) and specific distance between one of the four pyrrole nitrogen atoms of TMPyP4 and one atom of the binding base (blue) for the F1K/TMPyP4 (A) and the F2K/TMPyP4 system (B).

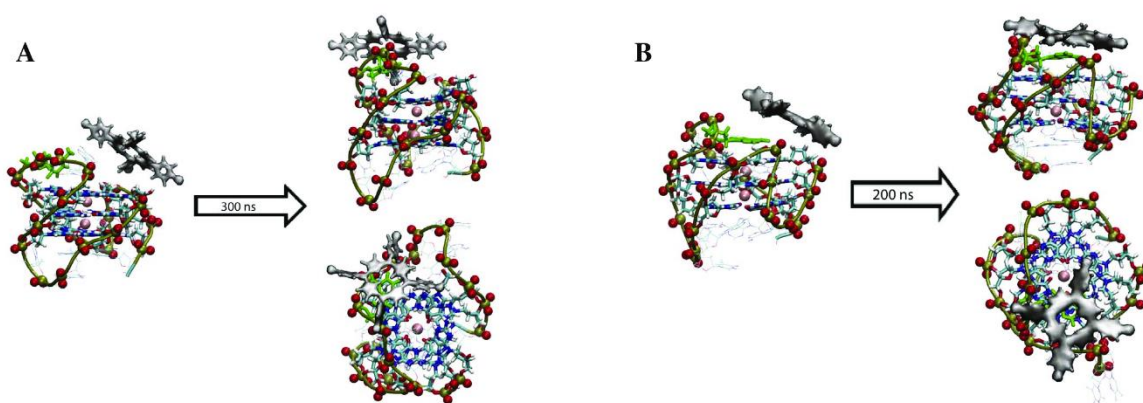


Fig. 7. Initial and final (top and side views) relative positions in the MD simulation of TMPyP4 (gray) and Tel22. Oxygen atoms in phosphate groups are represented as red balls; water and counterions have been removed. (A) Hybrid-1 F1K; the thymine base interacting with TMPyP4 is highlighted in green. (B) Hybrid-2 F2K; the adenine base interacting with TMPyP4 is highlighted in green.

kinetics involves the binding of TMPyP4 to the hybrid-2 form, F2K, whereas the slower kinetics is related to the binding of TMPyP4 to the hybrid-1 form, F1K. The  $k_{f,i}$  and  $k_{d,i}$  values of reactions 4 and 5 are defined and assigned in Scheme 1 for  $K^+$  buffer.

The possibility of building different conformations from the same

sequence is a complex issue that confers G-quadruplexes very interesting physical chemistry features. When the biological relevance of these conformations becomes well-known, we shall be aware of the importance conveyed by the fact that a ligand may stay more or less time bound to a particular G4 conformation. For example, in ligand/

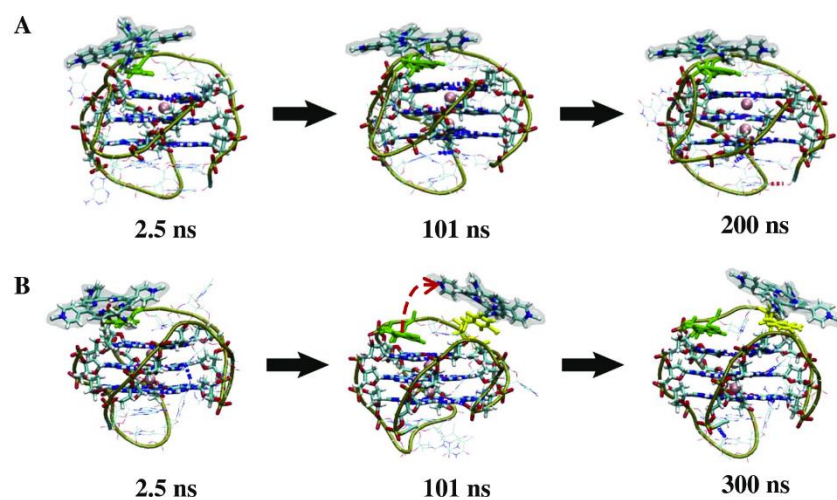


Fig. 8. Molecular recognition scheme during the MD simulation of the F2K/TMPyP4 system (A) and the F1K/TMPyP4 system (B).

DNA intercalation reactions, slow dissociation rates are viewed as an important criterion regarding their efficiency as cancer therapeutics, because such drugs remain longer in the intercalation position and are assumed to alter the DNA transcription [45].

#### 4. Conclusions

We have shown for the first time by experimental measurements and molecular modeling that a small ligand such as the cationic porphyrin TMPyP4 interacts in a distinct way with the two forms of G-quadruplex present in solution for the human telomeric sequence Tel22, both in Na<sup>+</sup> and K<sup>+</sup> buffers. In fact, for a particular buffer, under the same experimental conditions, two different sets of rate constants ( $k_f$  and  $k_d$ ) differing by one order of magnitude but yielding the same affinity constant  $K_1 = k_f/k_d$  were observed. MD simulations performed with the Tel22 structures in the presence of K<sup>+</sup> ions suggest that the hybrid-2 reaches the equilibrium with TMPyP4 faster than with hybrid-1. However, the structural difference between the two final equilibrium complexes is small, rendering the two types of Tel22/TMPyP4 complex thermodynamically indistinguishable and accounting for the only thermodynamic constant value obtained for  $K_1$ . Moreover, it provides convincing explanation for the observation that, although the coexistence of different conformations in solution has been probed for several G-quadruplex sequences, only kinetic techniques can fully characterize the binding mechanism of small ligands to the different structures when the final equilibrium states are nearly equivalent.

#### Conflict of interest

The authors have no conflict of interest to declare.

#### Transparency document

The Transparency document associated with this article can be found, in online version.

#### Acknowledgements

The research leading to these results has received funding from “la Caixa” Foundation (project OSLC-2012-007), MINECO, (CTQ2014-58812-C2-2-R) and Junta de Castilla y León, (BU042U16), FEDER Funds Spain, are gratefully acknowledged. C.P.-A. is grateful for the FPU grant from Ministry of Education, Culture and Sports, Spain (FPU13/00180).

#### Appendix A. Supplementary data

Supplementary data to this article can be found online at <https://doi.org/10.1016/j.bbagen.2017.10.020>.

#### References

- [1] D. Monchard, M.-P. Teulade-Fichou, A hitchhiker's guide to G-quadruplex ligands, *Org. Biomol. Chem.* 6 (2008) 627–636.
- [2] P. Murat, S. Balasubramanian, Existence and consequences of G-quadruplex structures in DNA, *Curr. Opin. Genet. Dev.* 25 (2014) 22–29.
- [3] V.S. Chambers, G. Marsico, J.M. Boutell, M. Di Antonio, G.P. Smith, S. Balasubramanian, High-throughput sequencing of DNA G-quadruplex structures in the human genome, *Nat. Biotechnol.* 33 (2015) 877–881.
- [4] A. Bedrat, J.-L. Mergny, L. Lacroix, Re-evaluation of G-quadruplex propensity with G4Hunter, *Nucleic Acids Res.* 44 (2016) 1746–1759.
- [5] S. Neidle, Human telomeric G-quadruplex: the current status of telomeric G-quadruplexes as therapeutic targets in human cancer, *FEBS J.* 277 (2010) 1118–1125.
- [6] H. Lodish, A. Berk, C.A. Kaiser, M. Krieger, M.P. Scott, A. Bretscher, H. Ploegh, P. Matsudaira, Intracellular ion environment and membrane electric potential, in: N.Y.W.H. Freeman (Ed.), 4th ed, Mol. Cell Biol. 2000.
- [7] A. Ambrus, D. Chen, J. Dai, T. Bialis, R.A. Jones, D. Yang, Human telomeric sequence forms a hybrid-type intramolecular G-quadruplex structure with mixed parallel/antiparallel strands in potassium solution, *Nucleic Acids Res.* 34 (2006) 2723–2735.
- [8] A.T. Phan, K.N. Luu, D.J. Patel, Different loop arrangements of intramolecular human telomeric (3 + 1) G-quadruplexes in K<sup>+</sup> solution, *Nucleic Acids Res.* 34 (2006) 5715–5719.
- [9] Y. Wang, D.J. Patel, Solution structure of the human telomeric repeat d[AG3(T2AG3)3]G-tetraplex, *Structure* 1 (1993) 263–282.
- [10] K.W. Lim, V.C.M. Ng, N. Martin-Pintado, B. Heddi, A.T. Phan, Structure of the human telomere in Na<sup>+</sup> solution: an antiparallel (2 + 2) G-quadruplex scaffold reveals additional diversity, *Nucleic Acids Res.* 41 (2013) 10556–10562.
- [11] C. Perez-Arnaiz, N. Busto, J.M. Leal, B. Garcia, New microsecond intramolecular reactions of human telomeric DNA in solution, *RSC Adv.* 6 (2016) 39204–39208.
- [12] M. Aznauryan, S. Sondergaard, S.L. Noer, B. Schiott, V. Birkedal, A direct view of the complex multi-pathway folding of telomeric G-quadruplexes, *Nucleic Acids Res.* 44 (2016) 11024–11032.
- [13] J. Palacky, M. Vorlickova, I. Kejnovska, P. Mojzes, Polymorphism of human telomeric quadruplex structure controlled by DNA concentration: a Raman study, *Nucleic Acids Res.* 41 (2013) 1005–1016.
- [14] J. Sponer, G. Bussi, P. Stadlbauer, P. Kuhrova, P. Banas, B. Islam, S. Haider, S. Neidle, M. Otyepka, Folding of guanine quadruplex molecules-funnel-like mechanism or kinetic partitioning? An overview from MD simulation studies, *Biochim. Biophys. Acta, Gen. Subj.* 1861 (2017) 1246–1263.
- [15] M. Boncina, G. Vesnaver, J.B. Chaires, J. Lah, Unraveling the thermodynamics of the folding and interconversion of human telomere G-quadruplexes, *Angew. Chem. Int. Ed.* 55 (2016) 10340–10344.
- [16] R.T. Wheelhouse, D. Sun, H. Han, F.X. Han, L.H. Hurley, Cationic porphyrins as telomerase inhibitors: the interaction of tetra(N-methyl-4-pyridyl)porphine with Quadruplex DNA, *J. Am. Chem. Soc.* 120 (1998) 3261–3262.
- [17] T.L. Ruan, S.J. Davis, B.M. Powell, C.P. Harbeck, J. Habdas, P. Habdas, L.A. Yatsunyk, Lowering the overall charge on TMPyP4 improves its selectivity for G-quadruplex DNA, *Biochimie* 132 (2017) 121–130.
- [18] A.J. Gaier, D.R. McMillin, Binding studies of G-Quadruplex DNA and porphyrins: Cu (T4) vs sterically friendly Cu(TD4), *Inorg. Chem.* 54 (2015) 4504–4511.
- [19] J.J. DuPont, K.L. Henderson, A. Metz, V.H. Le, J.P. Emerson, E.A. Lewis, Calorimetric and spectroscopic investigations of the binding of metallated porphyrins to G-quadruplex DNA, *Biochim. Biophys. Acta, Gen. Subj.* 1860 (2016) 902–909.
- [20] I. Haq, J.O. Trent, B.Z. Chowdhry, T.C. Jenkins, Intercalative G-Tetraplex stabilization of telomeric DNA by a cationic porphyrin, *J. Am. Chem. Soc.* 121 (1999) 1768–1779.
- [21] G.N. Parkinson, R. Ghosh, S. Neidle, Structural basis for binding of porphyrin to human telomeres, *Biochemistry* 46 (2007) 2390–2397.
- [22] C. Wei, G. Jia, J. Zhou, G. Han, C. Li, Evidence for the binding mode of porphyrins to G-quadruplex DNA, *Phys. Chem. Chem. Phys.* 11 (2009) 4025–4032.
- [23] M. Boncina, C. Podlipnik, I. Piantanida, J. Eilmes, M.-P. Teulade-Fichou, G. Vesnaver, J. Lah, Thermodynamic fingerprints of ligand binding to human telomeric G-quadruplexes, *Nucleic Acids Res.* 43 (2015) 10376–10386.
- [24] L. Martino, B. Pagano, I. Fotticchia, S. Neidle, C. Giancola, Shedding light on the interaction between TMPyP4 and human telomeric quadruplexes, *J. Phys. Chem. B* 113 (2009) 14779–14786.
- [25] R. Rigler, C.R. Rabl, T.M. Jovin, Temperature-jump apparatus for fluorescence measurements, *Rev. Sci. Instrum.* 45 (1974) 580–588.
- [26] J. Dai, C. PUNCHIHEWA, A. Ambrus, D. Chen, R.A. Jones, D. Yang, Structure of the intramolecular human telomeric G-quadruplex in potassium solution: a novel adenine triple formation, *Nucleic Acids Res.* 35 (2007) 2440–2450.
- [27] J.J.P. Stewart, Optimization of parameters for semiempirical methods V: modification of NDDO approximations and application to 70 elements, *J. Mol. Model.* 13 (2007) 1173–1213.
- [28] Y. Zhao, D.G. Truhlar, The M06 suite of density functionals for main group thermochemistry, thermochemical kinetics, noncovalent interactions, excited states, and transition elements: two new functionals and systematic testing of four M06-class functionals and 12 other function, *Theor. Chem. Accounts* 120 (2008) 215–241.
- [29] V. Barone, M. Cossi, Quantum calculation of molecular energies and energy gradients in solution by a conductor solvent model, *J. Phys. Chem. A* 102 (1998) 1995–2001.
- [30] M. Cossi, N. Rega, G. Scalmani, V. Barone, Energies, structures, and electronic properties of molecules in solution with the C-PCM solvation model, *J. Comput. Chem.* 24 (2003) 669–681.
- [31] J. Wang, R.M. Wolf, J.W. Caldwell, P.A. Kollman, D.A. Case, Development and testing of a general Amber force field, *J. Comput. Chem.* 25 (2004) 1157–1174.
- [32] J. Wang, W. Wang, P.A. Kollman, D.A. Case, Automatic atom type and bond type perception in molecular mechanical calculations, *J. Mol. Graph. Model.* 25 (2006) 247–260.
- [33] A.T. Guy, T.J. Piggot, S. Khalid, Single-stranded DNA within nanopores: conformational dynamics and implications for sequencing: a molecular dynamics simulation study, *Biophys. J.* 103 (2012) 1028–1036.
- [34] D. Van Der Spoel, E. Lindahl, B. Hess, G. Groenhof, A.E. Mark, H.J.C. Berendsen, GROMACS: fast, flexible, and free, *J. Comput. Chem.* 26 (2005) 1701–1718.
- [35] B. Hess, C. Kutzner, D. van der Spoel, E. Lindahl, GROMACS 4: algorithms for highly efficient, load-balanced, and scalable molecular simulation, *J. Chem. Theory Comput.* 4 (2008) 435–447.
- [36] G. Bussi, D. Donadio, M. Parrinello, Canonical sampling through velocity rescaling, *J. Chem. Phys.* 126 (2007) 014101/1–014101/7.
- [37] T. Darden, D. York, L. Pedersen, Particle mesh Ewald: an N-log(N) method for Ewald sums in large systems, *J. Chem. Phys.* 98 (1993) 10089–10092.
- [38] I. Jelesarov, H.R. Bosshard, Isothermal titration calorimetry and differential scanning calorimetry as complementary tools to investigate the energetics of

- biomolecular recognition, *J. Mol. Recognit.* 12 (1999) 3–18.
- [39] A. Arora, S. Maiti, Effect of loop orientation on quadruplex-TMPyP4 interaction, *J. Phys. Chem. B* 112 (2008) 8151–8159.
- [40] R.D. Gray, J.O. Trent, J.B. Chaires, Folding and unfolding pathways of the human telomeric G-quadruplex, *J. Mol. Biol.* 426 (2014) 1629–1650.
- [41] A. De Rache, J.-L. Mergny, Assessment of selectivity of G-quadruplex ligands via an optimised FRET melting assay, *Biochimie* 115 (2015) 194–202.
- [42] A. Spinello, G. Barone, J. Grunenberg, Molecular recognition of naphthalene diimide ligands by telomeric quadruplex-DNA: the importance of the protonation state and mediated hydrogen bonds, *Phys. Chem. Chem. Phys.* 18 (2016) 2871–2877.
- [43] C. Wei, G. Jia, J. Yuan, Z. Feng, C. Li, A spectroscopic study on the interactions of porphyrin with G-Quadruplex DNAs, *Biochemistry* 45 (2006) 6681–6691.
- [44] W.D. Wilson, C.R. Krishnamoorthy, Y.H. Wang, J.C. Smith, Mechanism of intercalation: ion effects on the equilibrium and kinetic constants for the interaction of propidium and ethidium with DNA, *Biopolymers* 24 (1985) 1941–1961.
- [45] A. Rhoden Smith, B.L. Iverson, Threading polyintercalators with extremely slow dissociation rates and extended DNA binding sites, *J. Am. Chem. Soc.* 135 (2013) 12783–12789.

# Kinetic evidence for interaction of TMPyP4 with two different G-quadruplex conformations of human telomeric DNA

Cristina Pérez-Arnaiz,<sup>a</sup> Natalia Busto,<sup>a</sup> Javier Santolaya,<sup>a,b</sup> José M. Leal,<sup>a</sup> Giampaolo Barone<sup>b\*</sup> and Begoña García<sup>a\*</sup>

## SUPPORTING INFORMATION

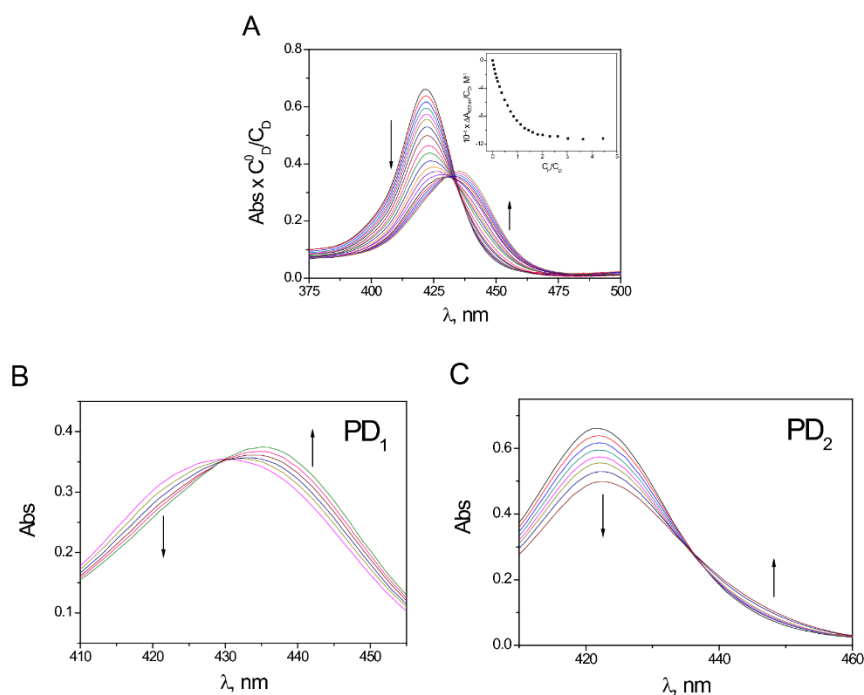


**Fig. 1S1.** Absorption spectra obtained from the titration of the TMPyP4/Tel22 system in 0.15 M KCl. Inset: Binding isotherm at 422 nm (A). The spectral curves of Fig. 1S1A show two different behaviours in diluted solution,  $C_D/C_P < 2$  (B) and in concentrated solution  $C_D/C_P > 2$  (C).  $C_D^0 = 3.5 \mu\text{M}$ , pH = 7.5 (10 mM Tris-HCl, 1 mM EDTA),  $T = 25^\circ\text{C}$ .

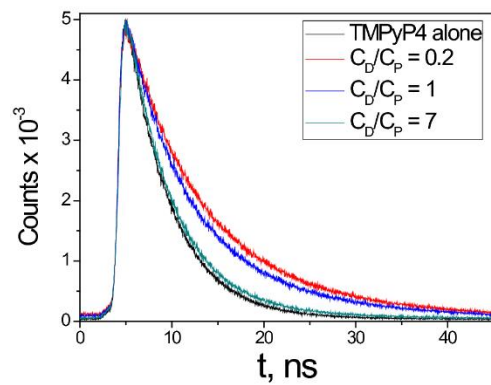


**Fig. 2SI.** Fluorescence lifetime decay for TMPyP4 ( $C_D = 3 \mu\text{M}$ ) in the presence of different concentrations of Tel22 in 0.15 M KCl using excitation at  $\lambda_{\text{exc}} = 405 \text{ nm}$  and emission at  $\lambda_{\text{em}} = 712 \text{ nm}$ . pH = 7.5 (10 mM Tris-HCl, 1 mM EDTA) and  $T = 25 \text{ }^\circ\text{C}$ .

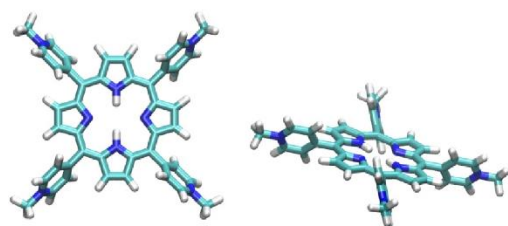


**Fig. 3SI.** Optimized structure of TMPyP4.



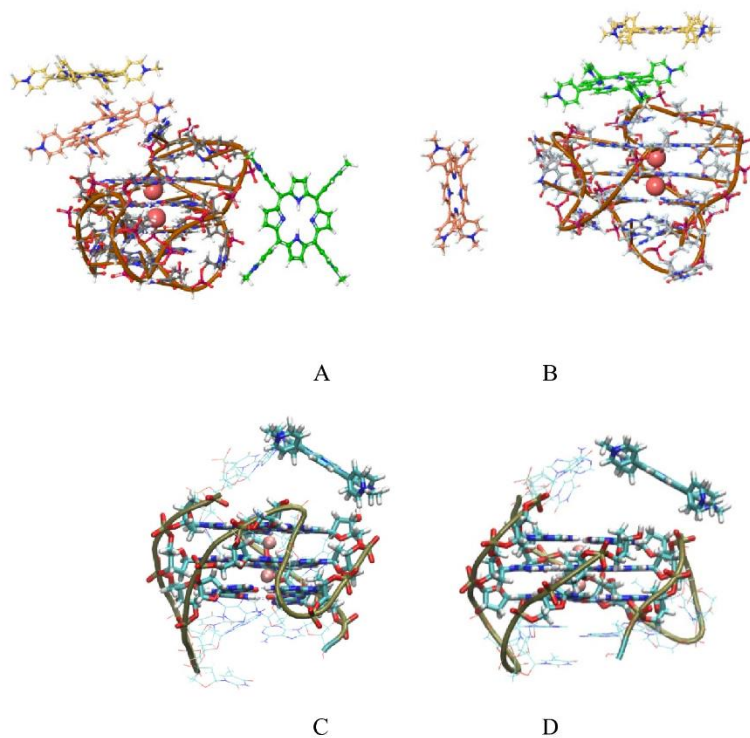


**Figure 4SI.** Initial relative positions for TMPyP4 and 2HY9 (F1K A) and 2JPZ (F2K B), opened F1K (C) and opened F2K (D)

**Table 1SI.** Fluorescence lifetime obtained for the Tel22/TMPyP4 system at different  $C_D/C_P$  ratios using  $\lambda_{exc} = 405$  nm and  $\lambda_{em} = 712$  nm.  $\tau_1$  and  $\tau_2$  stand for the lifetime of TMPyP4 and the Tel22/TMPyP4 complex (PD<sub>1</sub>), respectively.  $f_1$  and  $f_2$  stand for the fractional amplitudes.

$C_D/C_P$ ratio	$Na^+$					$K^+$				
	$\tau_1$ (ns)	$\tau_2$ (ns)	$f_1$ (%)	$f_2$ (%)	$\chi^2$	$\tau_1$ (ns)	$\tau_2$ (ns)	$f_1$ (%)	$f_2$ (%)	$\chi^2$
0	4.79	-	100	-	1.06	4.77	-	100	-	1.08
0.2	5.11	10.06	15.2	84.8	1.06	5.02	11.01	12.8	88.2	1.04
1	5.13	10.57	40.6	59.4	1.02	4.75	10.73	34.2	65.8	0.99
7	4.71	10.55	85.8	14.2	0.93	4.72	10.73	81.6	18.4	1.01

# **Chapter VII**

---

**Fishing for G-quadruplexes in solution with a perylene diimide derivative labeled with biotins**

## Summary

A new fluorescent perylene di-imide derivative with two biotins at the peri positions, called **PD12B**, has been synthesized by the group of our collaborator Dr. Torroba, Organic Chemistry, (University of Burgos, Spain). As reported in the present chapter, it has been experimentally shown that this structure selectively binds G-quadruplex structures. Thermodynamic parameters (such as the binding constant, as well as  $\Delta H$  and  $\Delta S$  values) of the binding of **PD12B** to Tell22 and Bom17 G-quadruplex, *PDB id: 2HY9*<sup>[133]</sup> and *1LYG*<sup>[135]</sup> respectively, were determined and reported. The aim of my contribution to this work was to provide, through MD simulations, an atomistic model in agreement with the experimental data concerning the binding mechanism of **PD12B** with both G-quadruplex conformations.

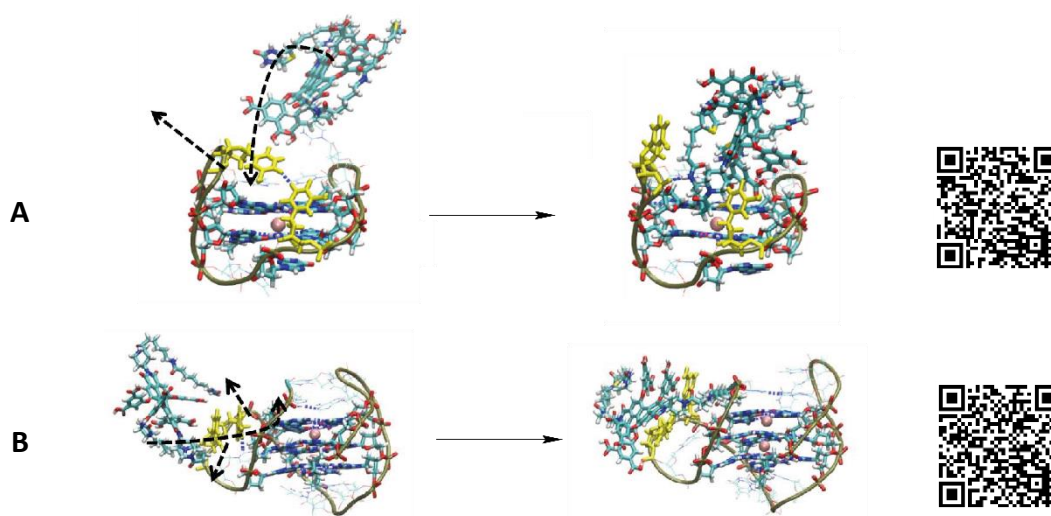


**Figure.1** Molecular recognition process, described as a host-guest interaction, proposed through MD simulations for both **PD12B/Bom17** (A) and **PD12B/Tell22** (B) systems. See QR codes.

The results obtained allowed us to conclude that for the **PD12B/Bom17** system, **Figure 1** (A), the binding can be described as a host-guest interaction, where **PD12B** is inserted into a DNA pocket of complementary shape, and the two structures are held together by non-covalent interactions, in particular hydrogen bonds and hydrophobic interactions. The corresponding video files are available as supplementary files, through the QR codes shown in **Figure 1**.

In a similar way, in the **PD12B/Tell22** system, **PD12B** is inserted into a molecular cleft formed during the MD simulation, leading to a host-guest interaction driven by the complementary shape of the drug and the DNA hosting site. The synthetic molecule binds to the DNA GGGTAA loop through  $\pi$ - $\pi$  stacking interactions between the 5-hydroxyisophthalic acid “bay group” and a thymine, and between the central aromatic



part of the organic molecule and an adenine base. The published article is attached below.

## G-Quadruplexes

## Fishing for G-Quadruplexes in Solution with a Perylene Diimide Derivative Labeled with Biotins

Natalia Busto,<sup>\*,[a]</sup> Patricia Calvo,<sup>[a]</sup> Javier Santolaya,<sup>[a, d]</sup> José M Leal,<sup>[a]</sup> Aurore Guédin,<sup>[b]</sup> Giampaolo Barone,<sup>[d]</sup> Tomás Torroba,<sup>[a]</sup> Jean-Louis Mergny,<sup>\*,[b, c]</sup> and Begoña García<sup>\*,[a]</sup>

**Abstract:** A new fluorescent, non-cytotoxic perylene diimide derivative with two biotins at the *peri* position, **PDI2B**, has been synthesized. This molecule is able to interact selectively with G-quadruplexes with scarce or no affinity towards single- or double-stranded DNA. These features have made it possible to design a simple, effective, safe, cheap, and selective method for fishing G-quadruplex structures in solution by use of **PDI2B** and streptavidin coated magnetic beads. The new cyclic method reported leads to the recovery of more than 80% of G-quadruplex structures from solution, even in the presence of an excess of single-stranded or duplex DNA as competitors. Moreover, **PDI2B** is a G4 ligand that can display higher thermal stabilization and greater affinity for 2- over 3-tetrad quadruplexes, which constitutes a novel type of behavior.

G-quadruplexes (G4s) are non-canonical secondary DNA or RNA structures formed by guanine-rich stretches. Four guanines can interact by Hoogsteen hydrogen bonds, forming a planar G-tetrad; two or more G-tetrads become stabilized by stacking interactions and by the presence of monovalent cations in the central channel.<sup>[1]</sup> The resulting folded structure is highly polymorphic.<sup>[2]</sup> The large number of potential G4 forming sequences spread throughout the genome<sup>[3]</sup> renders G4 an attractive research field, as these structures have been report-

ed to be involved in a wide range of biological processes such as telomere maintenance,<sup>[4]</sup> genome stability, regulation of oncogene expression, replication, translation, etc.<sup>[5]</sup> Therefore, the development of a new molecule capable of interacting with these structures and catching them selectively in solution could contribute significantly to achieve progress in the G4 research field.

Perylene diimide (PDI) derivatives are very versatile molecules, extensively used as dyes in, for example, the car industry, the development of photovoltaic devices, labeling of biomolecules, supramolecular assemblies, and as catalysts as well.<sup>[6]</sup> PDIs with five condensed aromatic rings in their structure are regarded as potential G-quadruplex ligands that offer the advantage of allowing suitable polar chains to be added to the aromatic core structure to increase solubility and/or promote G4 groove binding. Actually, a number of PDI derivatives have been shown to interact with G-quadruplexes.<sup>[7]</sup> A classical example is the widely studied PIPER (*N,N'*-bis-(2-(1-piperidino)ethyl)-3,4,9,10-perylene tetracarboxylic acid diimide), which was described for the first time in 1998 as a G4 binder.<sup>[8]</sup> PIPER can bind to G-quadruplexes by  $\pi$ - $\pi$  stacking with the 3' terminal G-tetrad and is able to induce the formation of the G-quadruplex structure.<sup>[9]</sup>

Therefore, we took advantage of these features to synthesize the molecule **5**, (*N,N'*-bis-[4-[1-oxo-6-biotinamidoethyl]piperidin-4-yl]-1,6,7,12-tetrakis[3,5-bis(hydroxycarbonyl)phenoxy]perylene-3,4,9,10-tetracarboxylic diimide), which is referred to as **PDI2B** (Scheme 1). Starting from an *N*-Boc protected bispiperidinyll derivative of a tetrachloroperylene-tetracarboxylic diimide, we have synthesized the octaester perylenediimide by an improved method from a previously known example<sup>[10]</sup> that was used for the synthesis of water-soluble perylenediimide-cored dendrimers.<sup>[11]</sup> Thus, microwave irradiation of a mixture of *N*-Boc bispiperidinyll tetrachloroperylene-tetracarboxylic diimide **1** and dimethyl-5-hydroxyisophthlate under copper-catalyzed cross-coupling Ullmann reaction conditions gave the intermediate **2**, which was then *N*-Boc deprotected under acid treatment to give **3**. The diamine **3** was coupled to a commercial biotin derivative to give **4** and the octaester was hydrolyzed under basic conditions to get **5**, hereafter denoted as **PDI2B** (See Figures S1–S28 in the Supporting Information).

In view that **PDI2B** is a fluorescent molecule with 64% quantum yield and  $6.57 \pm 0.03$  ns lifetime under our working conditions, its potential application as a fluorescent probe to target G-quadruplex structures has been evaluated. No changes in the **PDI2B** fluorescence lifetime were observed in the presence

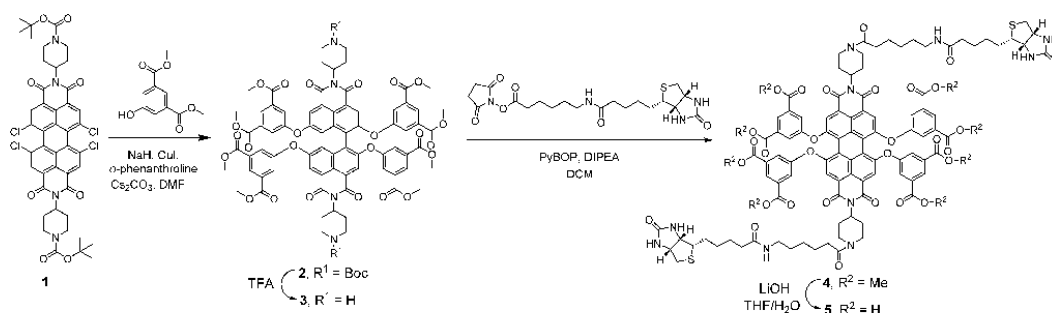
[a] Dr. N. Busto, Dr. P. Calvo, J. Santolaya, Prof. J. M. Leal, Prof. T. Torroba, Dr. B. García  
Chemistry Department, University of Burgos  
Pza. Misael Bañuelos s/n, 09001 Burgos (Spain)  
E-mail: nataliabv@msn.com  
begar@ubu.es

[b] A. Guédin, Dr. J.-L. Mergny  
ARNA Laboratory, INSERM U1212, CNRS UMR 5320  
IECB, University of Bordeaux, 33600 Pessac (France)  
E-mail: jean-louis.mergny@inserm.fr

[c] Dr. J.-L. Mergny  
Institute of Biophysics, AS CR  
v.v.i. Kralovopolska 135, 612 65 Brno (Czech Republic)

[d] J. Santolaya, Dr. G. Barone  
Dipartimento di Scienze e Tecnologie Biologiche  
Chimiche e Farmaceutiche, Università di Palermo  
90128 Palermo PA (Italy)

Supporting information and the ORCID identification number for the author of this article can be found under:  
<https://doi.org/10.1002/chem.201802365>.



**Scheme 1.** Synthesis of **5** (*N,N'*-bis-(4-[1-oxo-6-biotinamido-hexyl]piperidin-4-yl)-1,6,7,12-tetrakis[3,5-bis(hydroxycarbonyl)phenoxy]perylene-3,4,9,10-tetracarboxylic diimide) which is referred to as **PDI2B**.

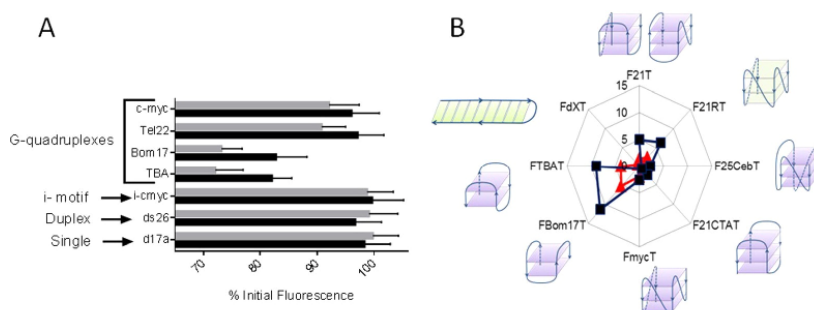


**Figure 1.** A) Percentage of **PDI2B** initial fluorescence in the presence of a (grey bars) threefold or (black bars) tenfold excess of DNA in several conformations: single strand, duplex, i-motif and 2-tetrad (TBA and Bom17) and 3-tetrad (c-myc and Tel22) G-quadruplexes.  $C_{\text{PDI2B}} = 2 \mu\text{M}$  and  $T = 25^\circ\text{C}$ . B)  $\Delta T_m$  Radar Plot of several oligonucleotides in the presence of **PDI2B** (▲)  $5 \mu\text{M}$  and (■)  $10 \mu\text{M}$ .  $C_{\text{oligo}} = 0.2 \mu\text{M}$ .  $I = 0.11 \text{ M}$  (90 mM LiCl, 10 mM KCl, 10 mM LiCaCl) and pH 7.2, except for i-motif (pH 5.8).

of different DNA G-quadruplexes (Figure S31) although a quenching effect is observed when **PDI2B** is titrated against G4 DNA. Interestingly, the quenching effect with 2-tetrad quadruplexes (Bom17 and TBA) is greater than with 3-tetrad quadruplexes (Tel22 and c-myc), whereas this quenching effect is almost negligible—within the experimental error—with the duplex, single strand and i-motif samples, revealing high selectivity of **PDI2B** towards G-quadruplexes (Figure 1A). These results suggest selectivity of **PDI2B** for G4 structures over other DNA conformations as well as higher affinity of **PDI2B** towards 2-tetrad quadruplexes than over 3-tetrad quadruplexes.

Moreover, the FRET melting experiments reveal thermal stabilization of G-quadruplex structures by **PDI2B** to different extents (the larger the  $\Delta T_m$ , the higher the observed stabilization) as a function of the number of G-tetrads (Figure 1B). Most of the G4 ligands exhibiting some selectivity for one quadruplex type over another prefer the parallel G4 conformation.<sup>[13]</sup> With **PDI2B** greater stabilization is observed for the 2-tetrad G-quadruplexes (FBom17T and FTBAT) than for the 3-tetrad quadruplexes (F21T, F21RT, F25CebT, F21CTAT, and FmycT), whereas no thermal stabilization is observed for the intramolecular duplex DNA, FdXT, where F and T stand for the Fam (F) and Tamra (T) fluorophores. To the best of our knowledge, **PDI2B** is

the first G4 ligand reported with higher thermal stabilization towards 2-tetrad than over 3-tetrad G-quadruplexes; this behavior has not been described hitherto: the radar plots of other known G4 ligands such as Braco19, TmPyP4, 360A, PhenDC3, TrisQ, and pyridostatin reported by De Rache et al.<sup>[12]</sup> indicate greater thermal stabilization of the 3-tetrad human telomeric G-quadruplex (F21T), in sharp contrast with the profile of **PDI2B**.

To properly assess the affinity of **PDI2B** with the different G4 structures, we have studied the interaction between **PDI2B** and *Bombyx* telomeric DNA (Bom17) and the human telomeric DNA (Tel22), as representative examples of 2- and 3-tetrad quadruplexes, respectively. ITC titrations of both G-quadruplex structures (P) with increasing amounts of **PDI2B** (D) have been conducted. The thermograms reveal a unique binding mode (Figure S32). The thermodynamic parameters of the interaction of **PDI2B** with Bom17 and Tel22 are collected in Table 1. In light of these data, it can be concluded that the binding is entropically driven for both systems. **PDI2B** displays fourfold greater affinity constant,  $K_s$ , towards 2-tetrads G4 than towards 3-tetrads G4. It should be noted that no binding was observed with calf thymus double-stranded DNA, confirming that **PDI2B** is selective for G-quadruplexes. The binding constants ob-

	$10^{-5} K_b [M^{-1}]$	$\Delta H [kJ mol^{-1}]$	$\Delta S [J mol^{-1} K^{-1}]$
PDI2B/Bom17	$3.00 \pm 0.02$	$-1.9 \pm 0.1$	98.3
PDI2B/Tel22	$0.75 \pm 0.02$	$-4.3 \pm 0.2$	79.1

tained with G4 are the same order of magnitude than those previously reported.<sup>[14]</sup> Thermal stabilization is one of the notable effects of stabilizing G4 ligands; nevertheless, the obtaining of a high affinity constant is not a guarantee for high  $\Delta T_m$ .<sup>[15]</sup> As to the PDI2B compound, it is possible to correlate higher affinity and quenching effect with enhancement of thermal stability (Figure 1).

On the other hand, no CD changes were observed in the molar ellipticity of Bom17 and Tel22 in the presence of different amounts of PDI2B (Figure S33), suggesting that PDI2B does not induce any significant conformational change in the G-quadruplexes conformations.

These findings are supported by MD simulations, which have allowed us to outline an atomistic model of the binding mode of PDI2B with both Bom17 and Tel22 G-quadruplexes. The equilibrium structures (Figures S34 and S35) show that the binding can be described as host-guest interaction. In particular, a molecular recognition process occurs along the MD trajectory (Figures S36 and S37), followed by important structural changes. In detail, PDI2B is inserted into a DNA pocket of complementary shape, and the two structures are held together by noncovalent interaction.

Selected interatomic distances related to H-bond formation or cleavage and to typical stacking interactions are reported in Figure 2 as a function of the simulation time. Concerning the PDI2B/Bom17 system, at about 20 ns PDI2B rapidly approaches the oligonucleotide, placing the "elbow" shaped group, (formed by folding one biotin arm) into a cavity formed between two thymine residues of the loop previously joined by H-bonding between H3 and O4 (Figure 2A, top left structure, black line). Whereas this part of the molecule remains fixed (Figure 2A, green line), the other biotin arm is oriented towards the G-quadruplex, interacting weakly with different DNA residues during the MD (Figure 2A, top right structure, red line).

On the other hand, the binding mechanism of PDI2B with Tel22 is somewhat different. PDI2B quickly approaches the G-quadruplex structure and, at about 200 ns, one biotin arm of PDI2B is inserted within the external GGGTAA loop, previously closed by a H-bond between the thymine 7 and adenine 9 bases (Figure 2B, top left structure, green). After the movement of adenine 9 (Figure 2B, red), one of the 5-hydroxyisophthalic acid "bay groups" interacts by  $\pi$ - $\pi$  stacking with adenine 9 (Figure 2B, black). Lastly, additional H-bond interactions occur between the biotin group and thymine and adenine bases in the GGGTTAGGG loop (Figure 2B, top right). Also in this case, the second biotin arm exhibits more flexible behavior and continuously changes its position. In particular, it can

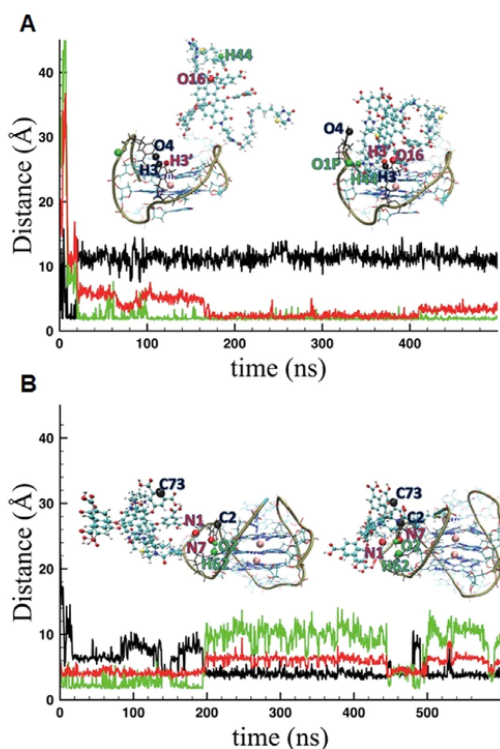


**Figure 2.** Selected interatomic distances of A) PDI2B/Bom17 system: H-bond breakage between T7/H3' and T12/O4 (black); H-bond formation between T7/H3' and PDI2B/O16 (red); H-bond formation between T13/H3 and T12/O1P (green) and B) PDI2B/Tel22 system: Stacking distance between PDI2B/C73 and A9/C2 (black); increasing distance between T8/N1 and A9/N7 (red); H-bond cleavage between T7/O2 and A9/H62 (green).

either be folded over the central part of the organic compound (Figure S35A) or extended on the other side of the loop, close to the other biotin arm, generating a structure in which the G-quadruplex loop is embraced by the two biotin arms (Figure S35B). Additional data and structural description of the final structures for PDI2B/Bom17 and PDI2B/Tel22 systems are reported in the Supporting Information (Figures S38–S41 and, as supporting material, video files PDI2B\_Tel22.mpg and PDI2B\_Bom17.mpg).

Because PDI2B is able to interact with G-quadruplexes displaying no affinity towards other DNA structures such as single- or double-stranded DNA, this molecule could be very useful for the recovery of G-quadruplexes structures in solution by means of streptavidin-coated magnetic beads. Actually, protein-coated magnetic beads are becoming increasingly popular for the recovery and purification of RNA/DNA. For example, magnetic beads have been employed recently in the detection of G4 structures in human genomic DNA by immobilization of the hf2 antibody.<sup>[16]</sup> The well-known high affinity of streptavidin-coated magnetic beads with biotin ( $10^{19}$ ) has enabled us to use this molecule with two biotin residues in its structure to



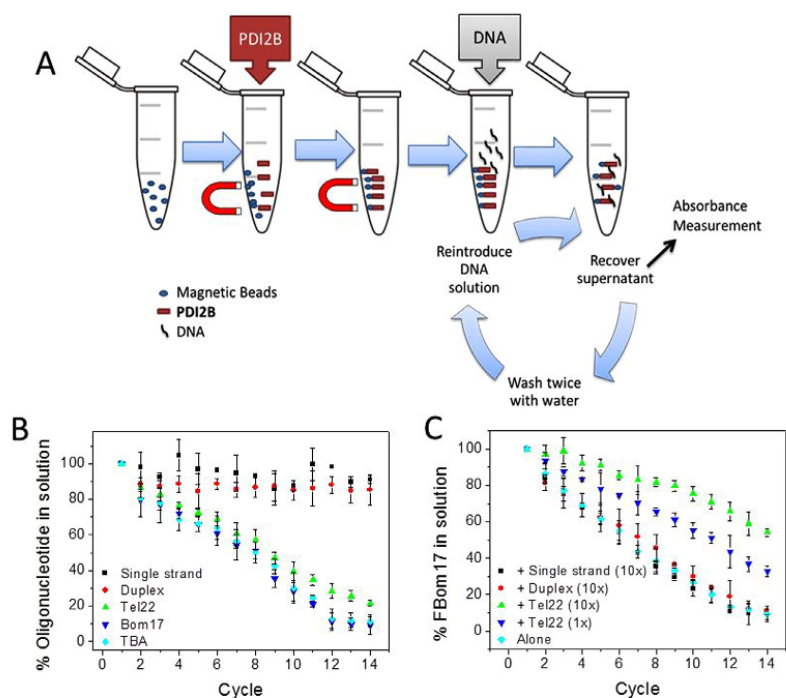


**Figure 3.** A) Experimental design for the fishing of DNA G-quadruplex structures in solution by means of streptavidin-coated magnetic beads. B) Fraction of oligonucleotide remaining in solution after each cycle. C) Fishing of labeled Bom17 with FAM (F-Bom17) followed by fluorescence measurements. Plot of the fraction of F-Bom17 remaining in solution in the presence of unlabeled competitors: single-stranded DNA (10 $\times$ ), duplex (10 $\times$ ), or Tel22 quadruplex either in equimolar amounts (1 $\times$ ) or with tenfold excess (10 $\times$ ).

selectively catch G-quadruplex molecules in solution. A method based on the use of a cytotoxic pyridostatin derivative ( $IC_{50} = 13.4 \mu\text{M}$  in HT1080 cells) consisting of a single step for recovery, has been previously described.<sup>[17]</sup> Our method, designed to recover large amounts of G-quadruplex structures in solution and implemented for the first time in this work, makes use of a cyclic methodology depicted in Figure 3A. The method makes no use of urea or heating for DNA recovery because it can be achieved by removal of  $K^+$  from the solution and, more importantly, PDI2B is much less cytotoxic ( $IC_{50} > 100 \mu\text{M}$ ) (Figure S42) than pyridostatin ( $IC_{50} = 2.5 \mu\text{M}$ )<sup>[18]</sup> in HeLa cell line. This absence of cytotoxicity constitutes an important advantage in terms of safety for its potential routine use in laboratory tasks. In addition, if pulling down G4 from cellular extracts were feasible, then the absence of cytotoxicity would be favorable in order to maintain the cellular integrity.

Taking advantage of the fluorescence of PDI2B, we have corroborated by fluorescence measurements that at least 97% of PDI2B remains attached to the streptavidin-coated magnetic beads after 5 min of incubation. Then, the PDI2B-streptavidin-coated magnetic beads were incubated for another 5 min with a solution of DNA oligonucleotide and the amount of DNA in the supernatant was determined by absorbance measurements. Afterwards, the DNA-PDI2B-streptavidin-coated mag-

netic beads were washed twice with warm water and the process was repeated for several cycles. As observed in Figure 3B, single- and double-stranded DNAs are not retained to the PDI2B-streptavidin-coated magnetic beads, because almost all the DNA remains in solution. In contrast, G4 structures are caught by this procedure even though multiple cycles are required, 12 cycles to recover 90% with 2-tetrads G4 (Bom17 and TBA) and 14 cycles to reach 80% with 3-tetrads G4 (Tel22), an effect that can be easily related to the higher affinity constant of PDI2B for Bom17 than for Tel22.

To unambiguously confirm the selective pulling down of G4 structures, some competitive fishing experiments were performed with a labeled oligonucleotide (F-Bom17), both alone and in mixtures containing unlabeled oligonucleotides acting as potential competitors. Figure 3C shows that, when F-Bom17 is incubated with tenfold excess of single stranded DNA or duplex, there are no changes in the recovery of F-Bom17 compared to that shown in the absence of competitor. On the other hand, when the pulling-down of the labeled Bom17 is conducted in the presence of an equimolar amount of non-labeled Tel22, the uptake efficiency is (roughly) 70%, whereas in the absence of competitor the efficiency rose to 90%. In contrast, with tenfold excess of Tel22 competitor, this efficiency is about 50%.

The efficacy of the G4 pull down by **PDI2B** is notable because, with only 1  $\mu\text{M}$  **PDI2B**, approximately 10% of Tel22 can be recovered in a unique step and up to 80% by using the presented cyclic methodology, even in the presence of single or double-stranded DNA as competitors (see Figure 3B,C). In contrast, 3  $\mu\text{M}$  of the pyridostatin derivative is required to recover 10% of Tel22.<sup>[17]</sup> Therefore, our procedure is effective, inexpensive (only involves warm water and the magnetic beads are recycled), and safe (not cytotoxic); by contrast, it takes longer, as it requires a limited number of cycles.

In conclusion, a new perylene diimide derivative, **PDI2B**, able to selectively interact with G-quadruplex structures, has been synthesized. The presence of the biotin residues at the *peri* positions as well as the absence of cytotoxicity has enabled us to design a new, effective, and safe method to selectively pull-down G-quadruplex structures in solution, even in the presence of other DNA structures as competitors.

### Acknowledgements

The financial support by "la Caixa" Foundation (LCF/PR/PR12/11070003), MINECO (CTQ2014-58812-C2-2-R and CTQ2015-71353-R, FEDER Funds), and Junta de Castilla y León, Consejería de Educación y Cultura y Fondo Social Europeo (Project BU051U16), Spain, is gratefully acknowledged. N.B. is grateful to Dr. Oscar Mendoza of the ARNA Laboratory for useful discussion and also to the financial support of the José Castillejo Program by the Spanish Ministry of Education, Culture and Sports (JC2015-00403). J.L.M. acknowledges support from Conseil Régional d'Aquitaine, Agence Nationale de la Recherche (ANR Quarpiem) and the Symbit program [CZ.02.1.01/0.0/0.0/15\_003/0000477] financed by the ERDF.

### Conflict of interest

The authors declare no conflict of interest.

**Keywords:** biophysics · DNA · G-quadruplexes · nucleic acids · perylene

- [1] a) M. N. Gellert, M. Lipsett, D. R. Davies, *Proc. Natl. Acad. Sci. USA* **1962**, *48*, 2013; b) D. Sen, W. Gilbert, *Nature* **1988**, *334*, 364; c) W. I. Sundquist,

- A. Klug, *Nature* **1989**, *342*, 825; d) J. R. Williamson, M. K. Raghuraman, T. R. Cech, *Cell* **1989**, *59*, 871.  
 [2] a) S. Burge, G. N. Parkinson, P. Hazel, A. K. Todd, S. Neidle, *Nucleic Acids Res.* **2006**, *34*, 5402; b) D. J. Patel, A. T. Phan, V. Kuryavyi, *Nucleic Acids Res.* **2007**, *35*, 7429.  
 [3] a) V. S. Chambers, G. Marsico, J. M. Boutell, M. Di Antonio, G. P. Smith, S. Balasubramanian, *Nat. Biotechnol.* **2015**, *33*, 877; b) A. Bedrat, L. Lacroix, J. L. Mergny, *Nucleic Acids Res.* **2016**, *44*, 1746.  
 [4] M. L. Bochman, K. Paeschke, V. A. Zakian, *Nat. Rev. Genet.* **2012**, *13*, 770.  
 [5] D. Rhodes, H. J. Lipps, *Nucleic Acids Res.* **2015**, *43*, 8627.  
 [6] a) A. Herrmann, K. Müllen, *Chem. Lett.* **2006**, *35*, 978; b) L. Chen, C. Li, K. Mullen, *J. Mater. Chem. C* **2014**, *2*, 1938; c) E. Kozma, M. Catellani, *Dyes Pigm.* **2013**, *98*, 160; d) A. S. Jalilov, L. G. Nilewski, V. Berka, C. Zhang, A. A. Yakovenko, G. Wu, T. A. Kent, A.-L. Tsai, J. M. Tour, *ACS Nano* **2017**, *11*, 2024.  
 [7] a) S. M. Kerwin, G. Chen, J. T. Kern, P. W. Thomas, *Bioorg. Med. Chem. Lett.* **2002**, *12*, 447; b) E. Michelia, D. D'Ambrosiob, M. Franceschina, M. Savino, *Mini-Rev. Med. Chem.* **2009**, *9*, 1622; c) Y. Hu, D. Han, Q. Zhang, T. Wu, F. Li, L. Niu, *Biosens. Bioelectron.* **2012**, *38*, 396; d) L. Hahn, N. J. Buurma, L. H. Gade, *Chem. Eur. J.* **2016**, *22*, 6314; e) Y.-L. Wu, N. E. Horwitz, K.-S. Chen, D. A. Gomez-Gualdron, N. S. Luu, L. Ma, T. C. Wang, M. C. Hersam, J. T. Hupp, O. K. Farha, R. Q. Snurr, M. R. Wasielewski, *Nat. Chem.* **2017**, *9*, 466.  
 [8] O. Y. Fedoroff, M. Salazar, H. Han, V. V. Chemeris, S. M. Kerwin, L. H. Hurley, *Biochemistry* **1998**, *37*, 12367.  
 [9] A. Rangan, O. Y. Fedoroff, L. H. Hurley, *J. Biol. Chem.* **2001**, *276*, 4640.  
 [10] a) S. K. Yang, X. Shi, S. Park, S. Doganay, T. Ha, S. C. Zimmerman, *J. Am. Chem. Soc.* **2011**, *133*, 9964; b) S. K. Yang, S. C. Zimmerman, *Adv. Funct. Mater.* **2012**, *22*, 3023.  
 [11] a) M. Sun, K. Mullen, M. Yin, *Chem. Soc. Rev.* **2016**, *45*, 1513; b) F. Würthner, C. R. Saha-Möller, B. Fimmel, S. Ogi, P. Leowanawat, D. Schmidt, *Chem. Rev.* **2016**, *116*, 962.  
 [12] A. De Rache, J.-L. Mergny, *Biochimie* **2015**, *115*, 194.  
 [13] J. M. Nicoludis, S. P. Barrett, J.-L. Mergny, L. A. Yatsunyk, *Nucleic Acids Res.* **2012**, *40*, 5432.  
 [14] J. Carvalho, T. Quintela, N. M. Gueddouda, A. Bourdoncle, J. L. Mergny, G. F. Salgado, J. A. Queiroz, C. Cruz, *Org. Biomol. Chem.* **2018**, *16*, 2776.  
 [15] a) N. H. Campbell, N. H. A. Karim, G. N. Parkinson, M. Gunaratnam, V. Petrucci, A. K. Todd, R. Vilar, S. Neidle, *J. Med. Chem.* **2012**, *55*, 209; b) L. Xu, X. Chen, J. Wu, J. Wang, L. Ji, H. Chao, *Chem. Eur. J.* **2015**, *21*, 4008.  
 [16] E. Y. N. Lam, D. Beraldi, D. Tannahill, S. Balasubramanian, *Nat. Commun.* **2013**, *4*, 1796.  
 [17] S. Müller, S. Kumari, R. Rodriguez, S. Balasubramanian, *Nat. Chem.* **2010**, *2*, 1095.  
 [18] S. Müller, D. A. Sanders, M. Antonio, S. Matsis, J. F. Riou, R. Rodriguez, S. Balasubramanian, *Org. Biomol. Chem.* **2012**, *10*, 6537.

Manuscript received: May 11, 2018

Accepted manuscript online: May 24, 2018

Version of record online: July 10, 2018

# CHEMISTRY

## A **European** Journal

### Supporting Information

#### **Fishing for G-Quadruplexes in Solution with a Perylene Diimide Derivative Labeled with Biotins**

Natalia Busto,<sup>\*[a]</sup> Patricia Calvo,<sup>[a]</sup> Javier Santolaya,<sup>[a, d]</sup> José M Leal,<sup>[a]</sup> Aurore Guédin,<sup>[b]</sup> Giampaolo Barone,<sup>[d]</sup> Tomás Torroba,<sup>[a]</sup> Jean-Louis Mergny,<sup>\*[b, c]</sup> and Begoña García<sup>\*[a]</sup>

chem\_201802365\_sm\_miscellaneous\_information.pdf

# SUPPORTING INFORMATION

## Table of Contents

Synthesis and characterization of perylene diimides.....	S1
Materials and Methods.....	S17
Additional Data	
A. Fluorescence Lifetimes Measurements.....	S20
B. Titrations.....	S21
C. Computational Results.....	S22
D. Cytotoxicity.....	S25
References.....	S26

Video Files with MD simulations

---

## Synthesis and characterization of perylene diimides

*N,N'*-Bis(*N''*-*tert*-butoxycarbonyl)piperidin-4-yl)-1,6,7,12-tetrachloro-*pery*lene-3,4,9,10-tetracarboxylic diimide **1**.

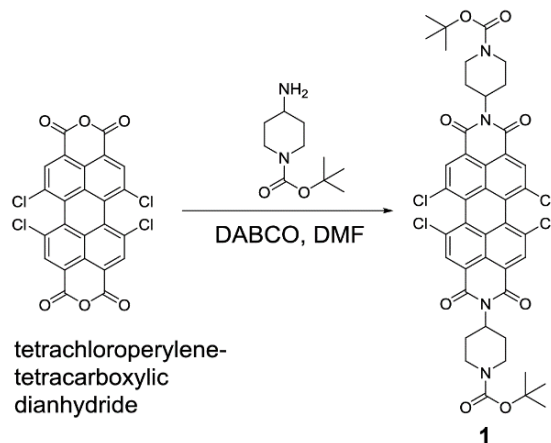


**Figure S1:** Synthesis of **1**

Anhydrous DMF (20 mL) and 4-amino-1-(*N''*-*tert*-butoxycarbonyl)piperidine (0.47 g, 2.30 mmol) were added under nitrogen to 1,6,7,12-tetrachloro-*pery*lenetetracarboxylic acid dianhydride (0.50 g, 0.94 mmol) and DABCO (0.26 g, 2.30 mmol). The mixture was irradiated in a microwave device at 110 °C for 1



hour. Then, it was poured on an aqueous solution of HCl 1M (15 mL), stirred for 1 hour, filtered and washed with water (30 mL). Purification was carried out by silica gel flash chromatography using DCM:MeCN (80:20) as eluent to give **1** as an orange solid in 95% yield (0.79 g, 0.89 mmol).  $R_f$  (DCM:MeOH 50:2): 0.6, mp > 350 °C. FT-IR (KBr,  $\text{cm}^{-1}$ ): 2977 (C-H), 2931 (C-H), 2852 (C-H), 1701 (C=O), 1661 (CONH), 1590 ( $\text{C}_{Ar}$ - $\text{C}_{Ar}$ ), 1420 ( $\text{CH}_2$ ), 1366 (C-N), 1337 (C-O), 1275, 1243, 1150, 1005, 951, 908, 749, 684, 547 (fingerprint region).  $^1\text{H}$  NMR (300 MHz,  $\text{CDCl}_3$ )  $\delta$ : 8.65 (s, 4H,  $\text{H}_{Ar}$ ), 5.24 – 5.15 (m, 2H, N-CH), 4.32 (s, 4H,  $\text{CH}_2$ ), 2.88 – 2.72 (m, 9H,  $\text{CH}_2$ ), 1.70 (d,  $J = 12.8$  Hz, 3H,  $\text{CH}_2$ ), 1.51 (s, 18H,  $\text{COOC}(\text{CH}_3)_3$ ).  $^{13}\text{C}$  NMR (75 MHz,  $\text{CDCl}_3$ )  $\delta$ : 162.7 (CO), 154.8 (CO), 135.5 ( $\text{C}_{Ar}$ ), 133.2 (CH), 131.5 ( $\text{C}_{Ar}$ ), 128.6 ( $\text{C}_{Ar}$ ), 123.6 ( $\text{C}_{Ar}$ ), 123.4 ( $\text{C}_{Ar}$ ), 79.9 (Cq), 52.6 (CH), 44.2 ( $\text{CH}_2$ ), 43.9 ( $\text{CH}_2$ ), 29.8 ( $\text{CH}_2$ ), 28.6 ( $\text{CH}_3$ ), 28.4 ( $\text{CH}_2$ ). HRMS (MALDI+, DCTB):  $m/z$  calcd. For  $\text{C}_{39}\text{H}_{33}\text{Cl}_4\text{N}_4\text{O}_6$  ( $[\text{M}+\text{H}-(\text{COOC}(\text{CH}_3)_3)]^+$ ): 793.1149; found: 793.1142.  $\Phi$  ( $\text{CHCl}_3$ ) =  $0.65 \pm 0.01$ . Fluorescence Lifetime  $\tau/\text{ns}$  ( $\text{CHCl}_3$ ,  $\chi^2$ ): 5.64 (1.06).

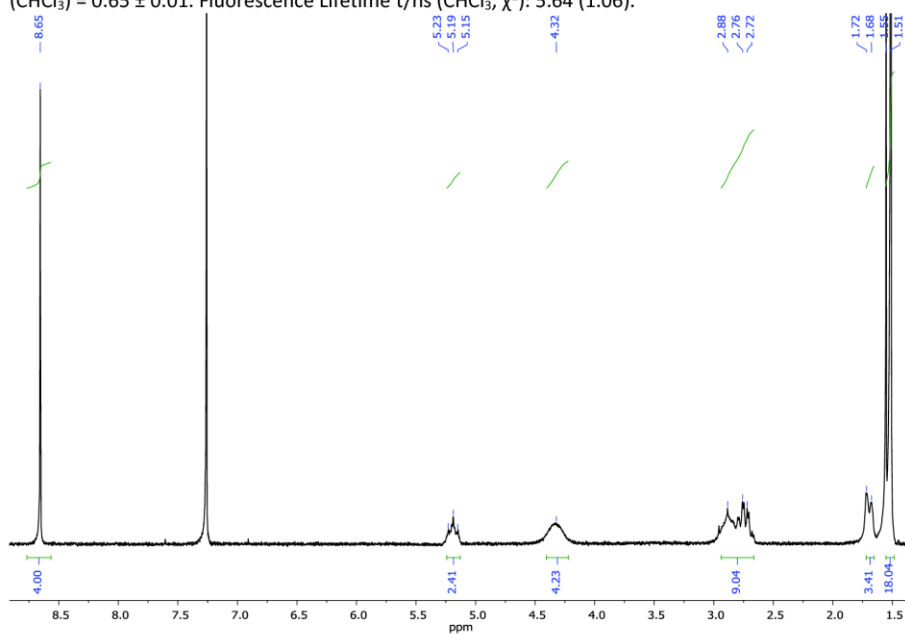


Figure S2.  $^1\text{H}$  NMR (300 MHz,  $\text{CDCl}_3$ ) of **1**

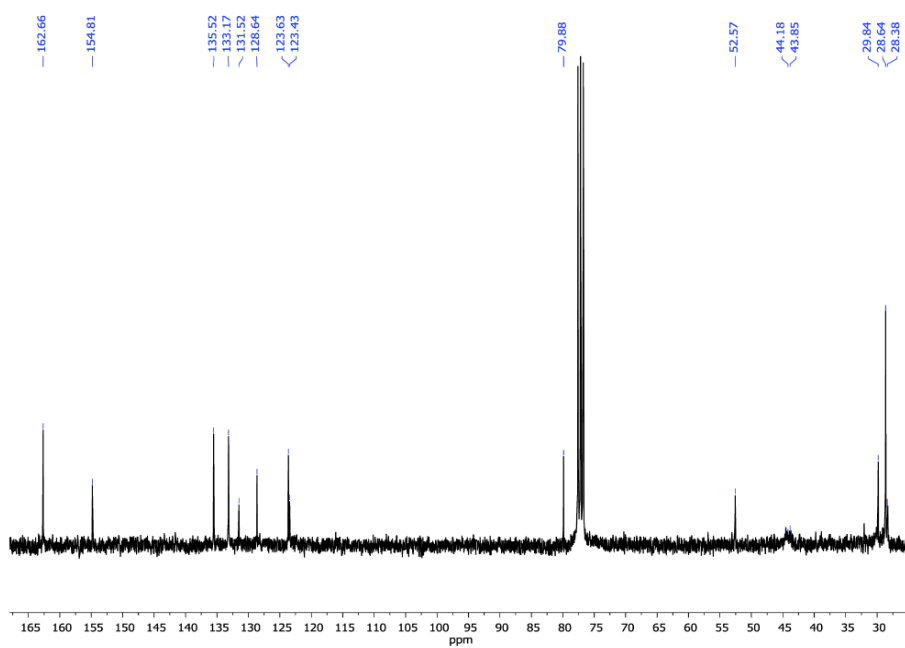


Figure S3.  $^{13}\text{C}$  NMR (75 MHz,  $\text{CDCl}_3$ ) of **1**

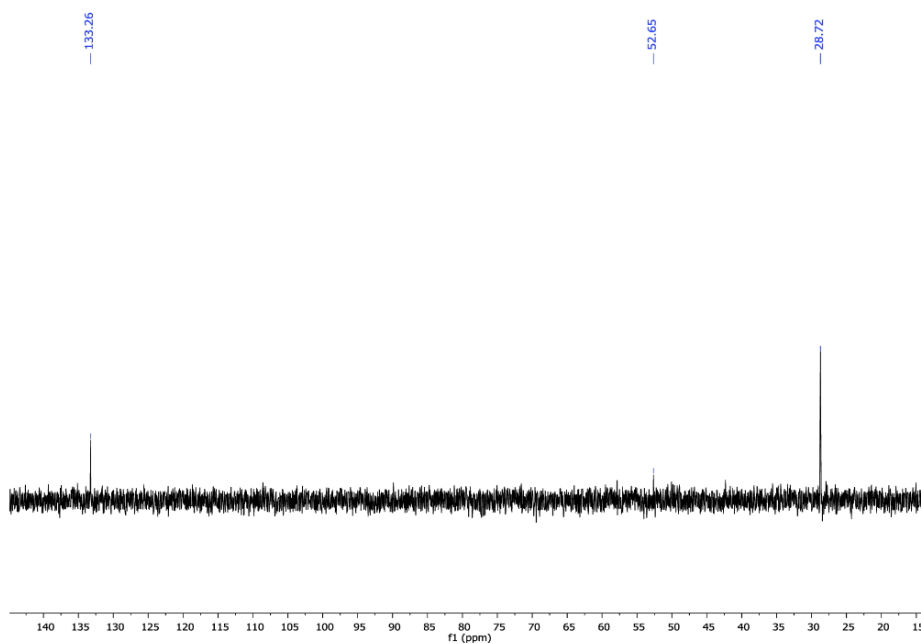


Figure S4.  $^{13}\text{C}$  NMR-DEPT-135 (101 MHz,  $\text{CDCl}_3$ ) of **1**

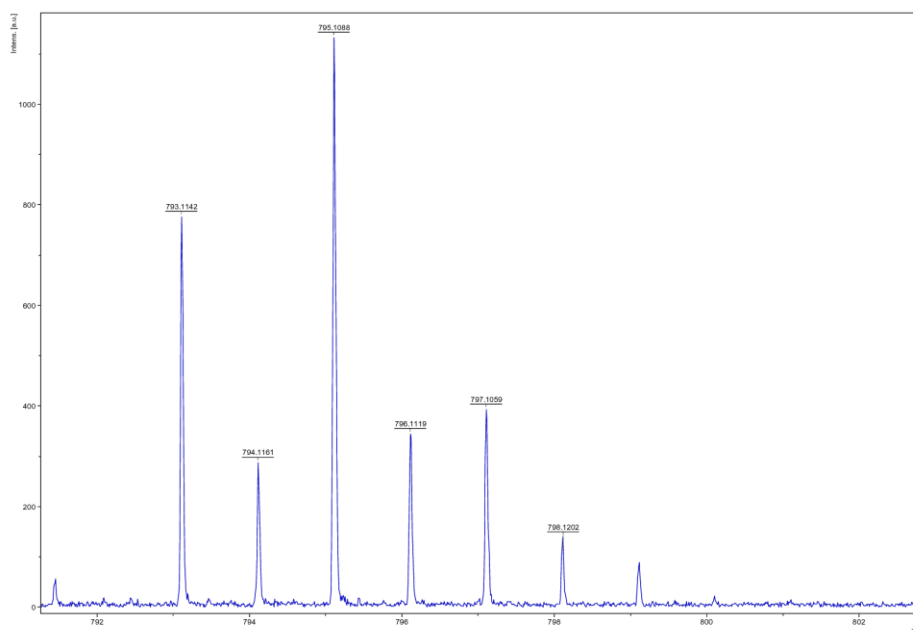


Figure S5. Mass spectrum (MALDI+, DCTB) of **1**

***N,N'***-Bis(*N''*-*tert*-butoxycarbonyl)piperidin-4-yl)-1,6,7,12-tetrakis(3,5-bis(methoxycarbonyl)phenoxy)perylene-3,4,9,10-tetracarboxylic diimide **2**.

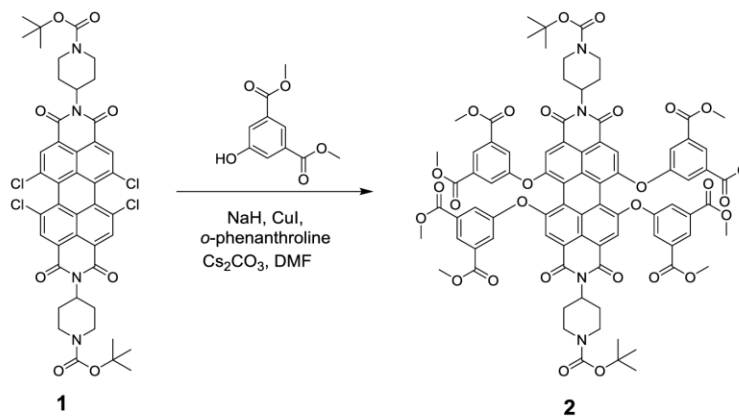


Figure S6. Synthesis of **2**

*N,N'*-bis(*N''*-*tert*-butoxycarbonyl)piperidin-4-yl)-1,6,7,12-tetrachloroperylene-3,4,9,10-tetracarboxylic diimide (100 mg, 0.1 mmol), *o*-phenanthroline monohydrated (13 mg, 0.06 mmol), copper(I) iodide (6 mg, 0.03 mmol) and caesium carbonate (430 mg, 1.32 mmol) were added under nitrogen to a suspension of NaH (18 mg, 0.44 mmol), anhydrous DMF (20 mL) and dimethyl-5-hydroxyisophthalate (104 mg, 0.49 mmol). The mixture was irradiated in a microwave device at 110 °C for 1 hour. The solvent was evaporated under reduced pressure. Purification was carried out by silica gel flash chromatography using DCM:MeCN (70:30) as eluent. **2** was obtained as deep pink solid in 40% yield (70 mg, 0.04 mmol).

R<sub>f</sub> (DCM:MeOH 50:2): 0.2, mp > 350 °C. FT-IR (KBr, cm<sup>-1</sup>): 2951 (C-H), 2925 (C-H), 2849 (C-H), 1735 (C=O), 1698 (C=O), 1664 (CONH), 1587 (C<sub>Ar</sub>-C<sub>Ar</sub>), 1505 (C<sub>Ar</sub>-C<sub>Ar</sub>), 1454 (CH<sub>2</sub>), 1431 (CH<sub>2</sub>), 1414 (CH<sub>2</sub>), 1320 (C-N), 1297 (C-O), 1280, 1249, 1175, 1004, 999, 792, 758, 721, 669 (fingerprint region). <sup>1</sup>H NMR (300 MHz, CDCl<sub>3</sub>) δ: 8.31 (t, *J* = 1.4 Hz, 4H, H<sub>Ar</sub>), 8.13 (s, 4H, H<sub>Ar</sub>), 7.67 (d, *J* = 1.4 Hz, 8H, H<sub>Ar</sub>), 5.08 – 5.00 (m, 2H, CH), 4.21 (s, 4H, CH<sub>2</sub>), 3.86 (s, 24H, CH<sub>3</sub>), 2.75 – 2.52 (m, 9H, CH<sub>2</sub>), 1.60 (d, *J* = 11.6 Hz, 3H, CH<sub>2</sub>), 1.40 (s, 18H, CH<sub>3</sub>). <sup>13</sup>C NMR (101 MHz, CDCl<sub>3</sub>) δ: 165.1 (CO), 163.1 (CO), 155.9 (C<sub>Ar</sub>), 154.9 (C<sub>Ar</sub>), 154.7 (CO), 133.1 (C<sub>Ar</sub>), 132.7 (C<sub>Ar</sub>), 132.0 (C<sub>Ar</sub>), 126.5 (CH), 124.5 (CH), 124.0 (C<sub>Ar</sub>), 121.2 (CH), 121.1 (C<sub>Ar</sub>), 120.9 (CH), 120.9 (C<sub>Ar</sub>), 79.8 (C<sub>q</sub>), 52.7 (CH<sub>3</sub>), 52.6 (CH), 52.4 (CH), 44.1 (CH<sub>2</sub>), 43.6 (CH<sub>2</sub>), 29.9 (CH<sub>2</sub>), 28.6 (CH<sub>3</sub>), 28.4 (CH<sub>2</sub>). HRMS (MALDI-, DCTB): *m/z* calcd. for C<sub>84</sub>H<sub>76</sub>N<sub>4</sub>O<sub>28</sub> ([M]): 1588.4641; found: 1588.0849. Φ (CHCl<sub>3</sub>) = 0.99 ± 0.01. Fluorescence Lifetime τ/ns (CHCl<sub>3</sub>, χ<sup>2</sup>): 7.41 (1.13).

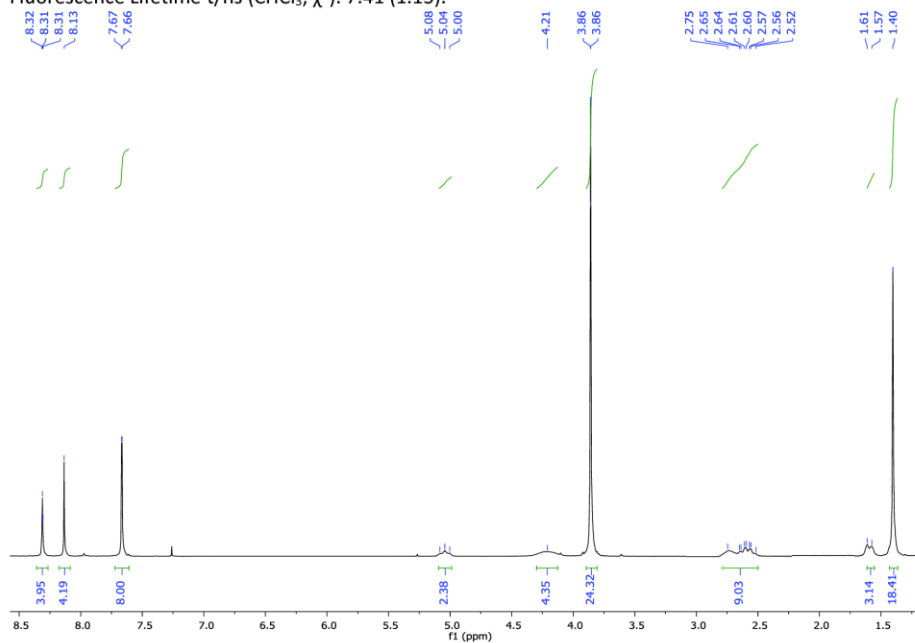


Figure S7. <sup>1</sup>H NMR (300 MHz, CDCl<sub>3</sub>) of 2

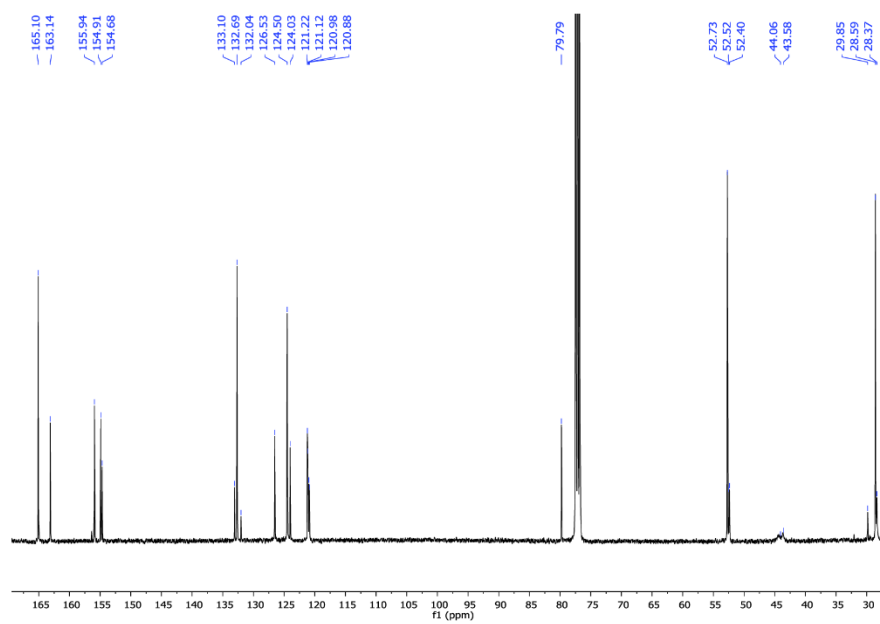


Figure S8.  $^{13}\text{C}$  NMR (101 MHz,  $\text{CDCl}_3$ ) of **2**

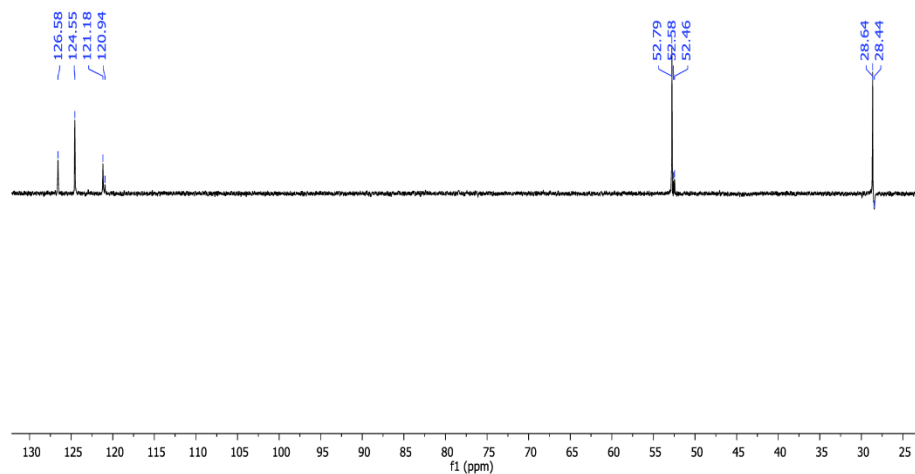


Figure S9.  $^{13}\text{C}$  NMR-DEPT-135 (101 MHz,  $\text{CDCl}_3$ ) of **2**

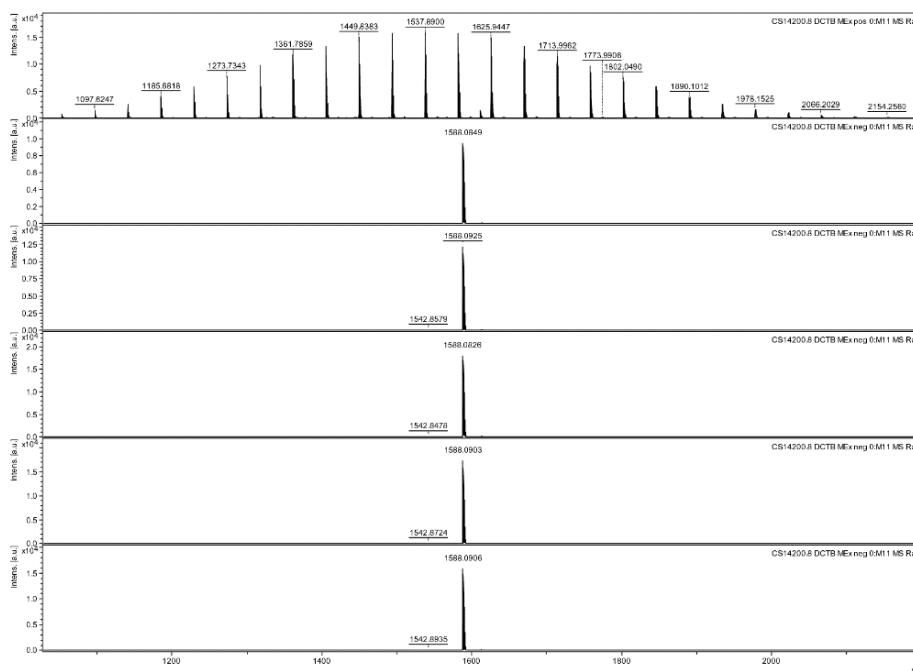


Figure S10. Mass spectrum (MALDI-, DCTB) of 2

***N,N'*-Bis(piperidin-1-yl)-1,6,7,12-tetrakis(3,5-bis(methoxycarbonyl)phenoxy)perylene-3,4,9,10-tetracarboxylic diimide 3.**

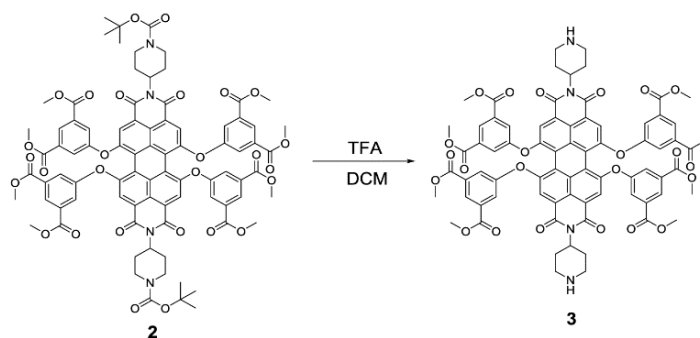


Figure S11. Synthesis of 3.

Trifluoroacetic acid (4.4 mL, 56.97 mmol) was added dropwise to *N,N'*-Bis(*N*'-tert-butoxycarbonyl)piperidin-4-yl)-1,6,7,12-tetrakis(3,5-bis(methoxy-carbonyl)phenoxy)perylene-3,4,9,10-tetracarboxylic diimide **2** (170 mg, 0.097 mmol) dissolved in degassed DCM (6.5 mL). The mixture was stirred at 25 °C for 2 hours, neutralized with 10% NaOH (15 mL) and extracted with DCM (3 x 20 mL). The combined organic extracts were evaporated under reduced pressure to obtain **3** as a pink-purple product in 97% yield (144 mg, 0.11 mmol).  $R_f$  (DCM:MeOH 50:4): 0, mp > 350 °C. FT-IR (KBr,  $\text{cm}^{-1}$ ): 3437 (NH), 2951 (C-H), 2923 (C-H), 2849 (C-H), 1732 (C=O), 1695 (C=O), 1661 (CONH), 1587 ( $C_{Ar}-C_{Ar}$ ), 1508 ( $C_{Ar}-C_{Ar}$ ), 1459 ( $\text{CH}_2$ ), 1431 ( $\text{CH}_2$ ), 1411 ( $\text{CH}_2$ ), 1385 ( $\text{CH}_3$ ), 1320 (C-N), 1300 (C-O), 1286 (C-O), 1252, 1181, 1007, 999, 903, 803, 752, 721 (fingerprint region).  $^1\text{H}$  NMR (400 MHz,  $\text{CDCl}_3$ )  $\delta$ : 8.34 (t,  $J = 1.4$  Hz, 4H,  $H_{Ar}$ ), 8.17 (s, 4H,  $H_{Ar}$ ), 7.70 (d,  $J = 2.1$  Hz, 8H,  $H_{Ar}$ ), 5.08 – 5.02 (m, 2H, N-CH), 3.89 (s, 24H,  $\text{COOCH}_3$ ), 3.20

(d,  $J = 12.5$  Hz, 4H, CH<sub>2</sub>), 2.74 – 2.55 (m, 9H, CH<sub>2</sub>), 1.64 (s, 3H, CH<sub>2</sub>). <sup>13</sup>C NMR (101 MHz, CDCl<sub>3</sub>)  $\delta$ : 165.1 (CO), 163.1 (CO), 155.9 (C<sub>Ar</sub>), 154.9 (C<sub>Ar</sub>), 133.1 (C<sub>Ar</sub>), 132.7 (C<sub>Ar</sub>), 126.5 (CH), 124.5 (CH), 124.2 (C<sub>Ar</sub>), 121.2 (CH), 121.1 (C<sub>Ar</sub>), 120.9 (C<sub>Ar</sub>), 120.9 (C<sub>Ar</sub>), 52.7 (CH<sub>3</sub>), 52.6 (CH), 46.9 (CH<sub>2</sub>), 30.1 (CH<sub>2</sub>), 29.9 (CH<sub>2</sub>). HRMS (MALDI+, DCTB):  $m/z$  calcd for C<sub>74</sub>H<sub>60</sub>N<sub>4</sub>O<sub>24</sub> ([M+H]<sup>+</sup>): 1389.3703; found: 1389.3803.  $\Phi$  (CHCl<sub>3</sub>) = 0.44 ± 0.01. Fluorescence Lifetime  $\tau$ /ns (CHCl<sub>3</sub>,  $\chi^2$ ): 5.64 (1.14).

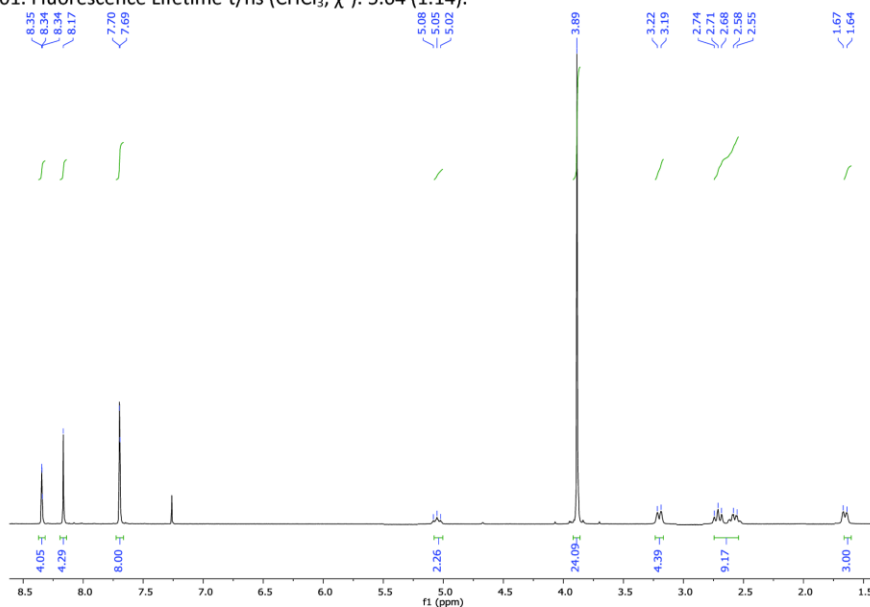


Figure S12. <sup>1</sup>H NMR (400 MHz, CDCl<sub>3</sub>) of 3

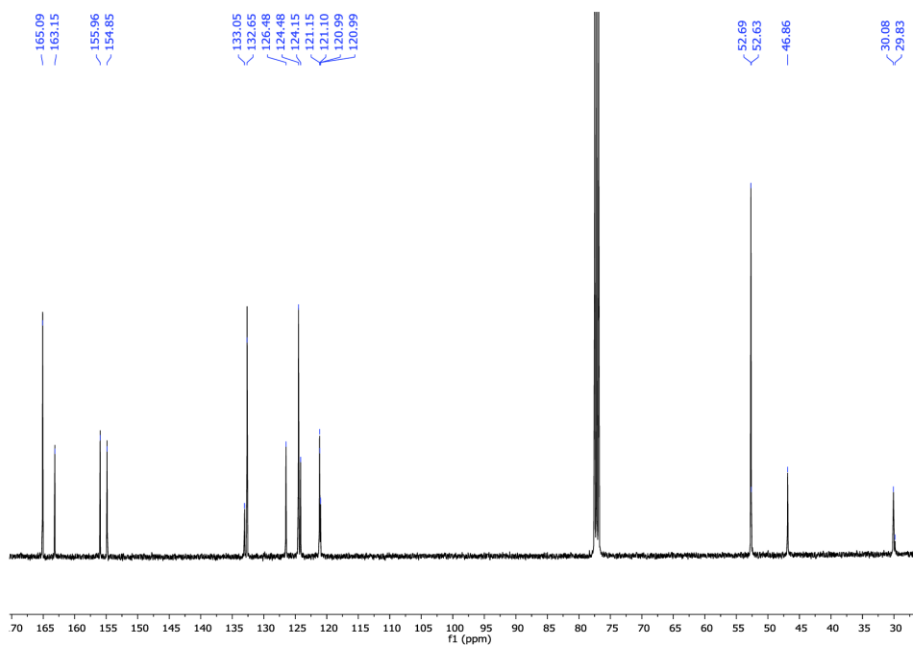


Figure S13. <sup>13</sup>C NMR (101 MHz, CDCl<sub>3</sub>) of 3

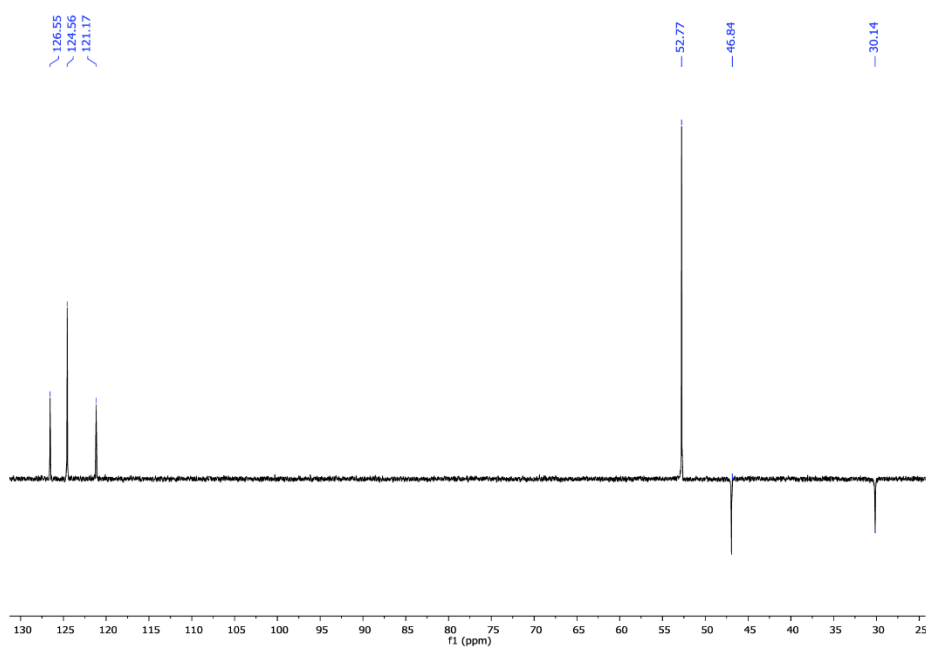


Figure S14.  $^{13}\text{C}$  NMR-DEPT-135 (101 MHz,  $\text{CDCl}_3$ ) of **3**

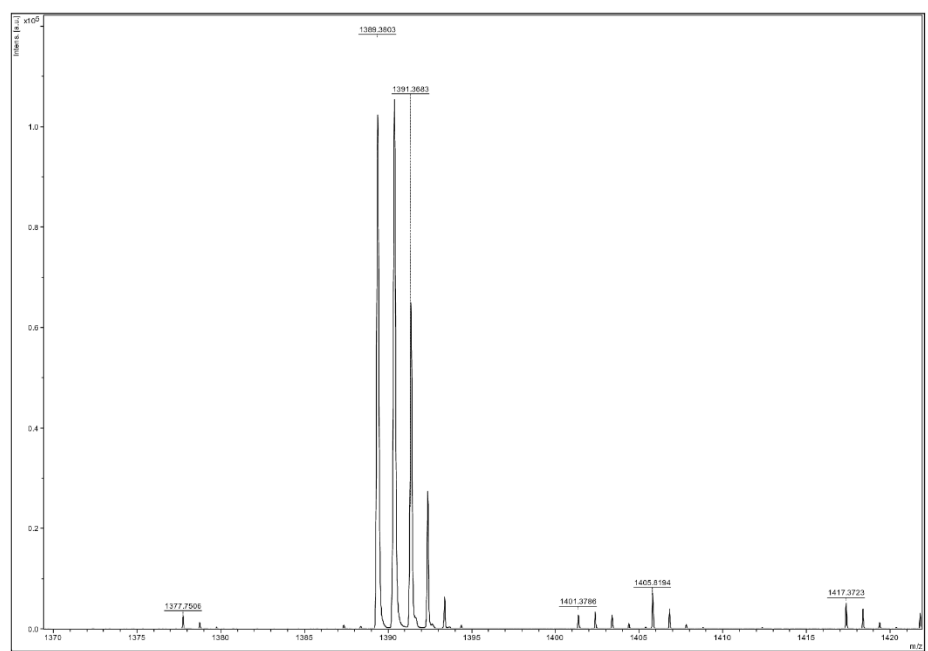
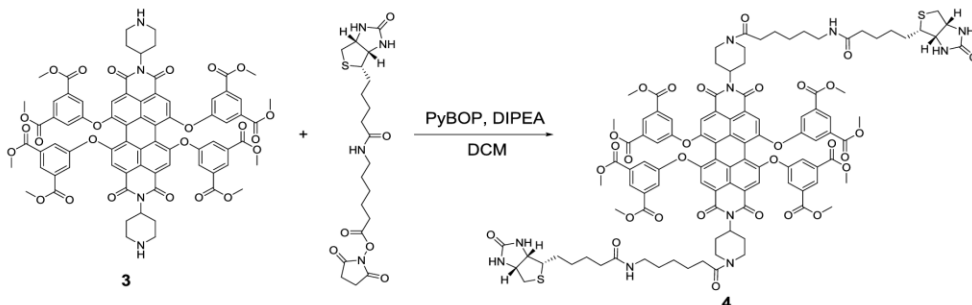


Figure S15. Mass spectrum (MALDI+, DCTB) of **3**



***N,N'*-bis-(4-(1-oxo-6-biotinamidohexyl)piperidin-1-yl)-1,6,7,12-tetrakis(3,5-bis(methoxycarbonyl)phenoxy)perylene-3,4,9,10-tetracarboxylic diimide **4**.**



**Figure S16:** Synthesis of **4**.

*N,N'*-Bis(piperidin-1-yl)-1,6,7,12-tetrakis(3,5-bis(methoxycarbonyl)phenoxy)perylene-3,4,9,10-tetracarboxylic diimide **3** (20 mg, 0.01 mmol) and PyBOP (15 mg 0.03 mmol) dissolved in DCM (1.1 mL) were added under nitrogen to *N*-succinimidyl-6-biotinamidohexanoate (13 mg, 0.03 mmol) and DIPEA (10  $\mu$ L, 0.06 mmol) dissolved in DCM (0.7 mL). The purple-pink mixture was stirred at room temperature for 2 hours until the reactant disappears in TLC. The solvent was removed under reduced pressure. Purification was carried out by silica gel flash chromatography using DCM:MeOH (80:20) as eluent to give compound **4** as a deep pink solid in 63% yield (18 mg, 0.01 mmol).  $R_f$  (DCM:MeOH 50:4): 0.41, mp > 350  $^{\circ}$ C. FT-IR (KBr,  $\text{cm}^{-1}$ ): 2957 (C-H), 2925 (C-H), 2854 (C-H), 1732 (C=O), 1701 (C=O), 1647 (CONH), 1590 ( $\text{C}_{\text{Ar}}-\text{C}_{\text{Ar}}$ ), 1462 ( $\text{CH}_2$ ), 1428 ( $\text{CH}_2$ ), 1326 (C-N), 1300 (C-O), 1286 (C-O), 1258, 1107, 996, 758 (fingerprint region).  $^1\text{H}$  NMR (300 MHz,  $\text{CDCl}_3$ )  $\delta$ : 8.31 (t,  $J = 1.5$  Hz, 4H,  $\text{H}_{\text{Ar}}$ ), 8.13 (s, 4H,  $\text{H}_{\text{Ar}}$ ), 7.67 (d,  $J = 1.5$  Hz, 8H,  $\text{H}_{\text{Ar}}$ ), 6.66 (s, 1H, NH), 6.07 (d,  $J = 6.0$  Hz, 1H, NH), 5.18 – 5.10 (m, 2H, CH), 4.72 (d,  $J = 9.6$  Hz, 3H,  $\text{CH}_2$ ), 4.47 – 4.43 (m, 2H, CH), 4.32 – 4.22 (m, 2H, CH), 3.86 (s, 24H,  $\text{CH}_3$ ), 3.70 – 3.61 (m, 2H, CH), 3.17 – 3.04 (m, 6H,  $\text{CH}_2$ ), 2.85 (dd,  $J = 12.9$  Hz and 4.9 Hz, 2H,  $\text{CH}_2$ ), 2.68 (d,  $J = 12.9$  Hz, 2H,  $\text{CH}_2$ ), 2.63 – 2.55 (m, 7H,  $\text{CH}_2$ ), 2.37 – 2.30 (m, 4H,  $\text{CH}_2$ ), 2.13 (t,  $J = 7.3$  Hz, 4H,  $\text{CH}_2$ ), 1.79 – 1.51 (m, 15H,  $\text{CH}_2$ ), 1.48 – 1.34 (m, 8H,  $\text{CH}_2$ ).  $^{13}\text{C}$  NMR (101 MHz,  $\text{CDCl}_3$ :MeOD)  $\delta$ : 174.1 (CO), 171.9 (CO), 165.1 (CO), 163.1 (CO), 162.9 (CO), 155.8 ( $\text{C}_{\text{Ar}}$ ), 154.7 ( $\text{C}_{\text{Ar}}$ ), 132.9 ( $\text{C}_{\text{Ar}}$ ), 132.5 ( $\text{C}_{\text{Ar}}$ ), 126.3 (CH), 124.3 (CH), 123.8 ( $\text{C}_{\text{Ar}}$ ), 123.7 ( $\text{C}_{\text{Ar}}$ ), 123.6 ( $\text{C}_{\text{Ar}}$ ), 120.9 (CH), 120.8 (CH), 61.9 (CH), 60.1 (CH), 55.3 (CH), 54.2 (CH), 52.5 ( $\text{CH}_3$ ), 43.8 ( $\text{CH}_2$ ), 43.7 ( $\text{CH}_2$ ), 40.3 ( $\text{CH}_2$ ), 38.9 ( $\text{CH}_2$ ), 36.3 ( $\text{CH}_2$ ), 35.6 ( $\text{CH}_2$ ), 30.7 ( $\text{CH}_2$ ), 29.6 ( $\text{CH}_2$ ), 28.5 ( $\text{CH}_2$ ), 28.1 ( $\text{CH}_2$ ), 27.8 ( $\text{CH}_2$ ), 26.4 ( $\text{CH}_2$ ), 25.4 ( $\text{CH}_2$ ), 25.1 ( $\text{CH}_2$ ). HRMS (MALDI+, DCTB):  $m/z$  calcd for  $\text{C}_{106}\text{H}_{110}\text{N}_{10}\text{O}_3\text{S}_2$  ( $[\text{M}+\text{H}]^+$ ): 2067.6904; found: 2067.6920.  $\Phi$  ( $\text{CHCl}_3$ ) = 0.69  $\pm$  0.01. Fluorescence Lifetime  $\tau/\text{ns}$  ( $\text{H}_2\text{O}$ ,  $\chi^2$ ): 6.82 (1.02).

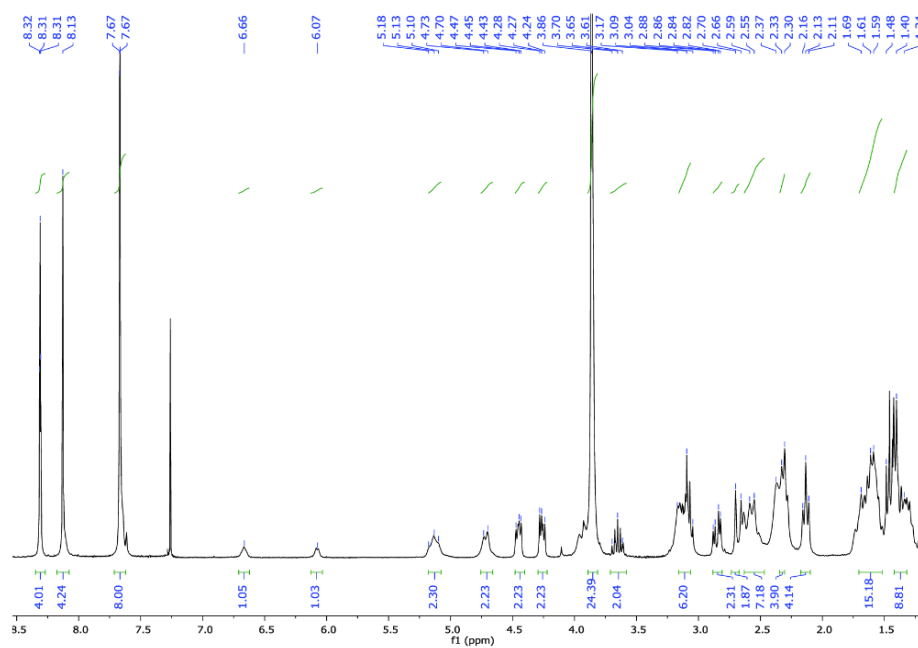


Figure S17.  $^1\text{H}$  NMR (300 MHz,  $\text{CDCl}_3$ ) of 4

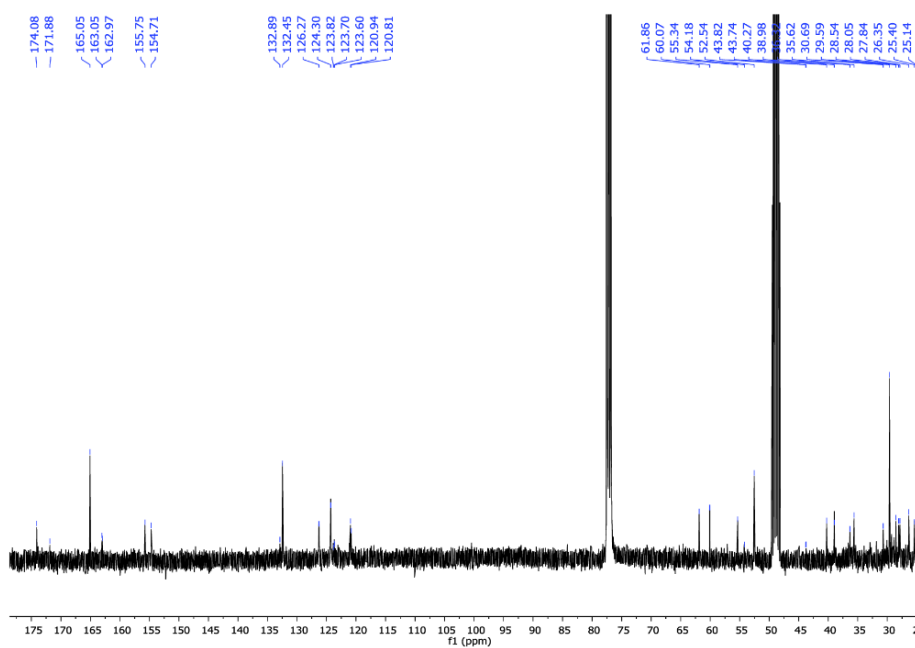


Figure S18.  $^{13}\text{C}$  NMR (101 MHz,  $\text{CDCl}_3$ :MeOD) of 4

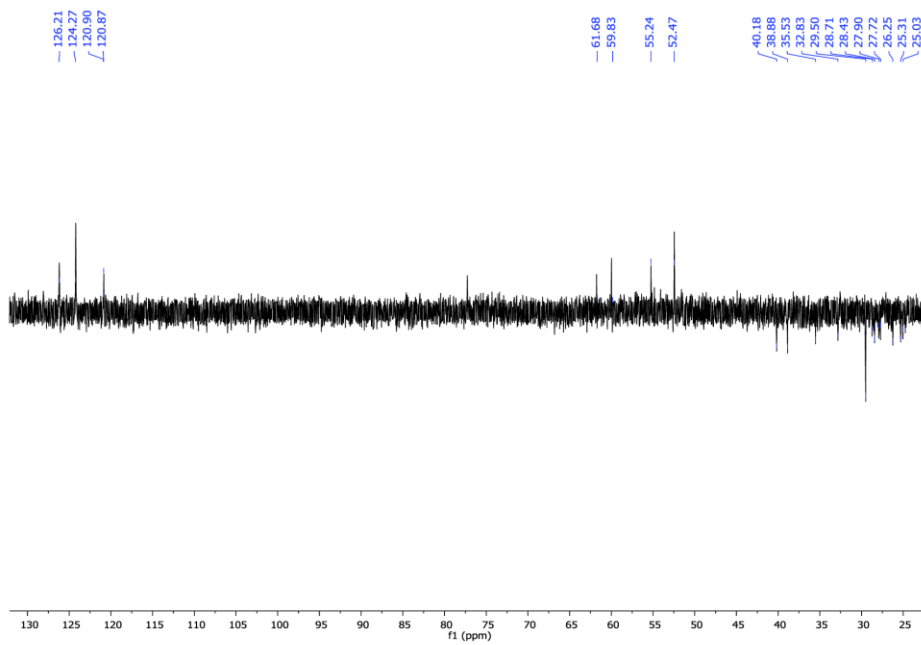


Figure S19.  $^{13}\text{C}$  NMR-DEPT-135 (101 MHz,  $\text{CDCl}_3:\text{MeOD}$ ) of **4**

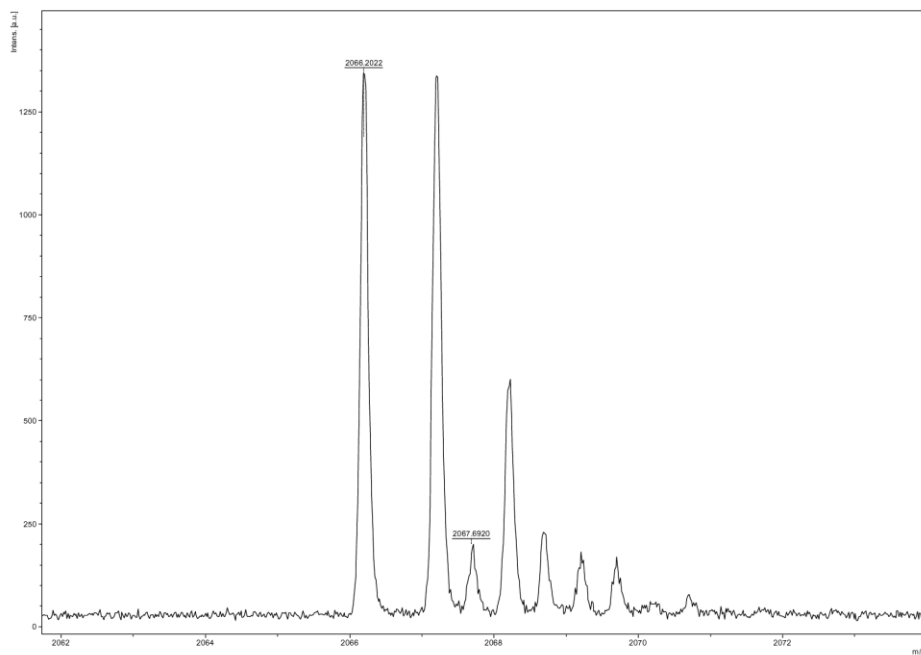
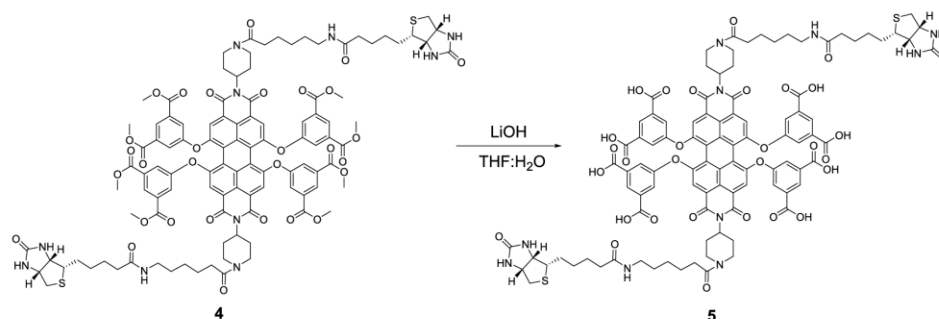


Figure S20. Mass spectrum (MALDI+, DCTB) of **4**

***N,N'*-Bis-(4-(1-oxo-6-biotinamidoethyl)piperidin-4-yl)-1,6,7,12-tetrakis(3,5-bis-(hydroxycarbonyl)phenoxy)perylene-3,4,9,10-tetracarboxylic diimide 5.**



**Figure S21.** Synthesis of **5**.

Lithium hydroxide (21 mg, 0.92 mmol) dissolved in H<sub>2</sub>O (2 mL) were added to *N,N'*-bis-(4-(1-oxo-6-biotinamidoethyl)piperidin-4-yl)-1,6,7,12-tetrakis(3,5-bis(methoxycarbonyl)phenoxy)perylene-3,4,9,10-tetracarboxylic diimide **4** (24 mg, 0.01 mmol) dissolved in THF (8 mL). The mixture was stirred at 45 °C overnight. The solvents were removed under reduced pressure and the residue neutralized with amberlite IR-120 ion exchange resin to obtain a brown oil-solid **5** in 99% yield (23.5 mg, 0.01 mmol). *R<sub>f</sub>* (MeOH): 0, mp > 350 °C. FT-IR (KBr, cm<sup>-1</sup>): 3431 (O-H), 2940 (C-H), 2857 (C-H), 2781 (C-H), 1976 (C-H), 1635 (CONH), 1567 (C<sub>Ar</sub>-C<sub>Ar</sub>), 1454 (CH<sub>2</sub>), 1408 (CH<sub>2</sub>), 1385 (O-H), 1320 (C-N), 1260 (C-O), 1206, 1152, 1124, 1104, 1022, 968, 871, 596 (fingerprint region). <sup>1</sup>H NMR (300 MHz, D<sub>2</sub>O) δ: 7.88 (s, 2H, H<sub>Ar</sub>), 7.77 (d, *J* = 8.7 Hz, 2H, H<sub>Ar</sub>), 7.64 (d, *J* = 6.8 Hz, 2H, H<sub>Ar</sub>), 7.53 (s, 4H, H<sub>Ar</sub>), 7.43 – 7.32 (m, 6H, H<sub>Ar</sub>), 4.56 – 4.53 (m, 2H, CH), 4.36 – 4.32 (d, 2H, CH), 3.62 – 3.50 (m, 2H, CH<sub>2</sub>), 3.32 – 3.22 (m, 4H, CH<sub>2</sub>), 3.13 (t, *J* = 6.8 Hz, 3H, CH<sub>2</sub>), 2.93 (dd, *J* = 18.1 Hz, *J* = 5.3 Hz, 4H, CH<sub>2</sub>), 2.73 (d, *J* = 13.1 Hz, 2H, CH<sub>2</sub>), 2.59 (m, 3H, CH<sub>2</sub>), 2.42 – 2.28 (m, 4H, CH<sub>2</sub>), 2.14 (m, 5H, CH<sub>2</sub>), 2.01 (s, 5H, CH<sub>2</sub>), 1.57 – 1.45 (m, 15H, CH<sub>2</sub>), 1.35 – 1.29 (m, 10H, CH<sub>2</sub>). <sup>13</sup>C NMR (101 MHz, D<sub>2</sub>O) δ: 176.8 (CO), 165.5 (CO), 143.4 (C<sub>Ar</sub>), 127.4 (C<sub>Ar</sub>), 125.3 (CH), 125.3 (CH), 117.9 (C<sub>Ar</sub>), 111.5 (CH), 62.2 (CH), 60.4 (CH), 55.5 (CH), 39.9 (CH<sub>2</sub>), 39.4 (CH<sub>2</sub>), 37.7 (CH<sub>2</sub>), 35.7 (CH<sub>2</sub>), 28.3 (CH<sub>2</sub>), 28.0 (CH<sub>2</sub>), 27.8 (CH<sub>2</sub>), 27.3 (CH<sub>2</sub>), 26.3 (CH<sub>2</sub>), 25.7 (CH<sub>2</sub>), 25.4 (CH<sub>2</sub>). HRMS (MALDI-, DHB neg.): *m/z* calcd for C<sub>98</sub>H<sub>94</sub>N<sub>10</sub>O<sub>30</sub>S<sub>2</sub> (M<sup>+</sup>): 1954.5573; found: 1954.5588. One single peak detected by HPLC by UV-vis and fluorescence detection. Φ (H<sub>2</sub>O) = 0.64 ± 0.01. Fluorescence Lifetime τ/ns (H<sub>2</sub>O, χ<sup>2</sup>): 6.57 (1.01).

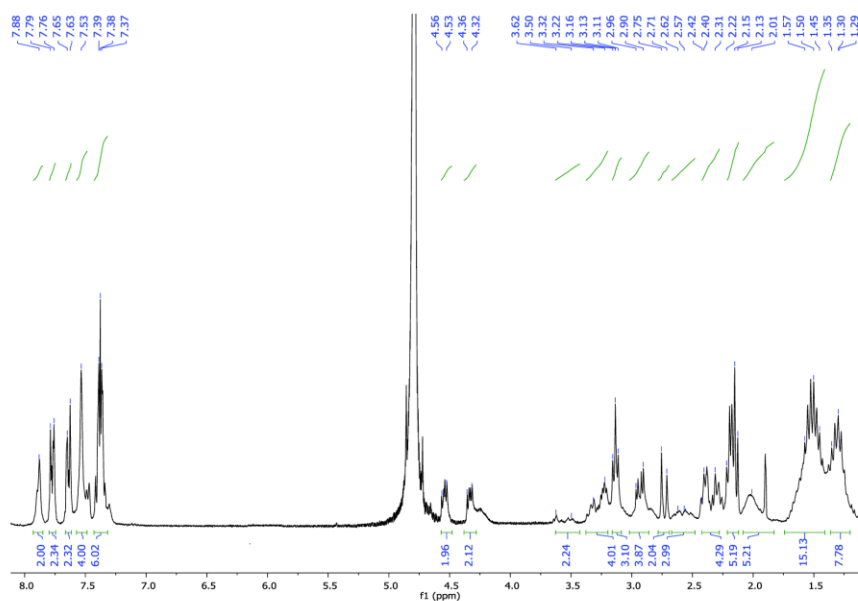


Figure S22.  $^1\text{H}$  NMR (300 MHz,  $\text{D}_2\text{O}$ ) of 5

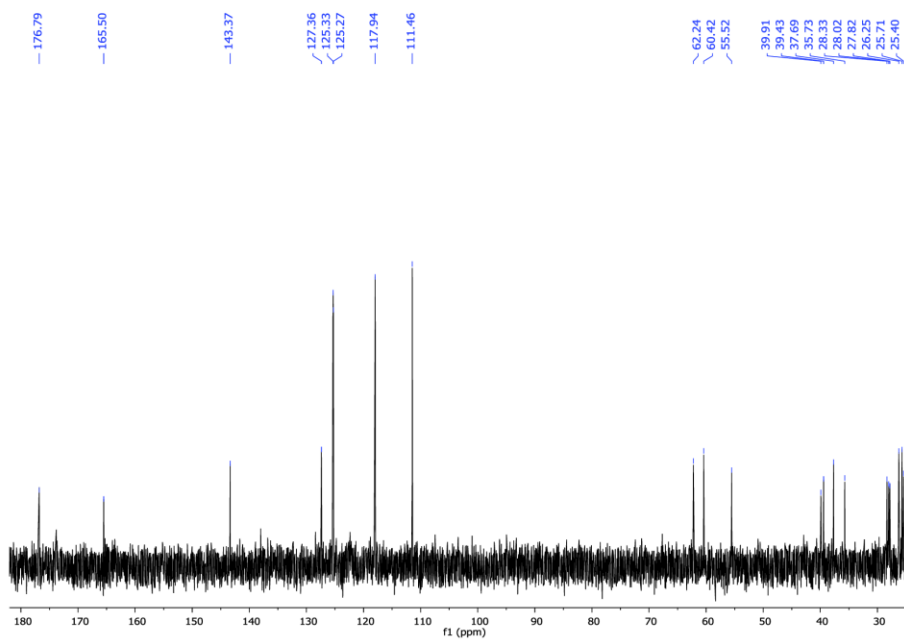


Figure S23.  $^{13}\text{C}$  NMR (101 MHz,  $\text{D}_2\text{O}$ ) of 5

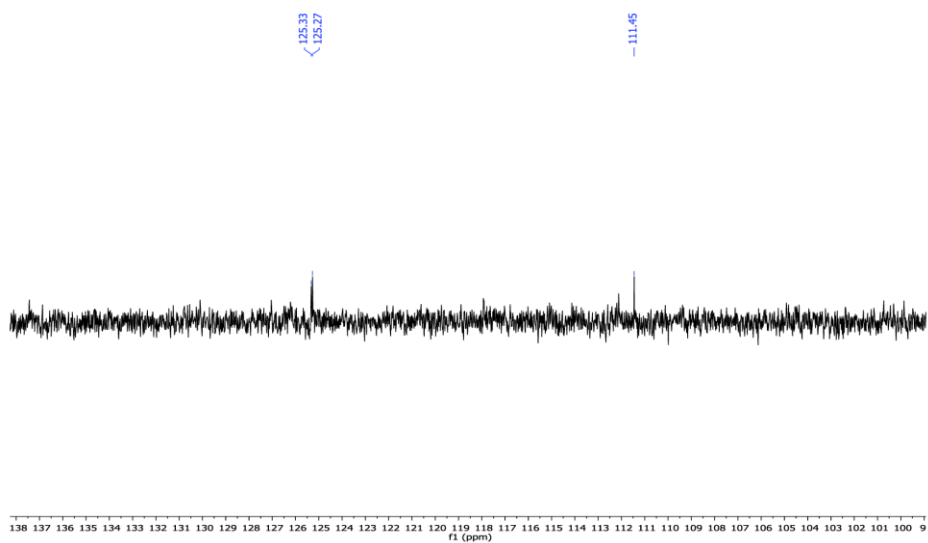


Figure S24.  $^{13}\text{C}$  NMR-DEPT-135 (101 MHz,  $\text{D}_2\text{O}$ ) of **5**

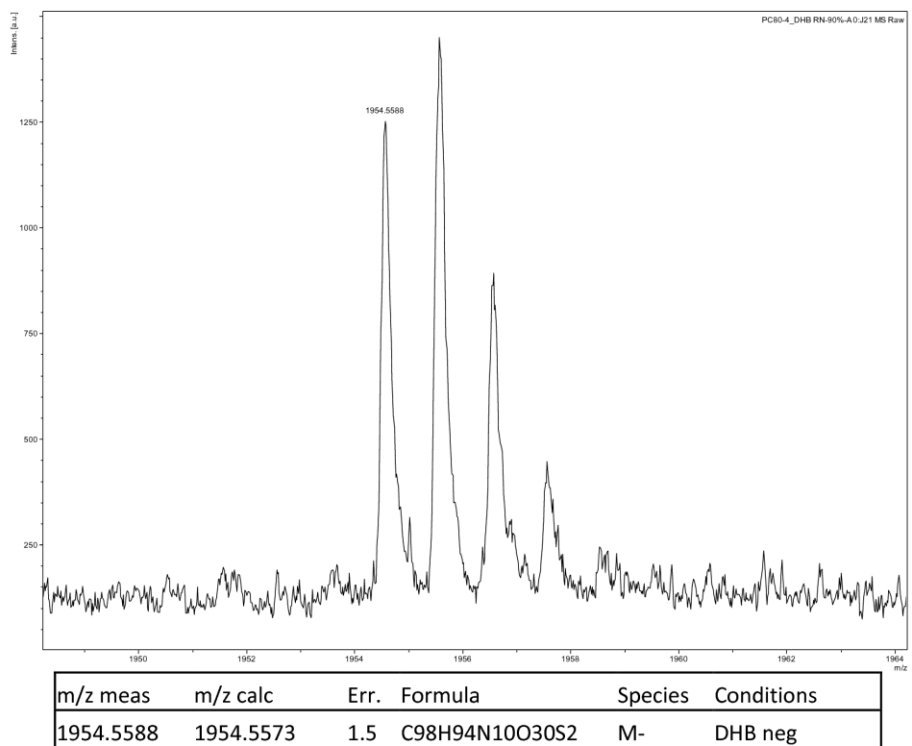
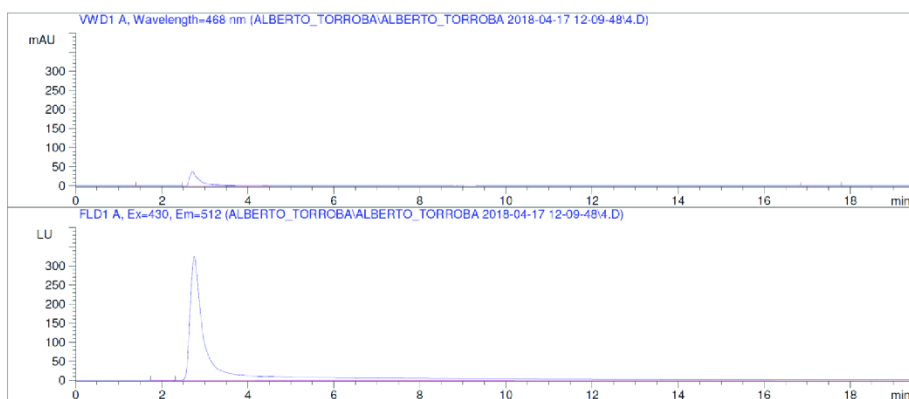
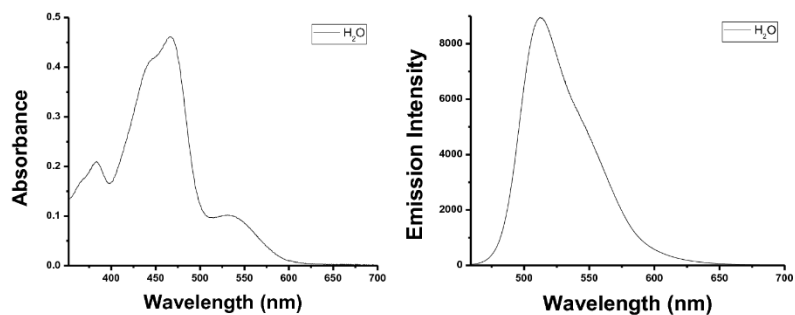


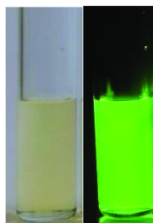
Figure S25. Mass spectrum (MALDI-, DHB neg) of **5**



**Figure S26.** HPLC of **5**. Signal 1 detected by UV-vis: VWD1 A, Wavelength = 468 nm. Signal 2 detected by fluorescence: FLD1 A, Ex = 430, Em = 512 nm



**Figure S27.** Left: Absorbance spectrum of **5**. Right: Fluorescence spectrum of **5**.



**Solvent:** Water.

**Figure S28.** Solutions of **5** under white light and UV light, 366 nm.



## Materials

All the oligonucleotides used in this work were purchased from Eurogentec as dried samples. Stock solutions of 100  $\mu$ M were prepared with doubly deionised water and stored at -20 °C. Oligonucleotide strands concentration were spectrophotometrically determined at  $\lambda = 260$  nm using the absorptivity coefficients provided by the manufacturer. The double-labelled oligonucleotides have as donor fluorophore in the 5' end FAM (6-carboxyfluorescein) and the acceptor fluorophore in the 3' end was TAMRA (6-carboxytetramethylrhodamine). Sequences of all the oligonucleotides used in this work are collected in Table S1.

**Table S1.** Sequences of the oligonucleotides used in this work

Name	Sequence (5'—3')	Type and Topology
cmyc	TGAGGGTGGGTAGGGTGGGTAA	3-tetrad Parallel DNA G-quadruplex of <i>c-myc</i> promoter
Tel22	AGGGTTAGGGTTAGGGTTAGGG	3-tetrad Hybrid DNA G-quadruplex of human telomere
Bom17	GGTTAGGTTAGGTTAGG	2-tetrad Antiparallel DNA G-quadruplex of <i>Bombyx</i> telomere
TBA	GGTTGGTGTGGTTGG	2-tetrad Antiparallel DNA G-quadruplex of Thrombin binding aptamer
i-cmyc	TTACCCACCCTACCCACCCTCA	DNA i-motif
ds26	CAATCGGATCGAATTCGATCCGATTG	DNA Duplex
d17a	CCAGTTCGTAGTAACCC	Single stranded DNA
F21T	FAM -GGGTAGGGTTAGGGTTAGGG-TAMRA	Doubly labelled 3-tetrad Hybrid DNA G-quadruplex of human telomere
F21RT	FAM-GGGUUAGGGUUAGGGUUAGGG-TAMRA	Doubly labelled 3-tetrad Parallel RNA G-quadruplex of human telomere
F25CebT	FAM-AGGGTGGGTGTAAGTGTGGGTGGGT-TAMRA	Doubly labelled 3-tetrad Parallel DNA G-quadruplex of human minisatellite
F21CTAT	FAM-GGGCTAGGGCTAGGGCTAGGG-TAMRA	Doubly labelled 3-tetrad Antiparallel DNA G-quadruplex of human telomere
FmycT	FAM-TTGAGGGTGGGTAGGGTGGGTAA-TAMRA	Doubly labelled 3-tetrad Parallel DNA G-quadruplex of <i>c-myc</i> promoter
FBom17T	FAM-GGTTAGGTTAGGTTAGG-TAMRA	Doubly labelled 2-tetrad Antiparallel DNA G-quadruplex of <i>Bombyx</i> telomere
FTBAT	FAM-GGTTGGTGTGGTTGG-TAMRA	Doubly labelled 2-tetrad Antiparallel DNA G-quadruplex of Thrombin binding aptamer
FdxT	FAM-TATAGCTAT-hexaethyleneglycol-TATAGCTATA-TAMRA	Intramolecular duplex

Oligonucleotides were prepared by dissolving the stock solutions in annealing buffer consisting of 90 mM LiCl, 10 mM lithium cacodylate (LiCaC) and 10 mM KCl at pH = 7.2 unless otherwise is stated. The resulting solutions were heated at 90 °C during 5 minutes and then slowly cooled to room temperature.

## Methods

**Quantum Yields and Fluorescence Lifetime measurements** were performed in a FLS980 equipment (Edinburgh Instruments). The quantum yield was measured with an integration sphere.<sup>[1]</sup> The precision of this method is checked by repeating three times each sample obtaining an error always inferior to 2%. The photoexcitation was made with a EPL 475 pulse diode laser and the data emission collected at 540 nm was analyzed by FAST 3.4.0 software.

**Quenching measurements** were carried out in 384-well plates (Greiner Bio-one 384-well black flat bottom) with a microplate reader (Tecan Infinite M1000). Fluorescence of a final volume of 40  $\mu\text{L}$  containing 2  $\mu\text{M}$  of **PDI2B** in the presence and absence of different amounts of DNA were recorded at  $\lambda_{\text{exc}} = 530 \text{ nm}$ ,  $\lambda_{\text{em}} = 657 \text{ nm}$  and 25  $^{\circ}\text{C}$  by triplicate. For the i-motif, i-cmyc, the buffer was adjusted at pH = 5.8.

**FRET Melting Assay** was performed in a real time PCR (Mx3005P, Stratagene). The doubly labelled oligonucleotides were annealed at a final concentration of 0.25  $\mu\text{M}$  in the annealing buffer by the procedure previously described instead F21RT which was prepared in buffer containing 99 mM LiCl, 10 mM LiCaC and 1 mM KCl at pH = 7.2. The samples containing 0.2  $\mu\text{M}$  oligonucleotide in the absence and in the presence of different excess of **PDI2B** were prepared in 96-well plates and scanned from 25 to 95 $^{\circ}\text{C}$  at 1 $^{\circ}\text{C}/\text{min}$ . The emission of FAM was measured during the denaturation in labelled oligonucleotide. The stabilisation induced by **PDI2B** was calculated as the difference between the mid-transition temperature of the oligonucleotide ( $\Delta T_m$ ) with and without **PDI2B**.

**Isothermal Titration Calorimetry (ITC) experiments** were carried out at 25 $^{\circ}\text{C}$  in a Nano ITC (TA Instruments, Newcastle, USA) by adding increasing amounts of **PDI2B** (D) to the calorimetric cell containing Tel22 or Bom 17 solutions (P). Prior to use all solutions were degassed during 30 minutes in a degassing station (TA Instruments, Newcastle, USA). Dilution control experiments were performed to determine the contribution of the heat of dilution of **PDI2B** and rule out drug aggregation. The thermograms (integrated area of the peaks corrected by the dilution effect/mole injectant as a function of  $C_D/C_P$  ratio) were fitted by means of NanoAnalyse Software (TA Instruments, Newcastle, USA) using the "Independent Sites" model.

**Circular Dichroism Titrations** were carried out in a JASCO J-815 CD spectrometer equipped with a temperature control Peltier system. Titrations were carried out by adding increasing amounts of **PDI2B** solution to the DNA solutions in 1 cm path-length cells with black quartz sides at 25  $^{\circ}\text{C}$ . The CD spectra were recorded after each addition and some of them (1:10 and 1:1 **PDI2B**-DNA ratio) also after heating to 90  $^{\circ}\text{C}$  during 5 min and slowly cooling down to 25  $^{\circ}\text{C}$ .

**MD simulations.** Sequence and structure of the employed G-quadruplexes in the experimental assays were taken from the *Protein Data Bank*, Bom17 PDB id "2LYG",<sup>[2]</sup> and Tel22 PDB id "2HY9".<sup>[3]</sup> The starting molecular structure and atomic partial charges of the organic compound **PDI2B** were obtained by geometry optimization through semiempirical PM6 calculations,<sup>[4]</sup> in the presence of water as implicit solvent, mimicked by the "conductor-like polarized continuum model" implicit method (Fig. 29SI).<sup>[5]</sup> Force-field parameters of **PDI2B** and the DNA model were generated with the ACPYPE software.<sup>[6]</sup> A triclinic box of TIP3P water was generated around the G-quadruplex and **PDI2B**, Figure 30SI, to a depth of 0.8 and 1.2 nm on each side of the solutes, for a total of about 5500 and 8750 solvent molecules for Bom17 and Tel22 G-quadruplex, respectively. 31  $\text{K}^+$  ions for Bom17 and 39  $\text{K}^+$  ions for Tel22 in addition to 17  $\text{Cl}^-$  ions were added to neutralize the DNA negative charge of the sugar-phosphate backbone and to set the solution ionic strength to about 0.15 M. Explicit water solvent molecular dynamics simulations of the **PDI2B**/DNA systems were performed in the canonical NPT ensemble (for which number of particles,  $N$ , pressure,  $P$ , and temperature,  $T$ , are constants), at a temperature of 300 K, under control of a velocity-rescaling thermostat.<sup>[7]</sup> The particle mesh Ewald method<sup>[8]</sup> was used to describe long-range interactions. Preliminary energy minimizations were run for 5000 steps with the steepest descent algorithm, during which the equilibration **PDI2B** and the G-quadruplex system were harmonically restrained with a force constant of 1000  $\text{kJ mol}^{-1} \text{ nm}^{-2}$ , gradually relaxed into five consecutive steps of 100 ps each, to 500, 200, 100 and 50  $\text{kJ mol}^{-1} \text{ nm}^{-2}$ . The MD simulations were conducted for 500 ns and 600 ns for the **PDI2B** /Bom17 and the **PDI2B** /Tel22 systems respectively.

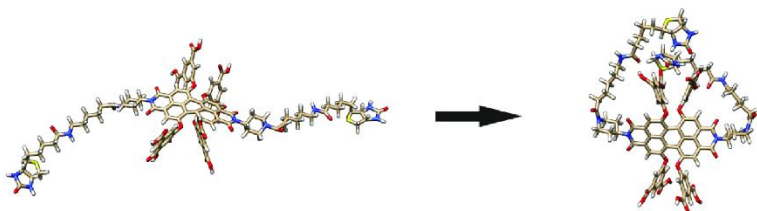


**Figure S29.** PD12B initial (left) and optimized (right) structures obtained by PM6 calculations.

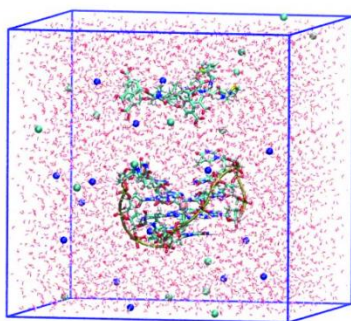


**Figure S30.** PBC box generated for the PD12B /Bom17 system; water molecules represented as red dots and ions as blue (Na<sup>+</sup>) and cyan (Cl<sup>-</sup>) spheres.

**Fishing with magnetic beads:** a vial containing 600  $\mu\text{L}$  of streptavidin coated magnetic beads (Streptavidin MagneSphere Paramagnetic Particles, Promega) was washed twice in annealing buffer. Then, 1 ml of 1  $\mu\text{M}$  of PD12B whose fluorescence was previously measured at  $\lambda_{\text{exc}} = 530 \text{ nm}$  and  $\lambda_{\text{em}} = 657 \text{ nm}$  in a Fluoromax 4 spectrofluorimeter (Horiba Scientific), was added to the vial containing the magnetic beads and incubated for 5 min at room temperature mixing by inversion every 1 – 2 min. The supernatant was magnetically separated from the beads, its fluorescence measured again to know the amount of PD12B attached to the magnetic beads and discarded. Approximately the 97% of PD12B remain attached to the magnetic beads. In a second step, 1ml of DNA oligonucleotide 1  $\mu\text{M}$  whose absorbance was previously measured by triplicate in a Nanodrop ND-1000 spectrophotometer (Thermo Scientific) was added to the modified magnetic beads and incubated for other 5 min at room temperature mixing by inversion every 1 – 2 min. The supernatant was magnetically separated and its DNA concentration was determined by absorbance measurements and conserved for further steps. The modified magnetic beads were washed twice with warm water (5' at 37°C) and then incubated again with the conserved supernatant of the previous step to start a new cycle. Several oligonucleotides in different conformations (d17a as single stranded DNA, ds26 as duplex, Bom17 and TBA as 2-tetrads G4 and Tel22 as 3-tetrads G4) were used, one at a time. As to the competition fishing experiments performed, the procedure is very similar. Once PD12B is attached to the magnetic beads, we added 1 ml of 1  $\mu\text{M}$  of a labelled Bom17 with FAM (FBom17) alone and/or in the presence of competitors whose fluorescence was previously read ( $\lambda_{\text{exc}} = 490 \text{ nm}$ ) on a microplate reader (Cytation 5 Cell Imaging Multimode Reader, Biotek Instruments, USA). As to competitors, 10 fold excess of single stranded DNA (d17a), duplex (ds26) and 3-tetrads G-quadruplex structure (Tel22) were used, the latter also in

equimolar conditions respect to FBom17. Next steps are almost the same described above, but the FBom17 content in the supernatant is now measured by fluorescence.

**Cytotoxicity** was studied by means of the CellTiter Non Radioactive Cell Proliferation Assay (Promega). Approximately  $3 \times 10^3$  HeLa cells were cultured in EMEM (Eagle's Minimum Essential Medium medium) supplemented with 10% Fetal Bovine Serum in 96-well plates and incubated at 37 °C under a 5% CO<sub>2</sub> atmosphere. The cells were grown for 24 h and then treated with different concentrations of **PD12B** for 72 h. Then, we proceed according to the technical specifications. Absorbance was read at 570 nm in a microplate reader (Tecan Infinite M1000). Three replicates per dose were included.

### A. Fluorescence Lifetimes Measurements

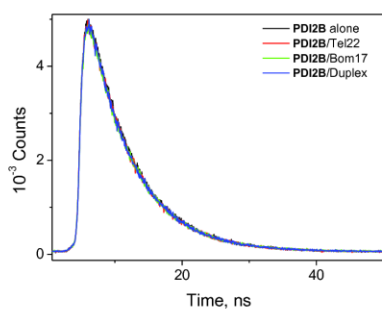


**Figure S31.** Fluorescence lifetime measurement for **PD12B** ( $C_D = 4 \mu\text{M}$ ) in the absence and in the presence of different telomeric G-quadruplexes, Tel22 and Bom17,  $C_P/C_D = 5$ ,  $\lambda_{\text{exc}} = 475 \text{ nm}$ ,  $\lambda_{\text{em}} = 540 \text{ nm}$ ,  $\text{pH} = 7.2$ ,  $I = 0.11 \text{ M}$  (90 mM LiCl, 10 mM KCl, 10 mM LiCaC) and  $T = 25 \text{ }^\circ\text{C}$ .

## B. Titrations

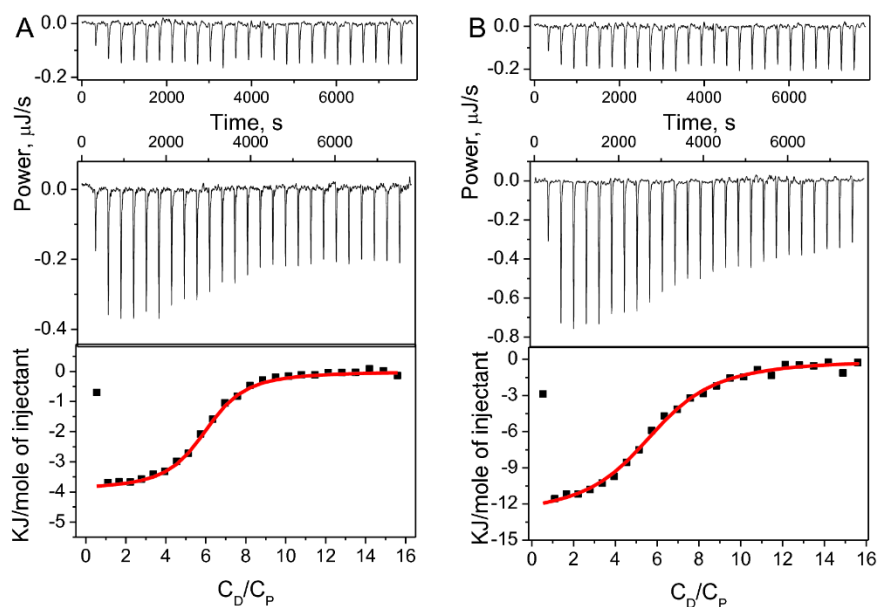


**Figure S32.** ITC Titrations of **PDI2B** with Bom17 (A) and with Tel 22 (B) and fitting for “Independent Sites” model of the obtained data pairs (red line).  $C_D = 1$  mM in (A) and 1.5 mM in (B),  $C_P/C_D = 0-15.6$ , pH = 7.2, I = 0.11 M (90 mM LiCl, 10 mM KCl, 10 mM LiCaC) and T = 25 °C.

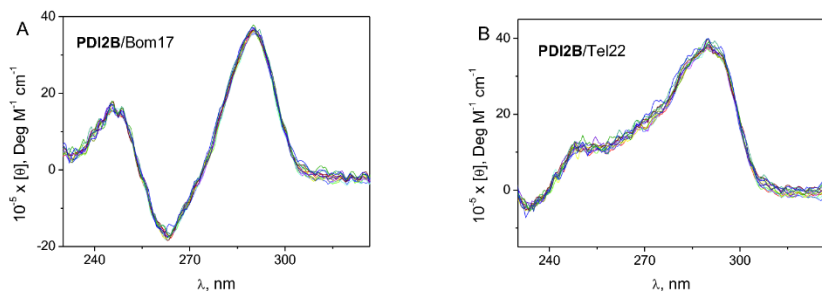


**Figure S33.** CD spectra for **PDI2B/Bom17** (A) and **PDI2B/Tel22** (B) systems.  $C_P = 2$   $\mu$ M  $C_D/C_P = 0-5$ , pH = 7.2, I = 0.11 M (90 mM LiCl, 10 mM KCl, 10 mM LiCaC) and T = 25 °C.

### C. Computational Results

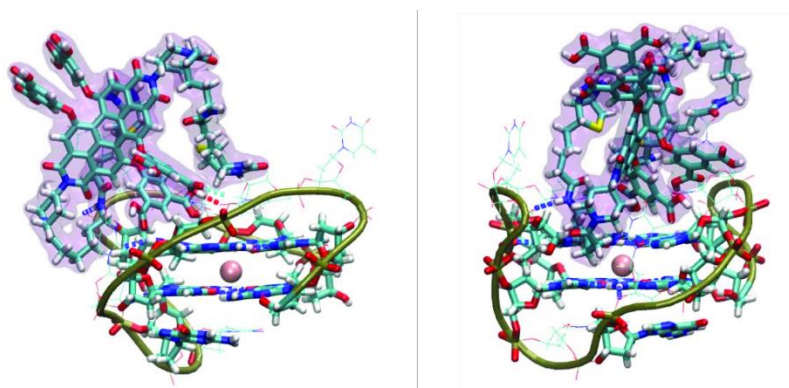


**Figure S34:** Two different views of the final structure of **PDI2B/Bom17**; **PDI2B** is highlighted by a purple surface.

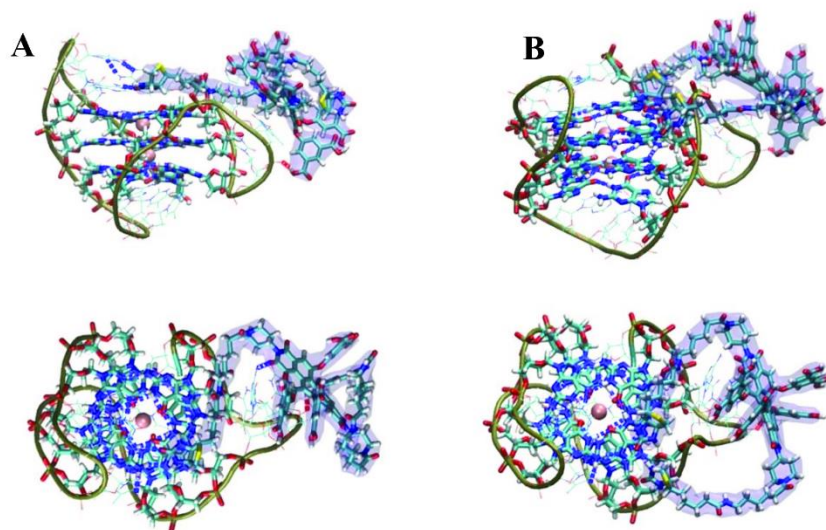


**Figure S35:** Top and side views of the most frequently occurring structures at the equilibrium phase of the MD simulation, mimicking the binding of **PDI2B** (purple surface) with Tel22. (A) **PDI2B** with one arm inserted into the DNA groove; (B) **PDI2B** “embraced” to the GGGTAA loop, through both arms.

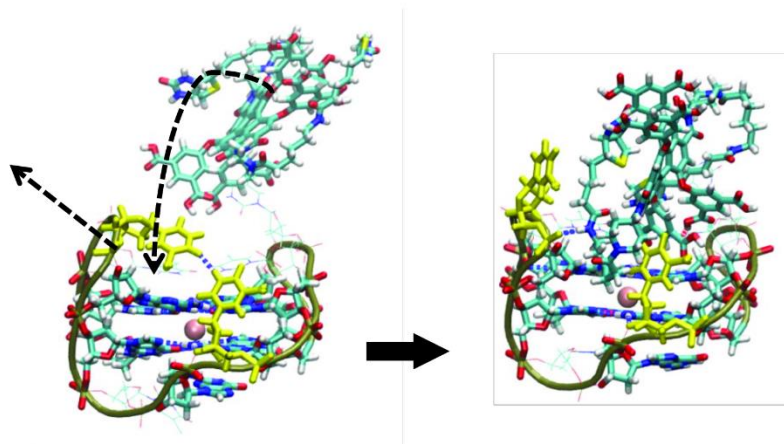


**Figure S36:** Insertion of **PDI2B** in the molecular cleft of Bom17 generated during the MD simulation.

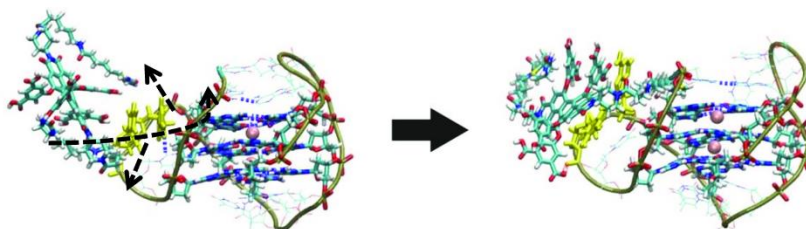


**Figure S37:** Key step in the molecular recognition process for **PDI2B/Tel22** system: the first biotin arm is inserted and stacking interactions begin. Interacting bases highlighted yellow, thymine above, adenine below.



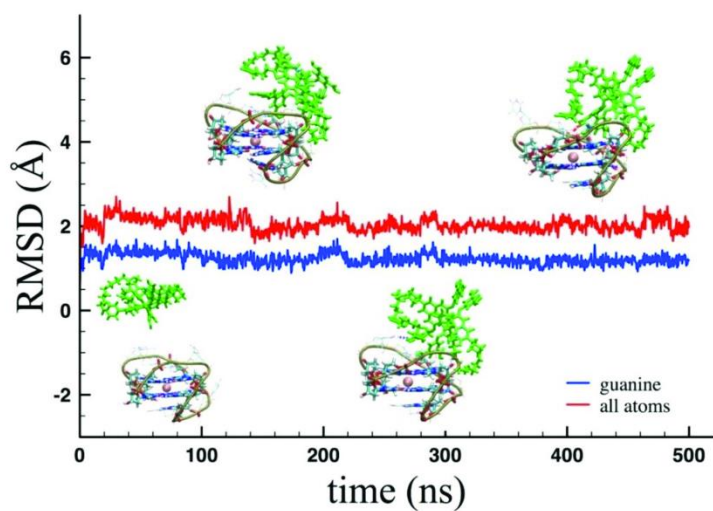


**Figure S38:** RMSD plot for Bom17 structure in the presence of **PDI2B** in green (all atoms: red, guanine bases: blue).

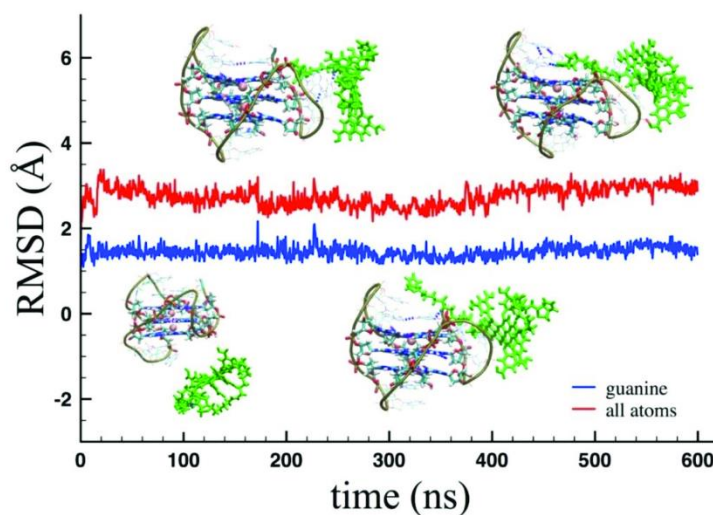


**Figure S39:** RMSD plot for Tel22 structure in presence of **PDI2B** in green (all atoms: red, guanine bases: blue).

Geometry clustering was performed to identify and sample the structures most often occurring during the last part (i.e. the equilibrium phase) of the MD for **PDI2B**/Tel22 system. The first seven most populated clusters can be grouped into two main structural types (see overlapped structures, Figures 40SI and 41SI) in which the clusters of each group only differs by the oscillation of side chains of the ligand molecules. These clusters represent 66% of equilibrium structures, therefore the two structures (Figure 35SI) can be considered as equilibrium structures.



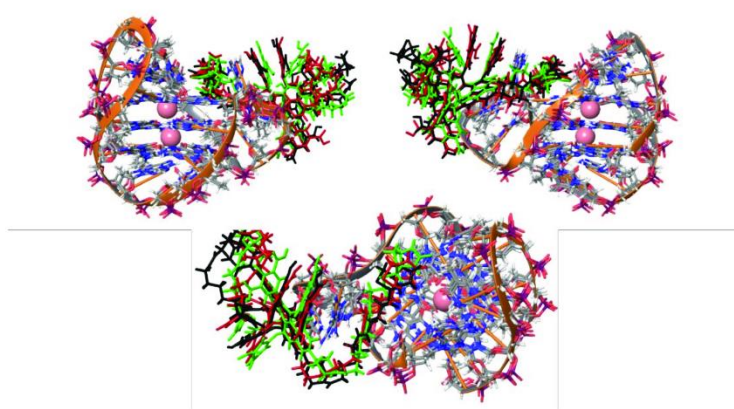


Figure S40. Cluster group 1 for the **PDI2B**/Tel22 system, each formed by 3 overlapped structures.

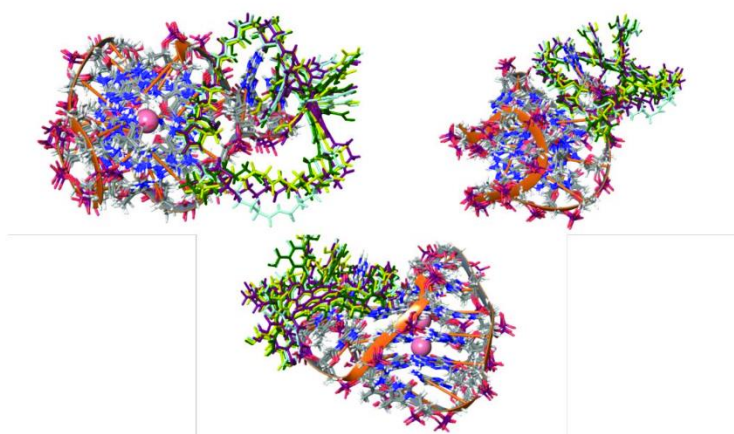


Figure S41. Cluster group 2 for the **PDI2B**/Tel22 system, each formed by 4 overlapped structures.

#### D. Cytotoxicity

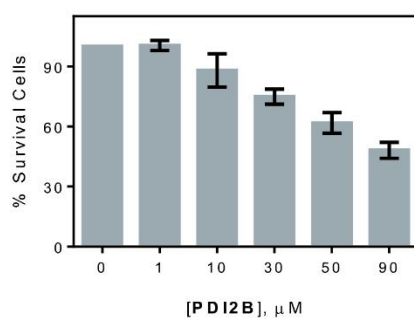


Figure S42. % Survival HeLa cells *versus* **PDI2B** concentration after 72 h of incubation.

## References

- [1] C. Würth, M. Grabolle, J. Pauli, M. Spieles, U. Resch-Genger, *Nat. Protoc.*, **2013**, *8*, 1535-1550.
- [2] I. Gómez-Pinto, E. Vengut-Climent, R. Lucas, A. Aviñó, R. Eritja, C. González and J. C. Morales, *Chem. Eur. J.*, **2013**, *19*, 1920-1927.
- [3] J. Dai, C. Punchihewa, A. Ambrus, D. Chen, R. A. Jones and D. Yang, *Nucleic Acids Res.*, **2007**, *35*, 2440-2450.
- [4] J. J. P. Stewart, *J. Mol. Model.*, **2007**, *13*, 1173-1213.
- [5] a) V. Barone and M. Cossi, *J. Phys. Chem. A.*, **1998**, *102*, 1995-2001. b) M. Cossi, N. Rega, G. Scalmani and V. Barone, *J. Comput. Chem.*, **2003**, *24*, 669-681.
- [6] a) A. W. Sousa Da Silva, W. F. Vranken, E. D. Laue, ACPYPE – Antechamber Python Parser Interface, <http://code.google.com/p/acpype>. b) J. Wang, R. M. Wolf, J. W. Caldwell, P. A. Kollman and D. A. Case, *J. Comput. Chem.*, **2004**, *25*, 1157-1174. c) J. Wang, W. Wang, P. A. Kollman and D. A. Case, *J. Mol. Graph. Model.*, **2006**, *25*, 247-260.
- [7] G. Bussi, D. Donadio and M. Parrinello, *J. Chem. Phys.*, **2007**, *126*, 014101.
- [8] T. Darden, D. York and L. Pedersen, *J. Chem. Phys.*, **1993**, *98*, 10089-10092.



# **Chapter VIII**

---

**The interaction of Rh and Ir complexes with different G-quadruplex conformations**

## 8.1 Introduction

As previously mentioned, FRET DNA melting assays allow to study the binding toward different G-quadruplex sequences in a very fast mode and with diluted samples without spending large quantities of reagents. Different series of 17 metal complexes, divided into 4 main groups, and some of their isolated ligands have been considered as potential G-quadruplex binders. The large number of potential G4 forming sequences spread throughout the genome<sup>[136,137]</sup> renders G4 an attractive research field, as these structures have been reported to be involved in a wide range of biological processes such as telomere maintenance,<sup>[138]</sup> genome stability, regulation of oncogene expression, replication or translation.<sup>[139]</sup> In particular, the role of different substituents in the ligands and of the metal center was also investigated. This preliminary study allowed to screen the selected compounds for further investigation of their properties.

## 8.2 Materials and methods

### 8.2.1 Materials

The complexes have been synthesized by the group of Dr. Espino, Inorganic Chemistry (university of Burgos, Spain), and can be grouped into 3 families as shown below in **Figures 1-4**.

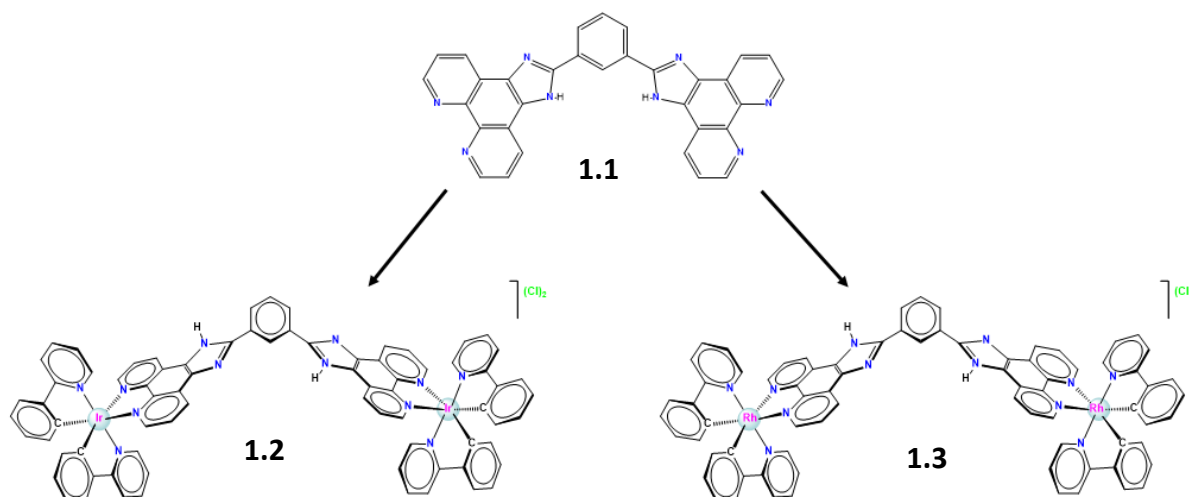


**Figure 1.** Group 1.

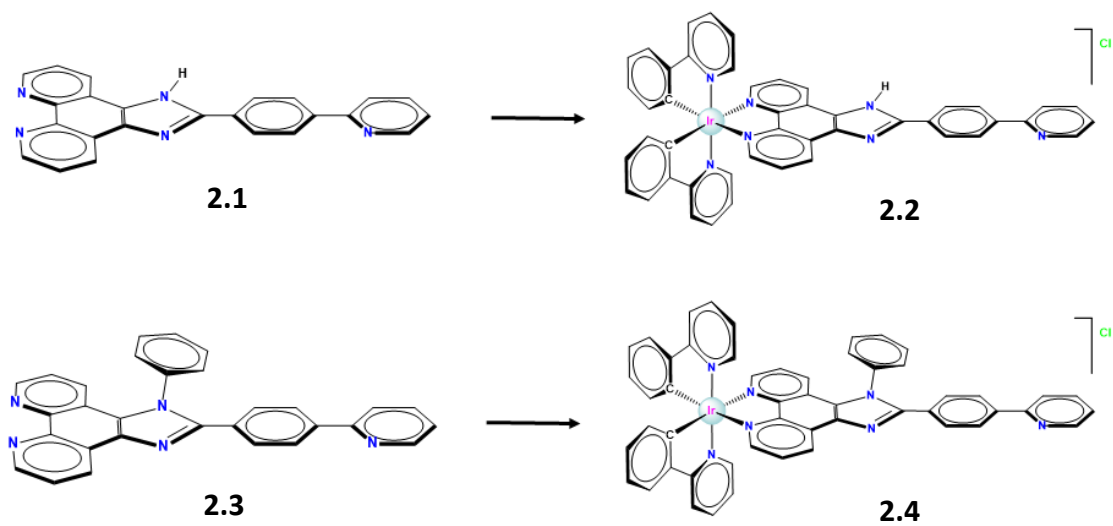


**Figure 2.** Group 2.

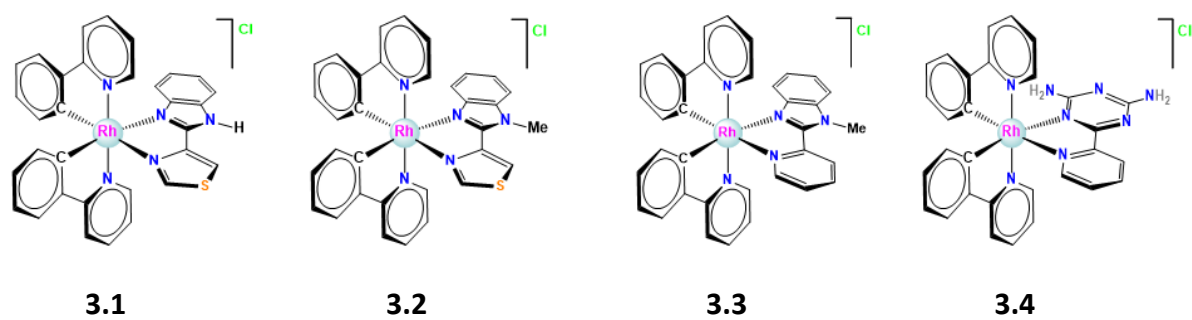


**Figure 3.** Group 3.

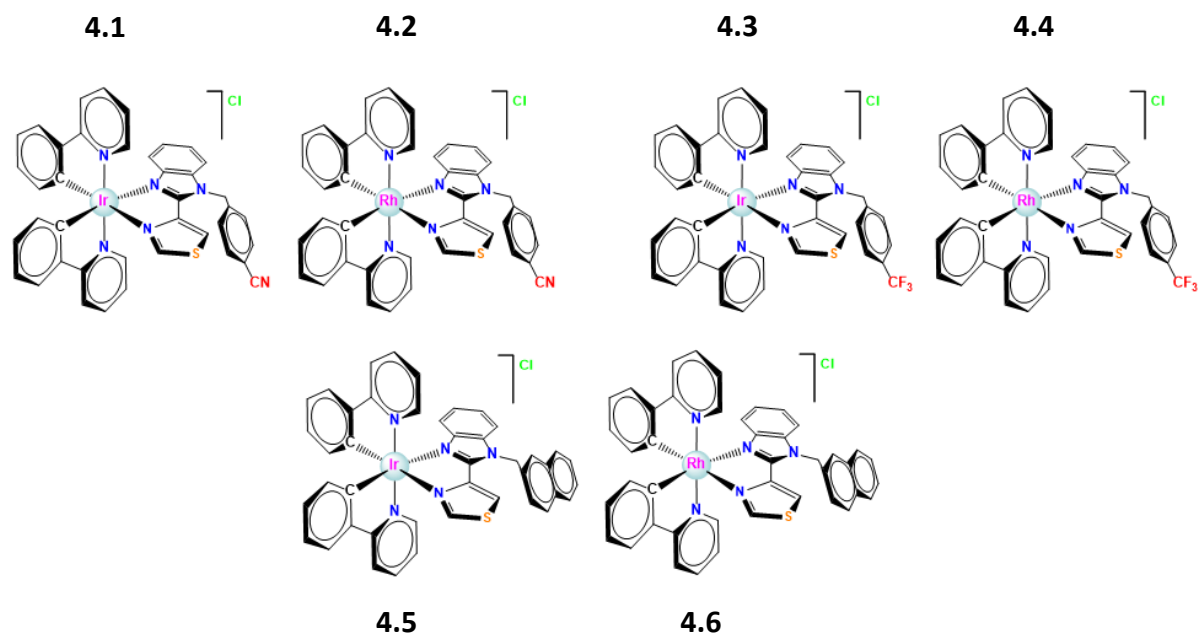


**Figure 4.** Group 4.

### 8.2.2 Experimental techniques

*FRET melting assays.* The employed oligonucleotides are described in **Table 1** section **2.2.1.** and the technique is described in **section 2.1.1.5** (See **Chapter II**).

*Competition assays.* The FRET melting can be performed in the presence of competitor such as double stranded DNA ds16 (5'-CAATCGGATCGAATTCGATCCGATTG-3') in order to determine the selectivity of **2.2** and **2.4** toward the G-quadruplex over the ds26 was added to **FTBAT**/drug mixture (TBAT has been chosen as it was the one which shows the higher  $\Delta T_m$ ). Since the ds26 is not labeled it does not interfere with the fluorescent measurements. Solutions were prepared analogously, except different concentrations of ds26 were added, from 0.2  $\mu\text{M}$  to 5  $\mu\text{M}$ , using a final volume of 25  $\mu\text{L}$ , 0.2  $\mu\text{M}$  of FTBAT, and 4  $\mu\text{M}$  of drug.

### 8.3 Results and discussion

*FRET DNA melting assays.* The collected results for each group are shown in a graph, **Figures 5-7**, that refers to the increase of the melting temperature values ( $\Delta T_m$ ) for each G-quadruplex conformation in the presence of the drug. First, for group 1, interesting and promising results were obtained, but they were not reproducible, working with stock solutions stored in the freezer, not reproducible results were obtained, surely due to the lack of stability of the drug in solution. Therefore group 1 was discarded and went back to the synthesis development. For group 2, initially the ligands were discarded as their  $\Delta T_m$  compared to the metal complexes was not



significant, but complexes **2.2** and **2.4** generated interesting results, shown in **Figure 5**.

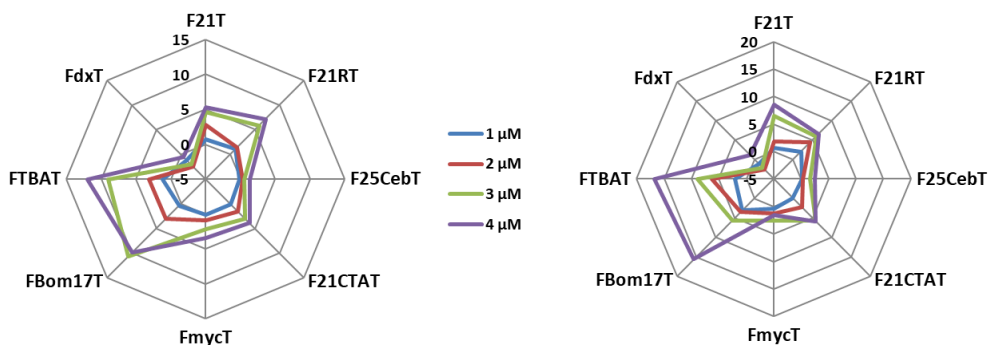


**Figure 5.**  $\Delta T_m$  spider plot for the different fluorescent oligonucleotides under increasing concentrations of **2.2** (left) and **2.4** (right)  $[C_{\text{oligo}}] = 0.2 \mu\text{M}$ ,  $\text{pH} = 7.4$  and  $I = 0.11$  (90 mM LiCl, 10 mM KCl and 10 mM LiCl, except for 21RT as described before).

Group 3 complexes do not show highly significant results, given that the temperature increases are quite low. However, it must be considered that the complexes are highly similar, so small changes in one of the substituents generates variations in  $\Delta T_m$ .

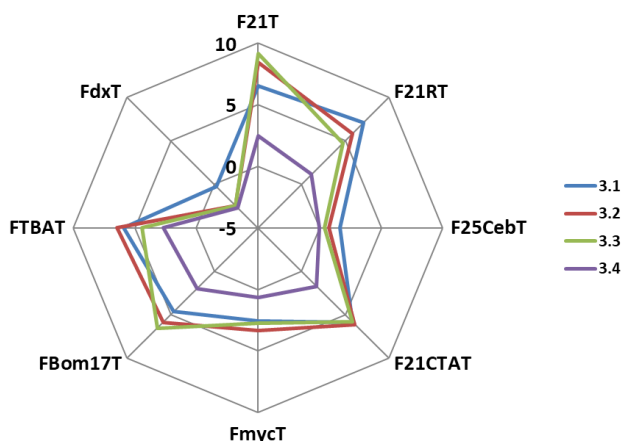


**Figure 6.**  $\Delta T_m$  spider plot for the different fluorescent oligonucleotides in presence of the complexes of group 3.  $[C_D] = 4 \mu\text{M}$ ,  $[C_{\text{oligo}}] = 0.2 \mu\text{M}$ ,  $\text{pH} = 7.4$  and  $I = 0.11$  (90 mM LiCl, 10 mM KCl and 10 mM LiCl, except for 21RT as described before).

In the case of group 4 quite different results were obtained, from complexes that barely interact, as **4.1**, to complexes that stabilize in more striking way, like **4.6**.

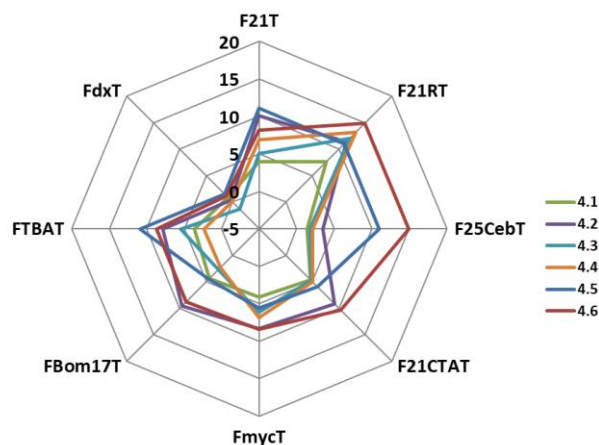


**Figure 7.**  $\Delta T_m$  spider plot for the different fluorescent oligonucleotides in presence of the complexes of group 4.  $[C_D] = 4 \mu\text{M}$ ,  $[C_{\text{oligo}}] = 0.2 \mu\text{M}$ ,  $\text{pH} = 7.4$  and  $I = 0.11$  (90 mM LiCl, 10 mM KCl and 10 mM LiCl, except for 21RT as described before).

Surprisingly, from the spider plots shown in **Figures 5-7**, it is noted that there is not stabilization for intramolecular duplex DNA, FdxT, suggesting a potential selectivity toward G-quadruplex. In order to verify this selectivity, it has been decided to accomplish the competition assays.

**Competition assays.** As it is shown in **Figure 5** complexes **2.2** and **2.4** exhibit strong affinity to FTBAT G-quadruplex, so that it was chosen for the competition assay. If the ligand is not selective, this value of  $\Delta T_m$  must decrease. The variation in the  $\Delta T_m$  values observed for **2.2** are not significant. By contrast, a slight decrease in the  $\Delta T_m$  values when the duplex DNA is in high excess (10-fold) respect G-quadruplex. Therefore, **2.2** seems to display rather selectivity towards G-quadruplex over duplex whereas **2.4** is not so a selective G-quadruplex binder.

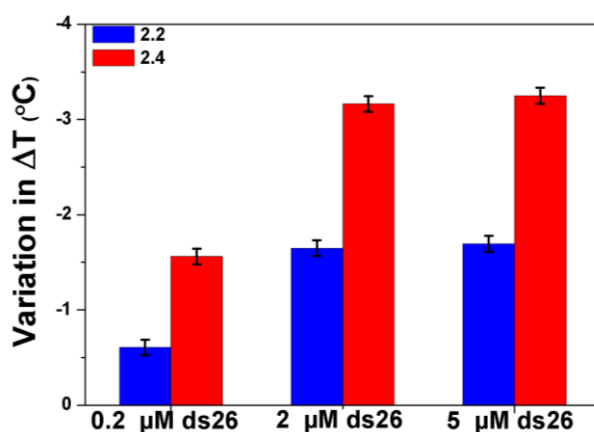


**Figure 8.**  $\Delta T_m$  change of FTBAT/2.2 (black) and FTBA/2.4 (red), under increasing concentrations of ds26.  $[C_{\text{oligo}}] = 0.2 \mu\text{M}$ ,  $[C_D] = 4 \mu\text{M}$ ,  $\text{pH} = 7.4$ ,  $I = 0.11$  (90 mM LiCl, 10 mM KCl and 10 mM LiCl). Means and standardized deviations for 3 experiments are shown.

## 8.4 Conclusions

Although results obtained by FRET-melting assays represent a modest stabilization, especially complexes of group 3 and 4, compared to other well-established G-quadruplex binders.<sup>[140,141]</sup> A remarkable stabilization for **Bom17** and **TBA** G-quadruplex was found in presence of complexes **2.2** and **2.4**, interestingly both formed by two tetrads, additionally **2.2** exhibits a remarkable selectivity for G-quadruplex than double helical DNA. But the most promising complex seems to be **4.6** since it generates high stabilization in several G-quadruplex conformation, while it has no affinity for the intramolecular helix DNA, consequently it will be considered for future studies. It is also of interest the possibility of evaluating the binding modes and make a comparison about how it affects G-quadruplex  $T_m$  depending on the ligands or the metal center, so that this study must still be continued.

According to the obtained results, as differences in  $T_m$  occur within each main group, it is being proposed to carry out MD analysis for each complex binding to G-quadruplex structures. The aim is to evaluate the effect of each substituent, within each main group, in the binding toward the G-quadruplex structures.



# **Chapter IX**

---

## **General overview**

### English

Despite the different subjects considered in **Chapters 3-8** presented in this thesis, they all have in common the combination of experimental and computational methods. This work methodology resulted to be very useful and has led to interesting results, as witnessed by the quality of the scientific journals in which they have been published. The combination of theoretical data and experimental results was originally presented as the main objective in the PhD project, and so it can be concluded that this aim has been achieved. From the student perspective, there has been a remarkable improvement of knowledge of different fields of theoretical and experimental and theoretical physical chemistry. This has led to the use of different techniques and methodologies, as well as the analysis and understanding of results in both experimental and computational fields

### Español

A pesar de que los **Capítulos 3-8** presentan estudios que conciernen a diferentes ámbitos, todos ellos presentan en común: la combinación de métodos tanto computacionales como experimentales. Esta metodología de trabajo ha resultado ser muy útil y ha conducido a resultados interesantes, como se demuestra en la calidad de las revistas científicas en las que han sido publicados. La combinación de datos teóricos y resultados experimentales se presentó como el objetivo principal de este proyecto de doctorado, de modo que se puede concluir que se ha conseguido. Desde la perspectiva de estudiante, se ha producido una mejora significativa en el conocimiento de distintos campos de la química física teórica y experimental. Ello ha conducido a la utilización de diferentes técnicas y metodologías, así como al análisis y comprensión de resultados en ambos campos experimental y computacional.

### Italiano

Nonostante i diversi argomenti considerati nei **Capitoli 3-8** presenti in questa tesi, tutti i capitoli presentano una caratteristica comune: la ricerca si basa sulla combinazione di metodi sperimentali e computazionali. Questa metodologia di lavoro si è rivelata molto utile e ha portato a risultati interessanti, come dimostrato dalla qualità delle riviste scientifiche in cui sono state pubblicate. La combinazione di risultati teorici e sperimentali è stata originariamente presentata come l'obiettivo principale del progetto di dottorato, e quindi si può concludere che questo obiettivo è stato raggiunto. Dal punto di vista dello studente, c'è stato un miglioramento significativo nella conoscenza di diversi campi della chimica fisica teorica e sperimentale. Ciò ha portato all'utilizzo di diverse tecniche e metodologie, nonché all'analisi e alla comprensione dei risultati in campi sia sperimentali che computazionali.

# **Chapter X**

---

## **Publications and conferences**

## ***Publications***

- Cristina Pérez-Arnaiz, Natalia Busto, Javier Santolaya, José M. Leal, Giampaolo Barone, Begoña García. Kinetic evidence for interaction of TMPyP4 with two different G-quadruplex conformations of human telomeric DNA, *BBA general subjects*. 1862 (2018) 522-531. doi: 10.1016/j.bbagen.2017.10.020.
- Natalia Busto, Patricia Calvo, Javier Santolaya, José M Leal, Aurore Guédin, Giampaolo Barone, Tomás Torroba, Jean-Louis Mergny, and Begoña García. Fishing for G-quadruplex in solution with a perylene diimide derivative labeled with biotins, *Chem. Eur. J.* 24 (2018) 1-6. doi: 10.1002/chem.201802365.
- Cristina Pérez-Arnaiz, Jorge Leal, Natalia Busto, María C. Carrión, Ana R. Rubio, Imanol Ortiz, Giampaolo Barone, Borja Díaz de Greñu, Javier Santolaya, José M. Leal, Mónica Vaquero, Félix A. Jalón, Blanca R. Manzano, and Begoña García. Role of seroalbumin in the cytotoxicity of cis-dichloro Pt(II) complexes with (N<sup>N</sup>)-donor ligands bearing functionalized tails, *Inorganic Chemistry*. 57 (2018) 6124-6134. doi:10.1021/acs.inorgchem.8b00713.
- *In preparation*: Javier Santolaya, Marta Martínez-Alonso, Natalia Busto, José M. Leal, Gustavo Espino and Begoña García. DNA binding of Ru(II) and Ir(III) half-sandwich complexes: experimental and computational studies.
- *In preparation*: Javier Santolaya, José M. Leal, Begoña García and Giampaolo Barone. Cis-dichlorodiamine complexes of Ni(II), Pd(II) and Pt(II): theoretical study of hydrolysis and DNA-binding.

## ***Conferences and schools***

- 13<sup>th</sup> European Biological Inorganic Chemistry Conference (EUROBIC 13), Budapest (Hungary). *Poster*: “Computational studies of the interaction of a dinuclear iridium complex and G-quadruplex DNA structures”
- IV Meeting Biotecnologie: “Ricerca di base interdisciplinare traslazionale in ambito biomedico”; November 2016. *Poster*: “Computational studies of the interaction of a dinuclear iridium complex and G-quadruplex DNA structures”. **Awarded** with Guiseppe Albeggiani prize, for the most creative poster.



- European Summer School in Quantum Chemistry (ESQC), Palermo, Sicily (Italy), September 2017.



# **Chapter XI**

---

## **Abbreviations and bibliography**

## **Abbreviations**

B-DNA	Deoxyribonucleic acid in double helical conformation
bp	Base pairs
bpyst	4,4'-bis( $\alpha$ -styrene)-2,2'-bipyridine
[C <sub>D</sub> ]	Ligand concentration
[C <sub>P</sub> ]	Polinucleotide concentration
[C <sub>oligo</sub> ]	Oligonucleotide concentration
ct-DNA	Calf thymus deoxyribonucleic acid
cispalladium	cis-diamminedichloropaladium(II)
cisplatin	cis-diamminedichloroplatinum(II)
cisnickel	cis-diamminedichloronickel(II)
DNA	Deoxyribonucleic acid
DFT	Density functional theory
FAM	6-carboxyfluorescein
FRET	Fluorescence resonance energy transfer
G / $\Delta$ G	Gibbs free energy / Gibbs free energy variation
H / $\Delta$ H	Enthalpy / Enthalpy variation
I	Ionic strength
KCl	Potassium chloride
kJ	Kilojoules
LiCaC	Lithium cacodilate, (CH <sub>3</sub> ) <sub>2</sub> AsO <sub>2</sub> Li
LiCl	Lithium chloride
M	Metal center
MD	Molecular dynamics
MM	Molecular mechanics
N7	Nitrogen 7 of a guanine residue
NaCaC	Sodium cacodylate, (CH <sub>3</sub> ) <sub>2</sub> AsO <sub>2</sub> Na

ns	nanoseconds
PDB	Protein data bank
QM	Quantum mechanics
RMSD	Root mean square deviation
$S / \Delta S$	Entropy /Entropy variation
$T_m / \Delta T_m$	Melting temperature / Melting temperature variation
TAMRA	6-carboxytetramethylrhodamine
TMPyP4	Tetra-(N-methyl-4-pyridyl) porphyrin

## Bibliography

1. Jemal A, Bray F, Center MM, Ferlay J, Ward E, Forman D. Global cancer statistics. *CA Cancer J Clin.* 61(2):69-90. doi:10.3322/caac.20107
2. Dobson J. John Hunter's Views on Cancer. *Ann R Coll Surg Engl.* 1959;25(2):176-181.
3. Watson JD, Crick FHC. Molecular Structure of Nucleic Acids: A Structure for Deoxyribose Nucleic Acid. *Nature.* 1953;171:737. <http://dx.doi.org/10.1038/171737a0>.
4. Crick F. On Protein Synthesis. *Symp Soc Exp Biol.* 1958;12:138-163.
5. Hanahan D, Weinberg RA. Hallmarks of Cancer: The Next Generation. *Cell.* 2011;144(5):646-674. doi:https://doi.org/10.1016/j.cell.2011.02.013
6. Sudhakar A. History of Cancer, Ancient and Modern Treatment Methods. *J Cancer Sci Ther.* 2009;1(2):1-4. doi:10.4172/1948-5956.100000e2
7. Alderden RA, Hall MD, Hambley TW. The Discovery and Development of Cisplatin. *J Chem Educ.* 2006;83(5):728. doi:10.1021/ed083p728
8. Saenger W. *Principles of Nucleic Acid Structure.* New York; 1984.
9. Kendrew JC, Lawrence E. *The Encyclopedia of Molecular Biology.* Oxford ; Cambridge, Mass., USA: Blackwell Science.; 1994.
10. Svozil D, Kalina J, Omelka M, Schneider B. DNA conformations and their sequence preferences. *Nucleic Acids Res.* 2008;36(11):3690-3706. doi:10.1093/nar/gkn260
11. Umehara T, Kuwabara S, Mashimo S, Yagihara S. Dielectric study on hydration of B-, A-, and Z-DNA. *Biopolymers.* 1990;30(7-8):649-656. doi:10.1002/bip.360300702
12. Dickerson REBT-M in E. [5] DNA structure from A to Z. In: *DNA Structures Part A: Synthesis and Physical Analysis of DNA.* Vol 211. Academic Press; 1992:67-111. doi:https://doi.org/10.1016/0076-6879(92)11007-6
13. Wang AH-J, Quigley GJ, Kolpak FJ, et al. Molecular structure of a left-handed double helical DNA fragment at atomic resolution. *Nature.* 1979;282:680-686. <http://dx.doi.org/10.1038/282680a0>.
14. Wing R, Drew H, Takano T, et al. Crystal structure analysis of a complete turn of B-DNA. *Nature.* 1980;287:755. <http://dx.doi.org/10.1038/287755a0>.
15. Hänsel R, Löhr F, Foldynová-Trantírková S, Bamberg E, Trantírek L, Dötsch V. The parallel G-quadruplex structure of vertebrate telomeric repeat sequences is not the preferred folding topology under physiological conditions. *Nucleic Acids Res.* 2011;39(13):5768-5775. doi:10.1093/nar/gkr174
16. Ou T, Lu Y, Tan J, Huang Z, Wong K-Y, Gu L. G-Quadruplexes: Targets in Anticancer Drug Design. *ChemMedChem.* 2008;3(5):690-713. doi:10.1002/cmdc.200700300
17. Brázda V, Hároníková L, Liao JCC, Fojta M. DNA and RNA Quadruplex-Binding Proteins. *Int J Mol Sci.* 2014;15(10):17493-17517. doi:10.3390/ijms151017493
18. Bhasikuttan AC, Mohanty J. Targeting G-quadruplex structures with extrinsic fluorogenic dyes: promising fluorescence sensors. *Chem Commun.* 2015;51(36):7581-7597. doi:10.1039/C4CC10030A

19. Burge S, Parkinson GN, Hazel P, Todd AK, Neidle S. Quadruplex DNA: sequence, topology and structure. *Nucleic Acids Res.* 2006;34(19):5402-5415. doi:10.1093/nar/gkl655
20. Qin Y, Hurley LH. Structures, folding patterns, and functions of intramolecular DNA G-quadruplexes found in eukaryotic promoter regions. *Biochimie.* 2008;90(8):1149-1171. doi:10.1016/j.biochi.2008.02.020
21. Adrian M, Heddi B, Phan AT. NMR spectroscopy of G-quadruplexes. *Methods.* 2012;57(1):11-24. doi:https://doi.org/10.1016/j.ymeth.2012.05.003
22. Huppert JL, Balasubramanian S. G-quadruplexes in promoters throughout the human genome. *Nucleic Acids Res.* 2007;35(2):406-413. doi:10.1093/nar/gkl1057
23. Cleare MJ, Hoeschele JD. Studies on the antitumor activity of group VIII transition metal complexes. Part I. Platinum (II) complexes. *Bioinorg Chem.* 1973;2(3):187-210. doi:https://doi.org/10.1016/S0006-3061(00)80249-5
24. Lim M., Martin RB. The nature of cis amine Pd(II) and antitumor cis amine Pt(II) complexes in aqueous solutions. *J Inorg Nucl Chem.* 38:1911-1914.
25. Brabec V, Kasparkova J. Modifications of DNA by platinum complexes: Relation to resistance of tumors to platinum antitumor drugs. *Drug Resist Updat.* 2005;8(3):131-146. doi:https://doi.org/10.1016/j.drug.2005.04.006
26. Lerman LS. Structural considerations in the interaction of DNA and acridines. *J Mol Biol.* 1961;3(1):18-30. doi:https://doi.org/10.1016/S0022-2836(61)80004-1
27. Berman HM, Young PR. The Interaction of Intercalating Drugs with Nucleic Acids. *Annu Rev Biophys Bioeng.* 1981;10(1):87-114. doi:10.1146/annurev.bb.10.060181.000511
28. Jennette KW, Gill JT, Sadowick JA, Lippard SJ. Metallointercalation reagents. Synthesis, characterization, and structural properties of thiolato(2,2',2''-terpyridine)platinum(II) complexes. *J Am Chem Soc.* 1976;98(20):6159-6168. doi:10.1021/ja00436a016
29. Biebricher AS, Heller I, Roijmans RFH, Hoekstra TP, Peterman EJG, Wuite GJL. The impact of DNA intercalators on DNA and DNA-processing enzymes elucidated through force-dependent binding kinetics. *Nat Commun.* 2015;6:7304. http://dx.doi.org/10.1038/ncomms8304.
30. Nafisi S, Sabourey AA, Keramat N, Neault JF, Tajmir-Riahi HA. Stability and structural features of DNA intercalation with ethidium bromide, acridine orange and methylene blue. *J Mol Struct.* 2007;827:35-43.
31. Canals A, Purciolas M, Aymam\`i J, Coll M. The anticancer agent ellipticine unwinds DNA by intercalative binding in an orientation parallel to base pairs. *Acta Crystallogr Sect D.* 2005;61(7):1009-1012. doi:10.1107/S0907444905015404
32. Cai X, Gray PJ, Von Hoff DD. DNA minor groove binders: Back in the groove. *Cancer Treat Rev.* 2009;35(5):437-450. doi:https://doi.org/10.1016/j.ctrv.2009.02.004
33. François JC, Saison-Behmoaras T, Hélène C. Sequence-specific recognition of the major groove of DNA by oligodeoxynucleotides via triple helix formation. Footprinting studies. *Nucleic Acids Res.* 1988;16(24):11431-11440. http://www.ncbi.nlm.nih.gov/pmc/articles/PMC339056/.
34. Hamy F, Asseline U, Grasby J, et al. Hydrogen-bonding Contacts in the Major Groove

- are required for Human Immunodeficiency Virus Type-1 tat Protein Recognition of TAR RNA. *J Mol Biol.* 1993;230(1):111-123.  
doi:<https://doi.org/10.1006/jmbi.1993.1129>
35. Nelson SM, Ferguson LR, Denny WA. Non-covalent ligand/DNA interactions: Minor groove binding agents. *Mutat Res Mol Mech Mutagen.* 2007;623(1):24-40.  
doi:<https://doi.org/10.1016/j.mrfmmm.2007.03.012>
  36. Baraldi PG, Bovero A, Fruttarolo F, et al. DNA minor groove binders as potential antitumor and antimicrobial agents. *Med Res Rev.* 2004;24(4):475-528.  
doi:10.1002/med.20000
  37. Vlieghe D, Sponer J, Meervelt L Van. Crystal Structure of d(GGCCAATTGG) Complexed with DAPI Reveals Novel Binding Mode,. *Biochemistry.* 1999;38(50):16443-16451.  
doi:10.1021/bi9907882
  38. Strekowski L, Wilson B. Noncovalent interactions with DNA: An overview. *Mutat Res Mol Mech Mutagen.* 2007;623(1):3-13.  
doi:<https://doi.org/10.1016/j.mrfmmm.2007.03.008>
  39. Wheelhouse RT, Sun D, Han H, Han FX, Hurley LH. Cationic Porphyrins as Telomerase Inhibitors: the Interaction of Tetra-(N-methyl-4-pyridyl)porphine with Quadruplex DNA. *J Am Chem Soc.* 1998;120(13):3261-3262. doi:10.1021/ja973792e
  40. Haider SM, Parkinson GN, Neidle S. Structure of a G-quadruplex–Ligand Complex. *J Mol Biol.* 2003;326(1):117-125. doi:[https://doi.org/10.1016/S0022-2836\(02\)01354-2](https://doi.org/10.1016/S0022-2836(02)01354-2)
  41. Gavathiotis E, Heald RA, Stevens MFG, Searle MS. Drug Recognition and Stabilisation of the Parallel-stranded DNA Quadruplex d(TTAGGGT)<sub>4</sub> Containing the Human Telomeric Repeat. *J Mol Biol.* 2003;334(1):25-36.  
doi:<https://doi.org/10.1016/j.jmb.2003.09.018>
  42. Bandeira S, Gonzalez-Garcia J, Pensa E, Albrecht T, Vilar R. A Redox-Activated G-Quadruplex DNA Binder Based on a Platinum(IV)–Salphen Complex. *Angew Chemie Int Ed.* 2017;57(1):310-313. doi:10.1002/anie.201709968
  43. Łęczkowska A, Gonzalez-Garcia J, Perez-Arnaiz C, Garcia B, White AJP, Vilar R. Binding Studies of Metal–Salphen and Metal–Bipyridine Complexes towards G-Quadruplex DNA. *Chem – A Eur J.* 2018;24(45):11785-11794. doi:10.1002/chem.201802248
  44. Fedoroff OY, Salazar M, Han H, Chemeris V V, Kerwin SM, Hurley LH. NMR-Based Model of a Telomerase-Inhibiting Compound Bound to G-Quadruplex DNA. *Biochemistry.* 1998;37(36):12367-12374. doi:10.1021/bi981330n
  45. Didenko V V. DNA Probes Using Fluorescence Resonance Energy Transfer (FRET): Designs and Applications. *Biotechniques.* 2001;31(5):1106-1121.
  46. Waring MJ. Complex formation between ethidium bromide and nucleic acids. *J Mol Biol.* 1965;13(1):269-282. doi:[https://doi.org/10.1016/S0022-2836\(65\)80096-1](https://doi.org/10.1016/S0022-2836(65)80096-1)
  47. Rodger, A.; Nordén B. *Circular Dichroism and Linear Dichroism.* 1st ed. Oxford University Press:Oxford; New York; 1997.
  48. Kypr J, Kejnovská I, Renčíuk D, Vorlíčková M. Circular dichroism and conformational polymorphism of DNA. *Nucleic Acids Res.* 2009;37(6):1713-1725.  
doi:10.1093/nar/gkp026
  49. Ranjbar B, Gill P. Circular Dichroism Techniques: Biomolecular and Nanostructural



- Analyses- A Review. *Chem Biol Drug Des.* 2009;74(2):101-120. doi:10.1111/j.1747-0285.2009.00847.x
50. Berova N, Nakanishi K, Woody RW. *Circular Dichroism: Principles and Applications.* 2nd ed. Wiley; 2000.
  51. Scruggs RL, Ross PD. Viscosity study of DNA. *Biopolymers.* 2018;2(6):593-609. doi:10.1002/bip.360020608
  52. Huang H-L, Liu Y-J, Zeng C-H, He L-X, Wu F-H. In Vitro Cytotoxicity, Apoptosis, DNA-Binding, and Antioxidant Activity Studies of Ruthenium (II) Complexes. *DNA Cell Biol.* 2010;29(5):261-270. doi:10.1089/dna.2009.0979
  53. Sastry KNV, Routhu SR, Datta SG, et al. Synthesis, DNA binding affinity and anticancer activity of novel 4H-benzo[g][1,2,3]triazolo[5,1-c][1,4]oxazocines. *Org Biomol Chem.* 2016;14(39):9294-9305. doi:10.1039/C6OB01077F
  54. Förster T. Zwischenmolekulare Energiewanderung und Fluoreszenz. *Ann Phys.* 1948;437(1-2):55-75. doi:10.1002/andp.19484370105
  55. Clegg RMBT-M in E. [18] Fluorescence resonance energy transfer and nucleic acids. In: *DNA Structures Part A: Synthesis and Physical Analysis of DNA.* Vol 211. Academic Press; 1992:353-388. doi:https://doi.org/10.1016/0076-6879(92)11020-J
  56. Lakowicz JR. *Principles of Fluorescence Spectroscopy.* 3rd ed. Springer US; 2006.
  57. De Cian A, Guittat L, Kaiser M, et al. Fluorescence-based melting assays for studying quadruplex ligands. *Methods.* 2007;42(2):183-195. doi:https://doi.org/10.1016/j.ymeth.2006.10.004
  58. Murat P, Singh Y, Defrancq E. Methods for investigating G-quadruplex DNA/ligand interactions. *Chem Soc Rev.* 2011;40(11):5293-5307. doi:10.1039/C1CS15117G
  59. Stewart JJP. Optimization of parameters for semiempirical methods V: Modification of NDDO approximations and application to 70 elements. *J Mol Model.* 2007;13(12):1173-1213. doi:10.1007/s00894-007-0233-4
  60. Zhao Y, Truhlar DG. The M06 suite of density functionals for main group thermochemistry, thermochemical kinetics, noncovalent interactions, excited states, and transition elements: Two new functionals and systematic testing of four M06-class functionals and 12 other function. *Theor Chem Acc.* 2008;120:215-241. doi:10.1007/s00214-007-0310-x
  61. Adamo C, Barone V. Toward reliable density functional methods without adjustable parameters: The PBE0 model. *J Chem Phys.* 1999;110(13):6158-6170. doi:10.1063/1.478522
  62. Becke AD. Density-functional thermochemistry. III. The role of exact exchange. *J Chem Phys.* 1993. doi:10.1063/1.464913
  63. Lee C, Yang W, Parr RG. Development of the Colle-Salvetti correlation-energy formula into a functional of the electron density. *Source Phys Rev B Condens Matter Mater Phys J.* 1988;109(2):37-785.
  64. Stevens WJ, Basch H, Krauss M. Compact effective potentials and efficient shared-exponent basis sets for the first-and second-row. *J Chem Phys.* 1984;81:6026.
  65. Stevens WJ, Krauss M, Basch H, Jasien PG. Relativistic compact effective potentials and

- efficient, shared-exponent basis sets for the third-, fourth-, and fifth-row atoms. *Can J Chem*. 1992;70:612-630. doi:10.1139/v92-085
66. Cundari TR, Stevens WJ. Effective core potential methods for the lanthanides. *J Chem Phys*. 1993;98(7):5555-5565. doi:10.1063/1.464902
67. Petersson GA, Bennett A, Tensfeldt TG, Al-Laham MA, Shirley WA, Mantzaris J. A complete basis set model chemistry. I. The total energies of closed-shell atoms and hydrides of the first-row elements. *J Chem Phys*. 1988. doi:10.1063/1.455064
68. Barone V, Cossi M. Quantum calculation of molecular energies and energy gradients in solution by a conductor solvent model. *J Phys Chem A*. 1998. doi:10.1021/jp9716997
69. Cossi M, Rega N, Scalmani G, Barone V. Energies, structures, and electronic properties of molecules in solution with the C-PCM solvation model. *J Comput Chem*. 2003;24:669-681. doi:10.1002/jcc.10189
70. Peng C, Bernhard Schlegel H. Combining Synchronous Transit and Quasi-Newton Methods to Find Transition States. *Isr J Chem*. 1993;33(4):449-454. doi:10.1002/ijch.199300051
71. Frisch, M. J.; Trucks, G. W.; Schlegel, H. B.; Scuseria, G. E.; Robb, M. A.; Cheeseman, J. R.; Scalmani, G.; Barone, V.; Petersson, G. A.; Nakatsuji, H.; Li, X.; Caricato, M.; Marenich, A.; Bloino, J.; Janesko, B. G.; Gomperts, R.; Mennucci, B.; Hratchian, DJ. No Title. 2016.
72. Kramer CJ. *Essentials of Computational Chemistry: Theories and Models*. 2nd ed. USA: Wiley; 2004.
73. Lindorff-Larsen K, Maragakis P, Piana S, Eastwood MP, Dror RO, Shaw DE. Systematic Validation of Protein Force Fields against Experimental Data. *PLoS One*. 2012;7(2):e32131. <https://doi.org/10.1371/journal.pone.0032131>.
74. Pérez A, Luque FJ, Orozco M. Frontiers in Molecular Dynamics Simulations of DNA. *Acc Chem Res*. 2012;45(2):196-205. doi:10.1021/ar2001217
75. Sagui C, Darden TA. MOLECULAR DYNAMICS SIMULATIONS OF BIOMOLECULES: Long-Range Electrostatic Effects. *Annu Rev Biophys Biomol Struct*. 1999;28(1):155-179. doi:10.1146/annurev.biophys.28.1.155
76. Wang J, Wolf RM, Caldwell JW, Kollman PA, Case DA. Development and testing of a general amber force field. *J Comput Chem*. 2004;25(9):1157-1174. doi:10.1002/jcc.20035
77. Wang J, Wang W, Kollman PA, Case DA. Automatic atom type and bond type perception in molecular mechanical calculations. *J Mol Graph Model*. 2006;25(2):247-260. doi:<https://doi.org/10.1016/j.jmgm.2005.12.005>
78. Van Der Spoel D, Lindahl E, Hess B, Groenhof G, Mark AE, Berendsen HJC. GROMACS: Fast, flexible, and free. *J Comput Chem*. 2005;26(16):1701-1718. doi:10.1002/jcc.20291
79. Hess B, Kutzner C, van der Spoel D, Lindahl E. GROMACS 4: Algorithms for Highly Efficient, Load-Balanced, and Scalable Molecular Simulation. *J Chem Theory Comput*. 2008;4(3):435-447. doi:10.1021/ct700301q
80. Pérez A, Marchán I, Svozil D, et al. Refinement of the AMBER Force Field for Nucleic Acids: Improving the Description of  $\alpha/\gamma$  Conformers. *Biophys J*. 2007;92(11):3817-

3829. doi:10.1529/biophysj.106.097782

81. Guy AT, Piggot TJ, Khalid S. Single-Stranded DNA within Nanopores: Conformational Dynamics and Implications for Sequencing; a Molecular Dynamics Simulation Study. *Biophys J*. 2012;103(5):1028-1036. doi:https://doi.org/10.1016/j.bpj.2012.08.012
82. Chung LW, Sameera WMC, Ramozzi R, et al. The ONIOM Method and Its Applications. *Chem Rev*. 2015;115(12):5678-5796. doi:10.1021/cr5004419
83. HONIG B, KARPLUS M. Implications of Torsional Potential of Retinal Isomers for Visual Excitation. *Nature*. 1971;229:558. http://dx.doi.org/10.1038/229558a0.
84. Warshel A, Karplus M. Calculation of ground and excited state potential surfaces of conjugated molecules. I. Formulation and parametrization. *J Am Chem Soc*. 1972;94(16):5612-5625. doi:10.1021/ja00771a014
85. Levitt M, Greer J. Automatic identification of secondary structure in globular proteins. *J Mol Biol*. 1977;114(2):181-239. doi:https://doi.org/10.1016/0022-2836(77)90207-8
86. Senn HM, Thiel W. QM/MM Methods for Biomolecular Systems. *Angew Chemie Int Ed*. 2009;48(7):1198-1229. doi:10.1002/anie.200802019
87. Vreven T, Morokuma K. *Chapter 3 Hybrid Methods: ONIOM(QM:MM) and QM/MM*. Vol 2.; 2006. doi:10.1016/S1574-1400(06)02003-2
88. *Global Cancer - Facts & Figures*. third edit. Atlanta: American Cancer Society; 2015.
89. Galluzzi L, Senovilla L, Vitale I, et al. Molecular mechanisms of cisplatin resistance. *Oncogene*. 2011;31:1869. http://dx.doi.org/10.1038/onc.2011.384.
90. Florea A-M, Buesselberg D. Cisplatin as an anti-tumor drug: cellular mechanisms of activity, drug resistance and induced side effects. *Cancers (Basel)*. 2011;3:1351-1371. doi:10.3390/cancers3011351
91. Yan YK, Melchart M, Habtemariam A, Sadler PJ. Organometallic chemistry, biology and medicine: ruthenium arene anticancer complexes. *Chem Commun*. 2005;(38):4764-4776. doi:10.1039/B508531B
92. Süß-Fink G. Arene ruthenium complexes as anticancer agents. *Dalt Trans*. 2010;39(7):1673-1688. doi:10.1039/B916860P
93. Martínez-Alonso M, Busto N, Jalón FA, et al. Derivation of Structure–Activity Relationships from the Anticancer Properties of Ruthenium(II) Arene Complexes with 2-Aryldiazole Ligands. *Inorg Chem*. 2014;53(20):11274-11288. doi:10.1021/ic501865h
94. Aird RE, Cummings J, Ritchie AA, et al. In vitro and in vivo activity and cross resistance profiles of novel ruthenium (II) organometallic arene complexes in human ovarian cancer. *Br J Cancer*. 2002;86:1652. http://dx.doi.org/10.1038/sj.bjc.6600290.
95. Yellol GS, Donaire A, Yellol JG, Vasylyeva V, Janiak C, Ruiz J. On the antitumor properties of novel cyclometalated benzimidazole Ru(ii), Ir(iii) and Rh(iii) complexes. *Chem Commun*. 2013;49(98):11533-11535. doi:10.1039/C3CC46239K
96. Hong-Ke L, J. BS, Fuyi W, et al. Diversity in Guanine-Selective DNA Binding Modes for an Organometallic Ruthenium Arene Complex. *Angew Chemie Int Ed*. 2006;45(48):8153-8156. doi:10.1002/anie.200602873
97. Liu H-K, Parkinson JA, Bella J, Wang F, Sadler PJ. Penetrative DNA intercalation and G-

- base selectivity of an organometallic tetrahydroanthracene Rull anticancer complex. *Chem Sci*. 2010;1(2):258-270. doi:10.1039/C0SC00175A
98. Liu Z, Habtemariam A, Pizarro AM, et al. Organometallic half-sandwich iridium anticancer complexes. *J Med Chem*. 2011;54(8):3011-3026. doi:10.1021/jm2000932
  99. Chen H, Parkinson JA, Parsons S, Coxall RA, Gould RO, Sadler PJ. Organometallic Ruthenium(II) Diamine Anticancer Complexes: Arene-Nucleobase Stacking and Stereospecific Hydrogen-Bonding in Guanine Adducts. *J Am Chem Soc*. 2002;124(12):3064-3082. doi:10.1021/ja017482e
  100. Pérez-Arnaiz C, Busto N, Santolaya J, Leal JM, Barone G, García B. Kinetic evidence for interaction of TMPyP4 with two different G-quadruplex conformations of human telomeric DNA. *Biochim Biophys Acta - Gen Subj*. 2018;1862(3):522-531. doi:https://doi.org/10.1016/j.bbagen.2017.10.020
  101. Martínez Alonso M. Ph.D. Thesis "Synthesis and Characterization of Ru(II), Rh(III) and Ir(III) Complexes Bearing Arylazole Ligands. Applications in Anticancer Chemotherapy, LEC devices and Photocatalysis." 2017.
  102. Natalia B, Patricia C, Javier S, et al. FISHING G- QUADRUPLEXES IN SOLUTION WITH A PERYLENE DIIMIDE DERIVATIVE LABELED WITH BIOTINS. *Chem – A Eur J*. 2018;0(ja). doi:10.1002/chem.201802365
  103. Rackers, J.A., Laury, M.L., Chao, L, Wang, Z., Lagardère, L., Piquemal, J.P., Ren, P., Ponder JW. TINKER 8: A Modular Software Package for Molecular Design and Simulation. 2017.
  104. Adebayo A, Peter A. Exploring the Ruthenium-Ligands Bond and Their Relative Properties at Different Computational Methods. *J Chem*. 2016:15. doi:https://doi.org/10.1155/2016/3672062.
  105. Banci, L., Comba P. *Molecular Modeling and Dynamics of Bioinorganic Systems*. first. Springer Science + Business Media; 1997.
  106. Hay PJ, Wadt WR. Ab initio effective core potentials for molecular calculations. Potentials for the transition metal atoms Sc to Hg. *J Chem Phys*. 1985;82(1):270-283. doi:10.1063/1.448799
  107. Busto N, Martínez-Alonso M, Leal JM, et al. Monomer–Dimer Divergent Behavior toward DNA in a Half-Sandwich Ruthenium(II) Aqua Complex. Antiproliferative Biphasic Activity. *Organometallics*. 2015;34(1):319-327. doi:10.1021/om5011275
  108. Busto N, Valladolid J, Martínez-Alonso M, et al. Anticancer Activity and DNA Binding of a Bifunctional Ru(II) Arene Aqua-Complex with the 2,4-Diamino-6-(2-pyridyl)-1,3,5-triazine Ligand. *Inorg Chem*. 2013;52(17):9962-9974. doi:10.1021/ic401197a
  109. Valladolid J, Hortigüela C, Busto N, et al. Phenanthroline ligands are biologically more active than their corresponding ruthenium(ii) arene complexes. *Dalt Trans*. 2014;43(6):2629-2645. doi:10.1039/C3DT52743C
  110. Cerón-Carrasco JP, Ruiz J, Vicente C, et al. DFT Simulation of Structural and Optical Properties of 9-Aminoacridine Half-Sandwich Ru(II), Rh(III), and Ir(III) Antitumoral Complexes and Their Interaction with DNA. *J Chem Theory Comput*. 2017;13(8):3898-3910. doi:10.1021/acs.jctc.7b00139
  111. Brandhorst K, Grunenberg J. Efficient computation of compliance matrices in

- redundant internal coordinates from Cartesian Hessians for nonstationary points. *J Chem Phys*. 2010;132(18):184101. doi:10.1063/1.3413528
112. Brandhorst K, Grunenberg J. How strong is it? The interpretation of force and compliance constants as bond strength descriptors. *Chem Soc Rev*. 2008;37(8):1558-1567. doi:10.1039/B717781J
  113. Clarke ML. Recent advances in homogeneous catalysis using platinum complexes. *Polyhedron*. 2001;20(3):151-164. doi:https://doi.org/10.1016/S0277-5387(00)00634-3
  114. Rimoldi I, Coccè V, Facchetti G, et al. Uptake-release by MSCs of a cationic platinum(II) complex active in vitro on human malignant cancer cell lines. *Biomed Pharmacother*. 2018;108:111-118. doi:https://doi.org/10.1016/j.biopha.2018.09.040
  115. Meng T, Qin Q-P, Wang Z-R, et al. Synthesis and biological evaluation of substituted 3-(2'-benzimidazolyl)coumarin platinum(II) complexes as new telomerase inhibitors. *J Inorg Biochem*. 2018;189:143-150. doi:https://doi.org/10.1016/j.jinorgbio.2018.09.004
  116. Alberts, B., Johnson, A., Lewis, J., Raff, M., Roberts, K. and Walter P. *Molecular Biology of the Cell*. fourth. New York; 2002.
  117. Lippard SJ. New chemistry of an old molecule: cis-[Pt(NH<sub>3</sub>)<sub>2</sub>Cl<sub>2</sub>]. *Science (80- )*. 1982;218(4577):1075 LP-1082. <http://science.sciencemag.org/content/218/4577/1075.abstract>.
  118. Komeda S, Lutz M, Spek AL, et al. A Novel Isomerization on Interaction of Antitumor-Active Azole-Bridged Dinuclear Platinum(II) Complexes with 9-Ethylguanine. Platinum(II) Atom Migration from N2 to N3 on 1,2,3-Triazole. *J Am Chem Soc*. 2002;124(17):4738-4746. doi:10.1021/ja0168559
  119. Poklar N, Pilch DS, Lippard SJ, Redding EA, Dunham SU, Breslauer KJ. Influence of cisplatin intrastrand crosslinking on the conformation, thermal stability, and energetics of a 20-mer DNA duplex. *Proc Natl Acad Sci U S A*. 1996;93(15):7606-7611. <https://www.ncbi.nlm.nih.gov/pubmed/8755522>.
  120. Coste F, Malinge JM, Serre L, et al. Crystal structure of a double-stranded DNA containing a cisplatin interstrand cross-link at 1.63 Å resolution: hydration at the platinated site. *Nucleic Acids Res*. 1999;27(8):1837-1846. <https://www.ncbi.nlm.nih.gov/pubmed/10101191>.
  121. Jakupec, M.A., Galanski, M. and Keppler BK. Tumour-inhibiting platinum complexes—state of the art and future perspectives. In: *Reviews of Physiology, Biochemistry and Pharmacology*. ; 2003:1-53.
  122. Alberto ME, Lucas MFA, Pavelka M, Russo N. The Second-Generation Anticancer Drug Nedaplatin: A Theoretical Investigation on the Hydrolysis Mechanism. *J Phys Chem B*. 2009;113(43):14473-14479. doi:10.1021/jp9056835
  123. Kettunen ASA-S and M. Platinum Group Antitumor Chemistry: Design and development of New Anticancer Drugs Complementary to Cisplatin. *Curr Med Chem*. 2006;13(11):1337-1357. doi:http://dx.doi.org/10.2174/092986706776872970
  124. Cochran K, Forde G, Hill GA, Gorb L, Leszczynski J. cis-Diamminodichloronickel and Its Interaction with Guanine and Guanine–Cytosine Base Pair. *Struct Chem*. 2002;13(2):133-140. doi:10.1023/A:1015752431266

125. Lau JK-C, Ensing B. Hydrolysis of cisplatin—a first-principles metadynamics study. *Phys Chem Chem Phys*. 2010;12:10348-10355. doi:10.1039/b918301a
126. Kuduk-Jaworska J, Chojnacki H, Jański JJ. Non-empirical quantum chemical studies on electron transfer reactions in trans- and cis-diamminedichloroplatinum(II) complexes. *J Mol Model*. 2011;17(9):2411-2421. doi:10.1007/s00894-011-1060-1
127. Sarmah P, Deka RC. Hydrolysis and binding mechanism of AMD473 (cis-[PtCl<sub>2</sub>(NH<sub>3</sub>)(2-picoline)]) with guanine: A quantum mechanical study. *J Mol Struct THEOCHEM*. 2010;955:53-60. doi:10.1016/j.theochem.2010.05.030
128. Pavelka M, Lucas MFA, Russo N. On the Hydrolysis Mechanism of the Second-Generation Anticancer Drug Carboplatin. *Chem – A Eur J*. 2007;13(36):10108-10116. doi:10.1002/chem.200700887
129. Schaftenaar G, Vlieg E, Vriend G. Molden 2.0: quantum chemistry meets proteins. *J Comput Aided Mol Des*. 2017;31(9):789-800. doi:10.1007/s10822-017-0042-5
130. Schaftenaar G, Noordik JH. Molden: a pre- and post-processing program for molecular and electronic structures\*. *J Comput Aided Mol Des*. 2000;14(2):123-134. doi:10.1023/A:1008193805436
131. Yao S, Plastaras JP, Marzilli LG. A Molecular Mechanics AMBER-Type Force Field for Modeling Platinum Complexes of Guanine Derivatives. *Inorg Chem*. 1994;33(26):6061-6077. doi:10.1021/ic00104a015
132. Takahara PM, Rosenzweig AC, Frederick CA, Lippard SJ. Crystal structure of double-stranded DNA containing the major adduct of the anticancer drug cisplatin. *Nature*. 1995;377:649. <https://doi.org/10.1038/377649a0>.
133. Dai J, Punchihewa C, Ambrus A, Chen D, Jones RA, Yang D. Structure of the intramolecular human telomeric G-quadruplex in potassium solution: a novel adenine triple formation. *Nucleic Acids Res*. 2007;35(7):2440-2450. doi:10.1093/nar/gkm009
134. Dai J, Carver M, Punchihewa C, Jones RA, Yang D. Structure of the Hybrid-2 type intramolecular human telomeric G-quadruplex in K<sup>+</sup> solution: insights into structure polymorphism of the human telomeric sequence. *Nucleic Acids Res*. 2007;35(15):4927-4940. <http://dx.doi.org/10.1093/nar/gkm522>.
135. Gómez-Pinto I, Vengut-Climent E, Lucas R, et al. Carbohydrate–DNA Interactions at G-Quadruplexes: Folding and Stability Changes by Attaching Sugars at the 5'-End. *Chem – A Eur J*. 2013;19(6):1920-1927. doi:10.1002/chem.201203902
136. Chambers VS, Marsico G, Boutell JM, Di Antonio M, Smith GP, Balasubramanian S. High-throughput sequencing of DNA G-quadruplex structures in the human genome. *Nat Biotechnol*. 2015;33:877. <https://doi.org/10.1038/nbt.3295>.
137. Bedrat A, Lacroix L, Mergny J-L. Re-evaluation of G-quadruplex propensity with G4Hunter. *Nucleic Acids Res*. 2016;44(4):1746-1759. <http://dx.doi.org/10.1093/nar/gkw006>.
138. Bochman ML, Paeschke K, Zakian VA. DNA secondary structures: stability and function of G-quadruplex structures. *Nat Rev Genet*. 2012;13:770. <https://doi.org/10.1038/nrg3296>.
139. Rhodes D, Lipps HJ. G-quadruplexes and their regulatory roles in biology. *Nucleic Acids Res*. 2015;43(18):8627-8637. <http://dx.doi.org/10.1093/nar/gkv862>.

140. Gama S, Rodrigues I, Mendes F, et al. Anthracene-terpyridine metal complexes as new G-quadruplex DNA binders. *J Inorg Biochem.* 2016;160:275-286.  
doi:<https://doi.org/10.1016/j.jinorgbio.2016.04.002>
141. Zhou C-Q, Liao T-C, Li Z-Q, et al. Dinickel-Salphen Complexes as Binders of Human Telomeric Dimeric G-Quadruplexes. *Chemistry.* 2017;23(19):4713-4722.  
doi:10.1002/chem.201700276





# Annexed

---

PERSONAL INFORMATION



Javier Santolaya Rubio

C/ José María Codón 45 4º C.P. 09007, Burgos, Spain

+34-947 47.690 +34 659307280

javito2408@hotmail.com

Sex Male | Date of birth 24/08/1991 | Nationality Spanish

JOB APPLIED FOR POSITION  
PREFERRED JOB STUDIES APPLIED FOR  
PERSONAL STATEMENT

Chemical researcher, R+D (research and development)

WORK EXPERIENCE

**Nov 2015- 2018** Scholarship, for a co-tutorship doctorate between Burgos and Palermo universities.

**Nov 2014 – Nov 2015, L'oreal** Work in production area.

**Feb 2014 – May 2014** Practices limit for 2 months in the company **Hispanagar** as a laboratory technician, with a subsequent extension of 2 months working in the company.

EDUCATION AND TRAINING

**Nov 2015-Nowadays** Ph.D in co-tutorship between Universidad de Burgos, doctorate course "Química avanzada" and Università degli studi di Palermo XXXI ciclo "Scienze molecolare e biomolecolare".

**2014-2015** Master's in advanced chemistry, Faculty of Science, University of Burgos.

**2009 -2014** Degree in Chemistry, Faculty of Science, University of Burgos.

**2003-2009** Compulsory secondary education and Health Sciences baccaureate in "Blanca de Castilla" school in Burgos.

PERSONAL SKILLS

Mother tongue(s) Spanish

Other language(s)

English

UNDERSTANDING		SPEAKING		WRITING
Listening	Reading	Spoken interaction	Spoken production	
B2	B2	B2	B2	B2

Italian

First				
B1	B1	B1	B1	A2

Communication skills

- Dissemination of research results including attended to congresses, conferences, and presentations.
- Good oral presentation skills acquired during the university studies.

Organisational / managerial skills

- Ability to work in a team and autonomously.
- Adaptability to multicultural environments.

Job-related skills

- Capacity for organization and planning when carrying out work or team projects.
- Good skills in communication skills acquired during my college experience and personal life.

Digital competence

SELF-ASSESSMENT

Information processing	Communication	Content creation	Safety	Problem solving
Independent user	Independent user	Independent user	Independent user	Independent user

Computer skills:

- Good knowledge of Microsoft Office and Open Office programs.
- Good knowledge of programs such as Mapple, Matlab, Scilab, Mestrenova and ChemSketch, Table curve, acquired during the Chemistry Degree and Master.
- Basic knowledge of graphic design of Photoshop and Adobe illustrator.
- Good knowledge of the programs *Gromacs* and *Gaussian*, acquired during the Ph.D., and of other software related with computational chemistry.
- Good knowledge of Linux and Windows operating systems

Driving licence

B1

ADDITIONAL INFORMATION

Presentations

Projects

Conferences

Seminars

Honours and awards

Publications

- 4<sup>th</sup> Research Biotechnology meeting, 2016 Dec 15-16, Palermo, Italy. "Guiseppe Albeggiani" prize for the most creative poster.
- 13<sup>th</sup> European Biological Inorganic Chemistry Conference (Eurobic13), poster presentation.
- Scifinder seminar.
- Schöridinger on-line seminars.
- Cristina Pérez-Arnaiz, Natalia Busto, Javier Santolaya, José M. Leal, Giampaolo Barone, Begoña García. Kinetic evidence for interaction of TMPyP4 with two different G-quadruplex conformations of human telomeric DNA, *BBA general subjects*. 1862 (2018) 522-531. doi: 10.1016/j.bbagen.2017.10.020
- Natalia Busto, Patricia Calvo, Javier Santolaya, José M Leal, Aurore Guédin, Giampaolo Barone, Tomás Torroba, Jean-Louis Mergny, and Begoña García. Fishing for G-quadruplex in solution with a perylene diimide derivative labeled with biotins, *Chem. Eur. J.* 24 (2018) 1-6. doi: 10.1002/chem.201802365
- Cristina Pérez-Arnaiz, Jorge Leal, Natalia Busto, María C. Carrión, Ana R. Rubio, Imanol Ortiz, Giampaolo Barone, Borja Díaz de Greñu, Javier Santolaya, JoséM. Leal, Mónica Vaquero, Félix A. Jalón, Blanca R. Manzano, and Begoña García. Role of seroalbumin in the cytotoxicity of cis-dichloro Pt(II) complexes with (N^N)-donor ligands bearing functionalized tails, *Inorganic Chemistry*. 57 (2018) 6124-6134. doi:10.1021/acs.inorgchem.8b00713





